Numerical Modelling of Strain Localisation and Failure in Dry/unsaturated Soils Using the Smoothed Particle Hydrodynamics Method

By

Shaohan Zhao

B.Eng. (First class honour)

A thesis submitted for the degree of Doctor of Philosophy at

Monash University in 2019

Department of Civil Engineering

This page is intentionally left blank

Copyright notice

© The author (2019).

I certify that I have made all reasonable efforts to secure copyright permissions for third-party content included in this thesis and have not knowingly added copyright content to my work without the owner's permission.

Abstract

Localisation failure is a mechanical phenomenon that has been observed in a wide variety of soils under dry, unsaturated and saturated conditions, which manifests as a distinct volume of displacement/strain field that embeds inside a soil bulk and signals the loss of material strength under certain boundary conditions. Although advancement has been made to the understanding of the localisation failure in soils from both theoretical and numerical perspectives, the current applications using a variety of numerical methods are not able to fully characterise the evolution of this phenomenon. The framework for the numerical modelling of geomechanical problems involving large deformation and localised failure is still not well established.

Therefore, this work focuses on the development of an advanced computational framework that is able to well capture both the onset and post-bifurcation regime of the strain localisation and its related failure process for dry and unsaturated soils. In the meantime, this framework preserves a very good computational efficiency for allowing capture of any large scale engineering problems. In particular, this framework is based on a continuum particle method smoothed particle hydrodynamics (SPH) featured with Lagrangian meshfree and nonlocal characteristics, which will allow a natural capture of strain localisation process without special regularisation technique. In parallel with this, an rigorous constituive framework that captures the strain softening process based on the fully coupled unsaturated soil mechanics and the elastoplasticity theory has been proposed and implemented in the SPH.

The primary outcome of this research consists of three main phases: first, a generic approach is proposed in SPH to modelling the confining boundary condition on flexible free surfaces. This method is demonstrated capable of continuously enforcing confinement while automatically tracking the curvature change of free surface boundaries under large deformation conditions; second, a rigorous elastoplastic model with strain softening Mohr-Coulomb yield surface is implemented into SPH, which is featured with a nonlocal plastic limiter that fully regularises the energy dissipation for modelling post-localisation problems. This framework is able to capture the material characteristic length effect, which predicts localised shear bands without dependency on the variation of numerical resolutions; third, a fully-coupled three-phase (solid, liquid, air) numerical framework is implemented into SPH for allowing the capture of unsaturated soil behaviours. A Mohr-Coulomb model featured with suction dependent state parameters is also considered, which enables characterising geomechanical problems including water infiltration in the soil bulk, rainfall-induced slope failure etc. The

above proposed approaches have been validated with either theoretical solutions or experimental results, as well as applied to simulate practical engineering applications. Therefore, taking advantage of the above-proposed framework, SPH can now be applied to solve an extensive range of geotechnical engineering problems.

Declaration

This thesis is an original work of my research and contains no material which has been accepted for the award of any other degree or diploma at any university or equivalent institution and that, to the best of my knowledge and belief, this thesis contains no material previously published or written by another person, except where due reference is made in the text of the thesis.

Signature:

Print Name: Shaohan Zhao

Date: 25th September 2019

List of publications

Journal articles

Zhao, S., Bui, H. H., Lemiale, V., Nguyen, G. D., & Darve, F. (2019). A generic approach to modelling flexible confined boundary conditions in SPH and its application. International Journal for Numerical and Analytical Methods in Geomechanics, 43(5), 1005-1031.

Zhao, S., Bui, H. H., Lemiale, V., Nguyen, G. D., A study of local and nonlocal features and its application to modelling strain localisation in geomaterials. International Journal for Numerical and Analytical Methods in Geomechanics. (in preparation).

Zhao, S., Bui, H. H. et al., A fully coupled three-phase SPH framework for unsaturated soils. Geotechnique. (in preparation).

Zhao, S., Bui, H. H. et al, Modelling rainfall-induced shallow landslides using a multi-phase SPH model for unsaturated soils., Journal of Geotechnical and Geoenvironmental Engineering. (in preparation).

Conference papers

Zhao, S., Bui, H. H., Lemiale, V., & Nguyen, G. D. (2017). SPH Simulation of Strain Localisation in Geomaterials Using a Visco-Plastic Constitutive Model. In Poromechanics VI (pp. 1876-1883).

Zhao, S., Bui, H. H., Lemiale, V., & Nguyen, G. D. (2017). Numerical modelling of shear band localisation in biaxial test with Smoothed Particle Hydrodynamics method. In 9th Australasian Congress on Applied Mechanics (ACAM9) (p. 842). Engineers Australia.

Thesis including published works declaration

I hereby declare that this thesis contains no material which has been accepted for the award of any other degree or diploma at any university or equivalent institution and that, to the best of my knowledge and belief, this thesis contains no material previously published or written by another person, except where due reference is made in the text of the thesis. The copyright consent of all republishing sketches that are used in this thesis have been sought where applicable.

This thesis includes one paper published in peer-reviewed journals. The core theme of the thesis is to establish an advanced computational framework based on the Lagrangian meshfree method SPH to capture the localised failure process in dry and saturated soils. The ideas, development and writing up of all the papers in the thesis were the principal responsibility of myself, the student, working within the Department of Civil Engineering under the supervision of Dr. Ha Hong Bui. The inclusion of co-authors reflects the fact that the work came from active collaboration between researchers and acknowledges input into team-based research.

In the case of Chapter 3 my contribution to the work involved the following:

Thesis Chapter	***Publication title***	***Status***	***Nature and % of student contribution***	***Co-author name(s) Nature and % of Co-author's contribution****	***Co-author(s), Monash student Y/N****
Chapter 4	A generic approach to modelling flexible confined boundary conditions in SPH and its application	Published	70%. Idea, doing experiments, analysis, interpretation and writing up	1. Ha H. Bui, technical review, interpretation and input into manuscript 15% 2. Vincent Lemiale, manuscript review, input into manuscript 5% 3. Giang D. Nguyen technical review input into manuscript 5% 4. Félix Darve manuscript review input into manuscript 5%	No

I have renumbered sections of published papers in order to generate a consistent presentation within the thesis.

I have renumbered sections of published papers in order to generate a consistent presentation within the thesis.

Student name: Shaohan Zhao

Student signature: Date: 25th September 2019

The undersigned hereby certify that the above declaration correctly reflects the nature and extent of the student's and co-authors' contributions to this work. In instances where I am not the responsible author I have consulted with the responsible author to agree on the respective contributions of the authors.

Main Supervisor name: Ha Hong Bui

Main Supervisor signature: Date: 25th September 2019

Acknowledgement

First and foremost, I would like to express the greatest gratitude to my principal supervisor Dr Ha Hong Bui. His invaluable advice and guidance have led me through my PhD research in the past few years. His spirit and passion towards the research are the most inspiring characters that encourage me to ever puisuit a higher quality of my work. His tremendous support helps me quickly adapt to both the research and career life. The skills and code of conduct that Dr Ha helps me to build up in the intensive working practice during my PhD experience are the most precious gifts that would ever follow me.

I would also like to thank very much my associate supervisor Dr Vincent Lemiale for his great support and valuable advice for my research work. His effort has facilitated not only the advancement of my research but also the establishment of my career. The advice and dedication from my associate supervisor A. Professor Giang D. Nguyen are also greatly appreciated. The discussion with him on some difficult research knots during my PhD journey has helped me a lot. I would also like to thank Professor Félix Darve at Polytechnique de Grenoble for providing insightful comments for improving my research and paper.

I am grateful to Lilian Khaw and Jane Moodie for their help and effort in improving the quality and proofreading of my thesis.

I acknowledge Monash University, CSIRO and Australian Research Council for providing finial support which helps me to focus on my research work.

I also thank all the MCG members and friends for making such an inclusive and supportive environment within our research group, which is like a greenhouse for sapling to grow.

Lastly, I would give my heartful thank to my wife Yingnan Wang who is also a colleague and teammate. Without her support, I would never make this far. Thank her for bringing me the most beautiful baby boy Henry, who has initiated a new chapter of my life. I also thank the full support from both my parents and Yingnan's parents for helping take care of the family during the busiest time of our research.

Shaohan Zhao

September 2019

Table of contents

List of figures

List of tables

Chapter 1

Introduction

1.1 Problem background

In the context of geomechanical engineering, strain localisation is generally described as the transition of mechanical states of material from pure resilient to non-resilient deformation which concentrates into certain areas within the material bulk (Desrues & Viggiani, 2004). The concentrated deformation area could merge and follow certain persistent patterns. Within the localised area, the micro-scale material characters such as grain distribution, moisture content and fibre evolution undergo highly dynamic kinematics. The elastic energy absorbed from the boundary condition is dissipated rapidly in a thermodynamics form within shear bands, sometimes manifesting as the fast evaporation and volume expansion of the capillary water content (Pinyol et al., 2012). Therefore, it is a highly unstable form of energy transformation, which may lead to a rapid loss of material integrity and the capacity for load-bearing.

Since strain localisation marks the transition from stable to unstable material behaviours, it is normally a precursor of geo-hazard events including soil cracking, embankment failure, debris flow, landslide and etc. (Figure 1.1) (Gao & Zhao, 2013), which in many cases lead to significant financial losses or human casualties. For example, a recent spatiotemporal study of the global landslide databases shows that there happened 4,862 landslides events during the year of 2004 to 2016, leading to a staggering number of 55,997 fatalities (Froude & Petley, 2018). Australia is one of the least affected countries by landslide events, nevertheless still witnessed 114 occurrences and 138 casualties during the year of 1842 to 2011 (Leiba, 2013). Therefore the comprehension of the mechanism for strain localisation phenomena underpins a safe design for civil infrastructures such as retaining wall, soil embankment, earth dam etc. At the current stage, this is normally achieved by applying high safety factors in practice which in many cases result in designs with unnecessarily high cost-benefit ratios. Therefore, there is a significant need for obtaining an understanding of localised deformation from both theoretical and experimental point of view.

The characterisation of the localisation phenomenon in geomaterials can be traced back to Coulomb's study on the stability of retaining wall in the 18th century, where Coulomb emphasised the localisation nature of soil during retaining wall failures (Coulomb, 1773). Since then, numerous experimental tests have been conducted to reproduce strain localisation in geomaterials to acquire a better understanding of its mechanism. For instance, Handin and co-workers conducted a series of axisymmetric triaxial tests on sedimentary rocks regarding the effect of confining stress, pore pressure and temperature of samples. A large range of confining pressures up to 300 atmospheres and temperature up to 300-degree Celsius were applied, which concluded that rock behaviours become ductile with increasing confinement and the peak strength reduces with increasing temperature. All test results showed an initially homogenous deformation pattern and then a bifurcation in the strain field around peak strength, followed by a localised shear band and loss of cohesion of the material (Handin et al, 1957; 1958; 1963). Other tests that focus on the analogous test apparatus demonstrated a similar pattern of material damage or loss of integrity due to the localised strain field which eventually lead to fractures or faults (Paterson 1958; Wawersik & Fairhurst, 1970; Brace 1972; Evans et al., 1990; Olsson 1999; Lenoir et al., 2007; Das et al., 2013). Laboratory plane strain biaxial and axisymmetric triaxial tests conducted on ductile geomaterials including silt, clay, sand and gravels show localised shear bands with much thicker shear zones, while demonstrating a relatively small energy dissipation rate compared to rock and a more ductile behaviour (Vardoulakis 1980; Desrues et al., 1985; Bésuelle et al., 2000).

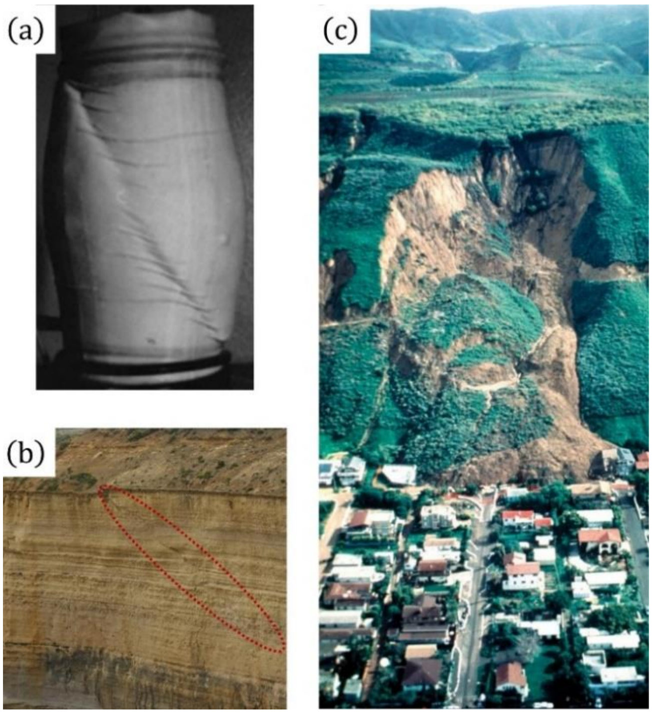

Figure 1.1: (a) localised shear band in triaxial test on fine sand (Desrues & Andò, 2015); (b) localised deformation on the cliff of the Great Ocean Road, Victoria (photo by the author); (c) La Conchita landslide in southern California 1995 (photo by R.L. Schuster, U.S. Geology Survey).

Recently, with the advancement in computer techniques for fast processing of high definition photos, the complicated nature of microscale structures of geomaterials can be captured and analysed on grain-scale levels and a quantitative manner. The most prevailing techniques including computed tomography (CT), X-ray computed tomography (X-ray CT) and false relief stereophotogrammetry (FRS) have been widely applied to characterise strain localisation in soils (Desrues & Viggiani, 2004; Desrues et al., 2007; Higo et al., 2013). These techniques are featured as non-intrusive which captures soil internal structures without any physical destruction to the sample. In addition, four-dimensional monitoring of the physical and mechanical behaviour of soil samples can be constructed (Figure 1.2), which greatly enhanced the knowledge for the mechanism of strain localisation phenomenon at scales down to a few hundred nanometers (Cnudde & Boone, 2013). This opens a pathway to a potentially full comprehension of the triggering factors and evolution laws of strain localisation phenomena. However, with the current advancement of CT and FRS methods, the interpretation of the scanning results are still highly dependent on the operator of the tests. Therefore, significantly dependency of the results on different interpretations can be expected for even the same experimental test (Cnudde & Boone, 2013). Apart from this, limited by the availability and scale of the scanning equipment as well as the computer processing capacity, these techniques are applied for small scale samples only. For an engineering scale problem, for instance, analysis of the stability of a slope, these approaches require resources that exceed the current technological advancement.

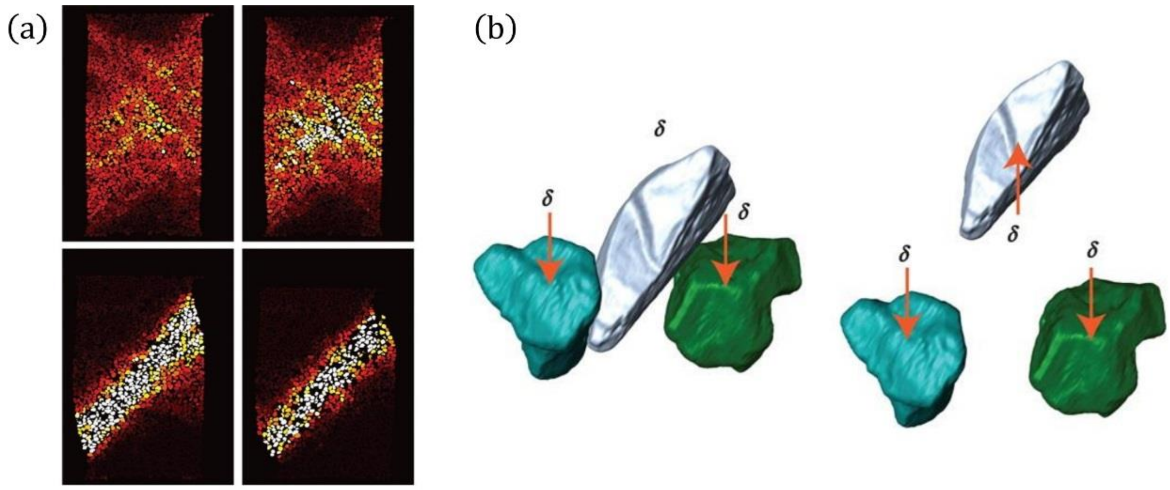

Figure 1.2: (a) shear band development captured by synchrotron micro-computed tomography (SMT); (b) 3D interpretation of particle translation during shear band formation (Druckrey et al., 2017).

On the other hand, theoretical and numerical investigations of strain localisation in geomaterials have been widely conducted, which are based on the classical theory of bifurcation. The majority of the work is focused on the elastoplastic rate-independent materials which feature a weak-discontinuity zone (strain localisation band). For this particular material, its behaviour is analysed under a continuously straining boundary condition, during which Hadamard first mathematically proved a loss of strong ellipticity of the governing equation under the quasi-static analysis (Hadamard, 1903). This is ever since defined as the key localisation criterion. Thomas, Hill and Mandel later extended Hadamard's work and established a so-called Thomas-Hill-Mandel shear band model which defines the shear band as a thin layer of material bounded by two parallel discontinuity surfaces of the incremental strain field (Thomas, 1961; Hill, 1962; Mandel 1966). In this model, the process of strain localisation is described as bifurcation of the material bulk from a homogenous deformation to the incipient of a shear plane where the majority of the input energy from boundary conditions is dissipated (Sulem & Vardoulakis, 2014). Rice and Rudnicki later mathematically studied the condition for which a discontinuous strain plane is to appear in a homogenous material bulk and interpreted the condition as the vanish of the so-called acoustic tensor (strain localisation tensor) (Rudnicki & Rice, 1975; Rice, 1976). However, the above theoretical framework is based on the analysis of a classical continuum. Therefore the fundamental assumption of a homogenous material field is violated, which can be mathematically interpreted as the well-known loss of positive-definite of the tangent stiffness tensor. Apart from this, there lacks a length scale parameter to characterise the size of the localisation zone, which results in a perfectly brittle material behaviour manifesting vanishing size of the localised shear zone. Countermeasures have been proposed to solve this issue by distinguishing the material inside and outside of the localisation zone, for instance, the strong discontinuity model (Simo et al., 1993; Simo & Oliver, 1994). This approach captures the discontinuity in the deformation field such as fracture, slip line shear band etc. by considering the material inside such highly localised deformation zone with a specific constitutive model that is able to maintain well-posedness of the governing equation during material softening behaviour (Oliver, 1996). Other countermeasures are mainly focused on enriching the current constitutive model by the incorporation of a length scale parameter. The representative approaches are: the Cosserat continuum approach (Cosserat & Cossera, 1909; De Borst, 1991), the smear crack methods (Oliver, 1989; Oliver te al., 1990), non-local constitutive equations (Pijaudier-Cabot & Bažant, 1987), Cosserat continuum (De Borst, 1991), gradient plasticity (De Borst et al., 1993), visco-regularised constitutive equations (viscoplasticity) (Needleman, 1988) and the double scale approach (Nguyen et al., 2014; Le et al., 2018; Wang et al., 2019).

From a numerical analysis standpoint, the most prevailing method that features with robust computational stability and high efficiency is the finite element method. It has been incorporated with the above methods and demonstrated success in capturing the onset of strain localisation and regularisation of the zero-energy dissipation mode in classical continuum analysis of localised failures. The benchmark and representative work during the past four decades is highlighted as follows: Oliver and co-workers proposed the so-called strong discontinuities approach and applied in the finite element method to model strain-softening problems in brittle materials. The approach captures very well the fracture initiation and propagation pattern, in the meantime demonstrate the ability to trace multiple fractures in the numerical domain as compared with experimental data (Figure 1.3a). However, due to the mesh discretisation of the FEM domain, a strong discontinuous surface (ruptures, fragmentation) in rock samples cannot be captured (Figure 1.3b).

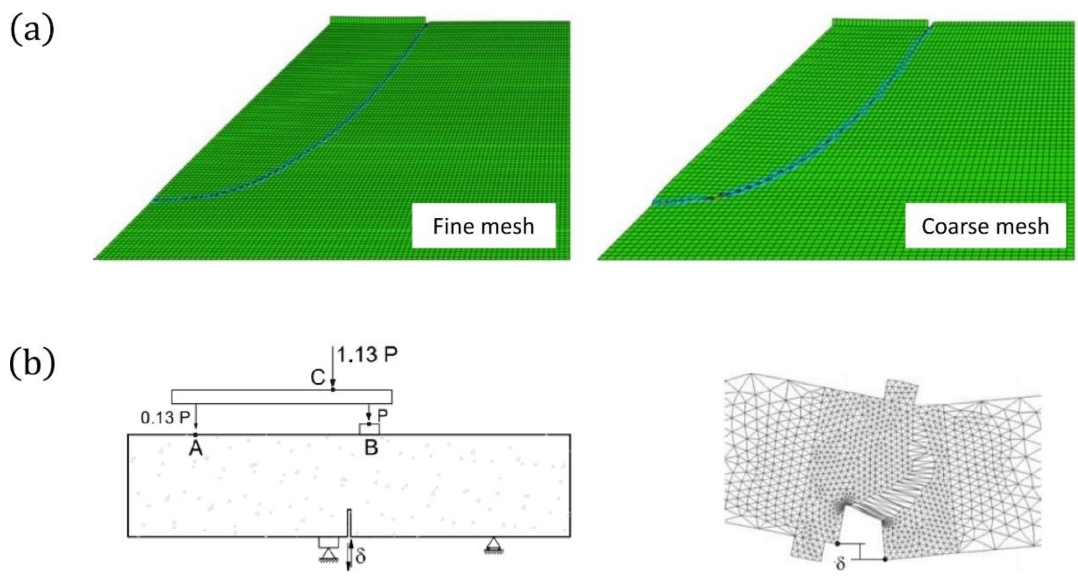

Figure 1.3: (a) slip line for soil slope modelled by the strong discontinuity theory (Liu, 2015); (b) FEM prediction of crack propagation in the four-point bending test (Oliver et al., 2002).

The attempt on improving this issue has led to the adaptive meshing technique proposed in the 1980s, which enriches and reconstruct the mesh discretisation in FEM domain where extreme deformation may lead to convergence issues (Babuvška & Rheinboldt, 1978). When localised deformation appears in the FEM domain, the discretisation error in the grid shape function starts to develop and soon hinders the successful capture of the shear band evolution. The adaptive meshing scheme then initiates to automatically enrich the finite element mesh according to the calculated error and construct a near-optimal mesh alignment while resolving the error until a prespecified accuracy is achieved (Kelly et al., 1983). This approach has pushed forward the FEM calculation of extreme shear deformation based on the conventional method, and predicted the fracture opening when combined with a mesh deleting algorithm. However, the algorithm to implement this method comes with high complexity and difficulty to interpret field variables, and the remeshing process renders a continuously refining mesh size which overburdens the computational resources during the numerical test (Zi & Belytschko, 2003). Although approaches such as the nodal enriched FEM (X-FEM) and elemental enriched FEM (E-FEM) have been proposed to bypass the remeshing process (Chessa et al., 2003; Oliver et al., 2006), the inherent limitation of mesh discretisation of the FEM approach still prevents it from a full characterisation of the large deformation field which can be very common in geomechanics applications.

Another continuum approach: the material point method (MPM), a hybrid numerical tool that combines the mesh discretisation and a set of freely moving Lagrangian particles to represent the computational domain has gained much attention recently for modelling localised and large deformation problems (Bardenhagen et al., 2000; Sulsky & Schreyer, 2004; Nguyen, 2014; Yerro et al., 2015). Different from the FEM, the mesh grid in MPM is fixed in position and applied for interpreting the field variables only. The field kinematics such as velocity, stress, density etc. are carried by the Lagrangian particles which move freely across the background mesh, giving this method the potential to avoid mesh pathologies. However, when the computational domain undergoes very large deformation and the Lagrangian particles cross the boundaries of the background mesh grid, numerical instability arises. Accordingly, a generalised interpolation function is proposed for MPM that occupies an area larger than the size of a single cell, which reduces numerical noise for particles to cross cell borders. This is known as the generalised interpolation material point (GIMP) approach (Bardenhagen & Kober, 2004). Recent applications with GIMP has shown its capability of capturing very large deformation field while demonstrating reasonable numerical stability and accuracy (Sadeghirad et al., 2011; Soga et al., 2015; Yerro et al., 2015; Kiriyama, 2013; Gao et al., 2017). Even though with the advancement of GIMP, this approach manifests significant computational cost, as it utilises both particle and mesh discretisations to describe the field dynamics. Apart from this, boundary conditions such as confining stress that involves largely deformed boundary surfaces or three-dimensional space cannot be enforced with a reasonable level of accuracy (Steffen et al., 2008). These disadvantages hinder the current GIMP approach to be applied in practical engineering applications with large scale domain and relatively complicated boundary conditions.

On the other hand, particle-based approaches that do not resort to any mesh discretisation of the computational domain have gained much attention during the past decade in geomechanical applications. The representative approaches are the discrete element method (DEM) with discontinuum basis and the smoothed particle hydrodynamics (SPH) with continuum basis. The advantage of applying the discontinuum DEM approach is on multiple aspects: first, the kinematics of the computational domain is based on direct contact of DEM particles, therefore the microscale soil properties such as porosity, grain distribution, fibre evolution etc. are very well captured. This facilitates the understanding of the triggering and evolving mechanism during strain localisation; second, a relatively simple constitutive relation accounting for the inter-particle contact model is applied. This bypasses the application of phenological-based constitutive models that have been long denounced for lack of physical significance; third, free-moving kinematics is allowed in DEM domain without any mesh restraint, which enables this approach to well characterise problems involving extreme deformations during strain localisation or material fragmentation/rupture. This approach has been widely applied to model the shear band and density evolution during biaxial, triaxial and direct shear tests which obtained comparable results with the experimental data (Iwashita & Oda, 1998; Kozicki & Tejchman, 2009; Marketos & Bolton, 2009; Wang & Gutierrez, 2010; Fu & Dafalias, 2011; Wang & Yan, 2013; Cil & Alshibli, 2014). Apart from this, a hierarchical multiscale approach that combines the DEM characterisation of soil constitutive response with the classical continuum method FEM for predicting laboratory-scale tests has achieved success for well-capturing the initiation of strain localisation (Guo & Zhao, 2014; Nguyen et al., 2014; Guo & Zhao, 2016). Recently, Bui and co-workers proposed an advanced constitutive model featured with double scale characterisation for plastic behaviours, which has been incorporated into DEM to capture the behaviour of the fatigue damage that occurred in brittle materials (Nguyen et al., 2017a; 2017b; Sounthararajah et al., 2017; Nguyen et al., 2019). Constitutive models that account for cohesive behaviour and unsaturated soil characters have also been applied in DEM, which successfully captures the fracture development in foamed concrete materials and soil curling process (Nguyen et al., 2017; 2019; Tran et al., 2019). Despite the above progress, the characterisation of micro-scale material properties would require up to tens of millions of DEM particles for even a laboratory-scale sample, which brings a significant computational overburden. Although a potential parallel computing technique can be implemented to boost the numerical efficiency, DEM application for engineering scale problems is not yet a readily available option.

The continuum meshfree method SPH, in contrast with DEM, demonstrates a high computational efficiency while allows free particle movement in the computational domain. This empowers SPH the capability to capture strain localisation and material failures in an effortless manner. The application of SPH for geomechanics problems was pioneered by Bui and co-workers, who have proposed a robust SPH framework and conducted simulations of slope failure and granular flow that demonstrate the SPH capability for well-capturing extreme deformations (Bui et al., 2006; 2007; 2008a; Nguyen et al., 2017). This framework is then applied to capture soil-structure interactions to analyse the stability of reinforcement structures such as the gravitational retaining wall, bracing strut etc. (Bui et al., 2008b; Verghese et al., 2013; Nguyen et al., 2013; Bui et al., 2015). The interaction between soil and fluid that is under a fully saturated condition is also considered to predict the static pore water pressure and its effect on the stability of slope structures (embankment, dam etc.) (Bui et al., 2007; 2008c; Bui & Fukagawa, 2009; Bui & Nguyen, 2017). Recently, an advanced constitutive framework featured with a double scale description for material behaviour in bifurcation problem has been implemented into the current SPH framework to capture the material damage during tensile cracking in ductile, quasi-brittle and brittle materials (Wang et al., 2017a; 2017b; Tran et al., 2017; Wang et al., 2019). For geomaterials that are subjected to compressive loading failures, a constitutive framework featured with viscoplastic Von Mises has also been applied to capture the strain localisation and progressive failure process (Zhao et al., 2017a; 2017b). Despite the above progress, there is still a significant need to advance the current SPH framework to allowing its application for strain localisation characterisations that involve complex boundary conditions, multiphase interaction while maintaining numerical objectivity. This includes an effective and accurate method to apply boundary conditions that require enforcing stress onto a highly deformable boundary surface; a robust elastoplastic constitutive model that is able to depict the loss of material integrity during strain-softening process and immune from numerical bias which mainly comes from different discretisation schemes of the computational domain; a numerical framework that couples multiphase (solid, liquid, air) to be able to capture the behaviour of unsaturated soil and its failure process under certain boundary conditions. This includes the popular geohazard problems such as a rainfall-induced slope failure and soil desiccation cracking due to water evaporation etc. In this work, we are dedicated to achieve these goals and propose an advanced computational framework based on the continuum SPH approach.

1.2 Aims and scope of the research

The broad aim of this research is to develop an advanced SPH computational framework that is able to capture the initiation and complete evolution cycle of the strain localisation phenomenon in soil until the residual material strength is achieved. Three target milestones are defined in order to achieve this broad aim. The first one is to propose a generic boundary condition for applying confining boundary conditions on flexible free surfaces. This approach would allow automatic enforcement of the confinement while maintaining a high level of accuracy and computational efficiency. In parallel with this, a robust constitutive model based on an elastoplastic Mohr-Coulomb yield criterion would be first incorporated into the current SPH method. This constitutive model is able to capture the plastic flow evolution showing both perfectly plastic and strain softening behaviours. It is also featured with a nonlocal plastic operating formulation that preserves the resolution objectiveness, demonstrating consistent plastic energy dissipating rate regardless of the choice of numerical discretisation scheme. Lastly, a fully coupled three phase numerical framework in SPH is proposed to model the behaviour of unsaturated soils under the change of saturation condition and its influence on the soil mechanical properties. The proposed model would be validated with the Terzaghi's consolidation theory and applied to capture the water infiltration in soil embankment and rainfall-induced slope failure problems.

The above research milestones can be explicitly identified and listed as follows:

Objective 1: Develop a generic approach to applying confining boundary condition on flexible free surfaces in the SPH domain for large deformation boundary value problems. This approach takes advantage of the SPH kernel truncation character to automatically enforce confining vectors in an accurate and effective manner. Implementation of this method would enable SPH to successfully characterise benchmark soil experiments including plane strain biaxial compression test and axisymmetric triaxial tests that are vital for determining basic soil parameter such as internal friction angle, apparent cohesion etc.

Objective 2: Analyse the nonlocal feature of the SPH method and its effect in facilitating capturing the localised failure process. This includes incorporating a robust elastoplastic constitutive model featured with Mohr-Coulomb yield criterion into the SPH framework. This numerical framework characterises soil plastic behaviours featuring both perfectly plastic and strain softening responses corresponding to the loss of material integrity during large deformation problems. In parallel with this, a nonlocal operating function is implemented for achieving a fully regularised energy dissipation rate. This maintains the resolution objectivity in SPH domain and shows numerical results that are independent on the choice of discretisation schemes.

Objective 3: Propose a fully coupled multiphase model in SPH to characterise unsaturated soil behaviours and simulate failure problems induced by the variation of moisture content in soil. This model considers the interaction among solid, liquid and air phases that dominate the capillary force state (or suction force) in soil bulk, which alters crucial soil properties including internal friction angle and apparent cohesion as water content changes. This proposed numerical framework is validated against Terzaghi's consolidation theory and then applied to capture the water infiltration in soil embankment and the rainfall-induced slope failures.

1.3 Outline of the thesis

This thesis has four main sections: the first section contains background information about the motivation of this research including Chapter 1 introduction and Chapter 2 literature review; The second section focuses on the methodology that is applied in this research. This includes a comprehensive layout of the current SPH framework and all relevant formulations (Chapter 3). In addition, a detailed explanation on the constitutive models that have been implemented and corresponding formulations are expanded; The third section contains all research contributions and numerical results, for instance, the generic boundary condition for applying confining stress is in Chapter 4, the local and nonlocal analysis of the SPH method is in Chapter 5 and the fully coupled multiphase SPH framework is in Chapter 6; The last section (Chapter 7) concludes this research and presents outlooks for future work regarding the topic.

A brief explanation for each chapter is outlined as follows:

In Chapter 1, a summary of the background and current state of the art is presented regarding the analysis of strain localisation in geomaterials. The approaches that have been applied to investigate this problem are presented with their key limitations discussed. The discussion provides the motivation for the current research. Individual milestones are divided for achieving the overall research aim, and the scope of this work is specified at last.

In Chapter 2, an in-depth review is presented for studies on the mechanisms of strain localisation phenomenon in geomaterials. This covers the methodologies of experimental tests, theoretical interpretations and numerical simulations. The current research progress regarding each methodology is expanded with their bottleneck problems explained. Emphasis has been placed on the numerical characterisation of the localisation process, particularly the problems that prevent existing approaches from characterising the full evolution of strain localisation. The review establishes that, the SPH method, among all current available numerical methods, has been demonstrated as a promising approach for achieving the proposed aims of this research work.

Chapter 3 presents a detailed explanation of the current SPH framework that has been applied in this work with all relevant formulations listed. The basis of the SPH method is first shown with its approximation for the governing equations for solid mechanism. A leap-frog time integration scheme is presented on a step-by-step basis. Then stabilisation techniques which are necessary to remove spurious oscillations in the SPH computational domain are demonstrated. Next, the conventional ways to apply virtual and ghost particle to enforce free-slip, non-slip and force vectors boundary conditions are introduced. Then a brief discussion is posted for other variants of the classical version of SPH method and relevant applications. In parallel with this, the constitutive models that have been implemented to SPH framework in this research are presented in detail. This includes an elastic-viscoplastic model featured with Von Mises strain softening yield criterion; an elastoplastic model featured with both perfectly plastic and strain softening Mohr-Coulomb yield criteria. A generic constitutive framework is first presented to allow the implementation of various yield conditions together with the treatment for the discontinuous surface gradient in the Mohr-Coulomb model. Benchmark validations, including element compression and simple shear tests, are then illustrated with comparisons between SPH results and theoretical solutions to demonstrate the robustness of the proposed SPH framework.

In Chapter 4, a generic approach to applying confining boundary conditions to flexible boundaries in SPH is proposed and expanded in detail. This approach takes advantage of the kernel truncation property that occurs near free surface boundaries in SPH domain to automatically account for the confinement on free surfaces. This approach outperforms the conventional ways to apply confining stress in terms of its accuracy, stability, efficiency and the ability to well-handle large deformation of the free surface. A benchmark test is carried out on a circular specimen which demonstrated the superior performance of this approach. It is then applied to capture plane strain biaxial and axisymmetric triaxial tests. Comparison among results from experiments, SPH, FEM and GIMP shows very good agreement.

In Chapter 5, the proposed numerical framework is applied to investigate strain localisation problems in geomaterials with emphasis made on the inherent nonlocal feature of the SPH method. This feature allows the current SPH to well capture the strain localisation process without additional regularisation techniques, despite showing resolution dependency issues analogous to that observed in FEM. The kernel approximation function is first applied to regularise such dependency issue, which shows a good convergence of the plastic energy dissipation rate with a fixed kernel domain. However, significant compromises are made regarding the numerical stability. Therefore, an additional nonlocal operator is incorporated into the current numerical framework, which demonstrates the ability to fully regularise energy dissipation rate with very good stability. This framework is then applied to investigate the initiation and evolution of strain localisation in heterogeneous soil samples. The theoretical conditions to interpret the incipient point of the localisation are applied namely the acoustic tensor condition and the second order work. The obtained results show exact agreement between the SPH captured process and the theoretical prediction.

In Chapter 6, a fully coupled multiphase framework is proposed to characterise the behaviour of unsaturated soils with the SPH method. Three phases including solid, liquid and air are considered as partitions of the mixture carried by each SPH particle. A generalisation of linear momentum and mass conservation conditions together with the effective stress concept forms the basis of this framework. The hydraulic constitutive model is selected on a case-to-case basis including the well-known Van Genuchten soil water characteristic relation. To allow the capillary force to alter soil mechanical behaviours, an elastoplastic model featured with suction dependent state parameters is applied to the SPH framework. The proposed approach is first validated with Terzaghi's consolidation theory and the water infiltration test in an embankment, then applied to simulate rainfall-induced slope failure problems.

Lastly, in Chapter 7, the conclusion of the current work is summarised. The main research contributions are highlighted and recommendations for future research into the numerical simulation of large deformation localisation failures in geomaterials are proposed.

Chapter 2

Literature review

2.1 Introduction

In this chapter, a review has been conducted regarding the research efforts on understanding the mechanism of the localised failure phenomenon in geomaterials as well as applications of existing theories and methods to capture localised kinematics during landslide events. The existing approaches on analysing strain localisation from a geomechanics standpoint are summarised from the theoretical; experimental and numerical aspects. At the end of this chapter, the knowledge gaps are identified together with the corresponding proposals to address them in this research work.

The localisation nature of failures in geomaterials has been long identified following Coulomb's work for analysing the stability of retaining walls (Coulomb, 1773). However, this particular phenomenon starts to draw more attention since the 20th century due to the advancement in modern building designs and construction technologies that more often involve heavier structures and deep excavation foundations. This largely increases the chance for weight-bearing materials such as soil and rock to be subjected to loads beyond their elastic limit, and thus enter the yield stage, in which the localised shear bands in the material bulk occur. In order to better understand the localisation phenomenon, geomechanics theories that are based on a continuum assumption of the soil bulk are proposed during the past century (Hadamard, 1903; Thomas, 1961; Hill, 1962; Mandel 1966; Rudnicki & Rice, 1975; Rice, 1976). In parallel with this, experiments are widely conducted on ductile, quasi-brittle and brittle geomaterials to capture the localised failure mode (Handin et al, 1957; Wawersik & Fairhurst, 1970; Desrues et al., 1985; Evans et al., 1990; Olsson 1999; Lenoir et al., 2007; Das et al., 2013). With the recent advancement of computer-aid tomography (CT) and X-ray, the microscale initiation and evolution of shear bands in ductile geomaterials are well captured in the laboratory (Desrues & Viggiani, 2004; Desrues et al., 2007; Higo et al., 2013). However, experimental characterisations of the localisation phenomenon are still limited in relatively small scale tests, which cannot provide direct design parameters or evaluation of safety factors for real engineering projects. In addition, there is a lack of prediction nature in experimental tests, which reproduces rather than evaluates and predicts field behaviours of soil samples. Therefore, numerical tools have been widely applied to compensate for the disadvantages of experimental studies in both research and design aspects regarding the localised failure problems in geomaterials. In this chapter, the emphasis has been placed on the numerical simulations of localised failures in geomaterials in order to demonstrate its key advantages and existing challenges. To better expand this topic, the key focuses of this chapter are listed as follows:

- Section 2.2: theoretical interpretation of localised failures
- Section 2.3: experimental analysis of localised failure in geomaterials
- Section 2.4: mesh-based numerical approaches to characterise localised failures in geomaterials
- Section 2.5: meshfree numerical approaches to characterise localised failures in geomaterials
- Section 2.6: conclusion

2.2 Theoretical interpretation of localised failures

The localised failure mode has been understood, from a theoretical standpoint, as a bifurcation process. This corresponds to the materials kinematics such as strain field, stress field, density etc. from an initially homogeneous state to a bifurcation point from which two distinct areas appear simultaneously inside the material bulk. One area demonstrates intensive and continuously evolving shear deformation, which often manifests as localised shear bands. The rest of the area demonstrates reversible deformation with the stress state largely lying below the material elastic limit. The mathematical description of the bifurcation process in continuum mechanics was pioneered by Hadamard who demonstrated the loss of the so-called ellipticity of the shape of the partial differential form of the governing equations under quasi-static analysis (Hadamard, 1903). This is later regarded as the key criterion to signal the appearance of the localised shear band. In the mid-twentieth century, based on the definition of velocity waves by Hadamard, Thomas, Hill and Mandel proposed the concept of a discontinuity plane in strain rate field and its corresponding stress rate field (not stress itself) to facilitate the characterisation of the bifurcation phenomenon, which is known as the Thomas-Hill-Mandel shear band model. The proposed concept identifies a jump in strain and stress rate field which is bounded by an isolated geometric surface as a form of bifurcation (Thomas, 1961; Hill, 1962; Mandel 1966). This concept is corresponding to a weak form of discontinuity, as it only assumes a discontinuous area in terms of strain and stress rate rather than the displacement itself (strong discontinuity). Therefore, it is more relevant in capturing the localisation and material softening process in ductile materials. In order to obtain a more generic description of the bifurcation process, Rudnicki and Rice proposed the so-called acoustic tensor concept in the mid-1970s (Rudnicki & Rice, 1975; Rice, 1976). Similar to the previous theoretical framework, discontinuity in the strain field is conceptualised as a plane that crosses the representative volume element (RVE) in the continuum domain (Figure 2.1). Material stiffness tensors, $\mathbf{D}^{+}$and $\mathbf{D}^{-}$on both sides of the discontinuity plane, are asuumed identical, which lead to a simplification from the traction contiuity condition shown as follows.

$$(\mathbf{n} \cdot \mathbf{D}^{+} \cdot \mathbf{n}) \cdot \mathbf{m} = 0 \tag{2.1}$$

In above, $\mathbf{n}$ is the normal vector of the plane and $\mathbf{m}$ is the polarisation vector that controls together with $\mathbf{n}$ the failure mode across the discontinuity plane. The angle between $\mathbf{n}$ and $\mathbf{m}$ ranges from 0 to 90 degrees representing the transition of failure modes from pure tension to pure shear. The acoustic tensor in Eq 2.2 (or more often referred to as the localisation tensor) is defined from the above equation, with the vanishing of its determinant corresponds to the incipient point of bifurcation.

$$\begin{cases} \mathbf{Q} = \mathbf{n} \cdot \mathbf{D}^{+} \cdot \mathbf{n} \\ \det(\mathbf{Q}) = 0 \end{cases} \tag{2.2}$$

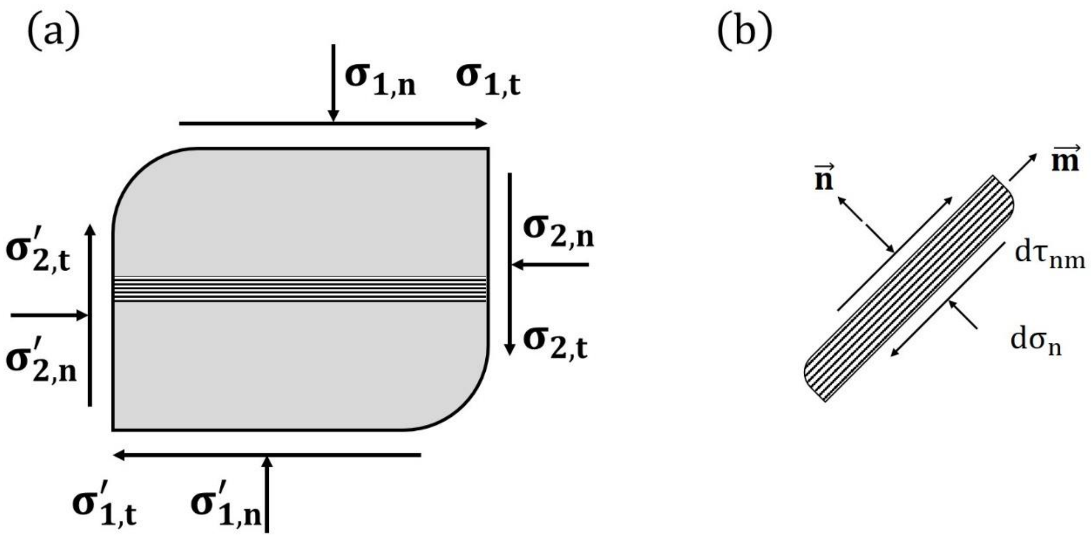

Figure 2.1: (a) the discontinuity plane in a continuum representative volume element; (b) discontinuous strain plane and its norms to control the failure mode (concept based on Rudnicki & Rice, 1975).

Although the above theoretical framework covers the initiation condition for the bifurcation process, it violates the basic assumption in continuum mechanics about a homogeneous RVE. This creates trouble at the incipient of the bifurcation, which leads to the loss of positive definiteness of the tangent stiffness tensor in the analysis domain. The inception of the discontinuity surface also defines itself with a zero thickness, which brings difficulties for the analysis of any further development of the bifurcation process that is supposed to lead to the localisation of the strain field with finite size. In order to overcome this issue, the current discontinuous plane in strain field is further advanced to the displacement field, implying a strong discontinuity corresponding to the complete rupture state of a continuum material (Oliver, 1989; Oliver te al., 1990). The constitutive model that is applied to characterise the material behaviour inside of such strong discontinuity plane differs from the one for describing the other part of the RVE. This approach avoids the interpretation of the discontinuity plane in a continuum sense, therefore, maintains a well-posed partial differential form of governing equations during a post-bifurcation analysis.

Despite this progress, both weak and strong form description of the discontinuity in continuum RVE above defines zero thickness of the discontinuous plane. As a consequence, the predicted post-bifurcation of the material manifests a perfectly brittle behaviour, as the plastic energy dissipates in an infinite rate in such scenario. This is originated from the fact that there lacks a characteristic length scale to govern the size of the discontinuous plane in above theories. Numerous countermeasures have been proposed to resolve this, which explicitly or implicitly incorporates a length scale parameter to enrich the kinematics of the continuum. The representative approaches are the smear crack method proposed in the 1990s (Simo et al., 1993; Simo & Oliver, 1994). This approach is proposed based on the framework of the strong discontinuous method described above. The key feature in the smear crack method is that the constitutive model for describing the discontinuity plane is described in a distributional sense (Simo et al., 1993). This involves an introduction of an interpolation function that features an influence radius to cover a ranged vicinity, which can be regarded as a length parameter to regularise the energy dissipation rate for plastic softening process.

A similar approach that resorts to the application a nonlocal interpolation function is the nonlocal damage theory proposed by Pijaudier-Cabot and Bažant (1987). The nonlocal damage theory applies a weighted function to interpret the damage variable from an area rather than an infinitesimal RVE. However, different from the strong discontinuous approach, the nonlocal damage theory can be applied to a weak discontinuous plane to characterise a localisation in strain field. The above two methods are introducing the characteristic length parameter in an explicit way through the implementation of a distributive function to the constitutive model. There are also approaches including the Cosserat continuum theory (Cosserat & Cossera, 1909; De Borst, 1991), the gradient plasticity theory (De Borst et al., 1993) and viscoplasticity theory (Needleman, 1988) that introduces the length parameter in various implicit manners.

Recently, a new double scale approach that is developed based on the strong discontinuity theory framework has been applied for capturing fractures in ductile, quasi-brittle and brittle geomaterials (Nguyen et al., 2014; Tran et al., 2017; Le et al., 2018; Wang et al., 2019). This approach is featured with a scale-dependent constitutive description of the strong discontinuity surface that is able to capture the size effect in most rock and concrete materials (Figure 2.2a). Apart from this, the approach is able to regularise the plastic energy dissipation to maintain a converged softening stress path immune from the conventional mesh/resolution bias issues (Figure 2.2b) (Le et al., 2018; Wang et al., 2019).

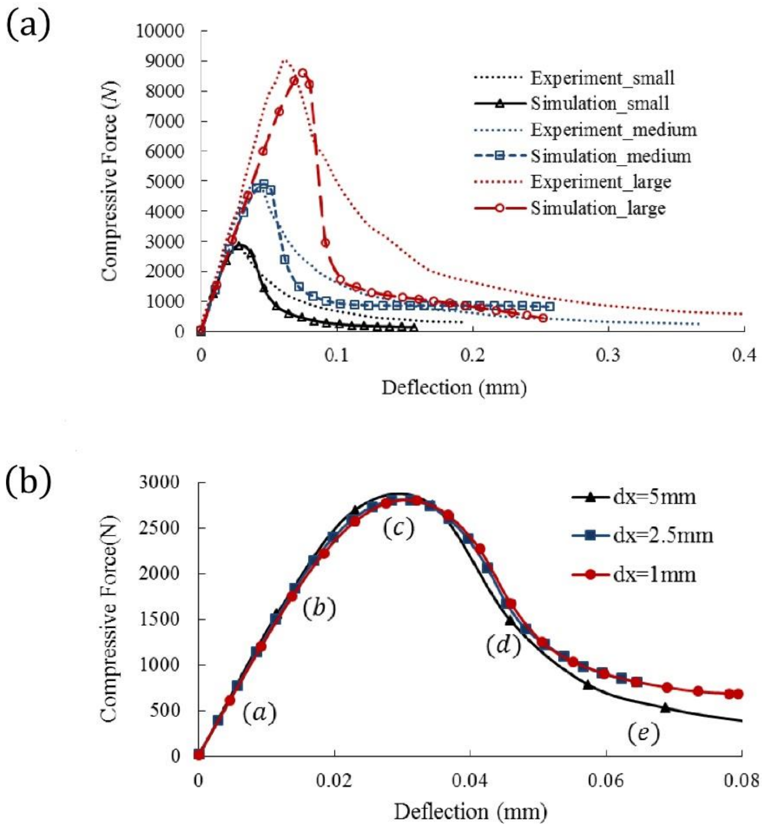

Figure 2.2: (a) three-point bending test with different sample size; (b) three-point bending test with different discretised resolution (Wang et al., 2019).

2.3 Experimental analysis of localised failure in geomaterials

In parallel with the theoretical interpretation of the bifurcation and localisation in plastic behaviour of materials, efforts have also been made to capture this process in the laboratory. The experimental tests have been conducted on a wide range of geomaterials including clay, silt, sand, asphalt mixtures, soft rock, hard rock and concrete (Niandou et al., 1997; Bésuelle et al., 2000; Masad et al., 2001; Kulasingam et al., 2004; Desrues & Viggiani, 2004; Amann et al., 2011). The main focus is to interpret the initiation and evolution of the localisation and post-localisation process in a macroscale sense. This includes capturing the stress and strain relationship within the sample as the strain field develops from elastic deformation to localised deformation and eventually a loss of the material integrity. From the experimental obtained stress and strain relationships, the constitutive models that describe the failure mode and evolution laws of the localisation phenomenon can be constructed and calibrated. Apart from this, a general description of the shear band configuration is also one of the key interests, which involves the measurement and track of the evolution of the shear band thickness, inclination angle and quantity of shear bands. Both the material properties and the applied boundary conditions can significantly affect the measured results.

In order to investigate this, Handin and co-workers conducted a series of parametric study on the boundary conditions that could affect the initiation and development of the localised failure mode. An axisymmetric triaxial apparatus (Figure 2.3) was applied to a range of sedimentary rock samples. The effect of confining stress (up to 300 atmospheres), temperature (up to 300 degree Celsius) and pore pressure (up to 2 kilobars) during the experiments was considered. The confining stress showed an influence on the peak stress with higher confinement leading to an increase in the peak stress that different samples can reach (Figure 2.4). In addition, the ductility is also affected, materials demonstrating brittle behaviour under low confinement and ductile behaviour under increased confinement.

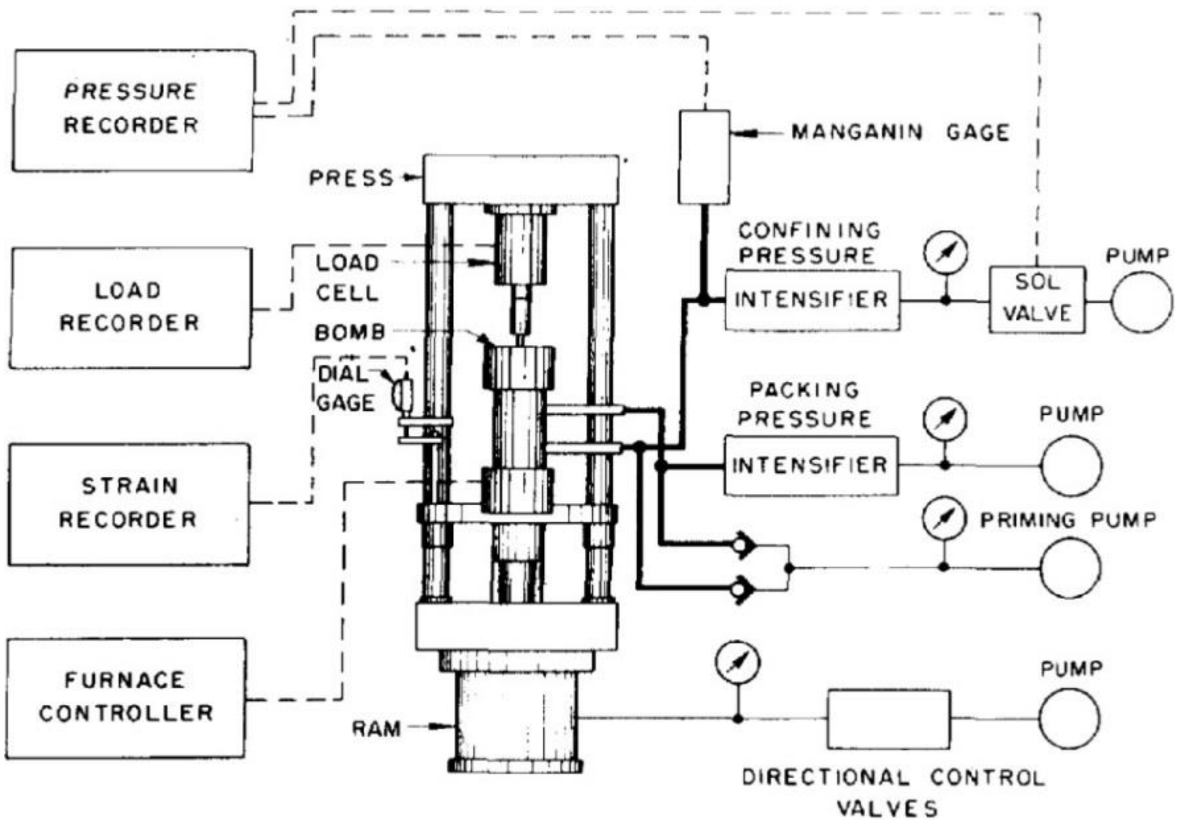

Figure 2.3: The axisymmetric triaxial experimental apparatus (Handin et al, 1957).

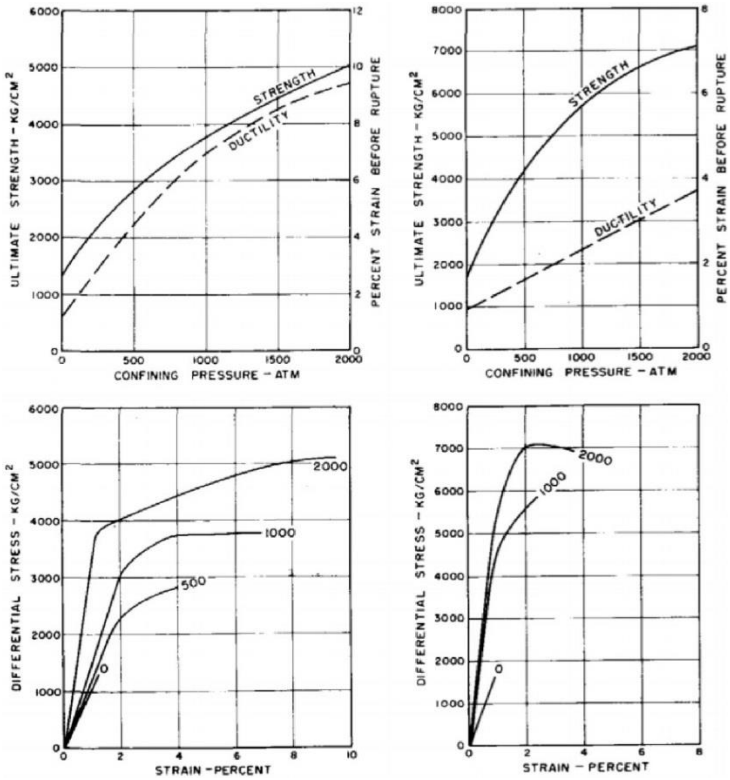

Figure 2.4: Effect of the confining stress on strength, ductility and stress-strain relations of the testing materials (left: Blaine Anhydrite; right: "Blair" Dolomite) (Handin et al, 1957).

The effect of the environment temperature was investigated under both lower and higher confining stress. In general, different groups of sedimentary rocks showed a reduction in their peak strength with increasing temperature. The ductility of the material shows a reducing trend at a higher temperature. The effect of the temperature and confining stress was compared with the field observation of sedimentary rocks in natural geology, which confirmed the behaviour that was observed in the laboratory with physical reality. Apart from this, an artificially increased pore water pressure was applied to the samples demonstrated its effect on reducing the peak strength of the samples. Photograph aided analysis was also applied to capture the deformation field in the sample which showed clearly a localised trend as the materials reach and pass their peak strength. However, there lacks a systematic interpretation of the initiation and development process of the localisation band in this work. Since there is not enough information exposed at the microscale of the material kinematics, correct track and characterisation of the shear band development are not feasible when only macroscale analysis is conducted.

Although initially applied since the late 1960s, a recent advancement during the past two decades of the computer-aided tomography (CT) and X-ray computed tomography (X-ray CT) techniques open a new pathway for researchers to investigate the microscale evolution of geomaterial structures and kinematics during a localised failure process. These methods are featured as non-destructive probing approaches that are able to track the microscale structures evolution regarding the inter-grain position, fibre reorientation/elongation etc. (Desrues & Viggiani, 2004; Desrues et al., 2007; Higo et al., 2013). The corresponding data can then be applied for computer simulations and calibrations to obtain a better understanding of the mechanism of the localisation process. The facility to capture a three dimensional CT scan of the sample generally involves three main components: the radiation generator, the sample and the charged coupled device (CCD) to capture the image (Figure 2.5).

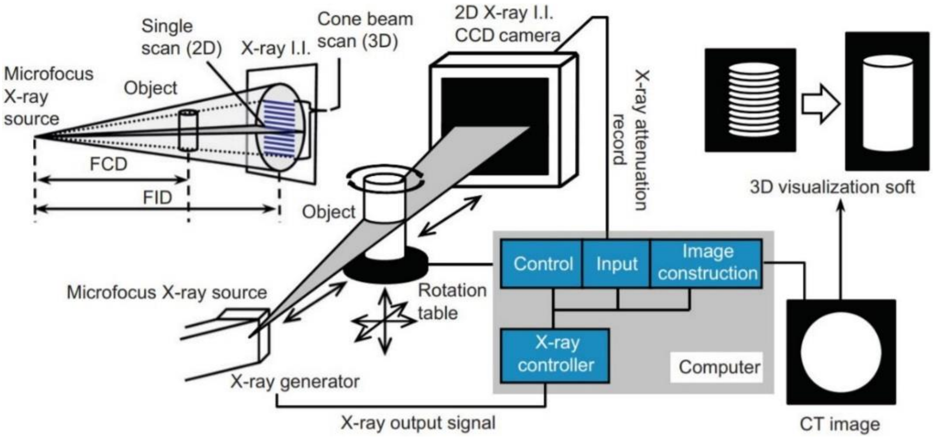

Figure 2.5: A general setup for computer tomography and X-ray scan for geomaterial samples (Higo et al., 2013).

From the illustration, it is clear that layered images are first obtained from the crossectional area of the sample, then combined and form the three-dimensional characterisation of the sample. With the current high definition technique, detailed stereoscopic description of a material grain at a hundred-nanometer level can be well presented (Figure 2.6). However, computer tomography or X-ray scan only provide stationary images of the test samples, in order to capture the kinematics during the localisation of deformation, techniques such as the false relief stereophotogrammetry (FRS), digital image correlation (DIC) and particle translation gradient are required (Desrues & Viggiani, 2004; Higo et al., 2013; Druckrey et al., 2017). In these techniques, the photos that are obtained from a fixed perspective at various time points are incorporated to characterise field kinematics such as the evolution of strain field. Therefore, the initiation and evolution of localisation bands can be clearly presented in terms of the shear strain development in both dry (Figure 2.6) and unsaturated (Figure 2.7) soil samples. In parallel with this, the discrete nature of the microstructure of geomaterials can be utilised and reproduced in numerical methods that are based on discontinuum mechanics such as the discrete element method (DEM). This feature allows the computer simulations to be applied together with CT and X-ray techniques to achieve a better understanding of microscale material kinematics as well as easily extending the current application other tests using the simulation.

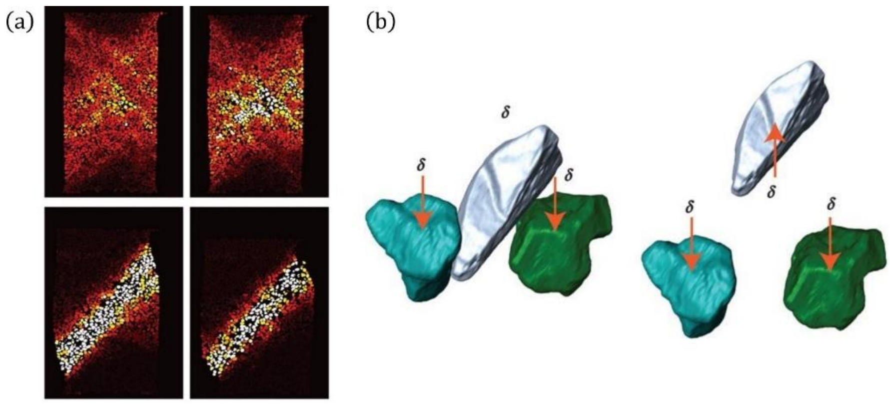

Figure 2.6: (a) the particle translation gradient of the development of shear strain in dry sand; (b) three-dimensional characterisation of the synchrotron micro-computed tomography (SMT) of particle kinematics (Druckrey et al., 2017).

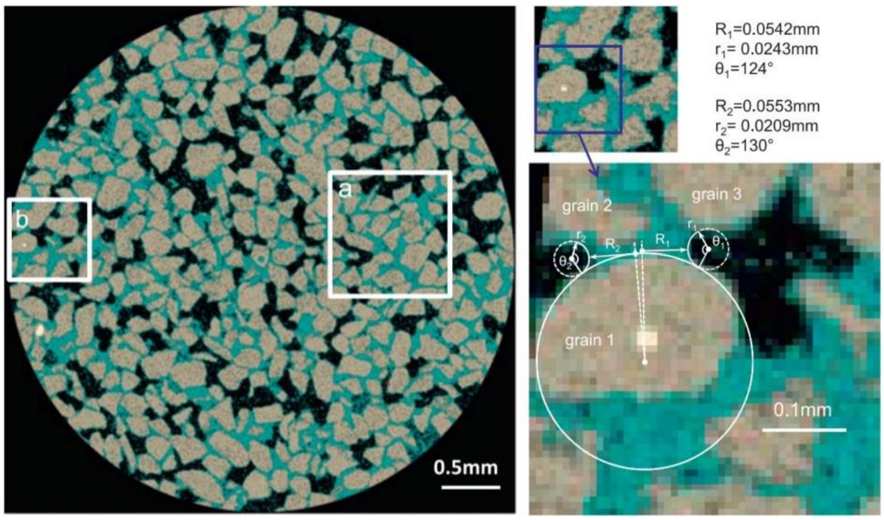

Figure 2.7: Measuring the water content and air content on a crossectional area of CT scan of unsaturated Toyoura sand (Higo et al., 2013).

Despite the above advantages that the current state of the art in CT and X-ray CT techniques bring to the geomechanics research, there also exists significant limitations which must be addressed before more progress can be achieved. The most relevant one is that no standard is available to interpret the image information from the above techniques. Therefore, it largely depends on the judgement and experience of the operator, which could potentially downgrade the objectivity and rigorousness of these approaches (Cnudde & Boone, 2013). Another difficulty comes from the availability of the current computational power and scale of scanning facility. Only laboratory sized samples can be applied for the current CT and X-ray approaches. For field applications involving earth or slope structures, there is no practical approach to apply these techniques. Apart from the above two disadvantages, a certain amount of computational error and imaging artefacts still exist and influence the accuracy of the obtained results.

2.4 Mesh-based numerical approaches to characterise localised failures in geomaterials

The numerical simulation of localised strain field and the corresponding failure process can be categorised based on specific methods. There are mainly two ways to characterise the computational domain, one is using a mesh discretisation and Gauss points another one is using Lagrangian particles to interpret field kinematics and properties. In this section, the most commonly applied mesh-based approaches are summarised, highlighting both their advantages and limitations.

2.4.1 The finite element method (FEM)

Among all relevant approaches that resort to mesh discretisation of the computational domain, the finite element method (FEM) is the most widely applied, which features high numerical stability and accuracy. It is also the most developed approach with many derivatives proposed in the past four decades to facilitate solving bifurcation and localisation problems. When first applied to quasi-static localisation problems under rate-independent assumptions in the 1960s, FEM demonstrated difficulties in multiple aspects. Among these challenges, three are in particular interests of researchers: first, when the FEM domain enters the bifurcation point, the boundary value problems become ill-posed. The tangent stiffness tensor that balances the relationship between deformation and the corresponding force field loses its positive definiteness. Second, the solution of the strain field and load-displacement relation when passing the bifurcation point exhibits a pathological dependence on the size of the mesh discretisation. The size of the localised strain area is vanishing as the mesh size refines, which renders in a mechanical response from a ductile to perfectly brittle behaviour. This is well-known as the mesh dependency pathology in the classical FEM approach. Apart from this, the nature of mesh discretisation poses certain limitations to the maximum deformation each mesh could achieve. This means that in case of predicting the strain localisation and failure process, FEM is likely to end up with excessively distorted mesh, and therefore terminates the analysis process. This significantly pulls back FEM application on geomechanical applications, since most relevant problems in this field involve extreme deformations.

The first two issues discussed above, in fact, originates from the assumption in the classical continuum mechanics, which requires the incorporation of a length scale parameter into the constitutive framework. This length parameter or a conceptually equivalent component should be applied to govern the plastic energy dissipation, which liberates the energy dissipation process from been underpinned by the mesh size. As discussed in section 2.2, approaches that have been proposed for this issue can be represented by: the smear crack model (Bažant, & Lin, 1988; Simo et al., 1993; Simo & Oliver, 1994), the nonlocal damage model (Pijaudier-Cabot & Bažant, 1987; Bažant & Jirásek, 2002; Tejchman, 2003; Grassl & Jirásek, 2006; Galavi & Schwriger, 2010; Nguyen, 2011; Nguyen et al., 2015; Huang et al., 2018; Mánica et al., 2018), the Cosserat continuum method (De Borst, 1991; Khoei & Karimi, 2008; Chang et al., 2014; Tang et al., 2017; Rattez et al., 2018), the higher-order gradient plasticity model (De Borst et al., 1993; Yang & Misra, 2012; Pardoen et al., 2015), the viscoplastic model (Needleman, 1988; Oka et al., 2002; 2011; 2019) and the recently proposed double scale model (Nguyen et al., 2014; Tran et al., 2017; Le et al., 2018; Wang et al., 2019). Apart from the above approaches, a hierarchical multiscale framework that bypasses the continuum constitutive model is also applied to solve this issue (Guo & Zhao, 2014; 2016; Nguyen et al., 2014; Zhao, 2017). Despite that the methods mentioned above have been reported with certain progress in the past decade regarding capturing the localised failure process, three of them namely the nonlocal approach, the double scale approach and the hierarchical multiscale model are in particular interest due to the significance of their progress.

The nonlocal approach

The nonlocal approach that had been applied to characterise the plastic softening during the bifurcation process was pioneered by Bažant and co-workers in the 1980s (Pijaudier-Cabot & Bažant, 1987). The core idea of this approach is to implement a distributive function to enrich the kinematics calculation of the constitutive relation. In the early nonlocal damage theory, the distributive function was applied to the variables that govern softening stress path, in order to regularise the conventional calculation of these variables at single Guass points to a weighted average manner with their surrounding counterparts. The original idea of the nonlocal damage theory has been extended to other methods, for instance, the smeared crack model (Bažant, & Lin, 1988; Simo et al., 1993). Later, the Vermeer and Brinkgreve discovered that the conventional distributive function in the nonlocal damage theory struggles to achieve a converged energy dissipation path. Therefore, a derivative of the original version was proposed in such a way that it further applies a linear distributive relation between the local and nonlocal counterparts of a specific variable instead of only using the nonlocal calculation (Vermeer & Brinkgreve, 1994). This approach was later recognised by researchers including Bažant himself as the over-nonlocal method (Di Luzio & Bažant, 2005). Since then, the over-nonlocal model has been applied and demonstrates a well-converged plastic energy regularisation in capturing bear capacity test (Huang et al. 2018), biaxial tests (Summersgill et al. 2017) and experimental results (Mánica et al. 2018) as shown in figure 2.8 below.

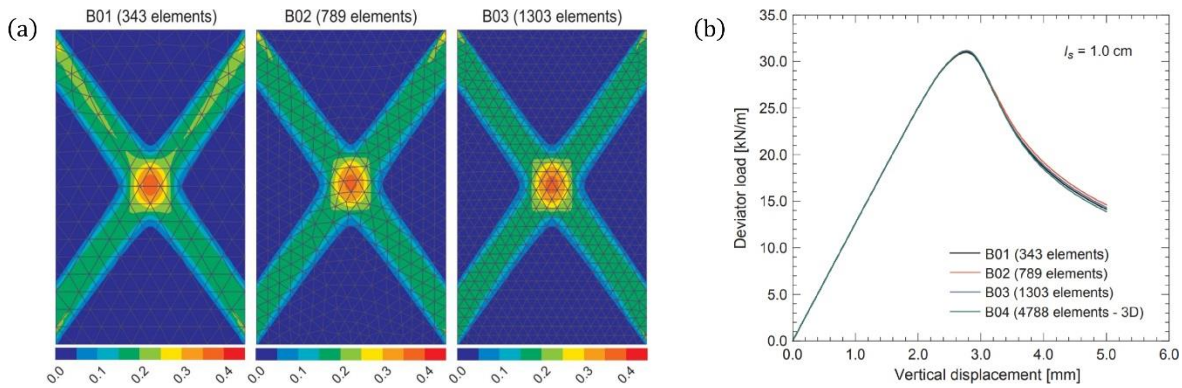

Figure 2.8: (a) the contour plot of shear strain predicted by over-nonlocal model; (b) a converged plastic energy dissipation path from the biaxial test using over-nonlocal model (Mánica et al. 2018).

The double scale approach

Another method that is based on the strong discontinuity theory to characterise the localisation process namely the double scale model is highlighted here. Originally proposed by Nguyen and coworkers (Nguyen et al., 2012; 2014), this approach features several key advantages: first, it characterises the localised deformation in continuum mechanics as a bifurcation process which aligns with the classical theoretical framework proposed by Rice. It allows this approach to rigorously define the configuration and location of the incipient of shear bands (Figure 2.9). In the meantime, the various localisation mode involving both tensile and mixed failure patterns are well captured (Figure 2.10). Second, the double scale model is featured with a length parameter that is able to capture the scale effect which is widely observed in experiments with different size of the sample demonstrating different mechanical responses. In parallel with this, the length parameter also regularises the energy dissipation process, which overcomes the mesh/resolution bias issue in the classical continuum. Furthermore, this method is able to capture the branching of the strong discontinuity plane, which can be challenging for conventional approaches. This allows the double scale model to characterise relatively complicated failure patterns.

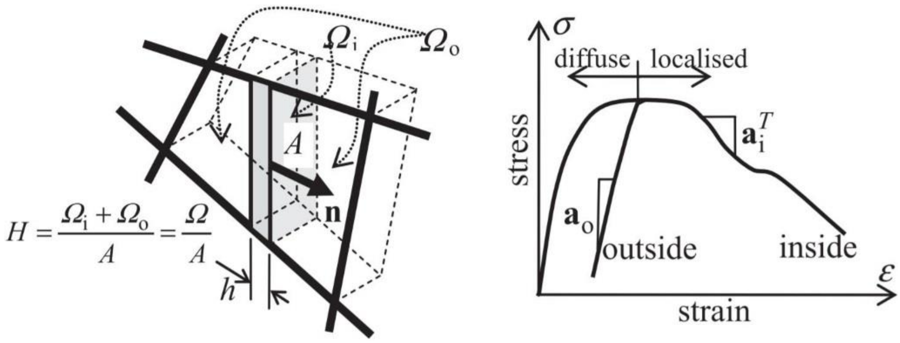

Figure 2.9: The double scale description of the bifurcation and localisation in a continuum (Nguyen et al., 2014).

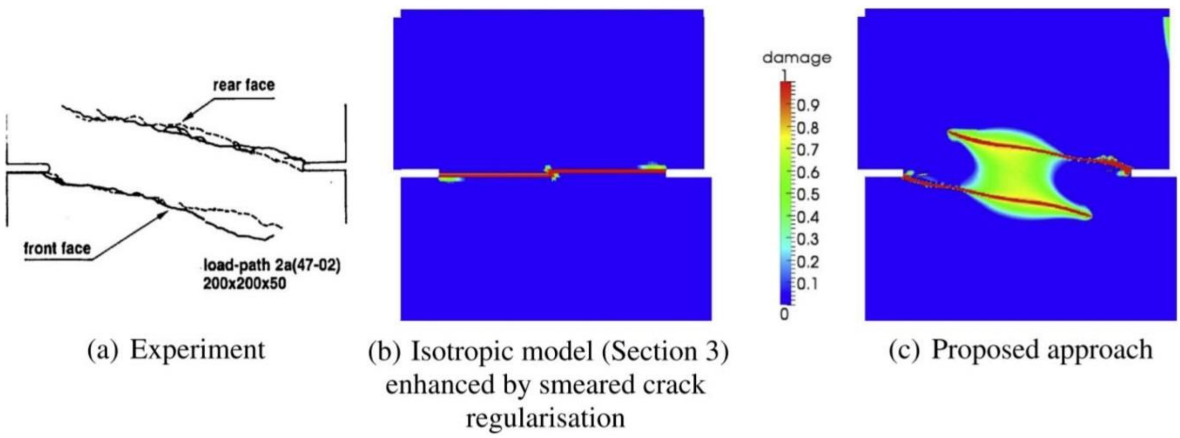

Figure 2.10: The double scale capture of a mixed-mode failure pattern compared with experimental results (Nguyen et al., 2014).

The hierarchical multiscale approach

The above-highlighted approaches describe the bifurcation process at a macro scale level, which may not provide enough information regarding the kinematics at the grain-scale. The recent evidence shows that the heterogeneity at the microscale level of sand governs the initiation and the subsequent evolution of the localisation area (Darve et al., 2007; Andò et al., 2012). Therefore, it is essential for the numerical approach to possess such characteristics. Although micromechanical based constitutive models have been applied and demonstrated capture well the localisation in deformation (Nemat-Nasser, 2000; Luding, 2004; Chang & Hicher, 2005; Yin et al., 2009), they are generally featured with complicated algorithms to predefine the constitutive relations which are also on a case-by-case basis (Qian et al., 2013). In this part, a hierarchical multiscale framework that combines a continuum description of the modelling kinematics field with a discontinuum description of the constitutive relation that is based on a microscale prediction from a representative volume element is introduced. The key feature of this approach is that instead of resorting to a predefined micromechanical constitutive model, it utilises the strain information from macroscale continuum to govern the deformation of the microscale RVE which yields a corresponding stress condition. This stress condition is then plugged back to the macroscale continuum to continue the analysis. Therefore it is able to capture the microscale mechanics of the materials while bypassing the complication in the traditional micromechanics algorithms. Figure 2.11 below schematically illustrates the framework of this approach.

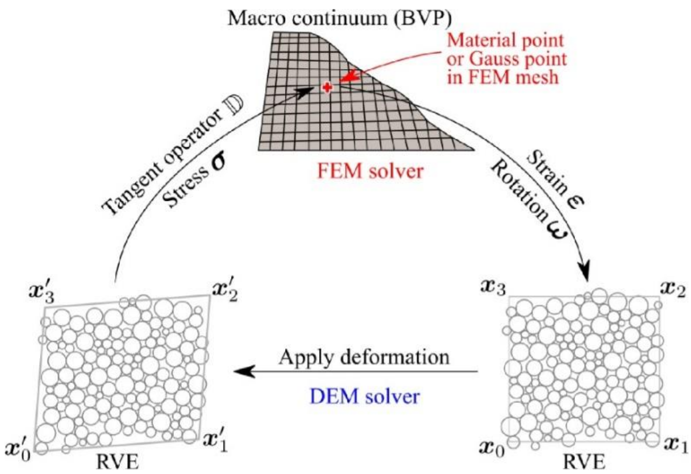

Figure 2.11: The framework for the hierarchical multiscale FEM-DEM approach (Guo & Zhao, 2014).

Since 2014 this approach has been widely applied to capturing the localisation of deformation in granular materials in biaxial tests (Guo & Zhao, 2014; 2016a; Nguyen et al., 2014), axisymmetric triaxial tests (Guo & Zhao 2016b). The material fabric effect and anisotropy are also considered through application non-spherical particles with various level of grades (Zhao & Guo, 2015). Apart from this, a coupled hydraulic effect is also applied to account for the behaviour of saturated soils (Guo & Zhao, 2016c). These FEM-based applications characterise well the initiation of the localised failure mode as demonstrated in Figure 2.12, which is later facilitated to a framework containing both the hybrid mesh-particle method MPM and DEM to capture large deformation problems involving granular flow and bear capacity etc (Liang & Zhao, 2019). Despite the above advantages, the hierarchical multiscale framework requires much more computational power and time. This is mainly due to two reasons: first, in order for the microscale RVE to represent a particular type of granular material, it is recommended that each RVE contains a minimum of 400 particles. Since each macroscale computational point corresponds to one RVE, this increases the computational requirement by several orders. Second, for correctly capturing the stress path history, the deformation of each RVE and the contained particles are saved during each test. This adds more pressure to the computational resources as it occupies a certain portion of the CPU memory during the entire process of a test. To overcome this issue, a paralleled computational framework is recently proposed, which utilises multiple CPU cores to conduct the test simultaneously. This has been demonstrated to potentially boost the computational efficiency of the multiscale framework significantly as illustrated in Figure 2.13 (Argilaga et al., 2018).

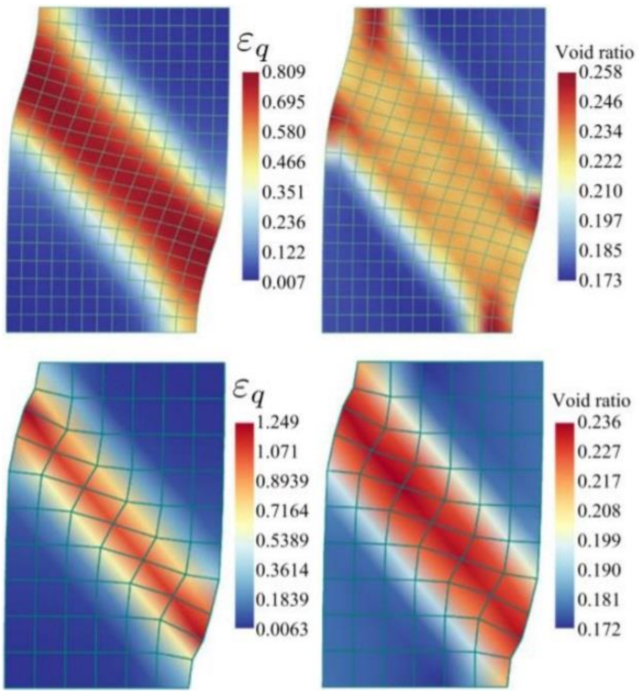

Figure 2.12: The localisation process during small deformation range captured by the hierarchical multiscale FEM-DEM approach (Guo & Zhao, 2014).

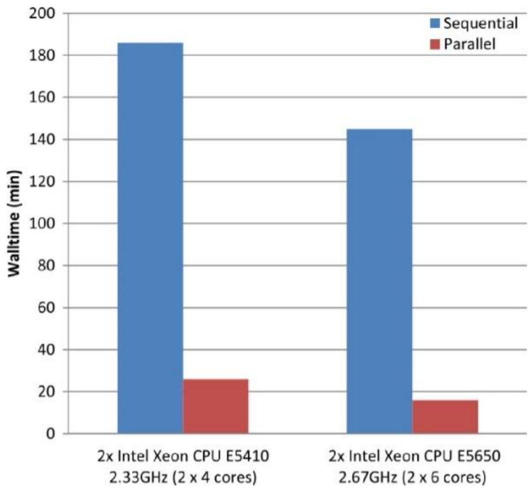

Figure 2.13: A comparison of the efficiency between the sequential and parallel access of the CPU in the hierarchical multiscale approach (Argilaga et al., 2018).

Fracture and distortion treatments in FEM

It has been demonstrated above that the mesh-based numerical approaches are able to well capture the initiation of the bifurcation and subsequently the localised strain field in a small deformation boundary problem. However, as mentioned above at the beginning of section 2.4.1, the third difficulty for the mesh-based approaches to capture large deformation problems is underlying in the potential excessive mesh distortion. This is by far the biggest challenge that still prevents the mesh-based approaches from advancing further in capturing large deformation geomechanical problems. Despite this, there are several countermeasures for improving this issue. In here, we will brief on the most widely applied three approaches namely the adaptive meshing, the extended finite element method (XFEM) and coupled FEM-DEM. The adaptive meshing technique updates the mesh discretisation in the FEM domain when the original mesh scheme no longer predicts a converging solution. In such case, the adaptive meshing technique reconstructs the discretisation scheme in order to find a certain mesh alignment that obtains a converged solution in the FEM domain (Kelly et al., 1983; Pastor et al., 1991). Although this approach is able to push further and FEM solution regarding a distortion deformation field, it is not solving the root of inability for mesh discretisation to predict large deformation or rupture process. In addition, it comes with extra computational cost and complication in the implementing algorithm. Therefore, it is not a favourable approach to be applied in the FEM solution of geomechanical problems. The extended finite element method, on the other hand, bypasses the limitation of the mesh discretisation and apply a unit of partition theory in the mesh domain. This allows an open surface to be formed inside FEM meshes while stiff satisfy the continuum assumption in the computational domain (Borja, 2008; Tejchman & Bobiński, 2012). It has been demonstrated with the capability of capturing the fracture pattern in ductile and quasi-brittle materials, and yield comparable results with experimental data for a short displacement range after the peak material strength (Sanborn & Prévost, 2011; Liu, 2015). However, it is not able to well capture the shear band configuration, as only a fracture plane is allowed to represent the localised failure zone. Furthermore, it allows a small deformation to be advanced after the peak material strength, therefore the post-localisation process can not be captured by this approach. On the other hand, the coupled FEM-DEM approach addresses the difficulties faced by the above two methods by coupling the mesh and particle discretisation of the computational domain to allow the mesh discretised area to tackle uniformly deformed area while the particle discretised area for localised or fracture area (Stránský & Jirásek, 2012; Zárate & Oñate, 2015; Zárate et al., 2018). This approach is able to naturally capture the fracture zone in the numerical domain as shown in Figure 2.14. However, it faces difficulties when capturing a complete collapse process in ductile or granular materials. In addition, the extra computational cost from using both mesh and particle discretisation may be unfavored for application with fine mesh requirements.

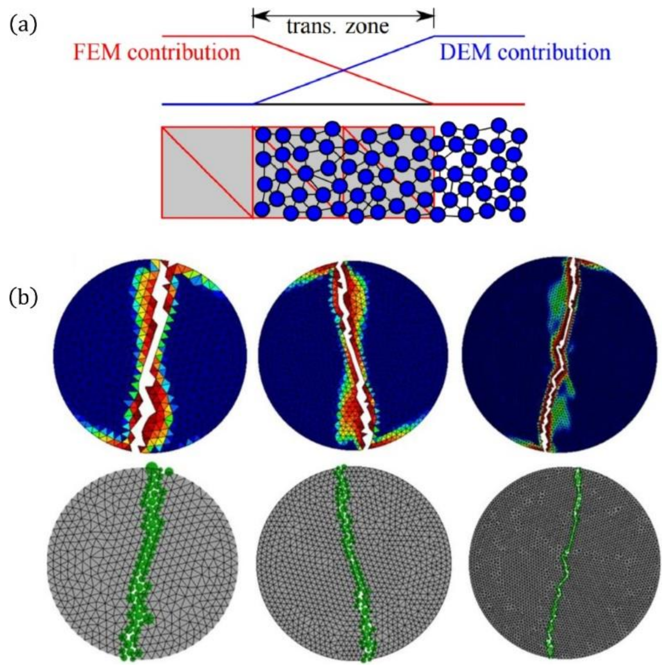

Figure 2.14: (a) numerical scheme of the FEM-DEM volume coupling (Stránský & Jirásek, 2012); (b) the Brazilian tensile strength test using the coupled FEM-DEM approach (Zárate & Oñate, 2015).

2.4.2 The material point method (MPM)

Another numerical approach namely material point method that resorts to both mesh and particle discretisation of the computational domain is also highlighted here for its progress on capturing the localisation and failure process in geomaterials. Different from the FEM, the mesh in MPM is fixed in place as a background grid to facilitate the calculation of field functions. The material properties and kinematics are carried by the assembly of Lagrangian particles which are allowed to move freely in the computation domain. Although the original version of MPM approach was expected to overcome the mesh distortion and complex mesh configuration in three-dimensional problems that could happen in FEM domain, another serious problem was discovered to significantly compromise the accuracy and reliability of this method. The issue was that the background interpolation function based on a Dirac delta form provides inadequate smoothness during the process when information is transferred between particles and background mesh. This is especially the case when a relatively large deformation occurs and particles cross the boundaries of their originally allocated cells. As this happens, the information contained by the original cell may not, at all or well communicate with the new cell that the particles have crossed in. Therefore, unphysical oscillations happen and the constitutive relationship of the particles loses their history path and manifests abrupt values (Bardenhagen & Kober, 2004). In order to solve this, a generalised form of the background interpolation function is applied in the classical MPM domain which adds an extra order of smoothness that passes grid information across their borders. This is known as the generalised interpolation material point (GIMP) method (Bardenhagen & Kober, 2004). This approach has been thereafter applied to a wide range of geomechanical problems that involves both multiphase materials and very large deformation (Sadeghirad et al., 2011; Soga et al., 2015; Yerro et al., 2015; Kiriyama, 2013; Gao et al., 2017; Müller & Vargas, 2019). For instance, Alonso and co-workers have proposed a multiphase framework to model the behaviour of unsaturated soil and applied it to characterise the rainfall-induced slope failure cases (Figure 2.15). Kiriyama applied the GIMP approach to model the soil behaviour under plane strain biaxial, axisymmetric triaxial and true triaxial loading conditions, then the obtained numerical results were compared with experimental data which showed very good agreement (Figure 2.16).

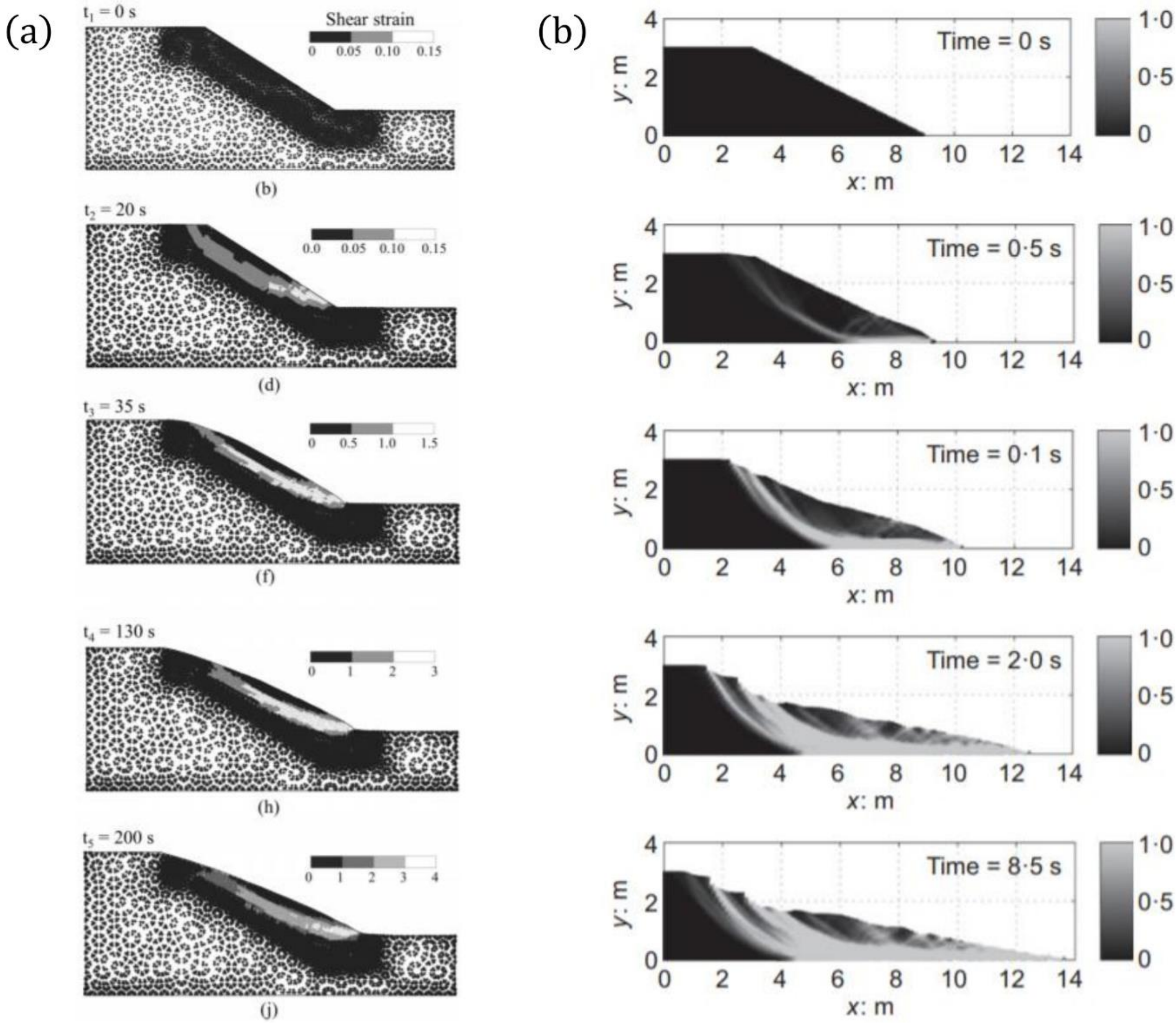

Figure 2.15: (a) GIMP modelling of rainfall induced slope failure (Yerro et al., 2015); (b) GIMP modelling of rainfall induced slope failure (with comparison with experimental data) (Soga et al., 2015).

Despite the above progress, the GIMP method still exhibits several disadvantages: first, it is relatively computational inefficient. This is due to the fact that the MPM approach utilises both mesh and particle discretisation to describe the computational domain. Therefore, the computational burden is likely doubled. Apart from this, the MPM framework exhibits difficulties when enforcing boundary conditions involving confining stress or in a complex three-dimensional space, which is likely to compromise the numerical accuracy (Steffen et al., 2008). Therefore, the performance of the current GIMP approach in problems involving boundary condition in complex configuration and multi-dimensional problems still requires further improvements.

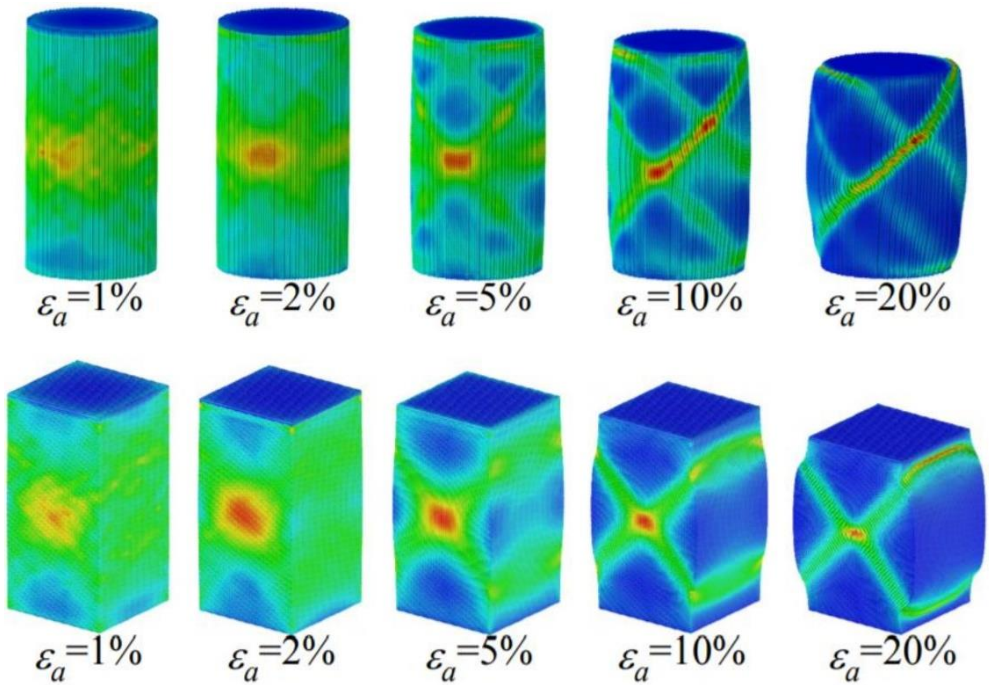

Figure 2.16: GIMP predicted shear band development under axisymmetric triaxial and true triaxial boundary conditions (Kiriyama, 2016).

From the above review regarding the mesh-baed numerical methods in capturing the bifurcation and localised failure process in geomaterials, it is clear that although a good accuracy and stability can be achieved in the modelling domain, extra computational complexity and computational costs are also required. As the geomaterials cover a wide spectrum of material properties and geomechanical problems often involve complex loading condition as well as extremely deformed problem domain, the mesh-discretised or mesh interpolated methods may seem less favourable in such cases. There is a significant need for another pathway towards solving the geomechanical problems. In the next section, a set of complete meshless approaches are reviewed to show their advantages, in the meantime posing the challenges they are facing.

2.5 Meshfree numerical approaches to characterise localised failures in geomaterials

In parallel with the mesh-based approaches, the complete meshfree methods have also been intensively engaged when applying for geomechanical problems for the past decade. The complete meshless feature of these methods gives them the potential of naturally capturing extreme deformation field through either a continuum or discotinuum description of the computational domain. The representative approaches are the smoothed particle hydrodynamics (SPH) method, the discrete element method (DEM), the element free Galerkin (EFG) method and the meshless local Petrov-Galerkin (MLPG) method. Despite these options, only the SPH and DEM methods are discussed in this section due to the significance of their progress in capturing the localised failures in geomechanical applications.

2.5.1 The discontinuum discrete element method (DEM)

The framework of the DEM approach was initially developed by Cundall and Strack in 1979. This method is based on a direct characterisation of the inter-particle contact mechanism following Newton's second law of motion. Specifically, the particles are assumed with rigid configuration, and overlapping is allowed between particle boundaries. As particles make contact and form overlapping area, the corresponding reaction force is calculated based on a predefined constitutive relation. This reaction force pushes the pairing particle in the opposite direction, therefore maintain the correct kinematics in the computational field. Based on this framework, various constitutive models are proposed to capture the DEM contact-displacement law which has successfully captured comparable results with experiments for a wide spectrum of geomaterials and tests. This includes: capturing the axisymmetric and true triaxial tests on dry/unsaturated cohesive and sandy soils (Belheine et al., 2009; Donzé et al., 2009; O'Sullivan, 2011; Cil & Alshibli, 2014), capturing uniaxial, triaxial and BTS tests on quasi-brittle and brittle materials (Wang & Tonon, 2009; Tran et al., 2011; Jiang et al., 2011; Oñate et al., 2015), incorporating the anisotropic and fabric effect to capture behaviour of cohesive, sandy and quasi-brittle materials (Laniel et al., 2008; Fu & Dafalias, 2011; Mahabadi et al., 2012; Guo & Curtis, 2015), the scale effect accounting for size-dependent behaviours in ductile and quasi-brittle materials (Wang & Gutierrez, 2010; Scholtès et al., 2011), the slope stability and toppling analysis in cohesive sandy soil and fractured rocks (Utili & Nova, 2008; Scholtès & Donzé, 2012), the curling process in unsaturated soils due to a loss of the moisture content (Tran et al., 2019). Recently, an advanced constitutive model featured with a cohesive fracture law has been implemented to DEM and applied to characterise the fracture process as well as facilitate the design for the fatigue damage in soft rock and cemented materials (Nguyen et al., 2017a; 2017b; 2019a; 2019b). The proposed numerical framework has obtained results that are in very good agreement with the experiments (Figure 2.17). Apart from this, a micromechanical investigation into the strength and the corresponding failure criteria of a foamed concrete has also been conducted with DEM approach. This work has put insight into the influence of the air-void distribution and pore size on the strength of foamed concrete and its relation to the design with such materials (Nguyen et al., 2017; 2019).

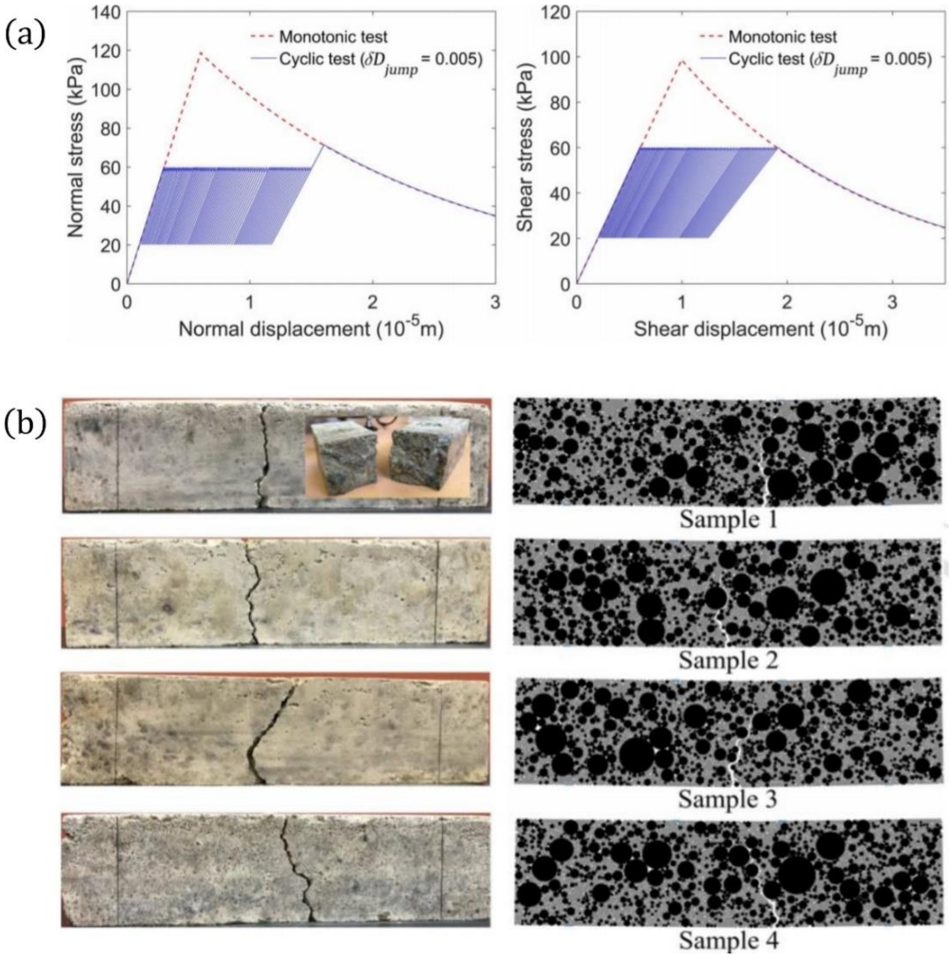

Figure 2.17: A DEM approach featured with cohesive fracture law for characterising fracture process: (a) the cyclic loading scheme; (b) a comparison between the experimental and numerical obtained fracture path (Nguyen et al., 2019a).

Despite the aforementioned impressive progress DEM has made, it is still facing a significant challenge: the computational cost. Due to the fact that DEM is a microscale based method, the size of DEM particles does not have a distinct difference with the real material grain size. Therefore, the number of computational particles required for a laboratory or even an engineering-scale problem is prohibitively large. With a currently available computational power in most computational laboratories, DEM simulations are often limited to a scaled-down or a small experimental sample size.

2.5.2 The continuum smoothed particle hydrodynamics (SPH) method

On the other hand, a continuum-based meshfree approach is much less vulnerable to the overburden issue of computational cost, which can be applied to modelling of large scale problems such as the complete process of landslides. This is represented by the SPH method, which was originally proposed for astrodynamics applications (Gingold & Monaghan, 1977; Lucy, 1977). Since then, numerous work has been conducted to improve the algorithm to accurately and effectively enforcing essential boundary conditions (Takeda et al., 1994; Randles & Libersky, 1996). Furthermore, stabilisation techniques are also proposed for eliminating the numerical noise and unphysical particle oscillations to obtain a smooth stress profile (Monaghan, 1992; 1994). The application of the SPH in the geomechanical area was pioneered by Bui and co-workers (Bui et al., 2008). They have proposed a robust numerical framework based on SPH to capture a wide range of geomechanical problems involving extreme deformations. This includes: a simulation of granular flow and slope failures, and their comparison with experimental results (Bui et al., 2006; 2007; 2008a; Nguyen et al., 2017); numerical modelling of soil-structure interaction and stability analysis of gravitational retaining wall, bracing strut etc. (Bui et al., 2008b; Verghese et al., 2013; Nguyen et al., 2013; Bui et al., 2015); a fully coupled SPH framework to capture saturated soil behaviour and analysis of slope failure case under seepage flow (Bui et al., 2007; 2008c; Bui & Fukagawa, 2009; Bui & Nguyen, 2017); the incorporation of the double scale constitutive model in SPH and its application in rock fracture with tensile, shear and mixed failure modes, as well as soil desiccation cracking process (Figure 2.18) (Wang et al., 2017a; 2017b; Tran et al., 2017; 2019; Wang et al., 2019); SPH prediction of strain localisation with an elastic-viscoplastic model (Zhao et al., 2017a).

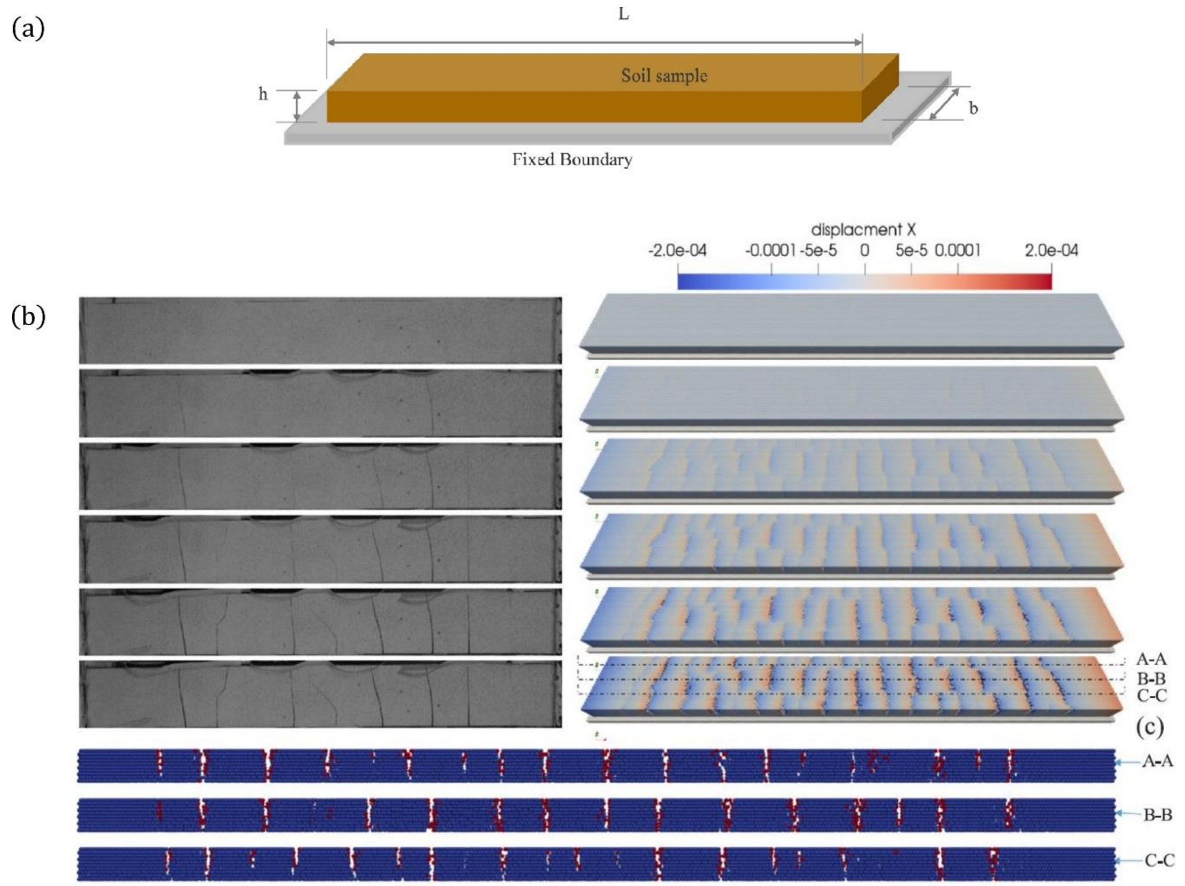

Figure 2.18: (a) the numerical setup for a dessication cracking test on Werribee clay; (b) the comparison between the experiment-captured and SPH-predicted evolution of cracks during the dessication process (Tran et al., 2019).

Even though with the promising progress, the current SPH framework is still facing several challenges. First, there lacks a generic approach to applying essential boundary conditions which involve confining stress on a flexible surface of the computational domain. The existing methods in SPH for enforcing confining boundary conditions require a time-consuming searching process for identifying the boundary surface and calculation of the corresponding normal vectors. When the computational domain undergoes large deformation, the identification of the boundary surface could be challenging for a particle-based approach, let alone correctly calculating the normal vectors. Apart from the first challenge, the SPH simulation still manifests resolution sensitive results despite the nonlocal nature of this approach. The material behaviour predicted by the current SPH method demonstrates a more brittle behaviour with finer mesh and ductile with coarser mesh analogous to the FEM mesh dependent issue. Lastly, the current SPH framework does not account for multiphase soil mechanics, which is not able to characterise the important geomechanical problems involving unsaturated conditions. This includes the prediction of rainfall-induced localisation and failure process in slope structures, the soil desiccation cracking due to loss of the moisture content, the seepage flow analysis in unsaturated soil bulk etc.

2.6 Conclusion

In this chapter, the research work regarding the localised failure process in the geomechanical field has been reviewed from various aspects. This includes the theoretical interpretation, the experimental investigation and numerical simulation of the localised failure mode. An emphasis has been made on the current state-of-art numerical approaches for analysing this problem, together with their progress and challenges. From this review of the literature, the following research gaps have been identified:

- ❖ Geomechanical problems are often featured with extreme deformation field. However, the current numerical approaches that resort to mesh discretisation or mesh interpolation more or less face inherent mesh-related difficulties when the computation domain captures localised failure process that often leads to persistent shear deformation or rupture of the material. The countermeasures proposed to improve this issue are generally complex in their algorithm and require more computational resources.
- ❖ The complete meshless approaches that are on discontinuum basis such as DEM captures very well the localisation and failure process in geomaterials. However, the micromechanical-based kinematics in these approaches limits the size of their computational particles to comparable with a real grain of materials such as sand. This requires a significant amount of particles to characterise even a laboratory-scale sample. Therefore, the current application of discontinuum numerical approaches are not well suitable for large scale geomechanical problems. On the other hand, the continuum meshfree method SPH is capable of naturally capture large deformation process for numerical samples in a wide spectrum of scale. Despite this feature, the current SPH approach faces three key challenges:
    1. There lacks a generic approach to accurately and effectively applying confining boundary condition on flexible surfaces in order to allow basic geomechanical experiments such as the plane strain biaxial test and triaxial test to be modelled by SPH.

2. Although featured with nonlocal interpolation process, the current SPH method still demonstrates a resolution sensitive behaviour, manifesting as the numerical solutions depending on the SPH discretisation scheme and resolution. This is rooted in an inadequate understanding of the local and nonlocal feature of SPH method and how it governs the energy dissipation in the computational domain.
3. There lacks a fully coupled multiphase SPH framework to capture the behaviour of unsaturated geomaterials. This prevents the SPH method from unleashing its meshfree advantage in characterising large deformation problems such as the rainfall-induced slope failure, the desiccation crack in soil due to loss of moisture content etc.

To address the above gaps, this research proposes an advanced computational framework based on the SPH method for capturing localised failure in laboratory tests and large scale applications with dry/unsaturated geomaterials. In this framework, a generic boundary condition to applying confining boundary condition on flexible surfaces is first proposed. It is followed by an investigation into the local and nonlocal feature of the conventional SPH method. An additional nonlocal operator is then proposed in the conventional SPH method to facilitate a full regularisation of the energy dissipation path, removing the resolution bias issue. Lastly, a fully coupled multiphase framework that contains solid, air and liquid components are incorporated into SPH for allowing its characterisation of seepage flow in soil and rainfall-induced slope failure process.

Chapter 3

Smoothed particle hydrodynamics and its approximation of soil governing equations

3.1 Introduction

In the previous chapter, a review regarding the current state-of-art approaches to analysing the localised failure and large deformation problems in geomaterials has been provided. From the review, it is clear that a complete meshfree approach based on the continuum mechanics description of the computational domain fits the current research topic very well. Therefore, in this chapter, the smoothed particle hydrodynamics method is introduced in detail, which will be the basis numerical method applied in this work.

This chapter explains the current SPH framework with the following emphasis: the basic formulations of SPH including the particle approximation of the computational domain and the governing equations of the field; the kernel functions in SPH which dominates the stability of the SPH domain. The differences between different kernel functions and the limitations of each function are summarised; the numerical techniques that have been applied in SPH to facilitate the computational process including the stabilisation factors and the advanced particle pairing process; the methods to enforce the essential nonslip and free-slip boundary conditions; the time integration schemes in SPH elaborating the leap-frog method.

Apart from this, the constitutive models that have been applied in this work to complete the stress and strain relationship in the field governing equations are explained in detail. Three main types of constitutive models are listed: the rate-dependent Perzyna type viscoplastic model featured with evolving Von Mises yield surface; the pressure-dependent elastoplastic model featured with non-evolving Mohr-Coulomb yield surface (perfectly plastic model); the pressure-dependent elastoplastic model featured with evolving Mohr-Coulomb yield surface (strain-softening model). A generic framework is then presented for incorporating these models in SPH environment and all relevant formulations are listed. Furthermore, the benchmark tests that have been applied to validate the performance of the above models in SPH are also elaborated. This includes an element test that is analogous to the FEM analysis and a simple shear test, the obtained results are compared with their analytical counterparts showing optimal agreements. This provides a solid basis to apply the proposed SPH framework for analysing the soil mechanical problems for this research.

3.2 Fundamental of SPH

The SPH method was first proposed in the 1970s for solving the kinematics problems in the astrodynamics field (Gingold & Monaghan, 1977; Lucy, 1977), and later largely applied to fluid dynamics (Morris, 1996; Monaghan, 1996). Starting from 2006, it is intensively applied for solving geomechanical problems due to the advancement for improving its numerical stability and boundary conditions pioneered by Bui and coworkers (Bui et al., 2006; 2007; 2008a). More specifically, an artificial viscosity and artificial stress term have been implemented in SPH for controlling the unphysical particle oscillation and pairing issue under tensile loading. In addition, the nonslip and free-slipe mechanical conditions have been enforced on SPH domain with the virtual and ghost particle methods. With this numerical framework established, the following work based on SPH has been engaged regarding the soil-structure interaction (Bui et al., 2008b; Verghese et al., 2013; Nguyen et al., 2013; Bui et al., 2015), soil-water interaction (Bui et al., 2007; 2008c; Bui & Fukagawa, 2009; Bui & Nguyen, 2017), slope stability analysis with and without reinforcement (Bui et al., 2008a; Nguyen et al., 2013; 2017), the desiccation soil cracking (Tran et al., 2017) and static/dynamic rock fracturing (Wang et al., 2017a; 2017b; 2019). From the above applications, SPH has been demonstrated as a powerful tool for analysing large deformation problems under a wide scale of problem domains. In order for a comprehensive understanding of SPH, its basic theory and algorithms are presented in the following sections.

3.2.1 SPH discretisation scheme

SPH describes the computational domain as an assembly of Lagrangian particles that follow the partition of unity principle. The particles carry information of all field variables and properties including the location, velocity, stress, strain, mass, density etc. The field information is incorporated and processed through a kernel interpolation process which calculates an unknown variable by averaging over its counterparts in the vicinity. The averaging is governing by a specific kernel function and the mathematical expression for this interpolation in SPH is as follows:

$$\mathrm{f}(\mathbf{r}) = \int_{\Omega} \mathrm{f}(\mathbf{r}')\mathrm{W}(\mathbf{r} - \mathbf{r}', \mathrm{h})\mathrm{d}\mathbf{r}' \tag{3.1}$$

where $\mathrm{f}(\mathbf{r})$ is the field variable at location $\mathbf{r}$, and $\mathrm{f}(\mathbf{r}')$ is the same field variable at location $\mathbf{r}'$ which acrosses the entire computational domain. W is the kernel function with smoothed length h and Ω represents the interpolation domain, which will be elaborated in the following section. In practice, the kernel function is only effective within a certain distance between $\mathbf{r}$ and $\mathbf{r}'$, therefore the Ω has a limited size. The above formulation 3.1 is written in an integration form, which becomes particle summation form when applied to the SPH domain as:

$$\mathrm{f}(\mathbf{r}_\mathrm{i}) \approx \sum_{\mathrm{j}=1}^{\mathrm{N}} \frac{\mathrm{m}_\mathrm{j}}{\rho_\mathrm{j}} \mathrm{f}(\mathbf{r}_\mathrm{j})\mathrm{W}(\mathbf{r}_\mathrm{i} - \mathbf{r}_\mathrm{j}, \mathrm{h}) \tag{3.2}$$

where m_j and ρ_j are the mass and density carried by particle j and their quotient is the volume occupied by the particle. N is the total number of particle included in each kernel interpolation, and the approximation mark $\approx$ indicates a certain but acceptable level of error when transferring Equation 3.1 to 3.2.

The approximation of the first-order gradient of field variables can be performed by performing derivative once for Equation 3.1 and applying divergence theorem, which yields the following form:

$$\frac{\partial \mathrm{f}(\mathbf{r}_\mathrm{i})}{\partial \mathbf{r}_\mathrm{i}} = \sum_{\mathrm{j}=1}^{\mathrm{N}} \frac{\mathrm{m}_\mathrm{j}}{\rho_\mathrm{j}} \mathrm{f}(\mathbf{r}_\mathrm{j}) \frac{\partial \mathrm{W}(\mathbf{r}_\mathrm{i} - \mathbf{r}_\mathrm{j}, \mathrm{h})}{\partial \mathbf{r}_\mathrm{i}} \tag{3.3}$$

Then by introducing the following notation:

$$\mathrm{W_{ij}} = \mathrm{W}\left(\left|\mathbf{r}_\mathrm{i} - \mathbf{r}_\mathrm{j}\right|, \mathrm{h}\right) \quad \text{and} \quad \frac{\partial \mathrm{W_{ij}}}{\partial \mathbf{r}_\mathrm{i}} = \frac{\partial \mathrm{W_{ij}}}{\partial \mathbf{r}_\mathrm{i}} \frac{\partial \mathbf{r}_\mathrm{i}}{\left|\mathbf{r}_\mathrm{i}\right|} \tag{3.4}$$

The expression of kernel interpolation in SPH can be simplified as follows:

$$\mathrm{f}(\mathbf{r}_\mathrm{i}) \approx \sum_{\mathrm{j}=1}^{\mathrm{N}} \frac{\mathrm{m_j}}{\rho_\mathrm{j}} \mathrm{f}(\mathbf{r}_\mathrm{j}) \mathrm{W_{ij}} \tag{3.5}$$

$$\frac{\partial \mathrm{f}(\mathbf{r}_\mathrm{i})}{\partial \mathbf{r}_\mathrm{i}} \approx \sum_{\mathrm{j}=1}^{\mathrm{N}} \frac{\mathrm{m_j}}{\rho_\mathrm{j}} \mathrm{f}(\mathbf{r}_\mathrm{j}) \frac{\partial \mathrm{W_{ij}}}{\partial \mathbf{r}_\mathrm{i}} \tag{3.6}$$

The above Equation 3.5 and 3.6 consists of the basic interpolation formulation in SPH for calculating field variables and their gradients. In some cases, SPH approximation of second or even higher-order formulations are required, which applying the conventional approach may lead to significant numerical instability (Chen et al., 1999). Therefore, a special treatment is required, which will be elaborated for second-order gradient functions for approximating unsaturated soil dynamics in Chapter 6.

3.2.2 Field governing equations

The deformation of an infinitesimal volume element within a continuum domain can be described using two fundamental governing laws, the mass and momentum conservation equations which are written as follows:

$$\frac{\mathrm{D}\rho}{\mathrm{Dt}} = -\rho \frac{\partial \mathrm{v}^\alpha}{\partial \mathrm{r}^\alpha} \tag{3.7}$$

$$\frac{\mathrm{Dv}^\alpha}{\mathrm{Dt}} = \frac{1}{\rho} \frac{\partial \sigma^{\alpha\beta}}{\partial \mathrm{r}^\beta} + \mathrm{f}^\alpha \tag{3.8}$$

where α and β denote x, y and z axes of the Cartesian coordinate system with Einstein's convention applied to the repeated indices; ρ is the material density, v^α is the velocity component; $\sigma^{\alpha\beta}$ is the stress tensor component, taken as negative in compression; f^α is the acceleration due to external loads such as gravitational force.

By using the SPH approximation of the gradient of a function, i.e. Equation 3.6, the above partial differential governing equations can be discretised as follows:

$$\frac{D\rho_i}{Dt} = \sum_{j=1}^{N} m_j \left(v_i^\alpha - v_j^\alpha\right) \frac{\partial W_{ij}}{\partial r_i^\alpha} \tag{3.9}$$

$$\frac{Dv_i^\alpha}{Dt} = \sum_{j=1}^{N} m_j \left(\frac{\sigma_i^{\alpha\beta} + \sigma_j^{\alpha\beta}}{\rho_i \rho_j}\right) \frac{\partial W_{ij}}{\partial r_i^\beta} + f_i^\alpha \tag{3.10}$$

where f_i^α is the force per unit mass due to gravitation. Finally, to solve the above system of governing equations, one needs a constitutive relation to calculate the stress tensor of the soil and this will be elaborated in the following section.

3.2.3 Kernel functions

The kernel function is one of the keys for SPH calculation, which underpins the weighted averaging interpolation process. An SPH kernel function is normally required to satisfy three basic conditions (Bui et al., 2008a): the normalisation condition which states that the integration of a kernel function over its domain equals unity; the delta function property which states that kernel function equals to Dirac delta function when its smoothing length approaches zero; the compact support condition which limits the effective influence radius of the kernel to a finite value.

The selection of the kernel function largely governs the stability of the computational domain. Each kernel function is able to contain a certain amount of particle during the interpolation while maintaining reasonable stability of the computational domain. If fewer particles are involved, the kernel interpolation loses its validity. However with more particle, the interparticle repulsive forces cannot be well maintained, which lead to the pairing instability in SPH domain (it is noted here that the pairing instability, although very similar to the tensile instability in SPH, is governed by a different mechanism from the tensile instability) (Dehnen & Aly, 2012). Specifically, the kernel functions that are featured with an inflection point (zero gradient point at peak of the kernel function) would manifest this issue when including more particles than its stability limit (Dehnen & Aly, 2012). Particles located near the inflection point would not gain enough repulsive force from the kernel gradient, therefore form pathological pairs. Therefore, choosing the appropriate kernel in a specific problem context is vital to maintain a stable numerical domain. In this geomechanical applications, the most popular kernel would be the cubic spline which has been widely applied and demonstrated with very good stability performance. In addition to this kernel, another two namely the Wendland and higher-order core triangle (HOCT) kernel are also introduced here (Read et al., 2010). Starting from the cubic spline kernel, it can be expressed as (Monaghan & Lattanzio, 1985):

$$W(q,h) = \alpha_d \times \begin{cases} 1 - \frac{3}{2}q^2 + \frac{3}{4}q^3 & 0 \le q < 1 \\ \frac{1}{4}(2-q)^3 & 1 \le q < 2 \\ 0 & q \ge 2 \end{cases} \tag{3.11}$$

where α_d is a normalisation coefficient, which is equal to $10/(7\pi h^2)$ and $3/(2\pi h^3)$ in two and three dimensional space, respectively; q is the ratio between $|\mathbf{r} - \mathbf{r}'|$ and h. The range of applicable smoothed length for the cubic spline function that demonstrates a numerically stable domain is from 1.2dx to 1.3dx in this research. For using a smoothing length that is larger than 1.3dx, a kernel that is featured with a wider range of maintaining a positive Fourier transform is required in Figure 3.1b (Dehnen & Aly, 2012). In this work the Wendland C2 kernel is chosen, which can be expressed as:

$$W(q,h) = \alpha_d \times \begin{cases} \left(1 - \frac{q}{2}\right)^4 (2q+1) & 0 \le q < 2 \\ 0 & q > 2 \end{cases} \tag{3.12}$$

where α_d is a normalisation coefficient, which is equal to $7/(4\pi h^2)$ and $21/(16\pi h^3)$ in two and three dimensional space, respectively; q is the ratio between $|\mathbf{r} - \mathbf{r}'|$ and h.

From Figure 3.1, it is clear that even though Wendland C2 kernel demonstrates a much wider positive Fourier transform range which is a vital indicator for kernel capability of maintaining the stability of the computational domain, it still features with an inflection point. This gives a larger applicable range of smoothing length of Wendland C2, yet is still potential to manifest the pairing instability. In order to completely eliminate any potential pairing pathology, a kernel without inflection point such as the HOCT4 is required which can be expressed as follows:

$$W(q,h) = \frac{N}{h^3} \begin{cases} Px + Q & 0 < x \le \alpha \\ (1-x)^{n_k} + A(\gamma - x)^{n_k} + B(\beta - x)^{n_k} & \alpha < x \le \beta \\ (1-x)^{n_k} + A(\gamma - x)^{n_k} & \beta < x \le \gamma \\ (1-x)^{n_k} & \gamma < x \le 1 \\ 0 & \text{otherwise} \end{cases} \tag{3.13}$$

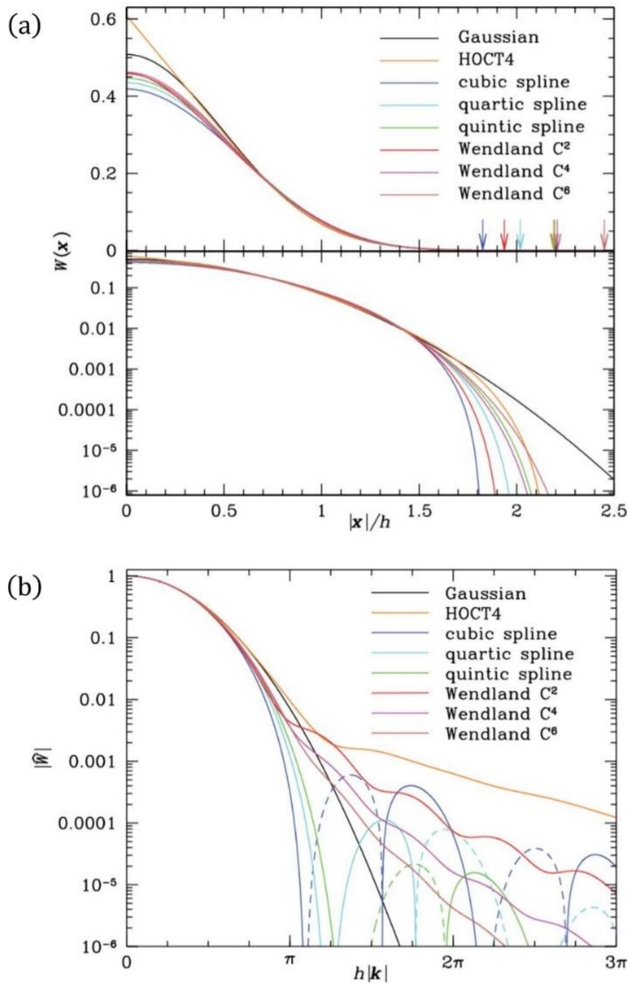

Figure 3.1: (a) comparison of kernel configuration scaled to a common resolution (top: linear plot; bottom: logarithmic plot); (b) Fourier transforms of different kernels (broken lines represent negative values) (Dehnen & Aly, 2012).

In above, n_k is a parameter that determines the order of the kernel, for instance $n_k = 4$ corresponds to HOCT4 kernel. The coefficients N, A, B, P, Q, α are related to the selection of n_k. β and γ are free parameters. The detailed parameters for different orders of HOCT kernels can be found in Read's work (2010). Despite the capability of HOCT to avoid any pairing instability, it has been found that its application in this work comes with significant extra computational cost compared with cubic spline and Wendland, which makes it not favourable in our applications for geomechanical problems.

3.2.4 Stabilisation techniques

Artificial viscosity

It has been observed in SPH domain that whenever a boundary condition is applied or the current equilibrium state is altered due to change in the boundary conditions, a shock wave will present and generates unphysical particle oscillations (Anderson & Wendt, 1995; Gingold & Monaghan, 1982). A proper dissipative term is then required for stabilising the numerical domain by damping out the excessive shock waves. In this work, an artificial viscosity term is considered in the momentum conservation law in Eq 3.10, which can be rewritten as:

$$\frac{Dv_i^\alpha}{Dt} = \sum_{j=1}^{N} m_j \left(\frac{\sigma_i^{\alpha\beta} + \sigma_j^{\alpha\beta}}{\rho_i \rho_j} - \Pi_{ij}^{\alpha\beta} \delta^{\alpha\beta} \right) \frac{\partial W_{ij}}{\partial r_i^\beta} + f_i^\alpha \tag{3.14}$$

where $\Pi_{ij}^{\alpha\beta}$ is the artificial viscosity term and $\delta^{\alpha\beta}$ is the Kronecker's delta function which equals unity when $\alpha = \beta$ and becomes zero when $\alpha \neq \beta$. The $\Pi_{ij}^{\alpha\beta}$ component is explicitly written as:

$$\Pi_{ij}^{\alpha\beta} = \begin{cases} \dfrac{-\alpha_\Pi c_{ij} \phi_{ij} + \beta_\Pi \phi^2}{\rho_{ij}} & \mathbf{v}_{ij} \cdot \mathbf{r}_{ij} < 0 \\ 0 & \mathbf{v}_{ij} \cdot \mathbf{r}_{ij} \geq 0 \end{cases} \tag{3.15}$$

where α_Π and β_Π are parameters controlling the viscosity effect which can be either updated based on time and space during the calculation or predefined a fixed value (Bui et al., 2008a). The density ρ_{ij} is an average value between particle i and j, other parameters such as c_{ij}, ϕ_{ij} and their determination process has been elaborated in Bui's work (2008a).

Viscous damping

In SPH domain, a sudden change in the boundary condition may lead to significant fluctuation in the stress field manifesting as a wave propagates through the numerical domain and rebound on a boundary surface. Such stress wave can cause undesirable instability in the computational domain especially when a quasi-static condition is required, and incorrect plasticity condition for pressure-dependent constitutive models. In order to allow the excessive wave energy to dissipate efficiently during the computation, a viscous damping term based on a variation of the Rayleigh damping coefficient has been introduced into the SPH method as follows (Bui & Fukagawa, 2013):

$$D_a^{\alpha} = -c_d \dot{v}_d^{\alpha} \tag{3.16}$$

$$c_d = \xi \sqrt{\frac{E}{\rho h^2}} \tag{3.17}$$

where $\dot{v}_d^{\alpha}$ is the acceleration of the SPH particles, ξ is a non-dimensional damping coefficient, E is Young's modulus. When applied in SPH, it leads to the following form of the momentum conservation equation:

$$\frac{Dv_i^{\alpha}}{Dt} = \sum_{j=1}^{N} m_j \left(\frac{\sigma_i^{\alpha\beta} + \sigma_j^{\alpha\beta}}{\rho_i \rho_j} - \Pi_{ij}^{\alpha\beta} \delta^{\alpha\beta} \right) \frac{\partial W_{ij}}{\partial r_i^{\beta}} + f_i^{\alpha} + D_a^{\alpha} \tag{3.18}$$

This approach has been applied to successfully facilitate obtaining a desired initial stress condition in the SPH domain subjected to gravitational load (Bui & Fukagawa, 2013), where the effect of the damping coefficient has been studied for stabilising stress wave in a saturated soil bulk (Figure 3.2). It is also demonstrated to effectively stabilise the SPH in a way analogous to the artificial viscosity term in a granular flow test (Nguyen et al., 2017).

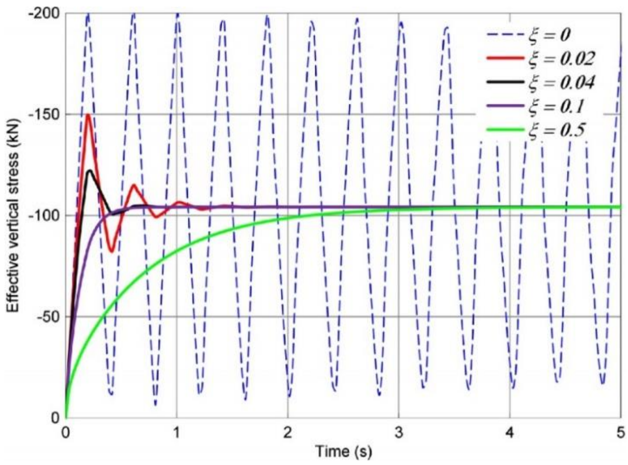

Figure 3.2: The effect of the viscous damping coefficient in stabilising the stress fluctuation in a saturated soil bulk with suddenly applied gravitational force (Bui & Fukagawa, 2013).

Artificial stress

The fundamental behaviour of SPH particles follow a certain pattern of the physical atoms, showing a repulsive effect when the inter-particle distance decreases and attractive effect when the inter-particle distance increases. However, when the SPH domain undergoes continuing tensile deformation with an increment of particle separations, the particles tend to form clumps in the numerical domain. The necessary condition for such clumping (or namely tensile instability) to occur involves a combination of the stress sign (tension/compression) and the gradients of the SPH kernel (Swegle et al., 1995). Despite various countermeasures that have been proposed in the literature, the artificial stress method first put forward by Monaghan and Gray is proofed very effective in removing the tensile instability for both non-cohesive and cohesive soils (Monaghan, 2000; Gray et al., 2001; Bui et al., 2008a). The basic idea is to introduce a repulsive force in a state of particles under tension to prevent forming clumps. In order to implement this approach, the SPH momentum balance in Eq 3.14 should be further expanded as:

$$\frac{Dv_i^{\alpha}}{Dt} = \sum_{j=1}^{N} m_j \left(\frac{\sigma_i^{\alpha\beta} + \sigma_j^{\alpha\beta}}{\rho_i \rho_j} - \Pi_{ij}^{\alpha\beta}\delta^{\alpha\beta} + f_{ij}^{n}\left(R_i^{\alpha\beta} + R_j^{\alpha\beta}\right) \right) \frac{\partial W_{ij}}{\partial r_i^{\beta}} + f_i^{\alpha} \tag{3.19}$$

where n is a state parameter dependent on the problem context, and in geomechanical applications it is chosen as 2.55 (Bui et al., 2008a), and f_{ij}^{n} is the repulsive force term which can be specified as:

$$f_{ij}^{n} = \frac{W_{ij}}{W(\Delta d, h)} \tag{3.20}$$

The $W(\Delta d, h)$ term is a constant with a non-evolving kernel function, therefore the ratio describes in the above equation normally exhibits an optimum value depending on the smoothing length. The $R_i^{\alpha\beta}$ and $R_j^{\alpha\beta}$ are the rotation of the local artificial stress tensor to their principal values, which are calculated from the stress state subjected to tensile loading. The detailed formulations and implementations of artificial stress have been elaborated in previous work (Bui et al., 2008a).

3.2.5 The normalised kernel and its gradient correction in SPH

The nature of the nonlocal interpolation process determines that the kernel influence area will always be truncated when performing the interpolation near a free boundary surface. This is due to a lack of field information outside of the SPH domain where kernel interpolation requires a full contribution from all area of its supporting domain. This problem presents insufficiently evaluated variables along the boundary surface which not only contradicts physical reality but creates undesirable boundary effects under certain problem context (Bui et al., 2013). There are mainly two ways to improve the kernel truncation effect including the application of boundary particles and the normalisation of kernel. Using boundary particles involves generation of extra SPH particles that are located outside of the free boundary surfaces, which in the meantime enforces essential boundary conditions. Approaches represented by using the so-called virtual particle and ghost particle will be elaborated in the following section. On the other hand, the normalisation of kernel is widely applied which features the following form with its effect of the correction illustrated in Figure 3.3:

$$\mathrm{f}(\mathbf{r}_\mathrm{i}) = \frac{\sum_{\mathrm{j}=1}^{\mathrm{N}} \frac{\mathrm{m_j}}{\rho_\mathrm{j}} \mathrm{f}(\mathbf{r}_\mathrm{j}) \mathrm{W_{ij}}}{\sum_{\mathrm{j}=1}^{\mathrm{N}} \frac{\mathrm{m_j}}{\rho_\mathrm{j}} \mathrm{W_{ij}}} \tag{3.21}$$

Apart from the normalisation of the kernel itself, the gradient of the kernel can also be corrected to achieve better accuracy in the SPH domain. In the numerical domain, Equation (3.5) and (3.6) can theoretically have second-order accuracy. However, this is not always achieved in SPH approximations, especially when particles undergo large deformation or the kernel supporting domain is truncated by boundaries. These deficiency problems are often called particle inconsistency and have been extensively studied in the past few decades. Different correction techniques have been proposed to restore particle consistency, thereby improving the accuracy of SPH approximations (Bonet & Lok, 1999; Chen et al. 1999; Liu & Liu, 2006; Oger et al. 2007). In this study, since the SPH approximation of the gradient of a function is mostly used to discretise the governing equations and to enforce confining boundary conditions, the accurate evaluation of the SPH approximation of the kernel gradient is essential. To achieve this, the SPH renormalisation technique (Bonet & Lok, 1999; Oger et al. 2007) is adopted, which modifies the conventional SPH approximation of function gradient, i.e. Equation (3.6), as follows:

$$\frac{\partial \mathrm{f}(\mathbf{r}_\mathrm{i})}{\partial \mathbf{r}_\mathrm{i}} \approx \sum_{\mathrm{j}=1}^{\mathrm{N}} \frac{\mathrm{m_j}}{\rho_\mathrm{j}} \mathrm{f}(\mathbf{r}_\mathrm{j}) \frac{\partial \mathrm{W}_\mathrm{ij}^\mathrm{R}}{\partial \mathbf{r}_\mathbf{i}} \tag{3.22}$$

where $\partial \mathrm{W}_\mathrm{ij}^\mathrm{R} / \partial \mathbf{r}_\mathrm{i} = \mathrm{L_i} \, \partial \mathrm{W_{ij}} / \partial \mathbf{r}_\mathrm{i}$ denotes the normalised kernel gradient at particle i and $\mathrm{L_i}$ is the renormalisation matrix, which has the following discretised form:

$$L_i = \begin{bmatrix} \sum_{j=1}^{N} \frac{m_j}{\rho_j}(x_j - x_i)\frac{\partial W_{ij}}{\partial x_i} & \sum_{j=1}^{N} \frac{m_j}{\rho_j}(x_j - x_i)\frac{\partial W_{ij}}{\partial y_i} & \sum_{j=1}^{N} \frac{m_j}{\rho_j}(x_j - x_i)\frac{\partial W_{ij}}{\partial z_i} \\ \sum_{j=1}^{N} \frac{m_j}{\rho_j}(y_j - y_i)\frac{\partial W_{ij}}{\partial x_i} & \sum_{j=1}^{N} \frac{m_j}{\rho_j}(y_j - y_i)\frac{\partial W_{ij}}{\partial y_i} & \sum_{j=1}^{N} \frac{m_j}{\rho_j}(y_j - y_i)\frac{\partial W_{ij}}{\partial z_i} \\ \sum_{j=1}^{N} \frac{m_j}{\rho_j}(z_j - z_i)\frac{\partial W_{ij}}{\partial x_i} & \sum_{j=1}^{N} \frac{m_j}{\rho_j}(z_j - z_i)\frac{\partial W_{ij}}{\partial y_i} & \sum_{j=1}^{N} \frac{m_j}{\rho_j}(z_j - z_i)\frac{\partial W_{ij}}{\partial z_i} \end{bmatrix}^{-1} \tag{3.23}$$

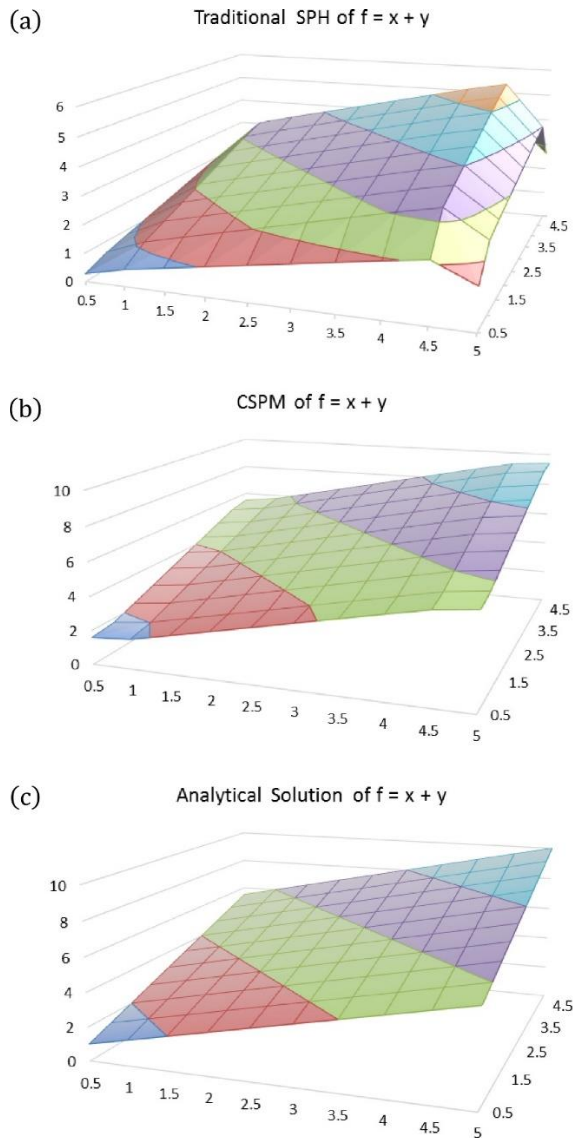

Figure 3.3 SPH interpolation of function f = x + y with (a) traditional SPH method; (b) corrective SPH method (CSPM); (c) the analytical solution.

3.2.6 The particle pair searching process

During the SPH computation process, particles are connected in order to identify their effective influence area and neighbouring counterparts in the kernel interpolation process. The process of establishing such connections or particle pairs is called searching which corresponds to a significant portion of the overall computational cost. Therefore an effective searching algorithm is able to help speed up the numerical simulations. The commonly applied searching approaches in SPH include the direct search method, the tree searching method (Hernquist & Katz, 1989), the linked list method (Liu & Liu, 2003) and the flink-list method (Bui et al., 2008a). In these methods, the direct search is the simplest in its algorithm, however, features the highest computational cost. The basic idea is to start with one particle, then go through the rest of all SPH particles in the computational domain and connect those which effectively interact with the concerned particle using pairs.

In order to improve the efficiency of the searching process, a linked list method was proposed which subdivides the computational domain before performing the search (Liu & Liu, 2003). The linked list method significantly improves the searching efficiency compared to the direct search method by disregarding the search between particles that are far-located. Specifically, an orthogonal virtual grid with square mesh and grid length of 2h (two times of smoothing length) is first constructed in the computational domain. When searching, only particles that are located in the neighbouring cells are considered. Starting from one cell, all its 9 surrounding cells are looped for search before moving to the next cell to conduct further searching. This process is schematically illustrated in Figure 3.4a.

Despite the improvement, the linked list method still features redundant process which could add unnecessary computational costs. For instance, all neighbouring cells are considered during the searching, which involves 9 and 27 cells in 2D and 3D space respectively. In order to further improve the searching technique, Bui and co-worker proposed an advanced version of the linked list method (namely flink-list method) which only loops through 5 and 14 cells under 2D and 3D problem domain respectively. The underlying idea is that the first search starts from one corner cell in the computational domain, once all its neighbouring cells are looped for pairing and the process moves to the next cell, the one-side-located cells are disregarded as they have already been searched. The illustration of this process is presented in Figure 3.4b.

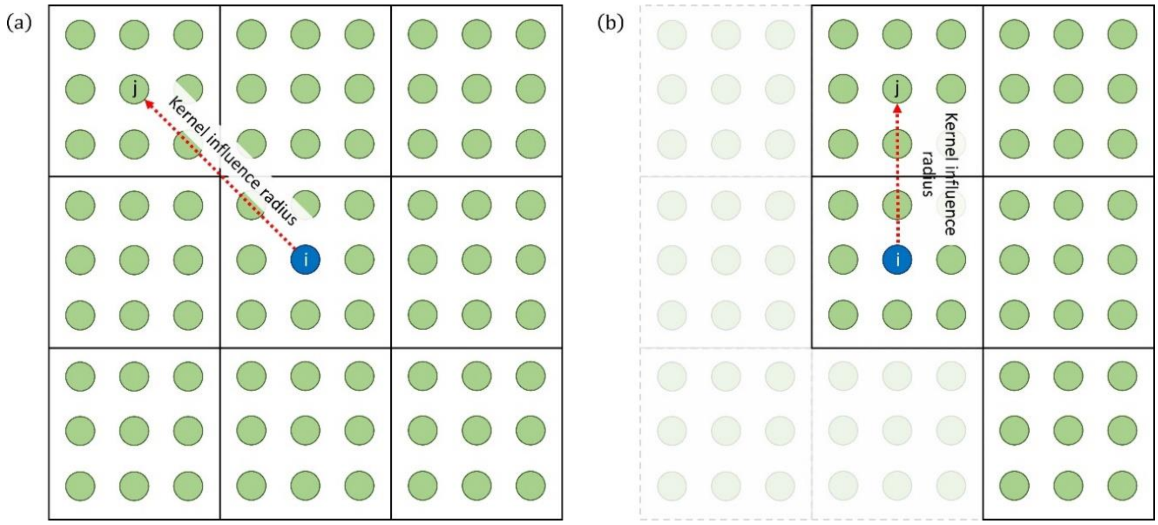

Figure 3.4: The scheme of the (a) linked list searching process; (b) flink list searching process.

3.3 Essential boundary conditions in SPH

Like any other numerical methods, the treatment of boundary conditions in SPH is required to facilitate its applications to a wide range of engineering problems. In particular, when an SPH particle is close to the boundary, its kernel function is truncated, resulting in inaccurate approximations of field variables. To resolve this problem, ghost and virtual boundary particles (Takeda et al. 1994), (Randles & Libersky, 1996), (Morris et al. 1997), (Bui et al. 2008a) have been introduced to replace solid boundaries. Specific conditions are then enforced through these particles to achieve desirable boundary conditions (e.g. non-slip, free-slip or axis-symmetric conditions). In this part, the conventional approaches to enforce mechanical boundaries that are featured with nonslip and free-slip conditions are introduced.

3.3.1 The virtual particle method

The virtual particle method is applied for solid boundary lines which generally features flat surfaces and aligns in an orthogonal manner in the Cartesian axis. In order to implement this method, a few layers of “virtual SPH particles” are created to align with the existing boundary surface. The number of layers is determined through the smoothing length, for instance, three layers of particles correspond to h=1.2dx (Figure 3.5). The virtual particles are created with the same mass, density and interparticle distance with the particles in the SPH domain. At the interface that locates at the middle point between the outermost SPH domain particles and the innermost virtual boundary particles, a zero velocity condition is assumed, which enforces the non-slip condition. Accordingly, the velocity tensor of the virtual particles are interpolated from the domain particle as follows:

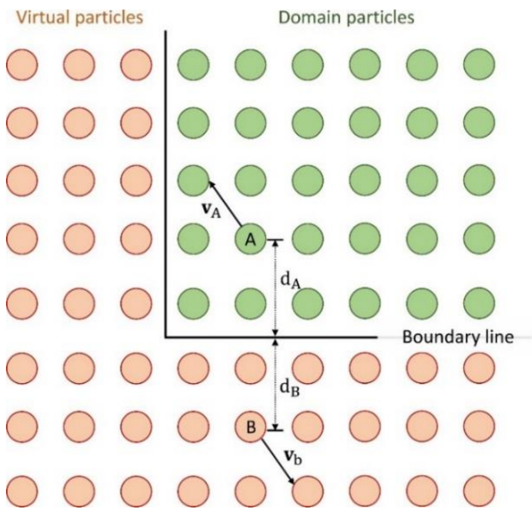

Figure 3.5: Illustration of the configuration of the virtual particle method.

$$\mathbf{v}_{ab} = \mathbf{v}_a - \mathbf{v}_b = \beta(\mathbf{v}_a - \mathbf{v}_{wall}) \tag{3.24}$$

where $\mathbf{v}_{ab}$ is the relative velocity between real and virtual particles. The coefficient β features a maximum value for excluding unreasonably large velocity interpolation for the virtual particles when real particles are too close to the solid boundary as follows:

$$\beta = \min\left(\beta_{max}, 1 + \frac{d_b}{d_a}\right) \tag{3.25}$$

In this study, the range of $\beta_{max} = 1.5\sim2$ has been applied for its good performance as demonstrated in previous work (Bui et al., 2008a). From the above equations, the velocity tensor assigned to the virtual boundary particles is written as:

$$\mathbf{v}_b = (1 - \beta)\mathbf{v}_a + \beta\mathbf{v}_{wall} \tag{3.26}$$

Apart from the velocity tensor, it is also necessary to assign stress tensor to the virtual particles in order to allow a correct calculation of Eq (3.19). Despite the existing approaches that are mostly derived based on the work of Randles and Libersky (1996), we apply in the research, a simplified method that based on the assumption of a locally uniform distributed stress profile is applied (Bui et al., 2008a). In this method, the pairs that link real and virtual particles are first identified. Then the stress tensors carried by the domain particles are assigned to their corresponding virtual counterparts, which is written as:

$$\boldsymbol{\sigma}_{\mathrm{b}} = \boldsymbol{\sigma}_{\mathrm{a}} \qquad \text{when either a or b is virtual particle} \tag{3.27}$$

The above approach to interpolate stress tensor for the virtual boundary particles has been demonstrated with both high computational efficiency and good accuracy (Bui et al., 2008a).

3.3.2 The ghost particle method

In order to achieve a free-slip condition on the SPH boundary surface, the ghost particle method proposed by Libersky and Petschek (1991) is applied here. The method creates the ghost particles based on a mirroring process of the particles in the modelling domain that are located within κh distance from the boundary line (κ is a coefficient which is selected as 2.5 in this work). Therefore the locations of the ghost particles are at exact mirroring point of the domain/real particles. The velocity tensor for the ghost particles representing the direction that is perpendicular to the boundary line is assigned with an inverse direction as compared to the domain particles for preventing the domain particles from penetrating into the boundary. The velocity tensor for the ghost particles that is parallel to the boundary line is set to be equal to the counterpart in domain particles. For the stress tensor, the interpolation can be expressed as follows:

$$\sigma_{\mathrm{ghost}}^{\alpha\beta} = \begin{cases} \sigma_{\mathrm{real}}^{\alpha\beta} & \text{if } \alpha = \beta \\ -\sigma_{\mathrm{ghost}}^{\alpha\beta} & \text{if } \alpha \neq \beta \end{cases} \tag{3.28}$$

The above approach has been demonstrated to be able to effectively enforce a free-slip boundary condition. However, this method is suitable for boundaries featured with straight surfaces. Furthermore, when the SPH domain undergoes large deformation which may lead to non-uniform interparticle translations, the ghost boundary particles becomes similarly disordered and fail to maintain the correct boundary conditions.

3.3.3 The interpolation particle method

The above virtual particle and ghost particle approaches are applicable for SPH boundary lines that are aligned with the axis of the Cartesian coordinate with elastic deformations. However, for boundary lines that are in an angle with the Cartesian axis, there require other solutions. In the work, a simple interpolation process based on the corrective SPH method is introduced for interpreting the stress and velocity tensors in the boundary particles (Figure 3.6). First, the boundary particles are created in a similar fashion with the virtual particle approach, which features the same mass, density and volume of each particle. When interpolating the stress in the boundary particles, the following formulation is applied in its general form:

$$\sigma_{\mathrm{boundary}}^{\alpha\beta} = \frac{\sum_{j=1}^{N} \frac{m_j}{\rho_j} \sigma_{\mathrm{real}}^{\alpha\beta} W_{ij}}{\sum_{j=1}^{N} \frac{m_j}{\rho_j} W_{ij}} \tag{3.29}$$

where $\sigma_{\mathrm{boundary}}^{\alpha\beta}$ and $\sigma_{\mathrm{real}}^{\alpha\beta}$ are the stress in both boundary and domain particles The velocity tensor can be interpolated in a similar fashion as in Eq (2.29) by replacing the stress tensor with velocity tensor. However, the direction that is perpendicular to the boundary line should be assigned the velocity in an opposite direction compared to the real particle for preventing penetration issue. For the direction that is parallel to the boundary line, the velocity tensor in boundary particles can be either in the same or opposite direction with the real particles to replicate either free-slipe or nonslip condition respectively.

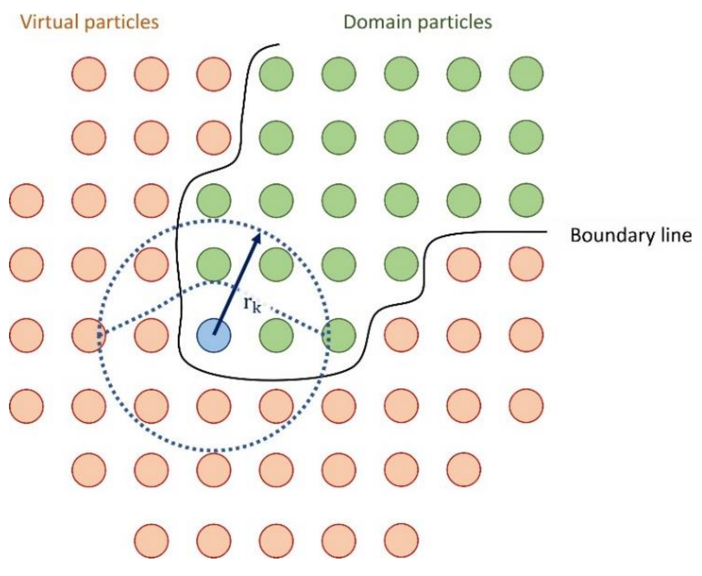

Figure 3.6 Illustration of the interpolation particle method.

3.4 The time integration scheme

The time integration in SPH is the key to correctly enforcing the basic consistency condition in the SPH constitutive models as well as updating of other field variables including velocity and density. There are mainly three types of time integration categories namely the fully explicit, semi-implicit and fully implicit. The advantages of using fully explicit schemes include their relatively simple algorithm, the relatively low computational cost etc. However, the accuracy of the explicit schemes is bounded by a timestep threshold which should not be exceeded. On the other hand, the fully-implicit integration schemes are able to achieve the consistency condition in a near-perfect manner with a predefined error allowance. A larger timestep increment can be applied for this type of integrations compared to explicit ones, which facilitates their computational efficiency even though explicit schemes still feature a lower computational cost. In between the explicit and implicit schemes is the semi-implicit algorithm also known as the predictor-corrector scheme. This approach is analogous to the fully-implicit scheme when predicting the elastic stress increment, however, using a different approach to correct the stress back to the yield surface. In this section, we introduce two widely applied explicit schemes namely the leap-frog and higher-order Runge-Kutta.

3.4.1 The leap-frog integration scheme

The leap-frog integration scheme (LF) is able to maintain a stable computational domain with second-order accuracy while occupying a relatively small computer memory (Bui et al., 2008a). In order to perform the integration, the following steps are taken. First, before the integration, the time rate of stress, velocity and density are calculated based on the SPH approximated governing equations. Second, at the first integration step, the stress, velocity and density are advanced to a half time step position, while the displacement of particles is advanced to a full time step position based on the velocity tensor at the half time step; third, at the beginning of the next integration step, the stress, velocity and density are further advanced to a full time step position in order to perform the calculation of the time rate of all field variables Then, the stress, velocity and density are advanced from the previous half time step position to the next half time step position based on their rate obtained at the full time step. This process can be mathematically described as:

$$\rho_{n+\frac{1}{2}} = \rho_{n-\frac{1}{2}} + \Delta t(\dot{\rho})_n \tag{3.30}$$

$$\mathbf{v}_{n+\frac{1}{2}} = \mathbf{v}_{n-\frac{1}{2}} + \Delta t(\dot{\mathbf{v}})_n \tag{3.31}$$

$$\boldsymbol{\sigma}_{n+\frac{1}{2}} = \boldsymbol{\sigma}_{n-\frac{1}{2}} + \Delta t(\dot{\boldsymbol{\sigma}})_n \tag{3.32}$$

$$\mathbf{r}_{n+1} = \mathbf{r}_n + \Delta t\left(\mathbf{v}_{n+\frac{1}{2}}\right) \tag{3.33}$$

where n represents the nth time step and Δt is the time increment for each integration step. The above process is illustrated in Figure 3.7 to facilitate the explanation.

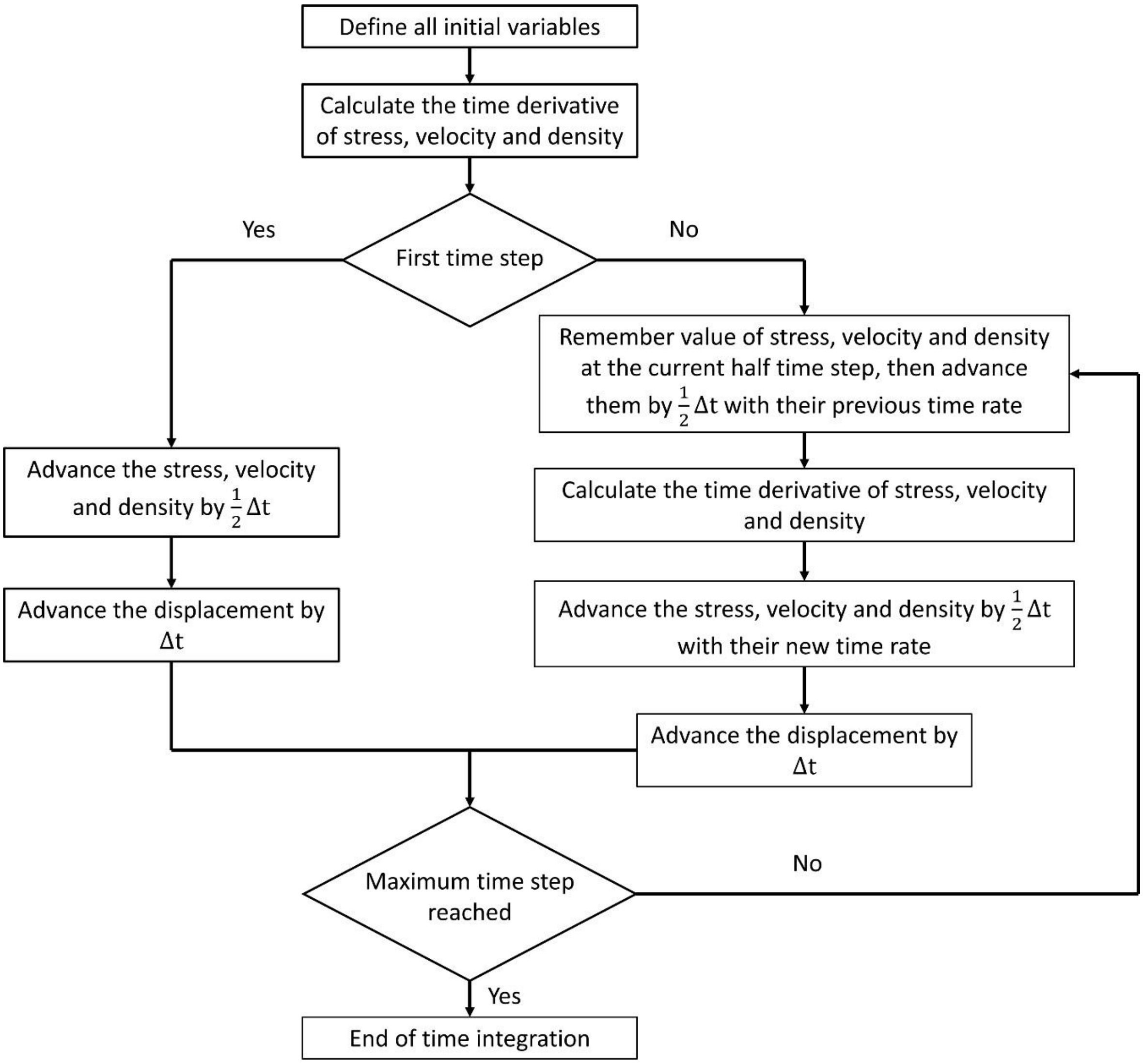

Figure 3.7: Illustration of the leap-frog integration scheme.

In order to maintain a reasonable level of accuracy for the consistency condition, the stress state for each particle is checked during at both the full time step position and the end of each integration step. Any identified tensile cracking or inconsistency between stress state and the yield surface will be corrected accordingly, which will be elaborated in Chater 4. The stability of the computational domain is governed by the so-called Courant-Friedrichs-Levy condition (Bui et al., 2008a), which defines a maximum applicable Δt as follows:

$$\Delta t \leq C_{courant}\left(\frac{h}{c}\right) \tag{3.34}$$

where c is the sound speed of the modelling material, which is chosen here to yield a very small timestep compared to conventional SPH and maintain a minimum fluctuation in the computational domain. $C_{courant}$ is the Courant number which has a typical value of $0.1 \sim 0.2$ in this work.

3.4.2 The higher-order Runge-Kutta scheme

The Runge-Kutta method is an explicit-based integration that is able to achieve an accurate approximation of the Taylor series expansion by only resorting to the first-order derivatives of the field variables. Various terms can be introduced into the Runge-Kutta method to derive its higher-order versions which normally feature with higher accuracy. The general form of the Runge-Kutta scheme can be mathematically expressed as:

$$f_{n+1} = f_n + \phi(k_1, k_2 \dots k_i)\Delta t \tag{3.35}$$

where f represents field variables including stress, velocity, density etc. for integration. i is the order of the Runge-Kutta scheme, indicating how many k factors are involved in the calculation. ϕ is a gradient component for f which is obtained from the procedure described below. In this section, we will focus on the most widely applied fourth-order Runge-Kutta method, which can be mathematically expressed as:

$$f_{n+1} = f_n + \frac{1}{6}(k_1 + 2k_2 + 2k_3 + k_4)\Delta t \tag{3.36}$$

the four coefficients can be explicitly expressed as below:

$$k_1 = f'_n \tag{3.37}$$

$$k_2 = f'_{\left(n+\frac{1}{2}\Delta t, k_1\right)} \tag{3.38}$$

$$k_3 = f'_{\left(n+\frac{1}{2}\Delta t, k_2\right)} \tag{3.39}$$

$$k_4 = f'_{(n+\Delta t, k_3)} \tag{3.40}$$

in above, k_1 is the gradient of f at n step, $f'_{\left(n+\frac{1}{2}\Delta t, k_1\right)}$ is the gradient of f at $n+\frac{1}{2}$ step calculated based on k_1 gradient, $f'_{\left(n+\frac{1}{2}\Delta t, k_2\right)}$ is the gradient of f at $n+\frac{1}{2}$ step calculated based on k_2 gradient, $f'_{(n+\Delta t, k_3)}$ is the gradient of f at $n+1$ step calculated based on k_3 gradient. The whole process can be illustrated in Figure 3.8.

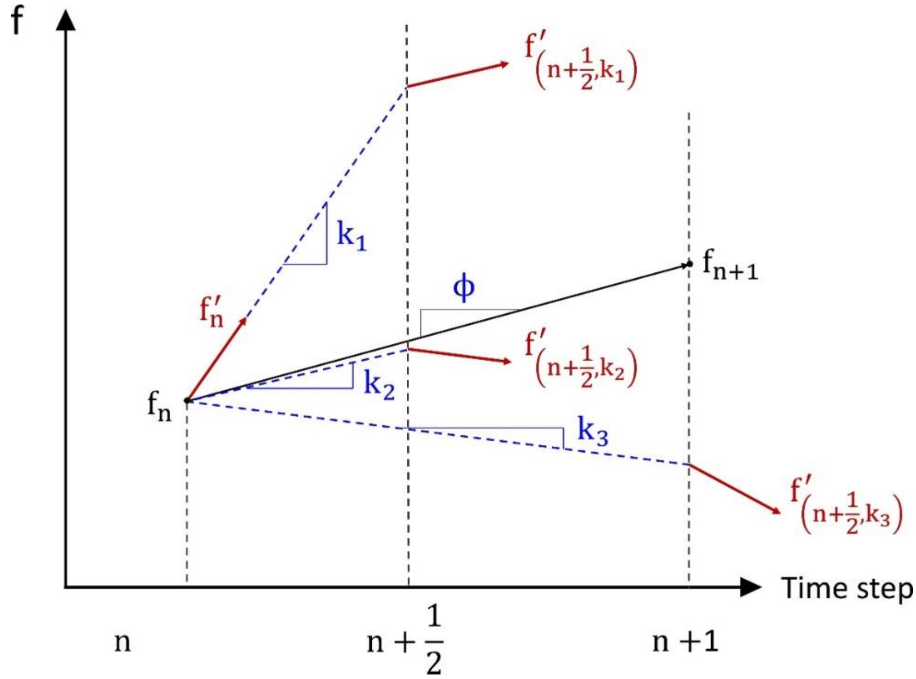

Figure 3.8: Illustration of the fourth-order Runge-Kutta integration scheme.

3.5 The constitutive models

The above formulations form the basis of the current SPH framework for solving geomechanical problems. However, in order to describe the kinematics of the field and complete the SPH conservation law of momentum for soil, the stress tensor in Eq (3.10) should be defined by a constitutive relationship that links the strain and stress tensors. A proper constitutive model for geomaterials would account for several key aspects including captures a resilient deformation when the stress states locate below the yield surface; describes a nonresilient deformation when the stress states coincide with the yield surface, which is mainly under a compressive stress state; captures the pressure-dependent phenomenon that is featured by most geomaterials. In this section, a generic framework for implementing constitutive models in SPH is presented for allowing the incorporation of various yield surfaces. Three models are introduced in detail, namely the rate-dependent elastic-viscoplastic model with evolving Von Mises yield surface (strain-softening); the pressure-dependent elastoplastic model with nonevolving Mohr-Coulomb yield surface (perfectly-plastic) and the pressure-dependent elastoplastic model with evolving Mohr-Coulomb yield surface (strain-softening). Benchmark tests are then conducted to validate these models in SPH environment. An element test and simple shear tests are applied respectively, with the numerical results compared to the analytical solutions.

3.5.1 A generic framework for SPH elastoplastic constitutive models

A generic relation between the stress and strain tensor in the SPH computational domain is described in this section, including the elastic and plastic parts. The elastic part is described with the general Hooke's law, while the plastic part is defined by the plastic potential and multiplier factors. In order to expand the above relation, the total strain tensor is first defined as a combination of elastic and plastic parts in their time rate form as:

$$\dot{\varepsilon}^{\alpha\beta} = \dot{\varepsilon}_e^{\alpha\beta} + \dot{\varepsilon}_p^{\alpha\beta} \tag{3.41}$$

where the subscripts e and p stand for elastic and plastic components, respectively. The elastic strain rate tensor can be described by generalised Hooke's law:

$$\dot{\varepsilon}_e^{\alpha\beta} = \frac{\dot{s}^{\alpha\beta}}{2G} + \frac{1}{9K}\dot{\sigma}^{\gamma\gamma}\delta^{\alpha\beta} \tag{3.42}$$

where $\delta^{\alpha\beta}$ is the Kronecker's delta. $\dot{s}^{\alpha\beta}$ is the deviatoric stress rate tensor, which forms the total stress with hydrostatic stress as follows:

$$\sigma^{\alpha\beta} = \sigma^{\gamma\gamma} + s^{\alpha\beta} \tag{3.43}$$

G and K are the material shear and bulk modulus which can be related to the material Young's modulus and Poisson's ratio as:

$$G = \frac{E}{2(1+\nu)} \qquad \text{and} \qquad K = \frac{E}{3(1-2\nu)} \tag{3.44}$$

The plastic strain rate tensor is calculated using the plastic flow rule:

$$\dot{\varepsilon}_p^{\alpha\beta} = \dot{\lambda}\frac{\partial g}{\partial \sigma^{\alpha\beta}} \tag{3.45}$$

where $\dot{\lambda}$ is the time rate of the plastic multiplier; g is the plastic potential function, which defines the direction of plastic strain increment on the yield surface.

By substituting Equation (3.42), (3.45) into Equation (3.41) and rearranging the obtained expression, the generalised stress-strain relationship for the elastoplastic material can be written as follows:

$$\dot{\sigma}^{\alpha\beta} = 2G\dot{e}^{\alpha\beta} + K\dot{\varepsilon}^{\gamma\gamma}\delta^{\alpha\beta} - \dot{\lambda}\left[\left(K - \frac{2G}{3}\right)\frac{\partial g}{\partial \sigma^{mn}}\delta^{mn}\delta^{\alpha\beta} + 2G\frac{\partial g}{\partial \sigma^{\alpha\beta}}\right] \tag{3.46}$$

where $\dot{e}^{\alpha\beta} = \dot{\varepsilon}^{\alpha\beta} - \frac{1}{3}\dot{\varepsilon}^{\gamma\gamma}\delta^{\alpha\beta}$ is the deviatoric strain rate tensor; K is the elastic bulk modulus; m and n are free indexes, which are independent from α and β.

Next, the general formula of the plastic multiplier for the elastic-perfectly plastic model can be derived from the consistency condition, which requires:

$$df = \frac{\partial f}{\partial \sigma^{\alpha\beta}}d\sigma^{\alpha\beta} = 0 \tag{3.47}$$

By substituting Equation (3.46) into Equation (3.47), the general form of the time rate of the plastic multiplier for an elastic-perfectly plastic material can be written as:

$$\dot{\lambda} = \frac{2G\dot{\varepsilon}^{\alpha\beta}\frac{\partial f}{\partial \sigma^{\alpha\beta}} + \left(K - \frac{2G}{3}\right)\dot{\varepsilon}^{\gamma\gamma}\frac{\partial f}{\partial \sigma^{\alpha\beta}}\delta^{\alpha\beta}}{2G\frac{\partial f}{\partial \sigma^{mn}}\frac{\partial g}{\partial \sigma^{mn}} + \left(K - \frac{2G}{3}\right)\frac{\partial f}{\partial \sigma^{mn}}\delta^{mn}\frac{\partial g}{\partial \sigma^{mn}}\delta^{mn}} \tag{3.48}$$

In the presence of evolving yield surface (strain or work dependent), the consistency condition is modified by considering the derivatives of the strain or work components, which will be elaborated in the following section.

3.5.2 The rate-dependent elastic-viscoplastic model

In this section, the generic constitutive formulations described above are closed by considering a Perzyna type viscoplastic consistency condition (Perzyna, 1966). The Perzyna type viscoplastic model is featured with a simple definition of the plastic multiplier, which does not resort to the consistency condition. Apart from this, an evolving Von Mises yield surface featuring softening mechanism is applied in Equation (3.48), with shrinkage of the column-shaped plastic yield surface with the accumulated plastic strain. To expand this model, the plastic multiplier, instead of using Eq (3.47), can be explicitly defined as:

$$\dot{\lambda} = \frac{\langle \Phi(f) \rangle}{\eta} \tag{3.49}$$

where $\dot{\lambda}$ is the rate of the plastic multiplier, η is the viscosity parameter, and Φ is the overstress function that depends on the rate-dependent yield surface f. The McCauley bracket $\langle \cdot \rangle$ is defined as follows:

$$\langle \Phi(f) \rangle = \begin{cases} \Phi(f) & \text{if } \Phi(f) \geq 0 \\ 0 & \text{if } \Phi(f) < 0 \end{cases} \tag{3.50}$$

The overstress function $\Phi(f)$ has the following form:

$$\Phi(f) = \left(\frac{f}{\sigma_o}\right)^N \tag{3.51}$$

with $N \geq 1$ and σ_o being the initial yield stress on the Von Mises surface. The overstress function should satisfy the following conditions (Simo, 1989):

$$\begin{cases} \Phi(f) \text{ is continuous in } [0, \infty) \\ \Phi(f) \text{ is convex in } [0, \infty) \\ \Phi(0) = 0 \end{cases} \tag{3.52}$$

In this work, the Von Mises yield condition, which is applicable to purely cohesive materials (Sukumaran, et al. 1999), was chosen. The yield function takes the following form:

$$f = \sqrt{J_2} - \left(\frac{\sigma_0}{\sqrt{3}} + H\varepsilon_{vp}\right) \tag{3.53}$$

where H is the hardening or softening modulus; ε_{vp} is the total viscoplastic strain; J_2 is the second deviatoric stress invariant; and σ_0 is the initial yield stress. The plastic potential function in Eq (3.46) is chosen to be identical to f here for maintaining an associated flow rule.

<u>Element test validation</u>

A 2D compression test under plane strain conditions is conducted. The geometry and boundary conditions of the testing model are shown in Figure 3.9a. Horizontally free-slip boundary conditions are imposed on the top and bottom boundaries; a vertically free-slip boundary condition is assumed on the left-side boundary and a group of constant downward loading rates has been assigned to the top boundary of the specimen. These boundary conditions are expected to produce a homogenous deformation field in the sample and therefore a simple analytical solution can be derived. In the SPH simulations, the vertical stress and strain are measured from the top boundary and this stress-strain relationship is compared with the analytical solution. The material properties used in the simulations are listed in Figure 3.9b. The comparison between analytical solutions and SPH simulations for different loading rates is shown in Figure 3.10. It demonstrates very good agreement for a variety of loading rates. From the loading path, it is clear that the material tends to gain strength as a higher loading rate is applied. Despite the application of softening mechanism, the loading path has not shown the entering of the softening stage in the sample with a relatively small strain achieved. As the loading rates reduces, the loading path demonstrates a converging trend predicting closer yield strength and stress path for different loading rates. The results demonstrate a stable and accurate prediction of the sample behaviour using SPH method with the incorporated Perzyna type elastic-viscoplastic model.

(a)

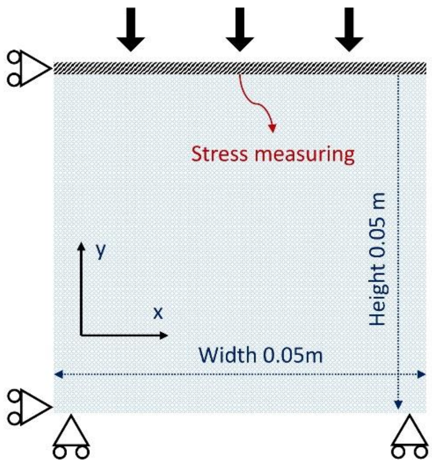

(b)

Idealised plane strain compression test	
Young`s modulus	$E = 80\ MPa$
Poisson`s ratio	$\nu = 0.2$
Initial yield stress	$\sigma^y = 400\ kPa$
Softening parameters	$H = -400\ kPa$
Viscosity parameter	$\eta = 0.05$ s

Figure 3.9: (a) numerical setup for the element test; (b) the parameters applied for the SPH simulation of the element test.

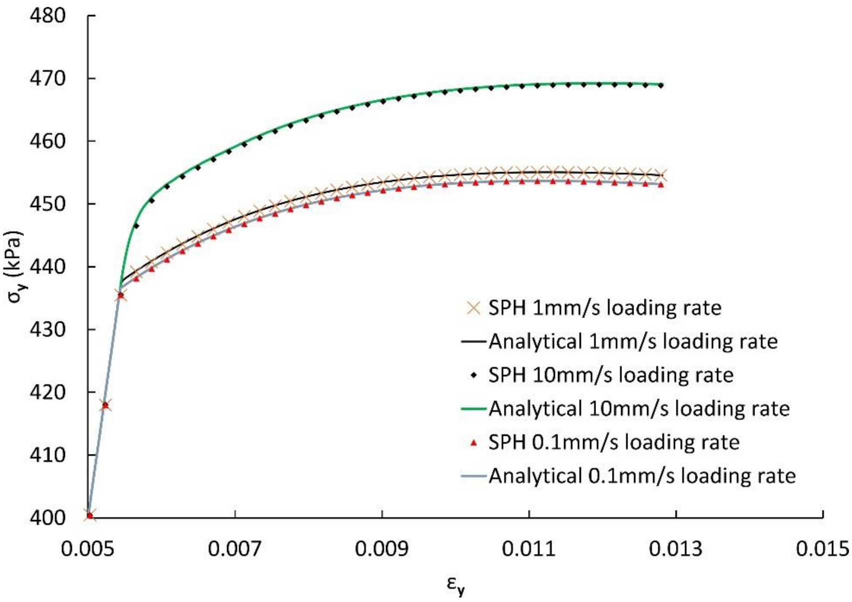

Figure 3.10: The comparison between the SPH obtained stress-strain relationships and the analytical solution for a variety of loading rates.

3.5.3 The pressure-dependent elastoplastic model with nonevolving Mohr-Coulomb yield surface

The Mohr-Coulomb elastoplastic model is widely used in practice owing to its simplicity in specifying the soil constitutive parameters (Abbo & Sloan, 1995; Borja et al., 2003; Ti et al., 2009). In particular, this model requires five basic soil parameters including elastic modulus, Poisson's ratio, friction angle, dilation angle and cohesion, which can be obtained from basic soil experiments such as triaxial or direct shear tests, thus making this model more appealing in practical applications. In this section, a robust framework to implement the Mohr-Coulomb constitutive model in SPH is elaborated, with details of the algorithm on solving the corner singularity issue. Apart from this, the tension crack treatment and stress scaling process are also introduced to avoid any inconsistency between the stress state and the yield surface that could potentially cause numerical errors with the explicit integration scheme applied in this work (collectively termed as stress return algorithm). First, to close Eq (3.46) and (3.48), The Mohr-Coulomb yield surface and its plastic potential function can be expressed in the pressure-dependent form as follows, respectively:

$$f = \sin\phi\, I_1 + \frac{1}{2}\left[3(1-\sin\phi)\sin\theta + \sqrt{3}(3+\sin\phi)\cos\theta\right]\sqrt{J_2} - 3c\cos\phi = 0 \tag{3.54}$$

$$g = \sin\psi \, I_1 + \frac{1}{2}\left[3(1-\sin\psi)\sin\theta + \sqrt{3}(3+\sin\psi)\cos\theta\right]\sqrt{J_2} - 3c\cos\psi \tag{3.55}$$

where ϕ and ψ are the soil internal friction and dilatant angles, respectively; $I_1 = \sigma^{\alpha\beta}\delta^{\alpha\beta}$, $J_2 = \frac{1}{2}s^{\alpha\beta}s^{\beta\alpha}$ and $J_3 = \frac{1}{3}s^{\alpha\beta}s^{\beta m}s^{m\alpha}$ are the first principal, second and third deviatoric stress invariants, respectively; c is soil cohesion; and θ is the Lode angle defined as:

$$\theta = \frac{1}{3}\cos^{-1}\left(1.5\sqrt{3}\frac{J_3}{J_2^{1.5}}\right) \tag{3.56}$$

By substituting (3.54) and (3.55) into (3.48), the general form of the plastic multiplier reads:

$$\dot{\lambda} = \frac{1}{H}\left[3K\frac{\partial f}{\partial I_1}\dot{\varepsilon}^{\gamma\gamma} + 2G\left(\frac{\partial f}{\partial J_2}s^{\alpha\beta} + \frac{\partial f}{\partial J_3}t^{\alpha\beta}\right)\dot{\varepsilon}^{\alpha\beta}\right] \tag{3.57}$$

where H and $t^{\alpha\beta}$ are defined as follows:

$$\begin{aligned} H = 9K\frac{\partial f}{\partial I_1}\frac{\partial g}{\partial I_1} + 4GJ_2\frac{\partial f}{\partial J_2}\frac{\partial g}{\partial J_2} + 6GJ_3\frac{\partial f}{\partial J_2}\frac{\partial g}{\partial J_3} + 6GJ_3\frac{\partial g}{\partial J_2}\frac{\partial f}{\partial J_3} \\ + 2G\left(s^{\alpha m}s^{m\beta}s^{\alpha n}s^{n\beta} - \frac{4}{3}{J_2}^2\right)\frac{\partial f}{\partial J_3}\frac{\partial g}{\partial J_3} \end{aligned} \tag{3.58}$$

$$t^{\alpha\beta} = \frac{\partial J_3}{\partial \sigma^{\alpha\beta}} = s^{\alpha m}s^{m\beta} - \frac{2}{3}J_2\delta^{\alpha\beta} \tag{3.59}$$

In the above equations, the differentiation of the yield function f against the stress invariants I_1, J_2 and J_3 are listed below:

$$\frac{\partial f}{\partial I_1} = \sin\phi \tag{3.60}$$

$$\begin{aligned} \frac{\partial f}{\partial J_2} = \frac{1}{4\sqrt{J_2}}\left[3(1-\sin\phi)\sin\theta + \sqrt{3}(3+\sin\phi)\cos\theta\right] \\ + \frac{3\sqrt{3}J_3}{8J_2^2\sin 3\theta}\left[3(1-\sin\phi)\cos\theta - \sqrt{3}(3+\sin\phi)\sin\theta\right] \end{aligned} \tag{3.61}$$

$$\frac{\partial f}{\partial J_3} = -\frac{\sqrt{3}}{4J_2\sin 3\theta}\left[3(1-\sin\phi)\cos\theta - \sqrt{3}(3+\sin\phi)\sin\theta\right] \tag{3.62}$$

The differentiation of the plastic potential function g with respect to the stress invariants are similarly defined by replacing the friction angle ϕ with the dilation angle ψ in Equations (3.60), (3.61) and (3.62). Furthermore, to maintain the objectivity of the constitutive model under large deformation, the Jaumann stress rate tensor is adopted. The final stress strain relation for Mohr-Coulomb elastic-perfectly plastic constitutive model can be now expressed as:

$$\dot{\sigma}^{\alpha\beta} = \sigma^{\alpha\gamma}\dot{\omega}^{\beta\gamma} + \sigma^{\gamma\beta}\dot{\omega}^{\alpha\gamma} + 2G\dot{e}^{\alpha\beta} + K\dot{\varepsilon}^{\gamma\gamma}\delta^{\alpha\beta} - \dot{\lambda}\left[3K\sin\phi\,\delta^{\alpha\beta} + 2G\left(\frac{\partial g}{\partial J_2}s^{\alpha\beta} + \frac{\partial g}{\partial J_3}t^{\alpha\beta}\right)\right] \tag{3.63}$$

where $\dot{\varepsilon}^{\alpha\beta}$ and $\dot{\omega}^{\alpha\beta}$ are the strain and spin rate tensors, which can be related to the gradient of the velocity as follows:

$$\dot{\varepsilon}^{\alpha\beta} = \frac{1}{2}\left(\frac{\partial v^{\alpha}}{\partial r^{\beta}} + \frac{\partial v^{\beta}}{\partial r^{\alpha}}\right) \tag{3.64}$$

$$\dot{\omega}^{\alpha\beta} = \frac{1}{2}\left(\frac{\partial v^{\alpha}}{\partial r^{\beta}} - \frac{\partial v^{\beta}}{\partial r^{\alpha}}\right) \tag{3.65}$$

It is noted that the above application of the Jaumann rate could lead to non-physical oscillations in some applications. However, in the current work, since the entire SPH governing equations are solved in an updated Lagrangian frame with a very small time step, the issues associated with the Jaumman rate can be significantly reduced (if not noticeable). This has been proven in simulations of granular flow with good stability (Bui et al. 2008a; Nguyen et al. 2017). Nevertheless, we acknowledge some existing state-of-art stress rates, such as Green-Naghdi (Badel et al. 2008), Truesdell (Sultanov & Davydov, 2014), Oldroyd (Bruhns et al. 2005) and logarithmic (Xiao et al. 2006), can be also adopted to maintain objective stress rates.

Singularity treatment and stress return algorithms

Figure 3.11 shows the Mohr-Coulomb yield surface in the π-plane and a treatment algorithm for its corner singularity problem. It can be seen from this figure that the yield and plastic potential functions are non-differentiable on the vertices ($\theta = 0^{o}$ or 60^{o}), which corresponds to the stress state lying either on the tensile or compressive meridian of the Mohr-Coulomb potential surface. Many numerical algorithms have been proposed and demonstrated to be effective for treating this singularity problem. Examples of these algorithms are the smoothing of Mohr-Coulomb yield surface corners (Chen & Mizuno, 1990), linearisation of the yield surface (Larsson & Runesson, 1996), hyperbolic approximation of the sharp corners (Abbo & Sloan, 1995), C1 and C2 continuous treatment of the model (Abbo et al. 2011). In this work, the approach proposed by Chen and Mizuno (1990) is adapted for implementing the Mohr-Coulomb model in SPH. This approached is featured with a relatively straightforward implementation procedure without compromising accuracy as Mohr-Coulomb and Drucker-Prager surfaces coincide where the surface gradient is discontinuous. The basic idea of this approach is to use the Drucker-Prager yield and potential functions to replace the Mohr-Coulomb ones when the stress state coincides with the tensile or compressive meridian of the Mohr-Coulomb model (Figure 3.11b).

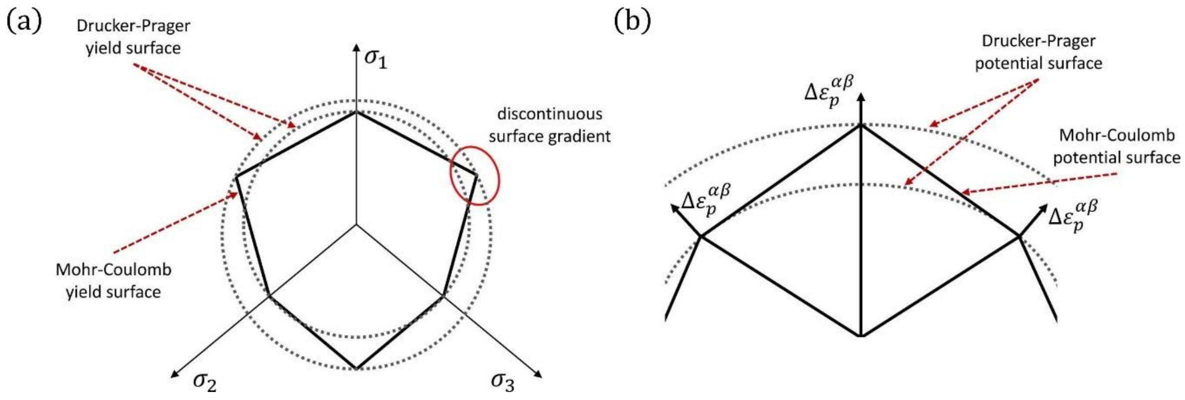

Figure 3.11: Illustration of the singularity problem in the Mohr-Coulomb model: (a) Mohr-Coulomb and Drucker Prager yield surfaces in π-plane; (b) Treatment for the singularity problem in the Mohr-Coulomb model.

To facilitate the implementation, the Mohr-Coulomb yield and plastic potential functions can be rewritten in the following forms:

$$f = \alpha_\phi I_1 + \sqrt{J_2} - k_\phi \tag{3.66}$$

$$g = \alpha_\psi I_1 + \sqrt{J_2} - k_\psi \tag{3.67}$$

where α_ϕ and k_ϕ are calculated by fitting Equations (3.66) and (3.67) to Equations (3.54) and (3.55), which leads to the following expression of α_ϕ and k_ϕ:

$$\alpha_\phi = \frac{2\sin\phi}{3(1-\sin\phi)\sin\theta + \sqrt{3}(3+\sin\phi)\cos\theta} \tag{3.68}$$

$$k_\phi = \frac{6c\cos\phi}{3(1-\sin\phi)\sin\theta + \sqrt{3}(3+\sin\phi)\cos\theta} \tag{3.69}$$

The coefficients α_ψ and k_ψ in Equation (3.67) are defined in a similar manner by replacing the friction angle ϕ with the dilation angle ψ in Equations (3.68) and (3.69).

By applying the above definitions, the stress-strain relationship and plastic multiplier for corner singularity treatment of the Mohr-Coulomb constitutive model can be calculated as follows:

$$\dot{\sigma}^{\alpha\beta} = \sigma^{\alpha\gamma}\dot{\omega}^{\beta\gamma} + \sigma^{\gamma\beta}\dot{\omega}^{\alpha\gamma} + 2G\dot{e}^{\alpha\beta} + K\dot{\varepsilon}^{\gamma\gamma}\delta^{\alpha\beta} - \dot{\lambda}\left[3K\alpha_\psi\delta^{\alpha\beta} + \left(G/\sqrt{J_2}\right)s^{\alpha\beta}\right] \tag{3.70}$$

$$\dot{\lambda} = \frac{3\alpha_\phi K\dot{\varepsilon}^{\gamma\gamma} + \left(G/\sqrt{J_2}\right)s^{\alpha\beta}\dot{\varepsilon}^{\alpha\beta}}{9\alpha_\phi K\alpha_\psi + G} \tag{3.71}$$

The condition for using the above stress-strain relation depends on the value of the Lode angle. In the principal stress space of the Mohr-Coulomb yield surface, the Lode angle falls within the range $0 \leq \theta \leq \pi/3$. Accordingly, if the Lode angle is equal to either the higher or lower bound of this range, the corresponding stress tensor is located on either the tensile or compressive meridian, meaning that the singularity problem occurs. This condition is expressed by the following equation:

$$\left|\frac{3\sqrt{3}}{2}\frac{J_3}{J_2^{3/2}}\right| < 1 \tag{3.72}$$

Apart from the corner singularity, another issue in the numerical implementation of the Mohr-Coulomb model is related to the tension crack problem. It manifests itself as the stress state in the soil falling beyond the apex of the yield surface on $\left(-I_1, \sqrt{J_2}\right)$ plane, which is defined by the following condition:

$$-\alpha_\phi I_1 + k_\phi < 0 \tag{3.73}$$

When the above condition is met, the normal stresses can be adjusted to shift the hydrostatic pressure back to the apex of the yield surface in order to correct the tension crack issue:

$$\tilde{\sigma}^{\alpha\beta} = \sigma^{\alpha\beta} - \frac{1}{3}\left(I_1 - \frac{k_\phi}{\alpha_\phi}\right)\delta^{\alpha\beta} \tag{3.74}$$

where $\sigma^{\alpha\beta}$ and $\tilde{\sigma}^{\alpha\beta}$ are the stress tensors before and after the correction, respectively.

In addition, due to the accumulation of computational errors during the simulation, the stress state of the model could be lying above the yield surface. This problem can be determined by the following condition:

$$-\alpha_\phi I_1 + k_\phi < \sqrt{J_2} \tag{3.75}$$

Equation (3.75) violates the basic assumption in the plasticity theory, which requires the stress state to remain on the yield surface during plastic deformation. Thus, whenever Equation (3.75) is satisfied, the stress state is scaled back to the yield surface using the following equations:

$$\tilde{\sigma}^{\alpha\beta} = r s^{\alpha\beta} + \frac{1}{3} I_1 \delta^{\alpha\beta} \tag{3.76}$$

$$r = \frac{-\alpha_\phi I_1 + k_\phi}{\sqrt{J_2}} \tag{3.77}$$

where r is a scaling factor. This procedure guarantees that the stress state during numerical integration is always on the Mohr-Coulomb yield surface.

simple shear test validation

In order to validate the proposed numerical framework, an SPH simulation of a simple shear test using Mohr-Coulomb elastoplastic constitutive model is conducted in this section, and its results are compared with theoretical solutions under plane strain condition (Gotoh, 1986). The geometry and boundary conditions of a square-shaped soil specimen of 0.3m length are shown in Figure 3.12. An initial particle distance of 0.01m is used, resulting in 900 particles for the specimen. Two areas are distinguished within the specimen: a centrally located area of 100mm length where SPH particles move freely and a boundary area enclosing the central area where a constant velocity field is predefined and maintained during the simulation following Equation

(3.78). The application of a predefined constant velocity field to the boundary area (Nonoyama, 2014) maintains the pure shear condition and is suitable for testing constitutive models in SPH:

$$v_{xi} = 0.01y_i \tag{3.78}$$

where i indicates any particle within the boundary area. Three values of confining stress of 50 kPa, 75 kPa and 100 kPa are tested to analyse the sample behaviour with its pressure-dependent yield surface. The soil properties are Young's modulus $E = 20$ MPa, Poisson's ratio $\nu = 0.3$, internal friction angle $\phi = 30^\circ$, dilation angle $\psi = 0^\circ$, cohesion $c = 10$ kPa and density $\rho = 2100\,\mathrm{kg/m^3}$.

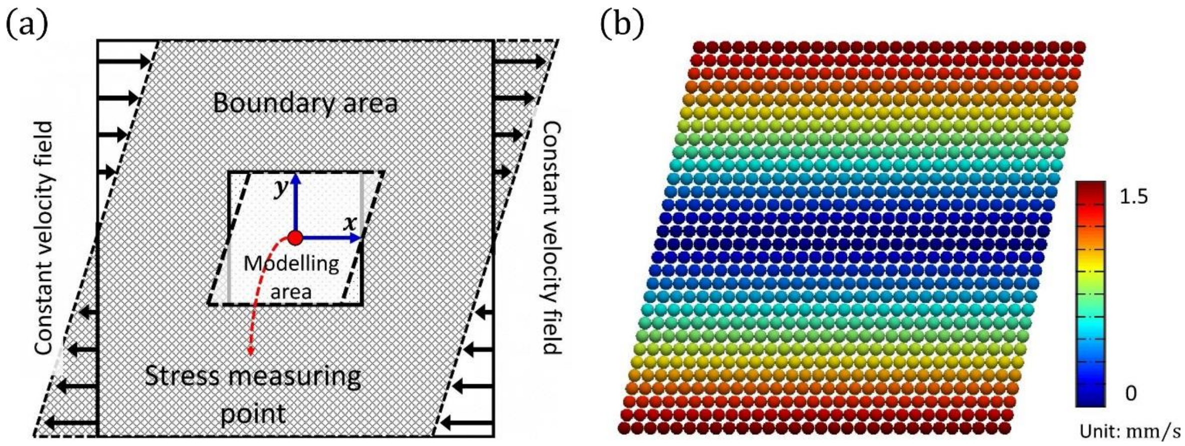

Figure 3.12: Simple shear test for Mohr-Coulomb model benchmark simulation: (a) simulation setup and (b) the contour plot of velocity.

The stress path and shear stress-strain relationships are obtained at the the centre (Figure 3.12a) and plotted in Figure 3.13 and 3.14, while the magnitude of the velocity profile in SPH simulations is shown in Figure 3.12b. In Figure 3.13 the stress states deviate from their initial hydrostatic confined states (150 kPa, 225 kPa and 300 kPa) as the shear starts. The stress path is vertical, indicating that the confining stress is correctly maintained during the shear test, and the stress state remains on the yield surface, as a verification of the consistency condition being respected during loading. For shear stress-strain relations (Figure 3.14), the numerical results agree well with theoretical calculations, showing pressure-dependent solutions. The above results demonstrate a stable and accurate performance of the Mohr-Coulomb model incorporated in SPH and its effective treatment to corner singularity problem.

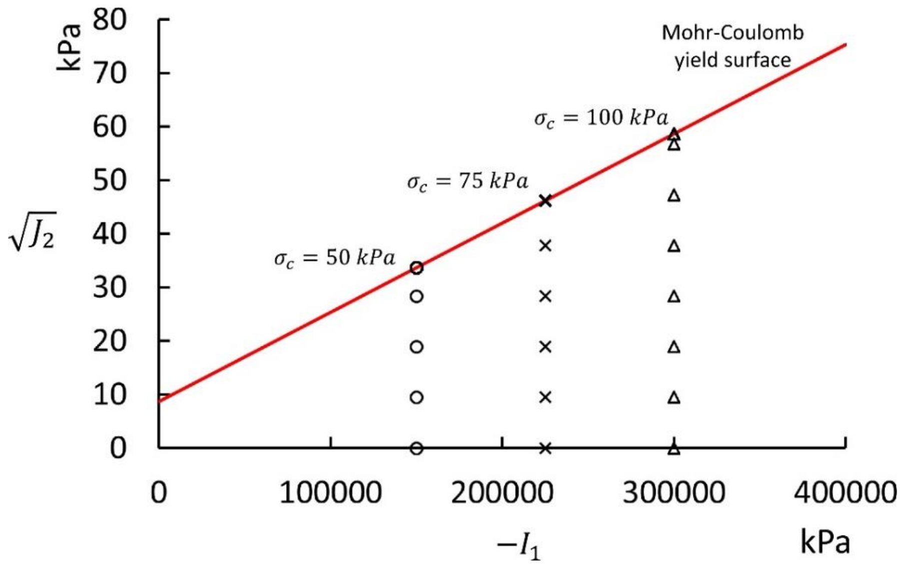

Figure 3.13: Loading path for varying confining stresses in the SPH simple shear test.

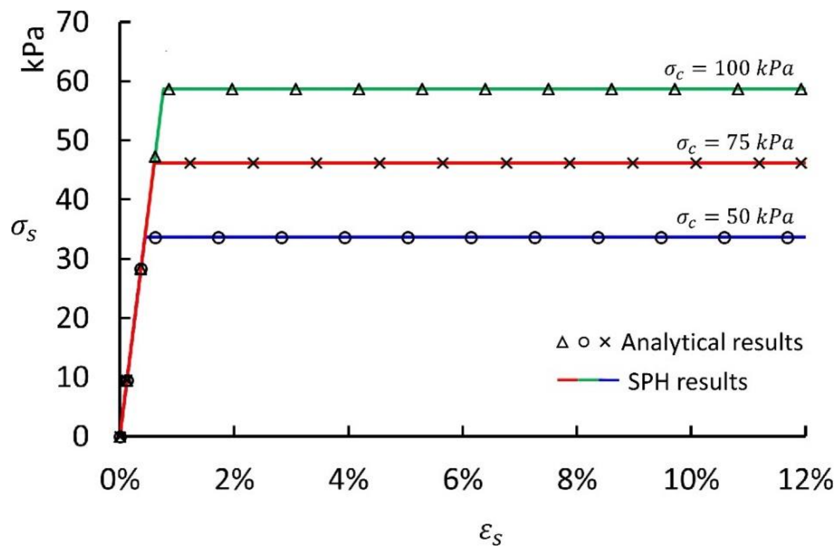

Figure 3.14: Shear stress-strain relationships for varying confining stresses in the SPH simple shear test.

3.5.4 The pressure-dependent elastoplastic model with evolving Mohr-Coulomb yield surface

In the previous section, a robust constitutive model featured with Mohr-Coulomb yield surface has been introduced to account for the inelastic geomechanical process demonstrating a perfectly plastic material response. However, it is common that the plastic behaviour in geomaterials is companied by the loss of material integrity and a softening process. Therefore it is necessary to implement a corresponding constitutive model capable of capturing this phenomenon. In this section, a Mohr-Coulomb yield surface that is evolving depending on the soil state parameters (e.g. internal friction angle and cohesion) during plastic deformations has been incorporated to the aforementioned constitutive framework in a rigorous manner. A typical soil behaviour that manifests both the undamaged and fully damaged states is reproduced with two sets of parameters consisting of the virgin and residual values of soil friction angle and cohesion. The evolution from the undamaged to damaged states is characterised by an exponential relationship between the state parameters and the accumulated equivalent plastic strain, which can be explicitly expressed as:

$$\phi = \phi_{res} + \left(\phi_{peak} - \phi_{res}\right)e^{-\eta\varepsilon_p^{eq}} \tag{3.79}$$

$$c = c_{res} + \left(c_{peak} - c_{res}\right)e^{-\eta\varepsilon_p^{eq}} \tag{3.80}$$

where the coefficient η controls the rate for the degradation of the material properties. The ε_p^{eq} is the equivalent plastic strain interpreted as the degree of plastic deformation of the numerical domain, which is explicitly defined as:

$$\varepsilon_p^{eq} = \sqrt{\frac{2}{3} e_p^{\alpha\beta} e_p^{\alpha\beta}} \tag{3.81}$$

where $e_p^{\alpha\beta}$ is the deviatoric plastic strain tensor defined as $e_p^{\alpha\beta} = \varepsilon_p^{\alpha\beta} - \varepsilon_p^{\alpha\beta}\delta^{\alpha\beta}/3$. By considering the definition of plastic strain in Eq (3.45) and the Mohr-Coulomb plastic potential function in Eq (3.55), the above expression of the equivalent plastic strain can be explicitly expressed as follows:

$$\dot{\varepsilon}_p^{eq} = \dot{\lambda}\sqrt{\frac{2}{3}\left(\frac{\partial g}{\partial \sigma^{\alpha\beta}}\frac{\partial g}{\partial \sigma^{\alpha\beta}} - \frac{1}{3}\frac{\partial g}{\partial \sigma^{mm}}\frac{\partial g}{\partial \sigma^{nn}}\right)} \tag{3.82}$$

In above, the derivative of the plasic potential function is consistent with the of derivative of the Mohr-Coulomb yield function as elaborated in the previous section. The time rate of plastic multiplier $\dot{\lambda}$ is derived by applying the consistency condition and considering the evolution of state parameters as follows:

$$df = \frac{\partial f}{\partial \sigma^{\alpha\beta}} d\sigma^{\alpha\beta} + \frac{\partial f}{\partial \varepsilon_p^{\alpha\beta}} d\varepsilon_p^{\alpha\beta} \tag{3.83}$$

in above, the differentiation of the yield surface f against the plastic strain corresponds to the differentiation of f against the state parameters namely the friction angle and cohesion, which can be expressed considering the chain rule as:

$$\frac{\partial \mathrm{f}}{\partial \varepsilon_{\mathrm{p}}^{\alpha\beta}} \mathrm{d}\varepsilon_{\mathrm{p}}^{\alpha\beta} = \frac{\partial \mathrm{f}}{\partial \phi} \frac{\partial \phi}{\partial \varepsilon_{\mathrm{p}}^{\mathrm{eq}}} \frac{\partial \varepsilon_{\mathrm{p}}^{\mathrm{eq}}}{\partial \varepsilon_{\mathrm{p}}^{\alpha\beta}} \mathrm{d}\varepsilon_{\mathrm{p}}^{\alpha\beta} + \frac{\partial \mathrm{f}}{\partial \mathrm{c}} \frac{\partial \mathrm{c}}{\partial \varepsilon_{\mathrm{p}}^{\mathrm{eq}}} \frac{\partial \varepsilon_{\mathrm{p}}^{\mathrm{eq}}}{\partial \varepsilon_{\mathrm{p}}^{\alpha\beta}} \mathrm{d}\varepsilon_{\mathrm{p}}^{\alpha\beta} \tag{3.84}$$

The differentiation of the Mohr-Coulomb yield surface against the state parameters can be written by considering Eq (3.54) as:

$$\frac{\partial \mathrm{f}}{\partial \phi} = \cos\phi\, \mathrm{I}_1 + \frac{1}{2}\left[-3\cos\phi\sin\theta + \sqrt{3}\cos\phi\cos\theta\right]\sqrt{\mathrm{J}_2} + 3\mathrm{c}\sin\phi \tag{3.85}$$

$$\frac{\partial \mathrm{f}}{\partial \mathrm{c}} = -3\cos\phi \tag{3.86}$$

The differentiation of the friction angle and cohesion against the equivalent plastic strain can be obtained by considering theire relationship in Eq (3.79) and (3.80), which is explicitly written as:

$$\frac{\partial \phi}{\partial \varepsilon_{\mathrm{p}}^{\mathrm{eq}}} = -\eta\left(\phi_{\mathrm{peak}} - \phi_{\mathrm{res}}\right)\mathrm{e}^{-\eta\varepsilon_{\mathrm{p}}^{\mathrm{eq}}} \tag{3.87}$$

$$\frac{\partial \mathrm{c}}{\partial \varepsilon_{\mathrm{p}}^{\mathrm{eq}}} = -\eta\left(\mathrm{c}_{\mathrm{peak}} - \mathrm{c}_{\mathrm{res}}\right)\mathrm{e}^{-\eta\varepsilon_{\mathrm{p}}^{\mathrm{eq}}} \tag{3.88}$$

Now by considering the consistency condition for a elastoplastic strain hardening/softening material in Eq (3.83), the generic form of the time rate of the plastic multiplier can be expressed as follows:

$$\dot{\lambda} = \frac{2\mathrm{G}\dot{\varepsilon}^{\alpha\beta}\frac{\partial \mathrm{f}}{\partial \sigma^{\alpha\beta}} + \left(\mathrm{K} - \frac{2}{3}\mathrm{G}\right)\dot{\varepsilon}^{\gamma\gamma}\frac{\partial \mathrm{f}}{\partial \sigma^{\alpha\beta}}\delta^{\alpha\beta}}{\left[\left(\mathrm{K} - \frac{2}{3}\mathrm{G}\right)\frac{\partial \mathrm{f}}{\partial \sigma^{\alpha\beta}}\frac{\partial \mathrm{g}}{\partial \sigma^{\mathrm{mn}}}\delta^{\alpha\beta}\delta^{\mathrm{mn}} + 2\mathrm{G}\frac{\partial \mathrm{f}}{\partial \sigma^{\alpha\beta}}\frac{\partial \mathrm{g}}{\partial \sigma^{\alpha\beta}}\right] - \frac{\partial \mathrm{f}}{\partial \phi}\frac{\partial \phi}{\partial \varepsilon_{\mathrm{p}}^{\mathrm{eq}}}\mathrm{val} - \frac{\partial \mathrm{f}}{\partial \mathrm{c}}\frac{\partial \mathrm{c}}{\partial \varepsilon_{\mathrm{p}}^{\mathrm{eq}}}\mathrm{val}} \tag{3.89}$$

where the coefficient val is straightforwardly derived from Eq (3.82) to (3.88) as:

$$\mathrm{val} = \sqrt{\frac{2}{3}\left(\frac{\partial \mathrm{g}}{\partial \sigma^{\alpha\beta}}\frac{\partial \mathrm{g}}{\partial \sigma^{\alpha\beta}} - \frac{1}{3}\frac{\partial \mathrm{g}}{\partial \sigma^{\mathrm{mm}}}\frac{\partial \mathrm{g}}{\partial \sigma^{\mathrm{nn}}}\right)} \tag{3.90}$$

the above formulations complete the framework of the elastoplastic constitutive model with a plastic strain dependent yield surface, where the generic form of the stress rate is still obtained by applying Eq (3.63).

The simple shear benchmark for Mohr-Coulomb strain-softening model

In order to validate the robustness of the proposed Mohr-Coulomb strain-softening model in SPH, a simple shear test under plane strain condition is carried out in this section. The setup is similar to that applied for the simple shear validation test of the Mohr-Coulomb perfectly plastic model described above. In the simulation, a square-shaped specimen is created with a $0.4\mathrm{m}$ edge length. Two areas are distinguished in the sample namely a boundary area and modelling area. The boundary area is assigned with a constant horizontal velocity field during the test, with its magnitude smoothly ranging from $0.002\,\mathrm{m/s}$ to $-0.002\,\mathrm{m/s}$. This creates a shearing stress condition in the specimen. The central modelling area is in a $0.1\mathrm{m}$ edge length, which is allowed to deform naturally with any applied boundary condition. The stress condition is then measured at the centre of the specimen and outputted to compare with the analytical solutions.

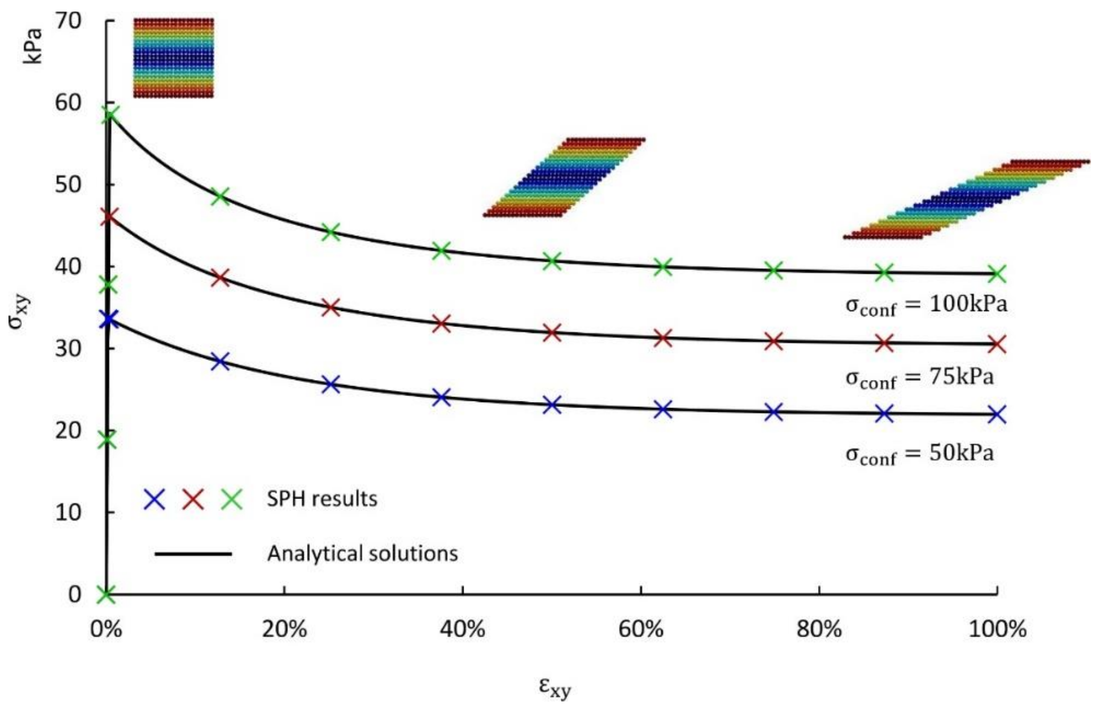

Figure 3.15: The shear stress-strain relationship obtained in the SPH simple test with elastoplastic strain-softening model and its comparison with the analytical solution.

The basic material properties applied are Young's modulus $\mathrm{E} = 20$ MPa, Poisson's ratio $\nu = 0.3$, friction angle $\phi = 30^{\circ}$, dilation angle: $\psi = 0^{\circ}$, cohesion $\mathrm{c} = 10$ kPa and soil density $\rho = 2100\,\mathrm{kg/m^3}$. Three groups of comparison tests are carried out with confining stress $\sigma_{\mathrm{conf}} = 50\mathrm{kPa}, 75\mathrm{kPa}$ and $100\mathrm{kPa}$ respectively, and the corresponding analytical solutions are calculated and compared with SPH results. The relation between the shear stress and strain are first illustrated in Figure 3.15.

It is clear from above that the material demonstrates a certain range of elastic response to the applied boundary condition and reaches their peak shear strength. Then a loss in the material strength is shown in the stress path in an exponential manner until reaching an ultimate strength state which features a perfectly plastic behaviour. The confining stress level shows its influence on the peak materials strength which is well captured by the pressure-dependent Mohr-Coulomb yield surface. The SPH predicted shear stress-strain path also demonstrates perfect agreement with the analytical solutions. In order to further examine the enforcement of the consistency condition, the entire loading path is plotted in Figure 3.16. Apart from this, the Mohr-Coulomb yield surfaces at both its peak and residual strength are also illustrated, which is then compared with the corresponding stress state obtained in the sample in Figure 3.17.

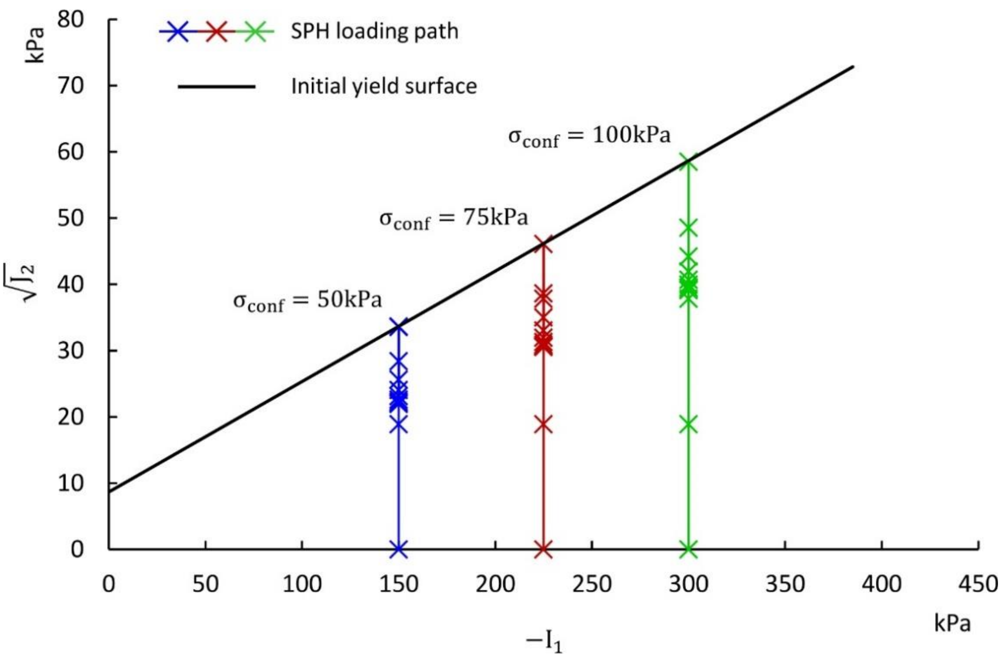

Figure 3.16: The loading path obtained in SPH simple shear test with elastoplastic strain-softening model.

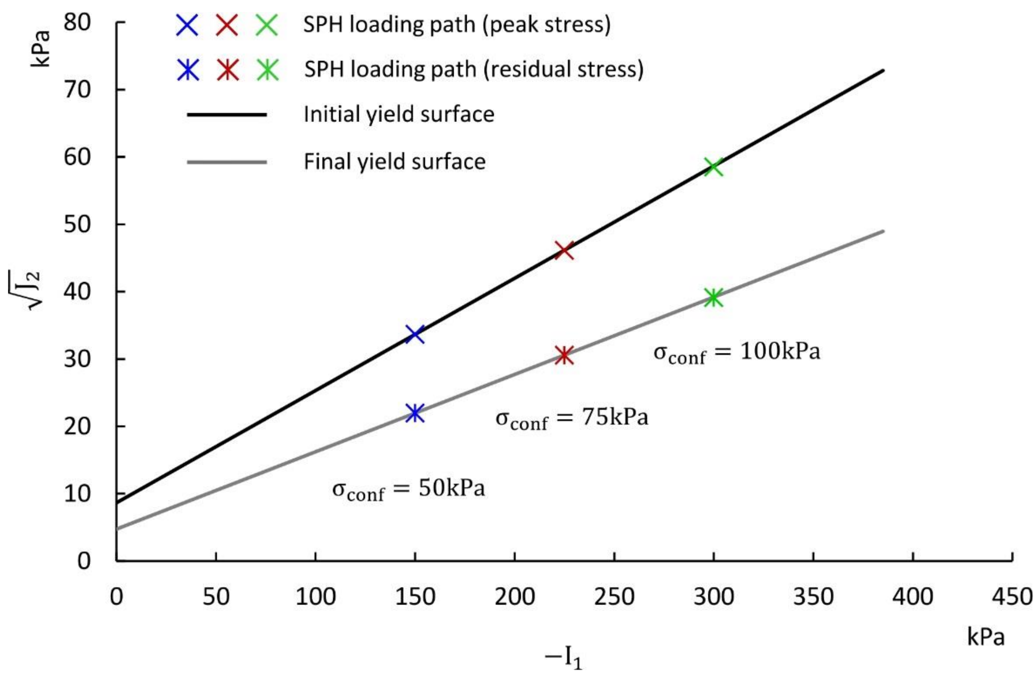

Figure 3.17: The comparison between peak and residual stress state and their corresponding Mohr-Coulomb yield surface.

In Figure 3.16, the stress states departure from their initial confining stage and following the deviatoric path heading to the yield surface. During this process, the confining stress is maintained exactly as its initial state. As the deviatoric stress in the sample hits the yield condition, it coincides and evolves with the yield surface. In Figure 3.16 the plotted yield surface corresponds to the one with virgin material strength (peak). In Figure 3.17, the Mohr-Coulomb yield surface is plotted both in its peak and residual strength states. The corresponding deviatoric stress is also illustrated, which shows exact agreement with the location of the yield surface. This indicates that the consistency condition has been enforced exactly as the theory defines. From the results demonstrated above, it is clear that the proposed SPH framework is able to well capture the material strain-softening behaviour featuring very large deformation, which proves its capability to be potentially applied to the geomechanics problems involving more complex boundary conditions. This will be demonstrated throughout the rest of the current work.

3.6 Conclusion

In this chapter, some fundamental knowledge of the smoothed particle hydrodynamics method applied for geomechanical problems in this research is presented. Specifically, the focus revolves the key concept and basic formulations of SPH. The SPH discretisation of the computational domain, the approximation of the momentum and mass conservation laws are summarised. The factors that would influence the stability and accuracy of the SPH domain including the kernel function, the correction of the kernel and its gradient are discussed briefly. Other aspects of the SPH method including the currently applied boundary conditions, the stabilisation techniques in SPH, the time integration schemes are also discussed. Furthermore, to correctly account for the plastic behaviours of the soil and complete the SPH discretisation of the motion governing equation, three constitutive models with various features are introduced in detail with their implementation algorithm in SPH. A group of benchmark tests are also illustrated to demonstrate the performance of the constitutive models in the proposed SPH numerical framework. The information presented in this chapter forms the fundamentals of the SPH method that has been applied for the current research work. Its applications and advancements regarding the boundary conditions, numerical stability and multiphase soil modelling will be explained in the following chapters.

Chapter 4

A generic approach to modelling flexible confined boundary conditions in SPH and its application

4.1 Introduction

In this chapter, a new approach to applying confining stress to flexible boundaries in the smoothed particle hydrodynamics method is developed to facilitate its applications in geomechanics. Unlike the conventional SPH methods that impose confining boundary conditions by creating extra boundary particles, the proposed approach makes use of kernel truncation properties of SPH approximations that occur naturally at free-surface boundaries. Therefore it does not require extra boundary particles and, as a consequence, can be utilised to apply confining stresses onto any boundary with arbitrary geometry without the need for tracking the curvature change during the computation. This enables more complicated problems that involve moving confining boundaries, such as confining triaxial tests, to be simulated in SPH without difficulties. To further enhance SPH applications in elastoplastic computations of geomaterials, a robust numerical procedure to implement Mohr-Coulomb plasticity model in SPH is presented for the first time to avoid difficulties associated with corner singularities in Mohr-Coulomb model. The proposed approach was first validated against 2D finite element (FE) solutions for confining biaxial compression tests to demonstrate its predictive capability at small deformation range when FE solutions are still valid. It is then further extended to 3D conditions and utilised to simulate triaxial compression experiments.

Simulation results predicted by SPH show good agreement with experiments, FE solutions and other numerical results available in the literature. This suggests that the proposed approach of imposing confining stress boundaries is promising and can handle complex problems that involve moving confining boundary conditions.

4.2 Background of the confined boundary condition in SPH

The confined boundary condition is commonly used in both experimental and numerical investigations of the mechanical behaviour of geomaterials, such as soils, rocks and concretes, to replicate the in-situ stress conditions these materials are subjected to in the field (Drescher et al. 1990; Tan, 2005). Two categories of mechanical boundary conditions, which are velocity/displacement and stress/force, are commonly enforced to a specimen. In the laboratory, velocity and stress can be applied to the specimen through moving pistons or pressurised cells controlled by a feedback system consisting of a series of sensors and gauges (Alshibli et al. 2003; Desrues & Viggiani, 2004). In contrast, in numerical modelling, the ways to enforce such mechanical boundaries vary among different methods. For instance, in the Finite Element Method (FEM), which has been regarded as the standard tool in continuum plasticity manifesting high stability and accuracy for applications involved small deformation, the boundary conditions can be directly applied to nodes on the surface meshes. In much well-developed commercial software such as ABAQUS, built in options allow these boundary conditions to be enforced in a straightforward manner. However, it is well established that the FEM may suffer from mesh pathologies such as mesh distortion and dependency, which hinders its applications to large deformation problems commonly encountered in engineering practice (Needleman, 1988; De Borst et al. 1993). Although enhancements such as adaptive remeshing (Zienkiewicz et al. 1995), updated mesh (Poodt et al. 2003), hybrid Euler-Lagrangian method (Haber, 1984) and smoothed FEM (SFEM) (Liu et al. 2007) have been proposed, mesh-based numerical methods are still vulnerable to very large or discontinuous deformation involved in post-failure. On the other hand, mesh-free continuum methods are considered alternatives to FEM, for instance, the material point method (MPM) (Sulsky & Schreyer, 2004) and Smoothed Particle Hydrodynamics (SPH) (Lucy, 1977; Gingold & Monaghan, 1977). In MPM, essential boundaries are enforced by replacing the interpolated velocities in the background mesh with predefined boundary values, while stress can be added to the surface of the computational domain in a similar way (Chen et al. 2002). However, boundaries of the MPM particle assembly have to be aligned with the background mesh in order for the boundary conditions to be implemented. This procedure can become complicated and result in significant inaccuracy with highly deformed boundaries or in three-dimensional space (Steffen et al. 2008). It is clear that the above issues with FEM and MPM are collectively related to mesh discretisation. Consequently, as a truly meshless method, SPH is a good alternative to MPM for modelling large deformation problems. SPH was originally proposed for astrophysical applications (Lucy, 1977; Gingold & Monaghan, 1977), it has been then advanced to numbers of applications in geomechanics such as large deformation and failure of geomaterials (Bui et al. 2007a; 2007b; 2008a; Peng et al. 2015; 2016; Zhao et al. 2017; Neto & Borja, 2018), slope failures and landslides (Pastor et al. 2009; Bui et al. 2011; 2013a), soil-structure interaction (Bui et al. 2008b; Bui et al. 2013b; Wang et al. 2014), coupled soil-water problems (Bui et al. 2007b; Zhang et al., 2016; Bui & Nguyen, 2017) and most recently the scale-dependent rock fracture (Wang et al. 2017; 2018). In SPH, velocity and displacement boundary conditions can be enforced through non-slip and free-slip solid boundary conditions by using ghost (Randles & Libersky, 1996) and virtual (Monaghan, 1994; Morris et al. 1997; Bui et al. 2008a) particles. On the other hand, the stress type boundary condition can be directly applied to SPH particles at the desired location where the confining stress is imposed. In such an approach, the applied stress should be converted to an equivalent acceleration, which can be subsequently added to the motion equation of each particle. The area over which the stress is applied and the corresponding particle masses are tracked in this approach. Furthermore, it requires the calculation of normal directions on boundary surfaces to apply the stresses correctly. Accordingly, a successful implementation of this approach requires: i) tracking of particles on the boundaries and ii) calculation of the normal vector and surface area to convert stresses to accelerations during the computation. However, these requirements would become extremely difficult to be satisfied when the computational domain undergoes large deformation and failure. This is because the highly curved boundary surfaces encountered in the large deformation of the numerical specimen could hinder the detection of the particles located on the surface boundaries, and thus the calculation of their normal vectors. In addition, an accurate enforcement of the stress on the computational domain is challenging due to the difficulties in determining and tracking the surface area and curvature of the boundaries during the simulation. Although methods utilising kernel gradient to derive the normal direction on SPH domain surface is proposed to simplify the above process (Monaghan et al. 2003; Pereira et al. 2017), there is still a need to accurately calculate surface area of boundary domain over which the confining stresses are applied and this still remains a challenging task for SPH when dealing with large deformation problems in solid mechanics.

To overcome the above issues, in this chapter a generic approach to applying confining stress to flexible boundaries is proposed for SPH. In contrast with previous approaches which are vulnerable to deformation of the confined boundaries, the current method automatically traces curvature change of the computational domain and enforces confining stress without being vulnerable to large deformation. In particular, the proposed method takes advantage of the kernel truncation near the boundaries of SPH domain. Such truncation in the kernel supporting domain would highlight the location of surface boundaries and allow accurate calculations of their normal directions as well as surface areas. As such, the proposed confining boundary condition outperforms the conventional methods in the following aspects: first, the boundaries of the computational domain are automatically located and their curvature change is accounted for without explicitly involving any searching process; second, the normal directions along the boundaries are automatically determined by the kernel truncation; and finally, the surface boundaries over which the confining stress is applied can be automatically determined during the computation. The above features can be automatically achieved through kernel approximation of the governing equation of the proposed method without explicitly calculate the area and normal on boundaries. These features enable the proposed method to perform effectively and accurately in enforcing confining pressures onto the computational domain. In addition, to further enhance the application of SPH to computational geomechanics, a modern elastoplastic model is required. For instance the modified Cam-Clay (Chen & Abousleiman, 2012), Val-Eekelen (Prunier et al. 2009), Matsuoka-Nakai (Fellin & Ostermann, 2013) and Lade-Duncan (Gao et al. 2010) models enable the solution of complicated boundary value problems. Other more advanced models that can handle both diffuse and localised failure at the constitutive level have also been explored in the SPH framework for modelling fracture (Wang et al, 2018), while further developments for applications in geomechanics are underway (Nguyen et al. 2016a; 2016b; Nguyen et al. 2017; Le et al. 2018). Despite this fact, the classical Mohr-Coulomb model is used here considering its simplicity in practical applications given the focus on theoretical work and corresponding algorithms for applying stress boundary conditions in SPH. For this, a robust numerical procedure to implement this model in SPH is presented for the first time to avoid difficulties associated with its well-known corner singularity. The Mohr-Coulomb based constitutive models have been long applied and widely recognised in geomechanics to describe soil behaviour (Labuz & Zang, 2012). Despite the popularity, this model possesses hexagon-shaped yield surface, which could lead to difficulties in modelling large deformation plasticity problems due to a discontinuous surface gradient. In this study, such instability is mitigated with a smooth approximation of the sharp corners using the Drucker-Prager yield surface, which features circular shape. The proposed approach is then validated against finite element solutions for biaxial and triaxial tests, GIMPM solutions by Kiriyama (2013) and triaxial compression experiment (Kiriyama, 2013).

The rest of this chapter is arranged as follows: The basic SPH concepts and governing equations are first presented. This is then followed by the general description of the numerical procedure to implement the Mohr-Coulomb elastic-perfectly plastic constitutive model in SPH. Next, the generic approach to applying confining boundary conditions in SPH is explained. Finally, the verification and application of the proposed framework are carried out to demonstrate the key features and potential of the proposed approach.

4.3 Boundary conditions in SPH to apply confining stress

Like any other numerical methods, the treatment of boundary conditions in SPH is required to facilitate its applications to a wide range of engineering problems. In particular, when an SPH particle is close to the boundary, its kernel function is truncated, resulting in inaccurate approximations of field variables. To resolve this problem, ghost and virtual boundary particles (Takeda et al. 1994), (Randles & Libersky, 1996), (Morris et al. 1997), (Bui et al. 2008a) have been introduced to replace solid boundaries. Specific conditions are then enforced through these particles to achieve desirable boundary conditions (e.g. non-slip, free-slip or axis-symmetric conditions). However, the above approaches are not directly applicable to moving or flexible boundaries subjected to confining stress and therefore specific treatments are required in such cases.

4.3.1 Conventional approach to apply confining stress in SPH

In engineering applications, confining stress is normally applied to open boundaries such as free-surfaces or confining membranes. To replicate this condition in SPH, the common procedure consists of three main steps (illustrated in Figure 4.1):

1. Identify particles on the open boundary where the confining stress is to be applied;
2. Calculate the normal vector for each particle on the open boundary;
3. Calculate the surface area at each particle over which the confining stress is applied;

The above procedure was, in fact, proposed by Monaghan (2003) in extending SPH to model the motion of a rigid solid boundary in water. It was then further developed by Kajtar and Monaghan (2010) to model swimming bodies. Recently, this approach has been applied to model confining stress in rectangular triaxial tests (Pereira et al. 2017).

To ensure the confining stress is correctly applied to the boundary, the above procedure has to be repeated at every integration step during the computation process, which is computationally expensive. Furthermore, when the computational domain undergoes large deformation, the normal direction and surface area cannot be accurately calculated, thus failing to maintain correct confining stress on the boundary and potentially leading to the termination of the computational procedure. As a consequence, basic soil experiments including biaxial and triaxial tests involving large deformation cannot always be modelled using this approach in SPH. Therefore, developing a new computational procedure is required to properly account for the confining stress in SPH modelling of soil plasticity problems.

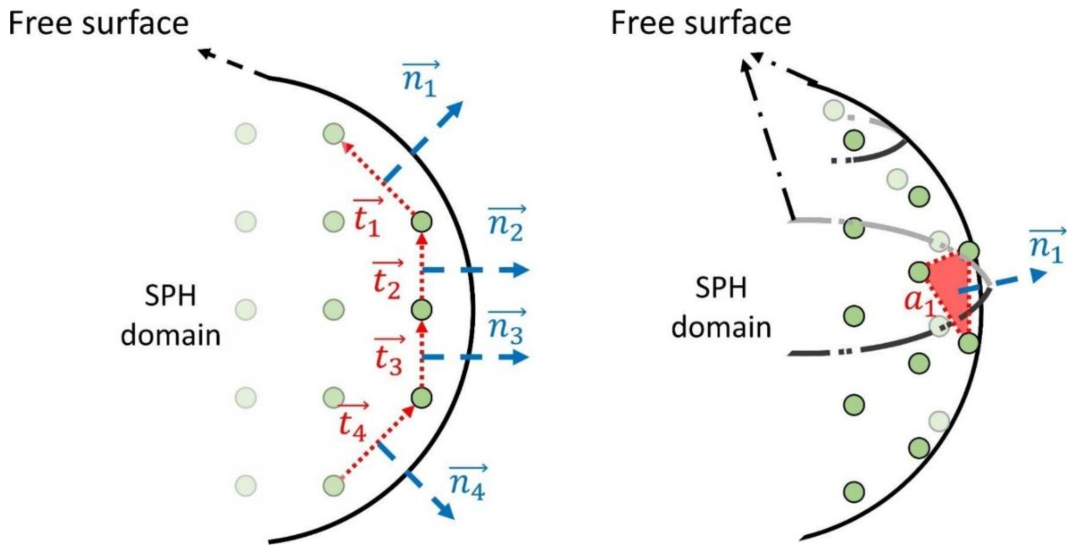

Figure 4.1: Conventional approach to apply confining stress in SPH (2D left and 3D right).

4.3.2 A new approach to applying confining stress to flexible boundaries in SPH – Theory

In this section, a generic approach to applying confining stress to flexible boundaries in SPH is developed. The proposed approach makes use of kernel truncation properties of SPH approximations near boundaries to facilitate the enforcement of confining stress on the boundaries, thereby allowing the extension of current SPH applications to more complex engineering problems that require confining stresses (such as biaxial or triaxial soil tests).

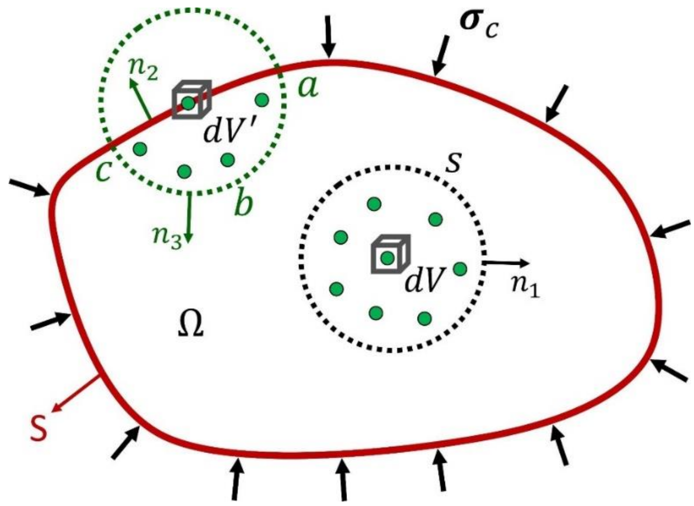

Figure 4.2: Illustration of the mechanism for the proposed confining boundary condition.

Let us first consider a dry solid body Ω of arbitrary shape subjected to a constant confining pressure field σ_c and is under equilibrium as shown in Figure 4.2. The stress state of any infinitesimal volume dV within Ω can be defined as follows:

$$\sigma^{\alpha\beta} = \sigma'^{\alpha\beta} + \sigma_c \delta^{\alpha\beta} \tag{4.1}$$

where $\sigma'^{\alpha\beta}$ is the effective stress component due to the deformation of the solid skeleton and σ_c is the confining pressure acting on dV.

The motion of the infinitesimal volume dV within Ω can be then described by substituting Equation (4.1) into the SPH momentum Equation (3.10), as follows:

$$\frac{Dv_i^\alpha}{Dt} = \sum_{j=1}^{N} m_j \left(\frac{\sigma'^{\alpha\beta}_i + \sigma'^{\alpha\beta}_j}{\rho_i \rho_j} + \frac{\sigma_{ci} + \sigma_{cj}}{\rho_i \rho_j} \delta^{\alpha\beta} \right) \frac{\partial W_{ij}^R}{\partial r_i^\beta} + f_i^\alpha \tag{4.2}$$

The above equation implies that any infinitesimal volume element dV located within Ω is subjected to a constant hydrostatic pressure component, which is equal to the constant applied confining stress σ_c. This suggests that the additional term associated with the confining stress in Equation (4.2) plays a role as the confining stress generator to the boundary surface of Ω, thereby producing a constant hydrostatic pressure everywhere within Ω. To demonstrate this, let us rewrite the term associated with the confining stress in Equation (4.2) in an integral form:

$$\sum_{j=1}^{N} m_j \left(\frac{\sigma_{ci} + \sigma_{cj}}{\rho_i \rho_j}\right) \frac{\partial W_{ij}^R}{\partial \mathbf{r}_i} = \frac{1}{\rho_i} \int_{\Pi} (\sigma_{ci} + \sigma_{cj}) \frac{\partial W_{ij}^R}{\partial \mathbf{r}_i} dV_j \tag{4.3}$$

where dV_j is the volume of particle j or a volume element j, which is located within the supporting domain Π of i defined by the kernel function W_{ij}. The right hand-side of Equation (4.3) can be further extended as follows:

$$\frac{1}{\rho_i} \int_{\Pi} (\sigma_{ci} + \sigma_{cj}) \frac{\partial W_{ij}^R}{\partial \mathbf{r}_i} dV_j = \frac{1}{\rho_i} \int_{\Pi} (\sigma_{cj} - \sigma_{ci}) \frac{\partial W_{ij}^R}{\partial \mathbf{r}_i} dV_j + \frac{1}{\rho_i} \int_{\Pi} (2\sigma_{ci}) \frac{\partial W_{ij}^R}{\partial \mathbf{r}_i} dV_j \tag{4.4}$$

Under the equilibrium condition, the confining pressure is constant everywhere within the domain Ω, causing the first term of Equation (4.4) to vanish everywhere in Ω. Next, it will be proven that the second term of Equation (4.4) produces the confining stress on the boundary surface S. Using the divergence theorem, the second term on the right-hand side of Equation (4.4), which is a volume integral, can be converted into a surface integral as follows:

$$\frac{1}{\rho_i} \int_{\Pi} (2\sigma_{ci}) \frac{\partial W_{ij}^R}{\partial \mathbf{r}_i} dV_j = -\frac{2\sigma_{ci}}{\rho_i} \left(\int_{s} W_{ij}^R \overrightarrow{n_1} ds \right) \tag{4.5}$$

where s is the surface of the kernel supporting domain Π and $\overrightarrow{n_1}$ is unit vector normal to s.

In SPH, the kernel function W is always defined to be symmetric and has a compacted supporting domain, thus the integral of $W\overrightarrow{n_1}$ (and thus $W_{ij}^R\overrightarrow{n_1}$) over any closed surface s is zero. This suggests that Equation (4.5) vanishes everywhere within Ω if s is a closed surface, or in other words, the supporting domain Π is not truncated. However, this is not the case when the volume element is located close to or on the surface boundary Ω. For this particular case, let us consider the volume element dV' as shown in Figure 4.2. The application of Equation (4.5) to this element leads to the following equation:

$$\frac{1}{\rho_i} \int_{\Pi} (2\sigma_{ci}) \frac{\partial W_{ij}^R}{\partial \mathbf{r}_i} dV_j = -\frac{2\sigma_{ci}}{\rho_i} \left(\int_{ac} W_{ij}^R \overrightarrow{n_2} ds + \int_{abc} W_{ij}^R \overrightarrow{n_3} ds \right) \tag{4.6}$$

where $\overrightarrow{n_2}$ and $\overrightarrow{n_3}$ are the normal vectors on surface sections ac and abc (see Figure 4.2), respectively. Because abc is a closed surface, the surface integral of the kernel function $W_{ij}^{R}\overrightarrow{n_3}$ over this surface is zero, thus the above equation can be further simplified as below:

$$\frac{1}{\rho_i}\int_{\Omega}(2\sigma_{ci})\frac{\partial W_{ij}^{R}}{\partial \mathbf{r}_i}dV_j = -\frac{2\sigma_{ci}}{\rho_i}\int_{ac}W_{ij}^{R}\overrightarrow{n_2}ds \tag{4.7}$$

The above equation integrates stress σ_c over the surface ac, which results in a force acting on the volume element dV' in the opposite direction to the normal vector $\overrightarrow{n_2}$. Consequently, when this surface integration is performed over the entire surface S of the domain Ω, it forms a constant confinement that is proportional to σ_c onto the surface area of the problem domain. Therefore, when applying Equation (4.2) to enforce confining stress, σ_c only takes effect on the free surface while automatically vanishing inside the domain. This suggests that the confining stress in SPH can be enforced through Equation (4.2) by assigning a constant pressure value, equal to the confining stress, to every SPH particle within the computational domain. This method provides a new pathway to effectively enforce a confining stress boundary condition in SPH without searching for particles located on or close to free-surfaces or open boundaries. Accordingly, for any problem under a constant confining stress, the following SPH motion equation can be applied with a constant confining pressure assigned to every SPH particle:

$$\frac{Dv_i^{\alpha}}{Dt} = \sum_{j=1}^{N} m_j\left(\frac{\sigma_i^{\alpha\beta}+\sigma_j^{\alpha\beta}}{\rho_i\rho_j}+C_{ij}^{\alpha\beta}\right)\frac{\partial W_{ij}^{R}}{\partial r_i^{\beta}} + \sum_{j=1}^{N}\frac{m_j}{\rho_i\rho_j}\left(\sigma_{ci}+\sigma_{cj}\right)\frac{\partial W_{ij}^{R}}{\partial r_i^{\alpha}} + f_i^{\alpha} \tag{4.8}$$

4.3.3 Verification of the proposed confining stress approach in SPH

In this section, an SPH benchmark test with a circularly shaped specimen subjected to a constant confining stress is carried out to verify the stability and accuracy of the proposed method to apply stress boundary condition in SPH. Figure 4.3 shows the outline of the model setup for numerical tests. The test is conducted with a 10 kPa confining stress and a linear elastic constitutive model is assumed in the numerical simulation for simplicity. The material properties are $E = 20$ MPa and $\nu = 0.3$, while the initial inter-particle distance was set to 1 mm. The sample has a radius of 50 mm, which is discretised using a fan shaped particle configuration resulting in a total of 1951 SPH particles as shown in Figure 4.3. Such fan shaped layout creates a smooth boundary surface compared to orthogonal particle layout, which can smear out numerical noise during simulation due to the zig-zag shape of the boundary. The confining stress is achieved by applying an initial hydrostatic pressure of $\sigma_c = 10$ kPa to every SPH particle together with the use of Equation (4.8) to describe the motion of SPH particles. Two numerical tests with and without an initial stress condition are conducted. In the former case, an initial stress condition that is equivalent to the applied confining stress of 10 kPa is assigned to every particle within the computational domain, and this can be achieved by setting $\sigma_{xx} = \sigma_{yy} = \sigma_{zz} = 10$kPa and $\sigma_{xy} = 0$kPa to every SPH particle. On the other hand, all initial stress components are set to zero in the latter case to simulate the sample without an initial stress condition. Confining stress is enforced in both cases.

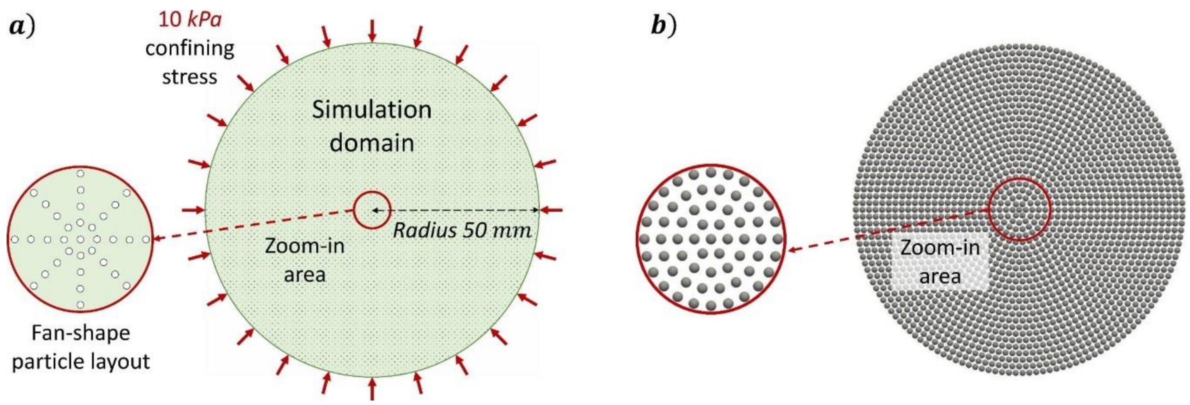

Figure 4.3: Model setup for numerical test: (a) Geometry of the problem; (b) Radial particle layout in SPH simulation.

In addition, viscous damping is required in SPH to stabilise the potentially excessive stress wave propagation due to the sudden application of the confining stress vectors on the computational domain without an initial stress condition. This viscous damping can be incorporated in the SPH motion equation following the approach proposed by (Bui & Fukagawa, 2013) as follows:

$$f_i^\alpha = f_i^\alpha - \xi \sqrt{\frac{E}{\rho h^2}} v_i^\alpha \tag{4.9}$$

where f_i^α is the acceleration of particle i due to internal stress and external force; ξ is a dimensionless damping coefficient chosen to be 0.1 (Bui & Fukagawa, 2013), (Nguyen et al. 2017).

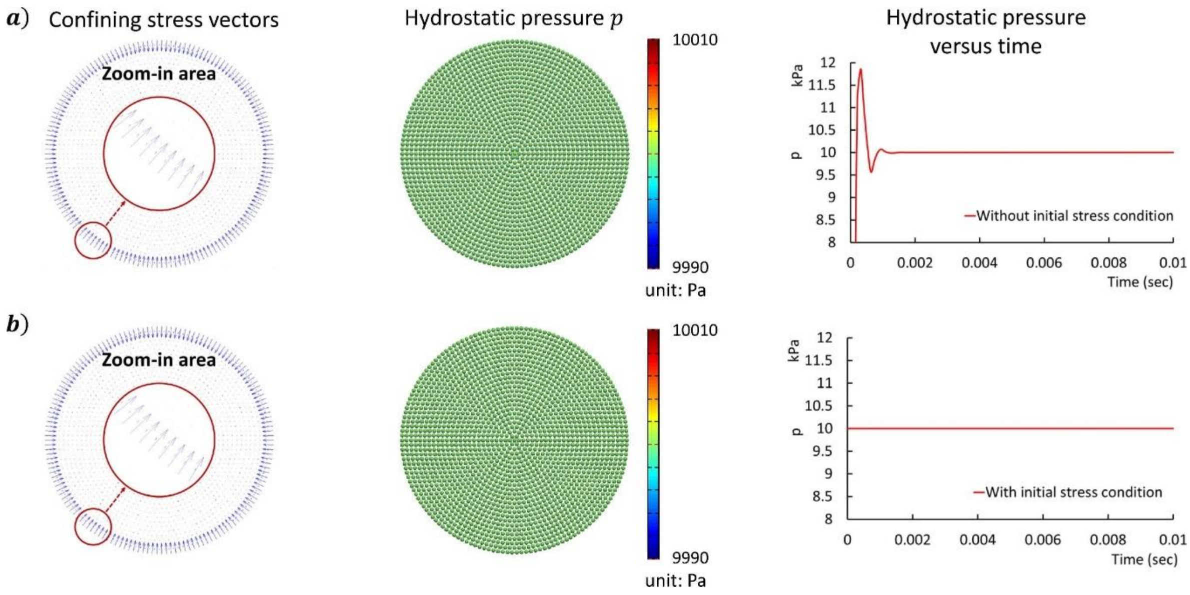

Figure 4.4: SPH simulation of confined compression test: (a) without imposing initial stress condition and (b) with imposing initial stress condition.

Figure 4.4 shows the SPH simulation results for the case of 10 kPa confining pressure applied to the circular specimen using Equation (4.8). It can be seen that the proposed method can correctly produce the confining stress direction and its magnitude acting on the numerical specimen without any extra effort required to search for particles on the boundary and imposing the confining stress to these particles. The plots of confining stress vectors indicate that all stress components produced by the additional confining stress term in Equation (4.8) vanish within the numerical specimen except those on the boundary where the SPH kernel is truncated. The truncation of the SPH kernel approximation on the boundary produces stress vectors normal to it and directing toward the centre of the circular specimen, suggesting that the proposed method presented in the previous section is correct. By comparing the results between two cases, with and without imposing an initial confining stress of 10kPa to the specimen, it shows that the latter case reaches an equilibrium after several hundreds of cycles of numerical iterations with the aid of the viscous damping force, while the former case achieves an equilibrium immediately. Both cases result in the same initial confining stress of 10kPa across the numerical specimen, suggesting that the additional confining stress term in Equation (4.8) can produce the confining stress that is of the same order of magnitude as with the initially imposed initial confining stress of 10kPa to the numerical specimen. These good agreements also imply that the viscous damping has no influence on the simulation results, but improves the stability of the numerical solutions.

The above numerical test indicates that the proposed method or Equation (4.8) can exactly produce the desirable confining stress to a computation domain by simply applying an initially uniform hydrostatic pressure to all SPH particles within the computational domain. No additional effort is required to search for particles on the confinement boundary and then impose the desirable confining stress to these particles. The proposed method can instantaneously achieve a desirable confining stress if a hydrostatic stress condition that is equivalent to the applied confining stress is imposed to all particles in the numerical specimen. Nevertheless, strictly speaking, the above numerical observation is only applicable for small deformation cases. In situations where large deformations occur, the relative movement of particles may affect the accuracy of the method. Therefore, further improvements are required to ensure stability and accuracy of the proposed method and these will be explained in the next section.

4.3.4 Treatment of confining boundary condition for large deformations

When the material undergoes large deformations, SPH particles representing the computation domain no longer maintain their initial relative positions and can become highly disordered, which may hinder the application of the proposed confining stress approach. In particular, Equation (4.5) may become non-zero for those SPH particles undergoing very large deformation even though their supporting domain is still located within Ω (i.e. theoretically remains a closed surface), causing an imbalance of confining forces acting on those SPH particles within the computational domain. One straightforward way to mitigate this issue in SPH applications involving very large soil deformation is to apply Equation (4.8) to only SPH particles which are located on or close to the boundary of Ω. The empirical condition to specify these SPH particles, which is optimised by trial and error, can be written as follows:

$$\mathrm{f_i} = \begin{cases} \leq 0.55 & \text{in} \quad 2\mathrm{D} \\ \leq 0.70 & \text{in} \quad 3\mathrm{D} \end{cases} \tag{4.10}$$

where $\mathrm{f_i}$ is an index value for a given SPH particle within the computational domain and it is calculated as follows:

$$f_i = \sum_{j=1}^{N} \frac{m_j}{\rho_j} W_{ij} \tag{4.11}$$

with N being the total number of SPH particles located within the supporting domain of particle i and j representing these neighbouring particles.

On the other hand, for those SPH particles located within Ω where their supporting domain remains a closed surface, the second term in the right-hand side of Equation (4.8) vanishes and Equation (4.8) reduces to the standard SPH formulation for elasto-plastic materials:

$$\frac{Dv_i^{\alpha}}{Dt} = \sum_{j=1}^{N} m_j \left(\frac{\sigma_i^{\alpha\beta} + \sigma_j^{\alpha\beta}}{\rho_i \rho_j} + C_{ij}^{\alpha\beta} \right) \frac{\partial W_{ij}^{R}}{\partial r_i^{\beta}} + g_i^{\alpha} \tag{4.12}$$

The above procedure guarantees that the confining stress vectors only take effect on the confinement boundary during the simulation and this is consistent with FEM and experimental results. It is worth emphasising here that, although an extra computational effort is required to identify SPH particles located on or close to the confinement boundaries (or free-surface boundaries), the current approach does not require the calculation of normal vectors and surface areas for particles over which the confining stress is applied. This will significantly reduce the overall computational effort required to apply the confining stress in SPH compared to the conventional approach as discussed in the preceding section.

In addition, owing to the fact that the smoothing length of SPH particles is kept constant in the current work, the interpolated value of the confining stress from Equation (4.5), or the second term on the right-hand side of Equation (4.8), may reduce when the particle separation increases. This may result in the reduction of the magnitude of the confining stress vectors and thus a loss of the required level of confinement on the modelling domain. One way to mitigate this issue is to update the smoothing length of SPH particles during the simulation (Benz, 1990), (Liu & Liu, 2004). Alternatively, the following simple approach can be applied to maintain the confining stress during the simulation. In particular, the second term on the right-hand side of Equation (4.8) is updated during the simulation using the following equation:

$$\sum_{j=1}^{N} \frac{m_j}{\rho_i \rho_j} \left(\sigma_{ci} + \sigma_{cj} \right) \frac{\partial W_{ij}^{R}}{\partial \mathbf{r}_i} = \sum_{j=1}^{N} \frac{m_j}{\rho_i \rho_j} \left(\sigma_{ci} + \sigma_{cj} \right) \frac{\partial W_{ij}^{R}}{\partial \mathbf{r}_i} * \left(\frac{l^0}{l^n} \right) \tag{4.13}$$

where n represents the nth time step; l^0 and l^n are the second term on the right-hand side of Equation (4.8) at the initial and nth time step, respectively, and can be expressed as follows:

$$l^n = \left\{ \sum_{j=1}^{N} \frac{m_j}{\rho_i \rho_j} \left(\sigma_{ci} + \sigma_{cj} \right) \left(\frac{\partial W_{ij}^R}{\partial \mathbf{r}_i} \right) \right\}^n \tag{4.14}$$

4.4 Numerical applications

In this section, the above proposed generic confining boundary condition in SPH is applied to capture the basic geomechanical experiments on soils. This includes a biaxial confined test under the plane strain condition and an axisymmetric triaxial test with cylinderic samples. Both tests have been conducted under various boundary conditions and a ranged level of confinements. The SPH obtained results are compared to the experimental data regarding the axial stress strain relations, as well as those from FEM and GIMP. Very good agreement is observed among results from different approaches, while SPH demonstrates its advantage of naturally capturing the large deformation plastic behaviours and kinematics inside the sample. Furthermore, an examination on the loading path of the triaxial test is conducted to validate the treatment algorithm (Chapter 3) for the corner singularity issue featured by the Mohr-Coulomb constitutive model, which proves that the discontinuous surface gradient issue has been well treated. This will be elaborated in this section.

4.4.1 SPH simulation for the biaxial test

Plane-strain biaxial tests are simulated in this section to further verify the proposed confining boundary condition and the Mohr-Coulomb elasto-plastic constitutive model in SPH. The obtained numerical results are then compared with those derived from the classical finite element method (ABAQUS) as well as the Generalised Interpolation Material Point Method (GIMPM) (Kiriyama, 2013) with elastoplastic Mohr-Coulomb model. The initial geometry setting and boundary conditions for the biaxial test are shown in Figure 4.5. The numerical sample has a rectangular shape with an initial dimension of 100 mm height and 50 mm width (Figure 4.5a). In the simulation, the numerical sample is first isotropically loaded to a predefined confining stress level (Figure 4.5b). The confining stress on the two side boundaries is then kept unchanged during the simulation, while the motions of top and bottom boundaries are controlled for axial loading. In this test, the motion along the bottom boundary is restrained in all directions, while that in the vertical direction of the top boundary is subjected to a constant downward velocity of $10\,\mathrm{mm/s}$. The horizontal motion along the top boundary is controlled to replicate the free-cap boundary (i.e. freely moved) and fixed-cap boundary (i.e. restrained) conditions, which are commonly reported in experiments. The material properties are summarised in Table 4.1 along with their predefined confining stress levels.

In SPH simulations, the above numerical sample is created using 1250 particles, which are arranged in a square lattice with an initial lattice size of 2 mm and an initial smoothing length of 2.4 mm (Figure 4.5c). In addition, 5 extra layers of SPH particles are created at both the top and bottom boundary areas to enforce boundary conditions. The fixed boundary or constant velocity boundary in SPH can be readily achieved by restricting particle position update or restricting particle velocity update, while the confining stress is enforced through the proposed confining boundary approach described in the preceding section. All other parameters for SPH simulations are selected following the suggestion by Bui et al. (2008a), except that the sound speed for the artificial viscosity is computed following the work of Bui et al. (2011). In FEM, to provide a quantitative comparison with SPH, an initial mesh size of 2 mm is also adopted (Figure 4.5b). However, different from SPH that requires extra particles to impose the displacement controlled boundary condition, the boundary conditions in FEM can be straightforwardly achieved by directly applying pre-defined values to nodes located on boundary surfaces of the computational domain. These boundary conditions are applied to the numerical sample through the built-in options in ABAQUS. It is also noted here that a built-in option Nlgeom, which proceeds non-linear deformation in computational domain, is activated to avoid ill-posed boundary values for all FEM simulations.

Table 4.1: Model parameters for the biaxial tests.

Test No	**Confining stress (kPa)**	**Shear modulus (kPa)**	**Density**	**Cohesion (kPa)**	**Friction angle (deg)**	**Dilatant angle (deg)**
1	50	6401	1.53	8.5	30.5	0
2	100	8514				

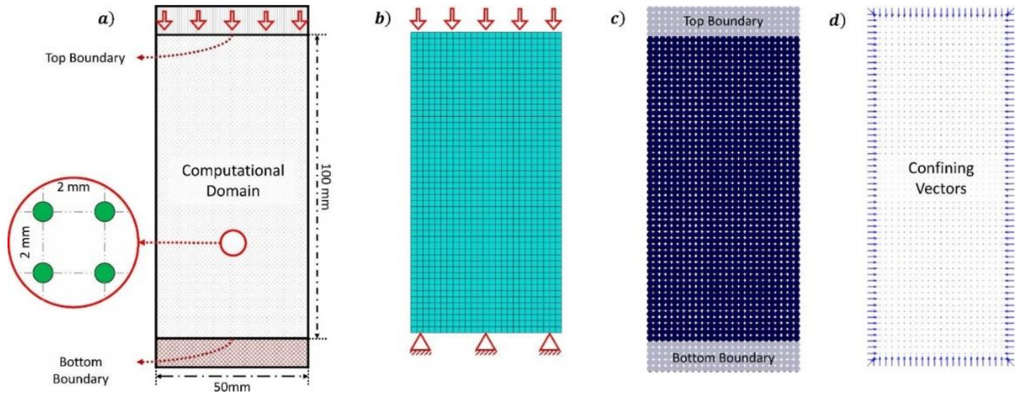

Figure 4.5: Initial setting geometry and boundary conditions used in simulations: (a) Initial geometry for the biaxial test; (b) FEM mesh discretisation; (c) SPH particle discretisation; (d) Confining stress vectors generated by Equation (4.13).

Biaxial test with fixed-cap boundary

The development of deviatoric strain in SPH biaxial tests and their quantitative comparisons with FEM results are illustrated in Figure 4.6 with a horizontally restricted top boundary condition. The sample responses are tested with confining stresses of 50 kPa and 100 kPa, respectively, and the deviatoric strain is calculated as $\varepsilon^{\mathrm{dev}} = \left(\frac{1}{2}\boldsymbol{\epsilon}:\boldsymbol{\epsilon}\right)^{1/2}$, where $\boldsymbol{\epsilon}$ is the deviatoric strain tensor. From the results, SPH yields a very similar prediction of strain localisation pattern compared to the classical FEM solution, which demonstrates a good stability of current SPH framework when simulating soil plasticity problems. During the SPH test with 50 kPa confinement (Figure 4.6a), a uniform distribution of the accumulated deviatoric strain is observed in the sample at an early stage of loading. When the stress state reaches the yield surface and the strain field bifurcates, a symmetric cross-shaped localisation of strain field forms within the sample, which is observed at 0.9% axial deformation. As the deformation proceeds, deformation accumulates within the shear band and facilitates the localisation process. At 1.2% axial strain, the originally symmetric cross-shaped shear bands start to develop in a non-symmetric manner, in which one branch of the cross shaped shear band develops more than the other. The developments of these two shear bands alternate and eventually leads to a strain localisation area with clear X-shaped shear bands at 15% axial strain. Similar process is also observed in the SPH test with 100 kPa confining stress (Figure 4.6c), which predicts more symmetric X-shaped shear bands. On the other hand, in the FEM tests (Figure 4.6b and 4.6d), an initially smeared deviatoric strain field is also observed. At the bifurcation stress state, a symmetric localisation pattern is also observed. Since the non-linear geometry deformation is considered in FEM (with Nlgeom), the elements within the shear localisation zone rapidly distort as the strain field becomes more localised. When 15% axial deformation is reached, a cross-shaped shear band forms and generally maintains its symmetry. The shear band inclination angle (θ) in both SPH and FEM is measured close to 50° with respect to the horizontal direction, which is close to the empirical relation $\theta = \frac{\pi}{4} + \frac{\phi}{4} + \frac{\psi}{4}$ proposed by Arthur et al. (1977). This result suggests that the current SPH framework could produce similar results to that of FEM at small deformation range, while outperforming the conventional FEM method when analysing large deformation soil plasticity problems.

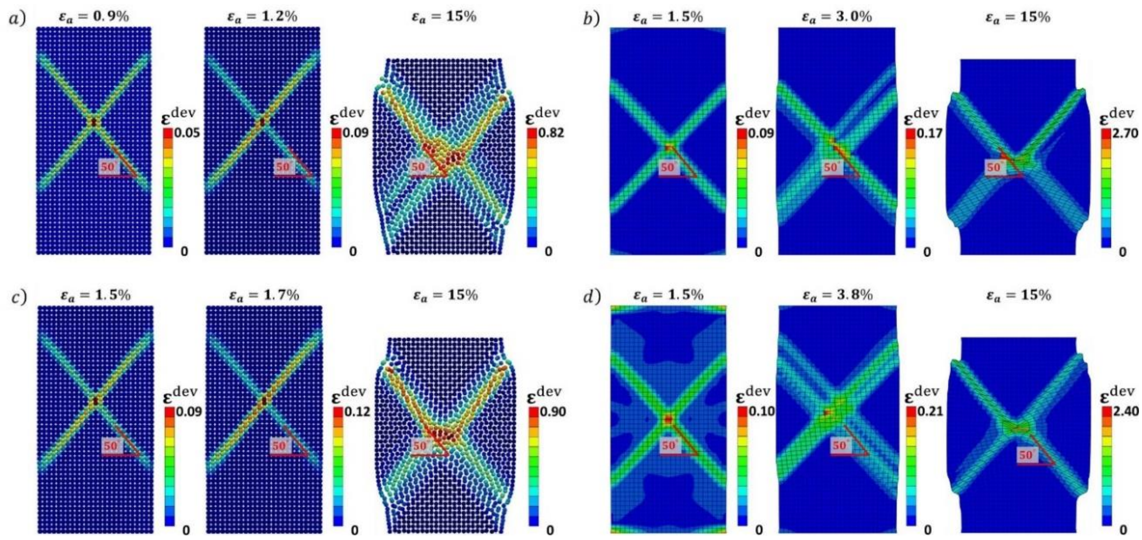

Figure 4.6: Total deviatoric strain plot for biaxial tests with horizontally fixed cap: (a) SPH with 50 kPa confinement; (b) FEM (with Nlgeom) with 50 kPa confinement; (c) SPH with 100 kPa confinement; (d) FEM (with Nlgeom) with 100 kPa confinement.

Biaxial test with free-cap boundary

The evolution of deviatoric strain in both SPH and FEM are compared for the free-cap boundary, and illustrated in Figure 4.7. When the lower confinement is applied (50 kPa), an initial elastic soil response leads to a uniform strain field across the sample. As the stress state is close to the peak point at 1.0% axial deformation (Figure 4.7a), the deviatoric strain field localises, manifesting as cross-shaped shear bands centred in the sample. At 1.2% axial deformation, the free-cap boundary triggers the strain field to localise into one branch of the cross-shaped shear bands. This leads to a continuous localisation of the deviatoric strain in a single inclined shear band while unloading takes place in the other previously localised areas. When the sample reaches 15% axial deformation (Figure 4.7a), a clear inclined shear band is observed with significant shear deformation accumulated within this area. A similar development is also observed in the SPH sample with 100 kPa confining stress as demonstrated in Figure 4.7c. For the FEM comparison test (Figure 4.7b), a uniform strain field is also observed during the elastic stage of deformation. When the stress state approaches its peak at 1.1% axial deformation, the free-cap boundary instantly triggers the deviatoric strain field to concentrate along the diagonal direction of the meshes. The deviatoric strain continues to localise in this area to form a single inclined shear band while the rest of the sample undergoes elastic behaviour. This localisation band gains its width as deformation grows and maintain its location as the sample achieves 15% axial deformationThe FEM predicted a similar shear band angle to that of SPH and these results are consistent with the empirical relation proposed by Arthur et al. (1977) as illustrated in Figure 4.7. From the above comparisons, the SPH method demonstrates its capability in modelling problems involving extreme soil deformation thanks to its mesh-free nature.

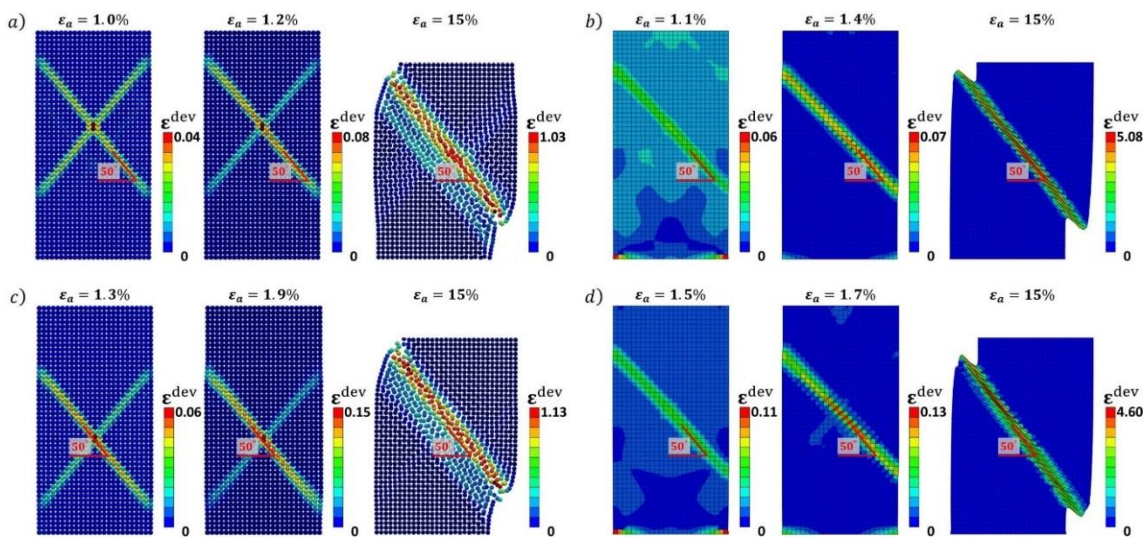

Figure 4.7: Total deviatoric strain plot for biaxial tests with horizontally free cap: (a) SPH with 50 kPa confinement; (b) FEM (with Nlgeom) with 50 kPa confinement; (c) SPH with 100 kPa confinement; (d) FEM (with Nlgeom) with 100 kPa confinement.

Stress-strain relations in the biaxial tests

A comparison of axial stress-strain history among SPH, FEM (ABAQUS) and GIMPM (Kiriyama, 2013) methods with fixed and free-cap boundaries is depicted in Figure 4.8. For fixed cap condition, all models predict an elastic soil response when the sample axial deformation is less than 1%, yet SPH and GIMPM yield an almost identical elastic modulus while FEM shows small variation. When the stress states in soil approach the peak point, nonlinearity becomes dominant as the increment of stress along with strain reduces and quickly demonstrates a perfectly plastic behaviour in all simulations. A peak stress value of around 125 kPa is predicted by all three methods at this point. These results suggest that SPH could yield similar results to that of FEM and GIMPM and is capable of solving boundary value problems that are consistent with the underlying elastic-perfectly plastic constitutive model. The good agreement among three numerical methods is also observed in the numerical samples with free-cap boundaries. In particular, both SPH and GIMPM again predict an identical elastic modulus, while FEM shows small variation. The SPH results manifest the perfectly plastic behaviour up to 3% axial deformation for 50 kPa confinement and 7% axial deformation for 100 kPa confinement, and then show steady and continuous global softening due to structural failure triggered by the free-cap boundary. A similar pattern is observed in GIMPM results with the perfect plasticity continues up to 2.5% (50 kPa confinement) and 2% (100 kPa confinement) axial strain and then following by softening responses, while FEM depicts an instantaneous softening behaviour after the peak stress point. With free-cap boundary, all models predict their residual stresses around 75% of the peak value as axial strain continues to 15%.

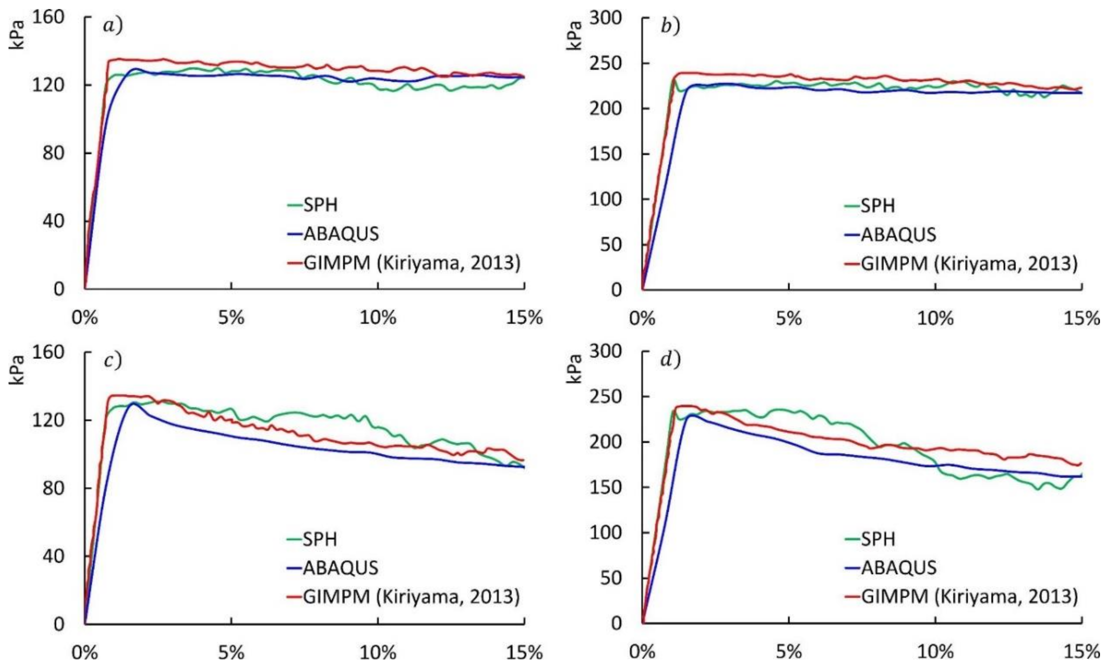

Figure 4.8: Axial stress versus strain of biaxial test from different numerical methods for (a) 50 kPa confining pressure with horizontally fixed top; (b) 100 kPa confining pressure with horizontally fixed top; (c) 50 kPa confining pressure with horizontally free top; (d) 100 kPa confining pressure with horizontally free top.

Analysis of the effect of the numerical resolution in the biaxial test

An analysis of varying spatial discretisations in both SPH and FEM is further carried out to verify the reliability of the proposed SPH approach. In particular, the fixed-cap biaxial test under 50 kPa confining stress is repeated with three initial interparticle distances (or mesh sizes in FEM) of dx=2mm, dx=3mm and dx=4mm. Figure 4.9 shows a comparison between SPH and FEM for the three lattice sizes. At 2% axial strain, both SPH and FEM predict a rather similar shear banding patterns as shown in Figures 4.9a & 4.9b. The strain localisation configurations are comparable between SPH and FEM for the resolutions of dx=2mm and dx=4mm, which are evidenced by the symmetric X-shaped shear band configuration observed in both samples. Nevetherless, the sample with dx=3mm shows a non-symmetric X-shaped shear configuration in the FEM solution, while SPH shows competing mechanisms between the symmetric and non-symmetric shear bands. The non-symmetric results can be attributed to the influence of spatial discretisations (i.e. mesh discretisations in FEM) as no weak zones were defined in the numerical samples to trigger localised deformation. However, owing to the SPH nature of particle approximations and probably the perfectly plastic MC model used in this study, its solutions seem to mitigate the influence of spatial discretisations. This explains why the SPH results of dx=3 mm show competing mechanism between symmetric and non-symmetric ones. Nevertheless, both methods predict the same shear band orientation, which is about 50^{o} to the horizontal direction. As the axial deformation reaches 15%, the localisation of deformation continues to develop, leading to thickening of shear bands. The SPH results show comparable symmetric X-shape shear bands among three numerical samples (Figure 4.9c), thanks to the particle approximation in SPH. In contrast, the final shear band configurations predicted by FEM are rather different among three numerical samples, both in terms of their symmetry and location (Figure 4.9d), and this can be attributed to the influence of both mesh discretisations and distortions. The comparison of axial stress-strain relations between SPH and FEM for the three tests are shown in Figure 4.10. Both SPH and FEM predict nearly identical stress-strain curves for different spatial discretisations (or meshes in FEM) and the results are comparable between two methods. This similarity can be attributed to the perfectly plastic model adopted in the current simulations, which enforce the stress to stay on its yield loci during the plastic deformation.

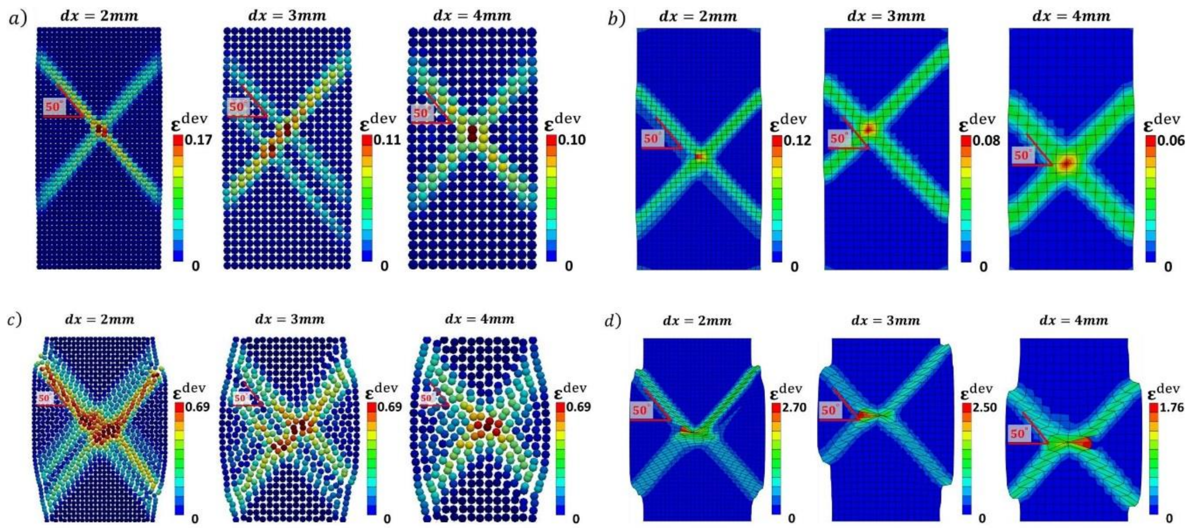

Figure 4.9: Total deviatoric strain plot for different domain resolutions (2mm, 3mm, 4mm): (a) 2% axial strain in SPH; (b) 2% axial strain in FEM; (c) 15% axial strain in SPH; (d) 15% axial strain in FEM.

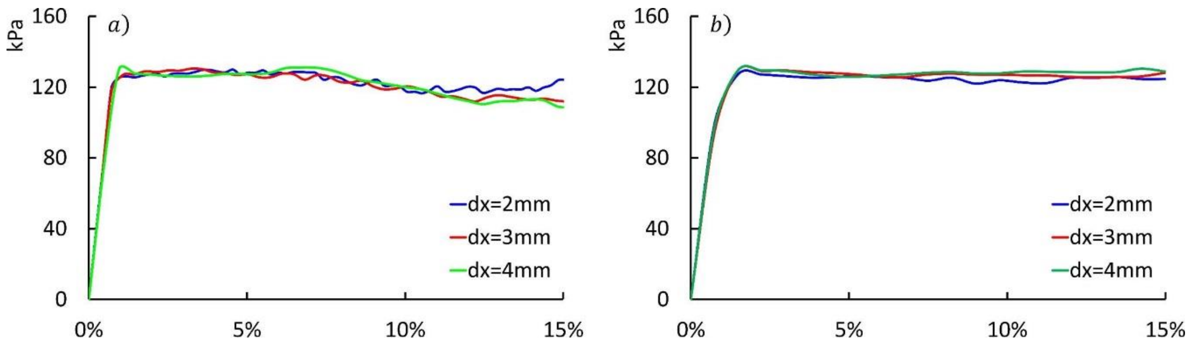

Figure 4.10: Axial stress-strain relations among varying resolutions: (a) SPH predictions; (b) FEM predictions.

The above results demonstrate that the SPH method can produce comparable results to those of the classical mesh-based FEM for small deformation and GIMPM for large deformation. The proposed confining boundary condition for SPH has been shown to be stable and is able to maintain the prescribed confining stress at very large deformation. The extension of this approach to three-dimensional applications and its predictive capability will be examined in the next section.

4.4.2 SPH simulation of the triaxial test

The proposed SPH framework has been compared with FEM and GIMPM solutions for plane strain soil plasticity problems and very good agreements among three numerical approaches have been achieved. In this section, the SPH framework is further extended to the three-dimensional application by conducting simulations of triaxial tests and numerical results are compared with triaxial experimental data reported by Kiriyama (2013), the FEM solution and GIMP solution. The performance of the proposed confining boundary condition is also examined under three-dimensional condition. The geometry and boundary conditions of this test are shown in Figure 4.11 together with both the SPH and FEM (ABAQUS) discretisation of the numerical sample. The cylindrical specimen has a dimension of 25 mm in radius and 100 mm in height. Fan-shaped particle lattice (mesh discretisation) is utilised to discretise the numerical sample with the aim to create a symmetric particle configuration in both cross-sectional and axial directions, thus minimising heterogeneous effects associated with the orthogonal particle (mesh) discretisation. A total number of 28140 SPH particles are used to create the numerical sample with an initial inter-particle distance of 2 mm. The loading platens are represented by five extra layers of particles created at top and bottom of the soil domain. Fixed-cap and free-cap boundary conditions are imposed at the top loading platen, while the bottom one remains fully fixed during the computation. The triaxial loading test is started by applying a constant downward speed of 10 mm/s to the top loading platen. Soil properties are taken from Kiriyama (2013) and other numerical parameters are set similar to those utilised in the biaxial tests, which are all listed in Table 4.1.

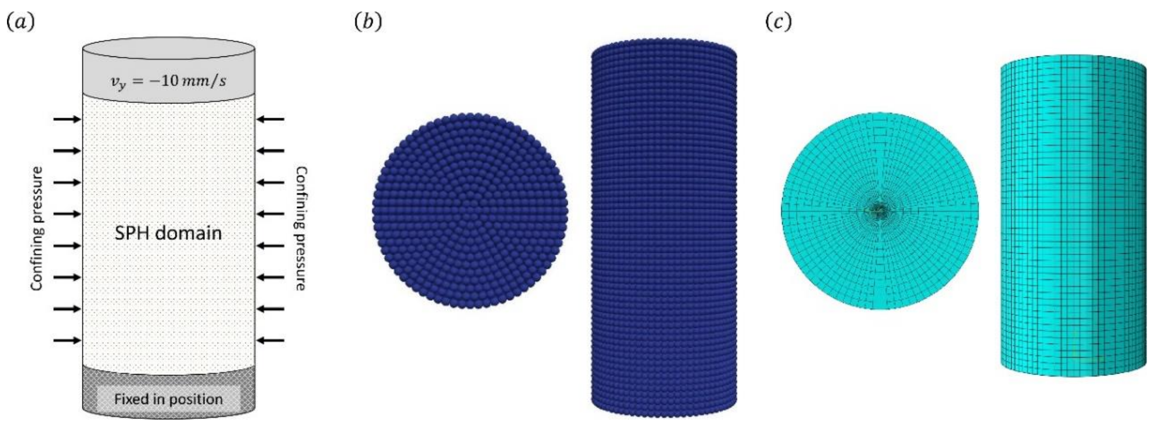

Figure 4.11: Triaxial test numerical setup in SPH: (a) Geometry and boundary condition; (b) SPH discretisation of the sample; (c) FEM (ABAQUS) discretisation of the sample.

Deviatoric strain evolution in SPH results

The evolutions of localised strain field with fixed-cap triaxial tests under 50 kPa and 100 kPa confining stresses are illustrated in Figure 4.12. The shear bands are observed in both perspective and cross-sectional views. In the test with 50 kPa confining stress (Figures 4.12a and 4.12c), the strain field is distributed across the sample at an early stage of elastic deformation. Immediately after the stress passes its peak point at 5% axial strain, the deviatoric strain field localises into symmetric X-shaped shear bands. As the axial deformation continues, the localisation of deformation becomes more apparent. Upon 15% axial strain, cross-shaped shear bands are observed, while multiple non-symmetric bands are formed at the centre of the soil cylinder (Figure 4.12c). The shear band evolution at 100 kPa confining stress is analogous to that at 50 kPa confining stress. However, once symmetric shear bands are formed inside the soil sample, their configuration and location are maintained during the plastic deformation. As 15% axial strain is achieved, shear bands demonstrate an increase in width while its symmetry, to some extent, is maintained (Figure 4.12b and 4.12d).

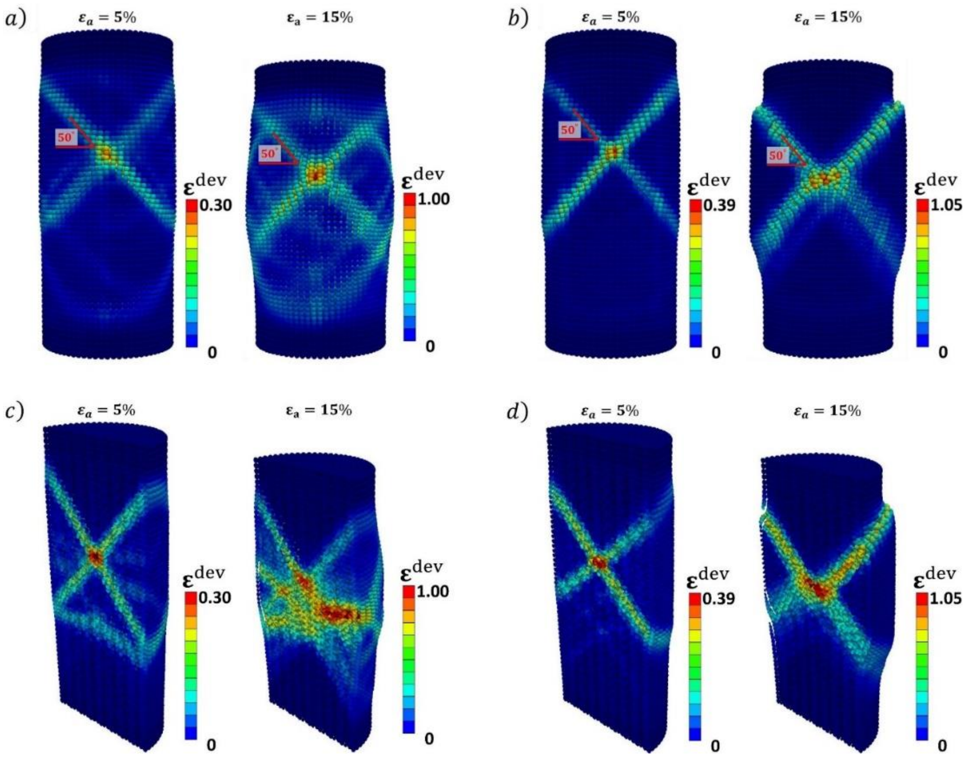

Figure 4.12: Total deviatoric strain in SPH triaxial tests with fixed cap condition: (a) 50 kPa confining stress; (b) 100 kPa confining stress; (c) cross-sectional plot of 50 kPa confining stress; (d) cross-sectional plot of 100 kPa confining stress.

For the test with free-cap boundary condition under 50 kPa confinement, the shear band development is shown in Figures 4.13a and 16c for 5% and 15% axial deformations, respectively. At 5% axial deformation, the free-cap boundary triggers multiple crossed and inclined shear bands. As deformation continues, the free-cap boundary facilitates a fast accumulation of shear deformation, and the shear bands start to localise into one branch with the outside zone undergoes unloading. Upon 15% axial deformation, a single inclined localisation band remains in the sample. For the test with 100 kPa confinement, the sample undergoes a similar process yet the shear deformation is more concentrated, manifesting a single shear band with smaller thickness compared to that of the 50 kPa confinement case. As for the shear band angle, tests with both fixed and free top boundaries predict the same inclining shear band angle of 50° as shown in Figure 4.12and 4.13. This result is consistent with the experimental observation reported by Kiriyama (2013).

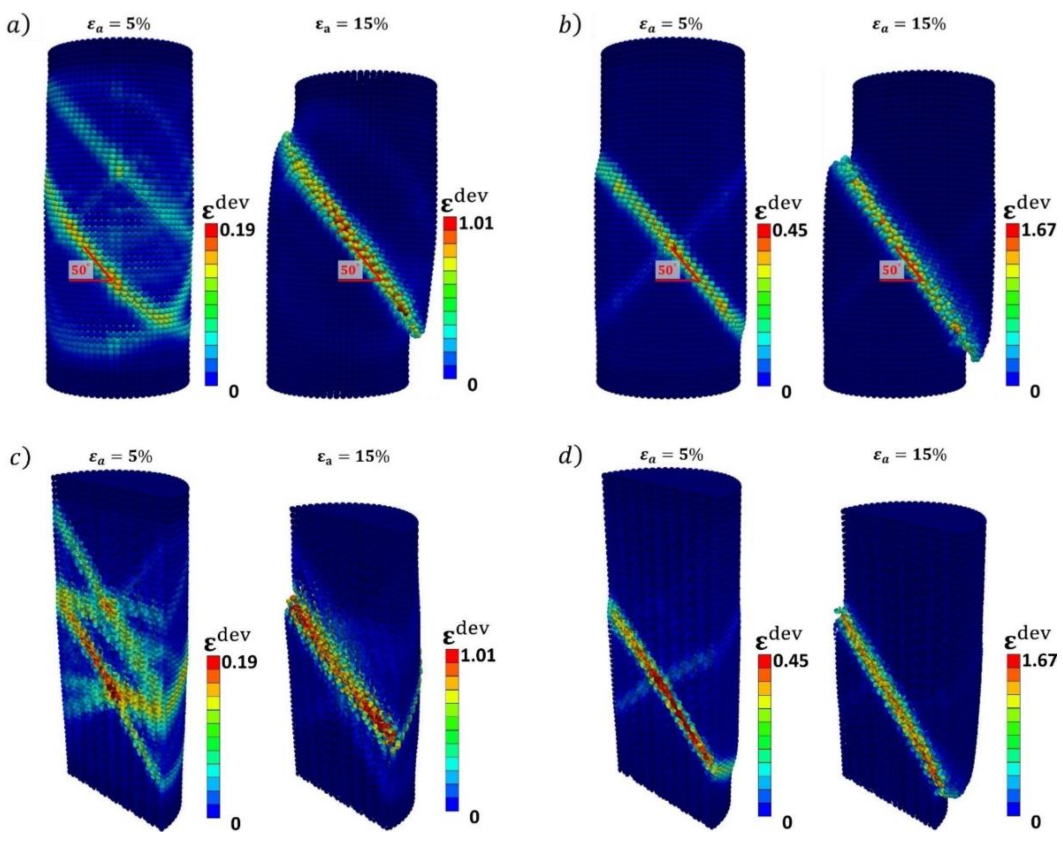

Figure 4.13: Total deviatoric strain in SPH triaxial tests with free cap condition: (a) 50 kPa confining stress; (b) 100 kPa confining stress; (c) cross-sectional plot with 50 kPa confining stress; (d) cross-sectional plot with 100 kPa confining stress.

Deviatoric strain evolution in FEM results

The same axisymmetric test has been conducted with the conventional mesh-based approach FEM for comparison with the SPH obtained results. The deviatoric strain plot is shown in Figure 4.14 below. From the plot, it is clear that the FEM is able to capture a certain degree of localised deformation in the sample for all confining stress levels and boundary condition setups. However, the tests with fixed-cap condition show a more smeared distribution of the deviatoric strain field at both 5% and 15% axial strain, while the tests with free-cap condition demonstrate more localised deformation field especially at 15% axial strain. This can be attributed to the fact that the computational meshes tend to maintain their hexahedron shapes for not compromising the well-posedness of the governing equations. Therefore, despite certain concentration of the strain field, the meshes in samples for both fixed-cap and free-cap tests are not deformed as much as the inter-particle relocations observed in the SPH results in Figure 4.12 and 4.13.

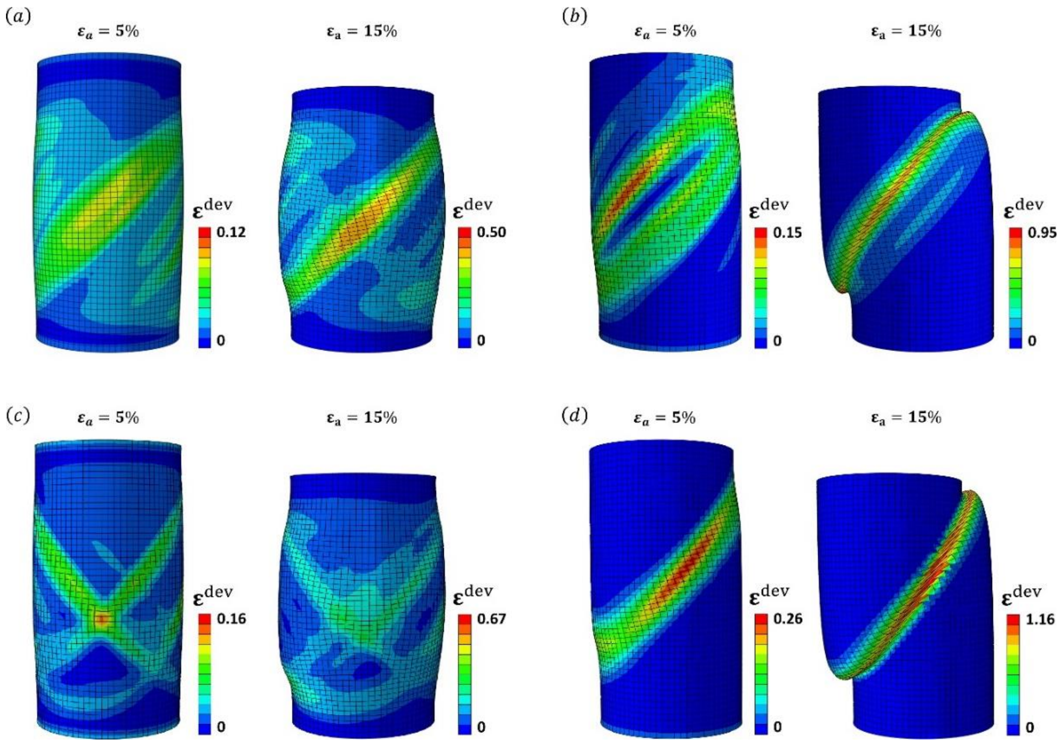

Figure 4.14: Total deviatoric strain in FEM simulated triaxial test: (a) with 50 kPa confining stress and fixed-top boundary condition; (b) with 50 kPa confining stress and free-top boundary condition; (c) with 100 kPa confining stress and fixed-top boundary condition; (d) with 100 kPa confining stress and free-top boundary condition.

Apart from this, the shaped function for some extremely deformed meshes shown in Figure 4.14b and 414d have already lose their validity as the Gauss points inside them are no longer at their initial relative positions which their theoretical solutions are based on. These predictions for the extreme deformation only occurs when the Nlgoem option in ABAQUS is ticked, otherwise the simulation would have stopped before reaching such deformation stage.

Stress-strain relationships in the triaxial tests

Figure 4.15 shows a comparison of axial stress-strain relationships obtained by three numerical methods (SPH, FEM and GIMPM) and experiments. For the simulations with fixed-cap boundary under both 50 kPa and 100 kPa confinements, the stress-strain curves exhibit an overall linear elastic-perfectly plastic behaviour and these results agree well with the experimental data. All simulations yield constant vertical stresses at around 120 kPa and 220 kPa for the low and higher confinement cases, respectively, and these results are again in good agreement with the experimental data reported by Kiriyama (2013).

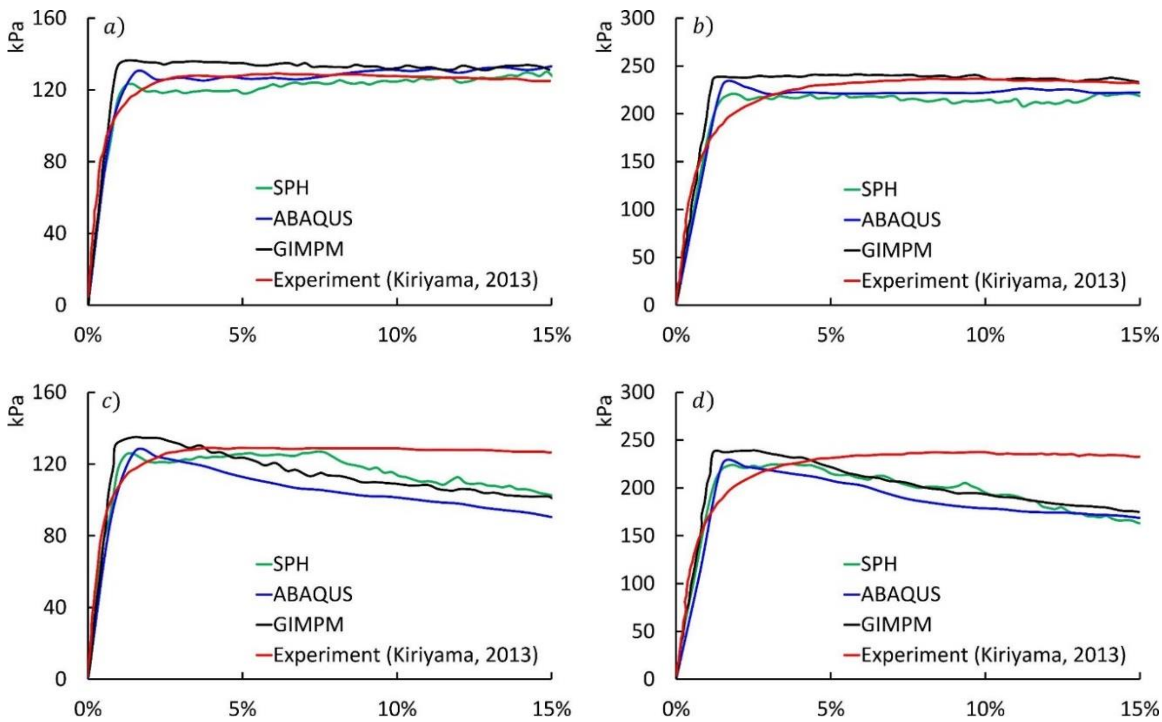

Figure 4.15: Axial stress versus axial strain of triaxial test from different numerical methods for: (a) 50 kPa confining pressure with the horizontally fixed top; (b) 100 kPa confining pressure with the horizontally fixed top; (c) 50 kPa confining pressure with the horizontally free top; (d) 100 kPa confining pressure with the horizontally free top.

For the cases with free-cap boundary, as the stress state passes the peak point, SPH and GIMPM demonstrate a short period of perfectly plastic behaviour. For example, at 50 kPa confinement, the perfect plasticity continues up to 7.9% and 3.6% axial deformation in SPH and GIMPM results, respectively. This is then followed by a persistent softening curve predicted by both methods. FEM yields persistent softening immediately after the peak stress. However, the experimental data demonstrates perfectly plastic curve until 15% axial strain. The possible explanation for this phenomenon is due to the fact that the strictly free-cap boundary condition is hardly achieved in the laboratory. Accordingly, the perfectly plastic behaviour in soil maintains up to 15% axial deformation. In contrast, the free-cap condition is easily achieved in the numerical simulations, which facilitates shear localisation and leads to the structural failure thus softening behaviour in the sample.

Examination of the triaxial loading path

Finally, to further demonstrate the effectiveness of the proposed confining boundary condition in maintaining the correct loading condition and its effectiveness of treating the corner singularities in the Mohr-Coulomb model, the local loading path of a particle located at the centre of the sample and the global loading path measured from the sample boundaries are plotted in Figure 4.16, on both meridian and deviatoric planes. Both loading paths start from point O, corresponding to the initial condition, where the sample is under hydrostatic pressure of 50kPa. As the axial load on the top surface starts increasing, the local loading path at the measuring point develops linearly until reaching point A and the sample is relatively homogeneous evidenced in the coincidence of local and global loading paths. At this stage, the deviatoric plastic strain is zero everywhere inside the sample. The slope of the local loading path OA measured in Figure 4.16a is $1/\sqrt{3}$, which coincides with the global triaxial loading path imposed on the sample shown as the black dashed line. As the local loading path goes past point A, some particles inside the sample enter their plastic state (evidenced by the development of deviatoric plastic strain at point B in Figure 4.16a). This leads to a slightly nonlinear section of the local loading path between point A and point C on the meridian plane. However, the global loading path measured at the boundaries continuously shows a linear behaviour, indicating that the triaxial loading condition over the entire sample is well maintained through the proposed boundary condition. This is also evidenced by the straight loading paths (both local and global) that evolve exactly towards the triaxial compressive meridian in the deviatoric plane (Figure 4.16b). Beyond the initial yield at point C, the local stress just stays on the yield envelope and moves from C to D in Figure 4.16a while still lying at the corner of the Mohr-Coulomb yield surface in Figure 4.16b. This confirms that the consistency condition is well satisfied at the measuring point and the triaxial loading path imposed on the sample is well maintained by the proposed confining boundary condition, even during the post yielding process. It is also noted that the loading path CD in Figure 4.16b corresponds to the triaxial compressive meridian on the Mohr-Coulomb yield surface, where the corner singularity issue arises. However, no numerical instability is observed in our simulations, suggesting that the proposed algorithm is effective in treating the corner singularity of the Mohr-Coulomb model, which maintains a valid flow rule during material plastic deformation.

The above numerical results verify that the proposed confining SPH boundary works well in both two- and three-dimensional conditions. The method is highly stable and is able to maintain the confining stress on highly non-linear curvature confining boundaries caused by excessively large soil deformation. Although a constant confinement scenario is considered for above tests, the proposed boundary method works equivalently for evolving confinement and can be applied, in general, for any SPH problems involving confinement. The Mohr-Coulomb perfectly plastic model when incorporated in SPH show comparable results to those of FEM for small deformation, GIMPM for large deformation and experiment. This demonstrates the capability of SPH in handling general soil plasticity problems, while outperforming the traditional FEM based methods in applications involved large deformation and failure. There still remains questions on the dependency of the solutions on SPH discretisation. The current results in the biaxial and triaxial tests show less dependence of numerical results on the domain discretisation, particularly in terms of load-displacement curves. This is not a true evidence to demonstrate mesh-independency of SPH given a perfectly plastic model was used. The fixed yield surface may regularise the energy dissipation during plastic deformation and lead to plausible mesh-independency of the method. To have further insights into this problem, a softening constitutive model is required. This is beyond the scope of the current paper and a subject of our ongoing investigations.

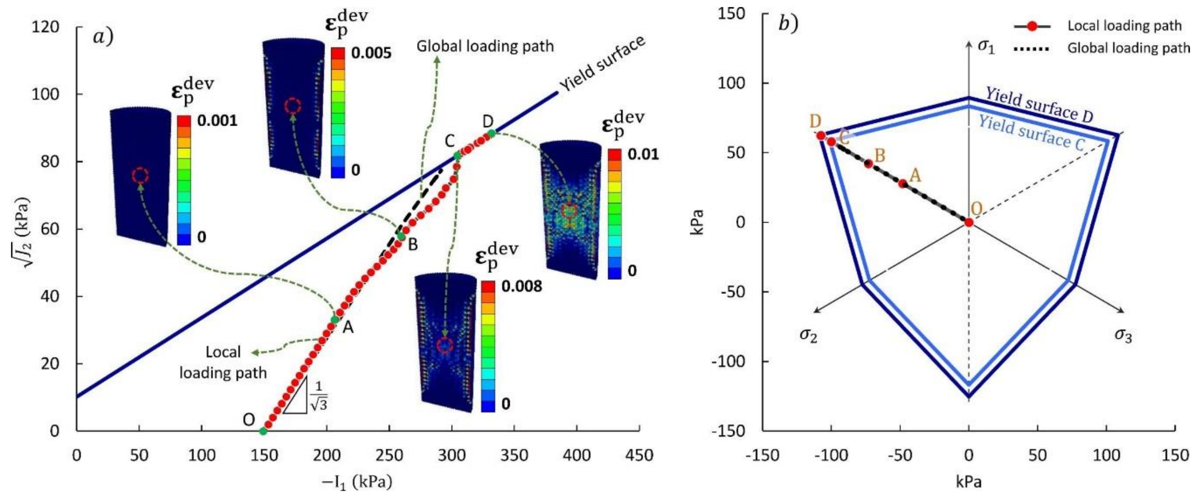

Figure 4.16: Global loading path and a local one of a particle located at the centre of the sample under 50 kPa confinement: (a) meridian plane; (b) deviatoric plane.

4.5 Conclusion

In this chapter, a generic method is proposed to effectively enforce flexible confining boundary conditions in SPH. The method makes use of its kernel truncation feature along free edges of SPH domain to automatically locate and trace curvature change of the boundary surfaces. The confining stress and its normal vectors are subsequently the natural outcomes of SPH approximations of the kernel gradient of confining stress for those SPH particles located on or close to the confining boundaries. This method has demonstrated its capability to effectively enforce a constant confining stress on to flexible boundaries, though in principle it works equivalently for evolving confinement. In parallel with this, a robust numerical procedure for implementation of the Mohr-Coulomb elastoplastic model in SPH, which avoids numerical difficulties associated with the well-known singularities that occur at the corners of the Mohr-Coulomb surface, is presented for the first time. The proposed numerical framework was first verified with theoretical solutions under simple shear condition. It was then used to simulate biaxial and triaxial tests with varying model parameters and numerical results were compared with those from the mesh-based method (FEM), advanced hybrid particle-mesh method (GIMPM) and experimental data available in the literature. Very good agreements between SPH and other counterparts were achieved, suggesting that the proposed confining boundary condition full-fills the need of SPH for general geotechnical applications that involved flexible and moving confining boundaries. The good agreement between SPH and experiment also suggests that, once a suitable constitutive model is selected and properly implemented in SPH, the method can be used to predict complex problems involved large deformation and failure. For this purpose, more advanced constitutive models capable of capturing realistic soil behaviour should be implemented and tested with the SPH method. These are beyond the scope of this chapter and will be left for future works.

Chapter 5

A study of local and nonlocal features of SPH and its application to modelling strain localisation in geomaterials

5.1 Introduction

In the classical continuum mechanics analysis of strain bifurcation/localisation in solid materials, the field kinematics is carried by representative volumes that are infinitesimally small. It fails to capture a micro-scale characteristic length effect in materials and predicts a physically meaningless discontinuous strain zone with vanishing size. A wide range of countermeasures is proposed to enrich either the continuum or the constitutive model with a predefined length scale parameter, which includes the application of higher-order gradient functions, nonlocal operator and continuum with rotational DOF etc. However, these enrichments come with additional complexity and computational cost, which may not achieve a full characterisation of the strain localisation process. On the other hand, the smoothed particle hydrodynamics (SPH) method introduced by Lucy, Gingold and Monaghan in 1977 is embedded with a nonlocal interpolation process, which is able to capture the strain bifurcation/localisation without extra regularisation (Bui et al. 2008; Vignjevic et al. 2014; Zhao et al. 2018). However, the length parameter in the SPH method has not been explicitly related to the material inherent characteristic scale, thus not allowing SPH to capture the scale effect that has been observed in many materials. Furthermore, the pathological mesh-dependency issue (resolution bias) in the finite element method is also observed in SPH, which implies that a clear definition of length parameter in SPH is still missing. Therefore, in this study, we further investigate the inherent SPH length parameter (the kernel radius) to investigate its impact on SPH performance as a nonlocal numerical method. In the proposed computational framework, a rigorous Mohr-Coulomb strain-softening model is implemented to characterise the strain-softening and localisation process. It is discovered that the SPH kernel radius can be related to a particular material scale and improve the resolution bias issue. However, due to its key role in maintaining the numerical stability of the SPH domain and particle dynamics, it cannot be applied as a generic length scale parameter to capture a wide spectrum of material scales. Therefore, a nonlocal plastic limiter is further implemented into the constitutive model to regularise the plastic energy dissipation. The results show that such plastic limiter co-works with the inherent SPH kernel function, and is able to capture any material length scale and completely regularise plastic energy dissipation immune from resolution bias. As a result, the proposed SPH framework is proven to be a very promising tool in the analysis of strain localisation phenomena and progressive failure problems with very large deformation.

5.2 Problem background

The numerical study of the progressive failure and strain localisation in geomaterials with conventional mesh-based methods such as FEA has been facing ill-posedness of boundary value problems when bifurcation starts to form in the computational domain and develops into a finite area of plastic strains (shear bands). This is due to the lack of an internal length scale in the conventional FEA methods, which makes the numerical solution solely dependent on the discretised mesh size and leading to a zero energy dissipation mode as the mesh is refined. Therefore the conventional FEA methods are characterised as “local” for it does not possess such internal length scale. Numerous countermeasures such as including rate dependency, using higher-order gradient functions, applying micropolar Cosserat continuum, using adaptive re-meshing and including nonlocal formulations have been proposed in the literature, among which the algorithm of applying the nonlocal formulation is readily implementable in our SPH framework and will be the focus of this work.

The nonlocal formulation derives field variables or gradients through a weighted average process over the neighbouring area of the location under consideration. Since only a finite influence area of the weighting function is considered, it introduces a length scale into the computational domain, specifically its influence radius. Therefore the plastic energy evolution is directly linked to this length scale parameter and its dissipation is regularised to avoid the dependency on mesh refinements. The application of the nonlocal formulation into the continuum analysis of plastic softening process was pioneered by Bažant and co-workers during 1980s, and later advanced and evolved by many (Pijaudier-Cabot & Benallal, 1993; Vermeer & Brinkgreve, 1994; Tvergaard & Needleman, 1995; Jirásek, 1998; Borino et al. 2003; Engelen et al. 2003; Desmorat et al. 2007; Galavi & Schweiger, 2010; Giry et al. 2011; Summersgill et al. 2017; Huang et al. 2018; Mánica et al. 2018). Among the above work, Vermeer and Brinkgreve proposed a linear combination of local and nonlocal variables to further improve the regularisation capacity of the nonlocal formulation (Vermeer & Brinkgreve, 1994; Planas et al. 1996; Strömberg & Ristinmaa, 1996). This is later systematically reviewed and characterised as “over-nonlocal” model by Di Luzio and Bažant (2005) who proved the achievement of a complete regularisation of plastic softening with this over-nonlocal model. Although numerous attempts with mesh-based methods have shown effective regularisation of plastic energy dissipation and mesh-independent results using the above technique, the current analysis is limited to small deformation stage. The excessive mesh distortion happened under very large deformation prevents the complete progressive failure process to be characterised, which limits its application from a full prediction of the failure process in geomechanics problems. Therefore, there exists a significant need for the nonlocal framework to be implemented into a complete meshless numerical method for large deformation geomechanics applications.

On the other hand, the smoothed particle hydrodynamics (SPH) method has been known as a meshfree continuum approach, which has the potential to overcome the above problems. In this work, the inherent nonlocal feature of SPH is carefully investigated regarding its numerical stability, efficiency and accuracy aspects. Since the SPH interpolation of state variables requires kernel weighting process, it introduces the kernel influence radius as a length scale parameter into the numerical domain. This feature allows SPH to naturally capture the bifurcation process without extra regularisation techniques. However, in order to preserve a stable dynamics of the computational domain, the kernel influence radius is coupled with a fixed linear relation with the size of numerical discretisation. It limits the number of particles that each kernel is able to contain. Therefore, numerical predictions of localised shear bands with traditional SPH manifest a resolution-dependent solution, analogous to the FEM mesh dependent pathology. This can be straightforwardly addressed by decoupling the kernel influence radius with the numerical discretisation size. As demonstrated later in section 5.5.1, SPH domain with a fixed kernel radius manifests a regularised energy dissipation path with resolution-independent shear band predictions and stress-strain relations. Nevertheless, a significant compromisation of numerical stability is also observed due to such decoupling. This implies a potential need for additional nonlocal operators in the current SPH framework. Therefore, a nonlocal plastic limiter is further incorporated to regularise the accumulated deviator plastic strain in the constitutive model, which controls the evolution of the yield surface. As suggested by Di Luzio and Bažant (2005), a linear combination of the local and nonlocal variables is applied in the plastic limiter to completely regularise the energy dissipation. This is validated by the SPH modelled drained biaxial tests, which demonstrate a converged stress path among a wide range of resolution spectrum with a specific characteristic length. It is also demonstrated that the plastic energy dissipation rate is linearly related to the characteristic length of the nonlocal plastic limiter, which suggests a potential link between the characteristic length and material internal length scale. It is noted that the implementation of the plastic limiter demonstrates a reasonable computational efficiency while preserves very good stability that has been observed in traditional SPH (Bui et al. 2008; Wang et al. 2018; Zhao et al. 2019).

To further facilitate capturing the strain localisation which is often accompanied with loss of material integrity, a robust elastoplastic strain softening constitutive model featured with Mohr-Coulomb yield surface is incorporated into the current SPH framework for the first time. In this model, the reduction of the material strength is controlled by an exponential relation between the state parameters (e.g. soil friction angle and cohesion) and the accumulated plastic strain deviator. This relation is featured with two groups of state parameters including virgin and residual values which correspond to the undamaged and fully damaged soil states. The proposed constitutive model is first validated against analytical solutions in a plane strain simple shear test and then brought to the drain biaxial tests. Numerical analysis shows that the proposed approach is able to well capture the complete failure and energy relaxation process in geomaterials while preserving a specific energy dissipation rate regardless of the resolution of the computational domain.

The rest of this chapter is arranged as follows: first, the basic SPH components including its particle approximation form and kernel function are discussed. Then, the elastoplastic Mohr-Coulomb strain-softening model is expanded with key formulations. This is followed by the nonlocal formulation and its algorithm in the current SPH framework. Then, three groups of drained biaxial tests featured with a wide resolution spectrum on analysing the nonlocal characteristic of SPH method are conducted. Lastly, the proposed numerical framework is applied for the capture of shear band development in a sandy soil featured with heterogeneity state parameters.

5.3 Local and nonlocal character for strain localisation in continuum mechanics

The classic continuum mechanics simplifies the problem domain as a uniform assembly of infinitesimal volumes which are interacting upon direct contact. When the domain is subjected to elastic boundary value problems, each infinitesimal volume has a linearly evolving strain tensor following the general Hooke's law. However, in the presence of strain bifurcation and localisation, the strain field diverges, with concentrated and uniform area coexist in the same domain. The classical continuum theory predicts the concentrated strain field with an infinitesimal width (if not zero), which evolves under direct contact of infinitesimal volumes located on both of its sides. This contradicts experimental facts that a localised strain area (shear band) is of finite width. Therefore, the hypothesis that infinitesimal volumes only interact upon direct contact with their neighbouring counterparts is no longer rigorous in this context. In fact, experiments show that microstructures of geomaterials such as grain, fracture and fibre are interdependent during global deformation at a certain scale which is characterised as a material length scale parameter. Therefore, in the numerical study, a characteristic length scale is required to govern the volume size in which the microstructures manifest significant interdependency. Such a concept has been introduced in numerous theories, for instance, the peridynamics theory (Silling 2000), nonlocal damage theory (Pijaudier-Cabot & Bažant, 1987), micropolar Cosserat continuum (De Borst 1991), among which the nonlocal theory, due to its simplicity, has gained much interest recently (Galavi & Schweiger, 2010; Giry et al. 2011; Summersgill et al. 2017; Huang et al. 2018; Mánica et al. 2018).

5.3.1 Bifurcation in the classical continuum

In order to mathematically expand the above theory, the kinematics in the classical continuum mechanics is first regulated to follow the momentum and mass conservation laws written in their derivative form as:

$$\frac{\mathrm{D}\rho}{\mathrm{Dt}} = -\rho \frac{\partial \mathbf{v}}{\partial \mathbf{r}} \tag{5.1}$$

$$\frac{\mathrm{D}\mathbf{v}}{\mathrm{Dt}} = \frac{1}{\rho}\frac{\partial \boldsymbol{\sigma}}{\partial \mathbf{r}} + \mathbf{f} \tag{5.2}$$

where ρ is the material density, $\mathbf{v}$ is the velocity tensor; $\boldsymbol{\sigma}$ is the stress tensor taken negative in compression; $\mathbf{f}$ is the bulk force tensor due to external loads such as gravity.

When the continuum domain Ω is subjected to a continuous strain field with small deformation, the stress tensor in above momentum Equation (5.2) can be linked with the strain tensor through:

$$\boldsymbol{\sigma} = \mathbf{D}^{\mathrm{e}}\boldsymbol{\varepsilon} \tag{5.3}$$

where $\boldsymbol{\sigma}$ and $\boldsymbol{\varepsilon}$ are total stress and strain tensor, $\mathbf{D}^{\mathrm{e}}$ is the elastic tangent stiffness tensor. As the domain continues to deform, a discontinuous strain-jump starts to appear at the incipient loss of strain continuity, which is commonly known as the bifurcation/localisation process. As illustrated in Figure 5.1, any infinitesimal volume ($\mathbf{x}_{\mathrm{i}}$) adjacent to this discontinuous surface S is subjected to traction and displacement continuity.

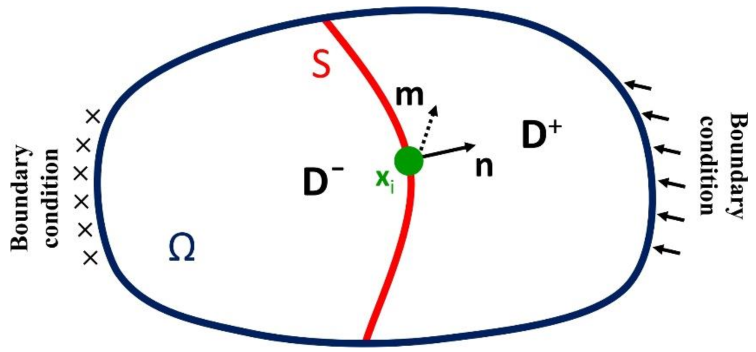

Figure 5.1: The general concept of a weak strain discontinuity (strain bifurcation/localisation).

In above, the normal vector $\mathbf{n}$ defines the direction of the traction continuity with a predefined primary direction. $\mathbf{m}$ is the polarization vector which has an angle with $\mathbf{n}$ from 0 to 90 degrees, controlling the failure mechanism from tensile to shear. $\mathbf{D}^{+}$ and $\mathbf{D}^{-}$ are the tangent stiffness tensors when approached from different sides of the discontinuous surface S. It is commonly accepted that the incipient loss of strain continuity can be distinguished by the following equation evolving from the traction continuity condition (Jirásek, 2007):

$$(\mathbf{n} \cdot \mathbf{D}^{+} \cdot \mathbf{n}) \cdot \mathbf{m}\dot{\mathrm{e}} = \mathbf{n} \cdot (\mathbf{D}^{-} - \mathbf{D}^{+}) : \dot{\boldsymbol{\varepsilon}}^{-} \tag{5.4}$$

where $\dot{\mathrm{e}}$ is a non-negative scalar denoting the magnitude of the strain jump in surface S, and $\dot{\boldsymbol{\varepsilon}}^{-}$ is the strain tensor approached from the opposite side of $\mathbf{n}$. With the assumption of a strictly isotropic and homogeneous material property ($\mathbf{D}^{+} = \mathbf{D}^{-}$), the right-hand side of Equation (5.4) vanishes, which limits the validity of the above Equation (5.4) to:

$$(\mathbf{n} \cdot \mathbf{D}^{+} \cdot \mathbf{n}) \cdot \mathbf{m} = 0 \tag{5.5}$$

which is commonly accepted as the condition to signal the onset of strain bifurcation/localisation. The parentheses on the left-hand side of Equation (5.5) contain the so-called localisation or acoustic tensor $\mathbf{Q} = \mathbf{n} \cdot \mathbf{D}^{+} \cdot \mathbf{n}$. Therefore, the above equation is equivalent to:

$$\det(\mathbf{Q}) = 0 \tag{5.6}$$

when Equation (5.5) is satisfied anywhere in the continuum, the acoustic tensor $\mathbf{Q}$ becomes singular and $\mathbf{m}$ is of zero eigenvalues. This corresponds to a loss of ellipticity of the governing differential equation under static analysis. The boundary value problems become rootless and the energy dissipation vanishes with an infinitesimal width of the discontinuous strain surface S. This issue can be attributed to the fact that there is a lack of a characteristic length in the classical continuum mechanics, which only allows a local interaction among infinitesimal volumes upon direct contact.

5.3.2 Nonlocal regularisation of the classical continuum

In order to overcome this difficulty, an integral type of strong nonlocality can be introduced to enrich the microscale description of the classical continuum (Pijaudier-Cabot & Bažant, 1987). Distinguished from directly solving kinematics equations at each infinitesimal representative volume in the classical continuum, the nonlocal theory emphasises a weighted averaging process of the representative volume over its neighbouring counterparts. This is mathematically expressed as:

$$\bar{\mathrm{f}}(\mathbf{r}) = \int_{\mathrm{V}} \mathrm{f}(\mathbf{r}') \mathrm{W}_{\infty}(\|\mathbf{r} - \mathbf{r}'\|) \mathrm{d}\mathbf{r}' \tag{5.7}$$

where $\bar{\mathrm{f}}(\mathbf{r})$ represents a nonlocal kinematics term/field variable at location $\mathbf{r}$; $\mathrm{f}(\mathbf{r}')$ is its local counterpart at surrounding location $\mathbf{r}'$ within the integral domain V; W_∞ is the weighting function solely dependent on the distance $\|\mathbf{r}-\mathbf{r}'\|$ between $\mathbf{r}$ and $\mathbf{r}'$. As the ∞ sign indicates, W_∞ is reaching the entire problem domain with its influence rapidly attenuates as $\|\mathbf{r}-\mathbf{r}'\|$ increases. This is particularly time-demanding from a computational point of view. Therefore in practice, W_∞ is truncated to only include the most relevant computational points while neglecting the far-located ones such that:

$$\mathrm{W}(\|\mathbf{r}-\mathbf{r}'\|) = \begin{cases} \mathrm{W}_\infty(\|\mathbf{r}-\mathbf{r}'\|), & \text{if } \|\mathbf{r}-\mathbf{r}'\| \le \mathrm{R} \\ 0, & \text{if } \|\mathbf{r}-\mathbf{r}'\| > \mathrm{R} \end{cases} \tag{5.8}$$

where R is a scalar value defining the radius of the effective influence area of W. In the presence of a constant field variable, the integral of W should satisfy:

$$\int_{\mathrm{V}} \mathrm{W}(\|\mathbf{r}-\mathbf{r}'\|)\,\mathrm{d}\mathbf{r}' = 1 \tag{5.9}$$

which maintains the objectivity of the computational domain. Therefore, when the radius of W approaches zero, it becomes the Dirac delta function and returns to the local analysis as in the classical continuum.

The gradient function can be approximated in a similar fashion by replacing field function with its gradient form in Equation (5.7) as:

$$\nabla\bar{\mathrm{f}}(\mathbf{r}) = \int_{\Omega} \nabla\mathrm{f}(\mathbf{r}')\mathrm{W}(\|\mathbf{r}-\mathbf{r}'\|)\mathrm{d}\mathbf{r}' \tag{5.10}$$

By applying the divergence theorem, Equation (5.10) consists of a flux term with closed surface circulating $\mathbf{r}$, and a source term regarding the gradient of the weighting function. The flux term becomes zero in a closed surface, while the source term can be written as:

$$\nabla\bar{\mathrm{f}}(\mathbf{r}) = -\int_{\Omega} \mathrm{f}(\mathbf{r}')\nabla\mathrm{W}(\|\mathbf{r}-\mathbf{r}'\|)\mathrm{d}\mathbf{r}' \tag{5.11}$$

For any continuum domain with free-surface boundary, Equation (5.7) exhibits deficiency issue due to a truncation of $\mathrm{W}(\|\mathbf{r}-\mathbf{r}'\|)$ at the vicinity of the boundary. Therefore a corrective form of Equation (5.7) is practically preferred:

$$\bar{\mathrm{f}}(\mathbf{r}) = \frac{\int_V \mathrm{f}(\mathbf{r}')\mathrm{W}_\infty(\|\mathbf{r}-\mathbf{r}'\|)\mathrm{d}\mathbf{r}'}{\int_V \mathrm{W}_\infty(\|\mathbf{r}-\mathbf{r}'\|)\mathrm{d}\mathbf{r}'} \tag{5.12}$$

Nonlocal approximation of gradient function in Equation (5.11) also manifests boundary deficiency issue which can be regularised in a similar fashion as it in Equation (5.12). the detailed formulations have been elaborated in Chapter 3.

Now the continuity and motion Equation (5.1) and (5.2) can be readily approximated by Equation (5.11) to obtain their nonlocal form. Before that, the governing Equation (5.1) and (5.2) are expressed in a more generic form to account for a vanished gradient of any constant field as follows:

$$\frac{\mathrm{D}\rho}{\mathrm{Dt}} = -\left[\frac{\partial(\rho\mathbf{v})}{\partial\mathbf{r}} - \mathbf{v}\frac{\partial\rho}{\partial\mathbf{r}}\right] \tag{5.13}$$

$$\frac{\mathrm{D}\mathbf{v}}{\mathrm{Dt}} = \frac{\partial}{\partial\mathbf{r}}\left(\frac{\boldsymbol{\sigma}}{\rho}\right) + \frac{\boldsymbol{\sigma}}{\rho^2}\frac{\partial\rho}{\partial\mathbf{r}} + \mathbf{f} \tag{5.14}$$

The nonlocal operator can then be used to approximate the above formulations to derive the commonly applied form of the nonlocal continuity and motion equations as:

$$\nabla\bar{\rho} = \frac{\mathrm{D}\rho}{\mathrm{Dt}} = \int_V \rho(\mathbf{v}-\mathbf{v}')\nabla\mathrm{W}(\|\mathbf{r}-\mathbf{r}'\|)\mathrm{d}\mathbf{r}' \tag{5.15}$$

$$\nabla\bar{\mathbf{v}} = \frac{\mathrm{D}\mathbf{v}}{\mathrm{Dt}} = \int_V \left(\frac{\boldsymbol{\sigma}}{\rho} + \frac{\boldsymbol{\sigma}'}{\rho'}\right)\nabla\mathrm{W}(\|\mathbf{r}-\mathbf{r}'\|)\mathrm{d}\mathbf{r}' + \mathbf{f} \tag{5.16}$$

The above formulations can be readily applied to the discretised computational domain for the integral type numerical methods such as Smoothed Particle Hydrodynamics (SPH) and reproduced kernel particle method (RKPM) (Bui et al. 2008a; Liu et al. 1995). Therefore these numerical methods can be regarded, more or less, as naturally possessing nonlocal features, and the effective influence radius of the weighting function W is the embedded characteristic length that governs energy dissipation rate in the existence of a discontinuous strain field, which will be demonstrated in the next part.

5.4 The nonlocal character of the SPH method

Since the SPH method is of key interest in this work, we shall now focus on its discretisation of the continuum domain with the inherent nonlocal feature. When the field variables and their gradient terms are approximated by SPH discretisation, a weighted average process is applied which can be written as follow:

$$\mathrm{f}(\mathbf{r}) = \int_{\Omega} \mathrm{f}(\mathbf{r}')\mathrm{W}(\mathbf{r}-\mathbf{r}',\mathrm{h})\mathrm{d}\mathbf{r}' \tag{5.17}$$

$$\frac{\partial \mathrm{f}(\mathbf{r})}{\partial \mathbf{r}} = \int_{\Omega} \mathrm{f}(\mathbf{r}')\frac{\partial \mathrm{W}(\mathbf{r}-\mathbf{r}',\mathrm{h})}{\partial \mathbf{r}'}\mathrm{d}\mathbf{r}' \tag{5.18}$$

Where $\mathrm{f}(\mathbf{r}_\mathrm{i})$ is the SPH approximation of the continuum field tensors. $\mathrm{W}(\mathbf{r}-\mathbf{r}',\mathrm{h})$ is the SPH kernel function determined by a location tensor $\mathbf{r}-\mathbf{r}'$ and a smoothing length h which defines the influence radius of the kernel. In numerical analysis, the above equations are formulated as particle summations as:

$$\mathrm{f}(\mathbf{r}_\mathrm{i}) \approx \sum_{\mathrm{j}=1}^{\mathrm{N}} \frac{\mathrm{m_j}}{\rho_\mathrm{j}}\mathrm{f}(\mathbf{r}_\mathrm{j})\mathrm{W}(\mathbf{r}_\mathrm{i}-\mathbf{r}_\mathrm{j},\mathrm{h}) \tag{5.19}$$

$$\frac{\partial \mathrm{f}(\mathbf{r}_\mathrm{i})}{\partial \mathbf{r}_\mathrm{i}} = \sum_{\mathrm{j}=1}^{\mathrm{N}} \frac{\mathrm{m_j}}{\rho_\mathrm{j}}\mathrm{f}(\mathbf{r}_\mathrm{j})\frac{\partial \mathrm{W}(\mathbf{r}_\mathrm{i}-\mathbf{r}_\mathrm{j},\mathrm{h})}{\partial \mathbf{r}_\mathrm{i}} \tag{5.20}$$

where N is the total number of neighbouring particles j that are located within the kernel influence radius of particle i. $\mathrm{m_j}/\rho_\mathrm{j}$ is the mass density ratio of particle j representing its occupied spatial volume. Now by introducing the following notations:

$$\mathrm{W_{ij}} = \mathrm{W}(|\mathbf{r}_\mathrm{i}-\mathbf{r}_\mathrm{j}|,\mathrm{h}) \quad \text{and} \quad \frac{\partial \mathrm{W_{ij}}}{\partial \mathbf{r}_\mathrm{i}} = \frac{\partial \mathrm{W_{ij}}}{\partial \mathbf{r}_\mathrm{i}}\frac{\partial \mathbf{r}_\mathrm{i}}{|\mathbf{r}_\mathrm{i}|} \tag{5.21}$$

the most common expressions for the SPH approximation of field variables and gradient terms can be written as:

$$\mathrm{f}(\mathbf{r}_\mathrm{i}) \approx \sum_{\mathrm{j}=1}^{\mathrm{N}} \frac{\mathrm{m_j}}{\rho_\mathrm{j}}\mathrm{f}(\mathbf{r}_\mathrm{j})\mathrm{W_{ij}} \tag{5.22}$$

$$\frac{\partial f(\mathbf{r}_i)}{\partial \mathbf{r}_i} \approx \sum_{j=1}^{N} \frac{m_j}{\rho_j} f(\mathbf{r}_j) \frac{\partial W_{ij}}{\partial \mathbf{r}_i} \tag{5.23}$$

The above SPH formulations are, in nature, the same as the nonlocal operator that has been introduced in Equation (5.7) and (5.10). This shows that the SPH method is characterised with inherent nonlocality, which is potentially capable to capture the microscale material length effect. Accordingly, the continuity and motion Equation (5.1) and (5.2) can be discretised in the SPH particle summation as follow:

$$\frac{D\rho_i}{Dt} = \sum_{j=1}^{N} m_j \left(v_i^{\alpha} - v_j^{\alpha}\right) \frac{\partial W_{ij}}{\partial r_i^{\alpha}} \tag{5.24}$$

$$\frac{Dv_i^{\alpha}}{Dt} = \sum_{j=1}^{N} m_j \left(\frac{\sigma_i^{\alpha\beta} + \sigma_j^{\alpha\beta}}{\rho_i \rho_j} + C_{ij}^{\alpha\beta} \right) \frac{\partial W_{ij}}{\partial r_i^{\beta}} + f_i^{\alpha} \tag{5.25}$$

the above SPH approximation of the mass and momentum governing equations for soil are similar to the particle approximation form of the ones described in Equation (5.15) and (5.16). By using the same weighted averaging functions (kernel functions), Equation (5.24) and (5.25) become exact particle approximation of the general nonlocal integration functions in the continuum mechanics environment. Therefore, it is clear that the SPH method is featured with nonlocal characteristic, which is able to naturally capture the bifurcation in the problem without applying special treatments that have been proposed in the FEM. Despite this fact, it has been demonstrated in the later section that the traditional SPH prediction of the plastic softening process in soil domain manifests a dependency on the selection of particle resolution (analogous to the mesh dependency issue in FEM). The reason for this phenomenon is due to the fact that the numerical resolution of the SPH method is linked to the size of the kernel supporting domain which has been acted as a characteristic length scale in the SPH domain. This means that whenever the resolution is changed, the nonlocal kernel function also changes its influence radius in order to maintain the numerical stability of the computational domain. Therefore SPH interpretation of the field kinematics is altered with different selections of the discretised resolution, demonstrating a dependency of its predictions of the stress path.

To overcome this issue, two approaches have been applied in this work with their performance compared. The first one is to conduct the SPH kernel interpolation with a fixed-size supporting domain which is independent from the selection of the numerical resolution. This approach can be straightforwardly implemented to the relation between the numerical resolution and the size of the kernel smoothing length described below:

$$\mathrm{hsml} = \xi \mathrm{dx} \tag{5.26}$$

where hsml is the kernel smoothing length and dx is the initial inter-particle distance (the numerical resolution) in the SPH domain when uniformly discretised. Coefficient ξ is normally predefined and kept in constant value (typically around 1.25) during the numerical simulation. In the first approach, hsml is defined as a characteristic length parameter which features constant value in a particular problem context, and the coefficient ξ is calculated accordingly. As the kernel interpolation is applied throughout SPH, this approach guarantees a consistent prediction of the field kinematics including the material behaviour during both elastic and plastic stage. In order to validate this concept, a numerical simulation of a biaxial test is conducted in the following section with different discretised resolution and a fixed size of the kernel supporting domain. The obtained results show an optimum agreement among various discretisation resolutions. However, Equation (5.26) underlies the stability of the computational domain. This approach is limited to a small range of material length parameter and selection of the numerical resolution. Apart from this, as the numerical domain enters large deformation stage, particle pairing issue (described in Chapter 3) becomes more violent and compromises the numerical stability.

In the second approach, an additional nonlocal operating function is incorporated into the current SPH framework to regularise the energy dissipation process as the material reaches the plastic stage. This facilitates the numerical simulation to achieve a converging stress path for the post-peak section of the stress-strain relation in the sample. The nonlocal operating function is defined similarly as the SPH kernel which features an effective influence radius and interpolates the unknow field variables by weighted averaging over their neighbouring counterparts. The nonlocal operator for interpolating field variable $\mathrm{f}(\mathbf{r})$ is implemented in its normalised form as described in Equation (5.12), and a bilinear function is applied in this work which is illustrated in Figure 5.2 and written as:

$$\alpha(\|\mathbf{r}-\mathbf{r}'\|) = \begin{cases} \exp\left(-\dfrac{\|\mathbf{r}-\mathbf{r}'\|}{\mathrm{l_c}}\right), & \text{if } \|\mathbf{r}-\mathbf{r}'\| \le \mathrm{R_c} \\ 0, & \text{if } \|\mathbf{r}-\mathbf{r}'\| > \mathrm{R_c} \end{cases} \tag{5.27}$$

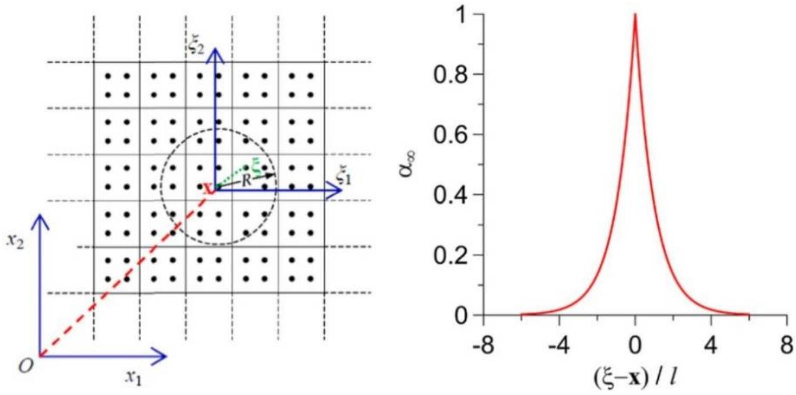

Figure 5.2: Illustration of the bilinear nonlocal function and its effective supporting domain (Huang et al., 2018).

in Equation (5.27), l_c is the material characteristic length parameter. R_c is the influence radius of the bilinear weighting function, which is related to l_c as $R_c = 6l_c$ for omitting the minor contribution from far-located particles and improving the overall computational efficiency.

In this work, the field variable regularised by the above nonlocal operator is the total equivalent plastic strain. The definition and corresponding formulations of the total equivalent plastic strain have been elaborated in Chapter 3, referring to Equation (3.81) and (3.82). As suggested in the literature, a linear relation that combines the original and nonlocal counterparts of the total equivalent plastic strain is further applied to facilitate a full energy regularisation in SPH as (Vermeer & Brinkgreve, 1994; Di Luzio & Bažant, 2005):

$$\hat{\varepsilon}_p^{eq} = \xi\, \bar{\varepsilon}_p^{eq} + (1 - \xi)\, \varepsilon_p^{eq} \tag{5.28}$$

where ξ is a scalar ranged from zero to a certain positive value. As suggested by Vermeer and Bažant (Vermeer & Brinkgreve, 1994; Bažant & Jirásek, 2002), $\xi = 2$ gives the best-converged solution, which is also applied throughout our model. The term $\hat{\varepsilon}_p^{eq}$ in Equation (5.28) is eventually applied in Equation (3.79) and (3.80) to control the evolution of the Mohr-Coulomb yield surface which can be explicitly written as:

$$\phi = \phi_{res} + \left(\phi_{peak} - \phi_{res}\right) e^{-\eta \hat{\varepsilon}_p^{eq}} \tag{5.29}$$

$$c = c_{res} + \left(c_{peak} - c_{res}\right) e^{-\eta \hat{\varepsilon}_p^{eq}} \tag{5.30}$$

The above nonlocal operator, as demonstrated in later sections, is able to remove the resolution dependency in the SPH domain by maintaining an objective material length scale while preserving a very good numerical stability and reasonable computational efficiency compared to the first approach as presented above.

5.5 Numerical simulations

In order to further investigate the local and nonlocal features that SPH method demonstrates, numerical simulations of biaxial tests are conducted in this section. A wide spectrum of particle resolutions of the computational domain has been considered for three groups of biaxial tests with: first, the traditional SPH; second, the application of a fixed kernel supporting domain in SPH; third, the application of a nonlocal operating formulation in SPH. As demonstrated with superior performance, the SPH framework with the nonlocal operator is then applied to analyse the initiation and development of the bifurcation and localisation of the strain field in the numerical domain considering the heterogeneity in soil materials. The evolution of the second-order work and the acoustic tensor are tracked to identify the initiation condition for a bifurcation process, which is also compared with the deviatoric strain plot in the sample.

5.5.1 Regularised SPH for shear band prediction in biaxial test

In this part, three groups of biaxial tests are conducted for demonstrating the energy regularisation in SPH methods. The comparison is made among: the conventional SPH method without considering any regularisation; the conventional SPH with energy regularisation through its embedded kernel; the SPH incorporated with a nonlocal operator. A rectangular-shaped specimen, containing sandy material, is applied here with the height of 0.12m and width 0.08m modelled under plane strain condition (Figure 5.3a). Five different initial inter-particle distances (resolutions) are selected here to conduct the tests as $\mathrm{dx} = 2\mathrm{mm}$, $\mathrm{dx} = 3\mathrm{mm}$, $\mathrm{dx} = 4\mathrm{mm}$, $\mathrm{dx} = 5\mathrm{mm}$ and $\mathrm{dx} = 6\mathrm{mm}$. This corresponds to SPH domains with 2800, 1350, 800, 544 and 390 particles (including the boundary particles) respectively. The bottom of the specimen is fixed in place, while a velocity field with constant $1\,\mathrm{mm/sec}$ downwards and $0\,\mathrm{mm/sec}$ horizontal components are prescribed to the top boundary replicating a non-slip condition. The material properties and other numerical parameters are listed in Table 5.1.

In Figure 5.3b, a scheme which utilises an extra layer of dummy particles that help to interpolate state variables at an exact location within the sample is illustrated. The dummy particles are created at a prescribed location in the computational domain and only used when interpolating kinematics states such as stress, strain etc. This technique allows the measurement of all field kinematic/mechanical variables that are carried by SPH particles at a prescribed location without being affected by the variation of numerical resolution. The detailed formulations are similar to those presented in Chapter 3.4.3, therefore they will not be repeated here.

Table 5.1: The material and model parameter for the biaxial compression test.

Young's modulus	E	10 MPa
Poisson's ratio	ν	0.2
Peak friction angle	ϕ_{peak}	25
Residual friction angle	ϕ_{res}	15°
Dilatant angle	ψ	0°
Soil density	ρ	$2000\,\mathrm{kg/m^3}$
Softening parameter	η	8
Confining stress	σ_c	50 kPa

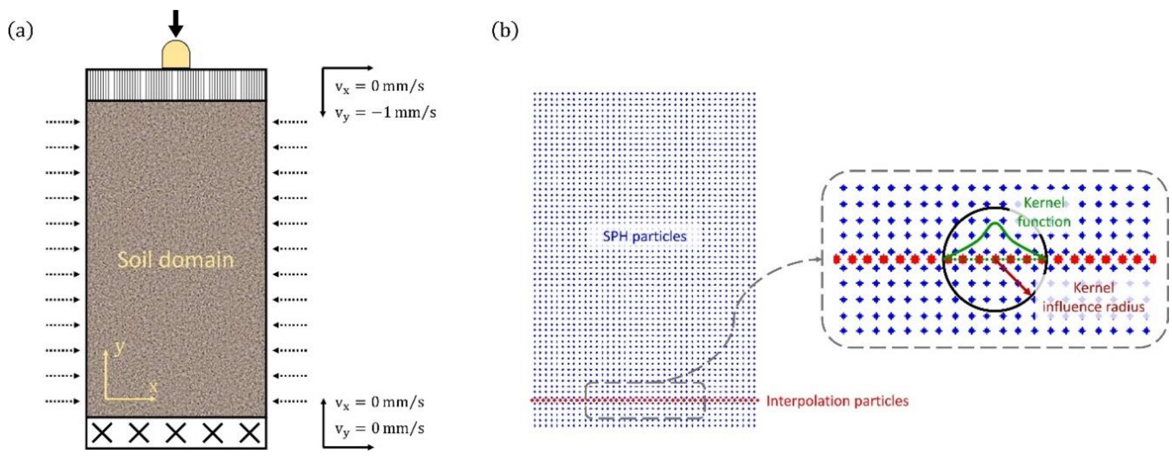

Figure 5.3: (a) the biaxial compression test setup; (b) illustration of measuring SPH field variables with interpolation particles.

Traditional SPH method

The traditional SPH method is applied here to predict the above biaxial tests. The obtained relationships between the deviatoric stress $(\sigma_y - \sigma_x)$ and the axial strain ε_y are plotted in Figure 5.4 for all numerical resolutions. As illustrated in the plot, all samples start from an equivalent condition with uniform confining stress of 50 kPa, as the boundary condition continuously imposes, the sample responses with an elastic behaviour until it reaches the peak strength at around 0.75% axial strain. The plastic yield surface is reached by the stress state, and plastic strain tensors start to develop. Accordingly, the friction angle is reduced according to Equation (5.29) and the sample demonstrates a softening behaviour as the increasing axial strain is companied by reducing deviatoric stress component. This softening process continues until the material reaches its ultimate or residual strength as listed in Table 5.1. As it is elaborated in the preceding sections for the theoretical background of the potential resolution dependency in the traditional SPH, the results illustrated in Figure 5.4 certainly validate this concept as the material softening behaviour is significantly governing by the selection of the numerical resolution. A finer discretisation scheme leads to a more brittle material response with a faster plastic energy dissipation rate (curve corresponds to dx=2mm), while a coarser discretisation scheme demonstrates ductile and slower energy dissipation rate. Apart from this, it is noted here that the difference between the predicted elastic stiffness among the various resolutions is also partially attributed to the resolution dependency issue in the traditional SPH. This can be explained by the results in the later section where a fixed SPH kernel domain is used, which shows an exact prediction of the elastic stiffness with various numerical resolutions. Similarly the results in Figure 5.12 show an exact prediction of the elastic stiffness of the material as the same resolution of dx = 2mm is applied. This also demonstrates that a different numerical resolution could potentially influence the measurement of the elastic stiffness in a traditional SPH domain.

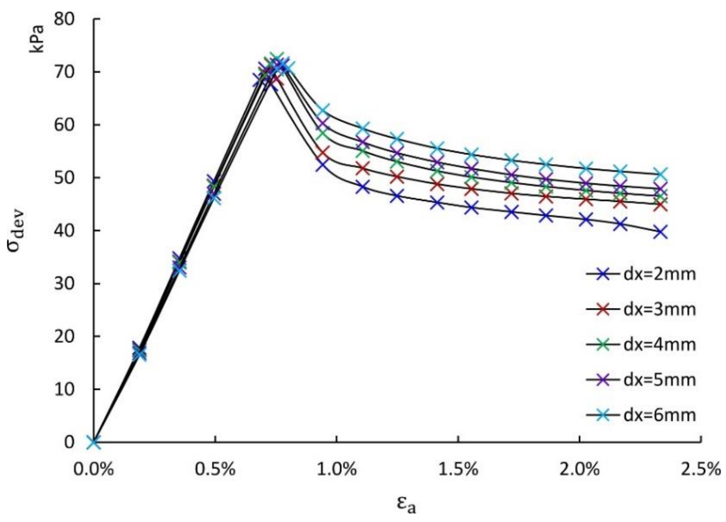

Figure 5.4: The deviatoric stress versus axial strain plot from traditional SPH prediction of biaxial tests under various discretised resolutions.

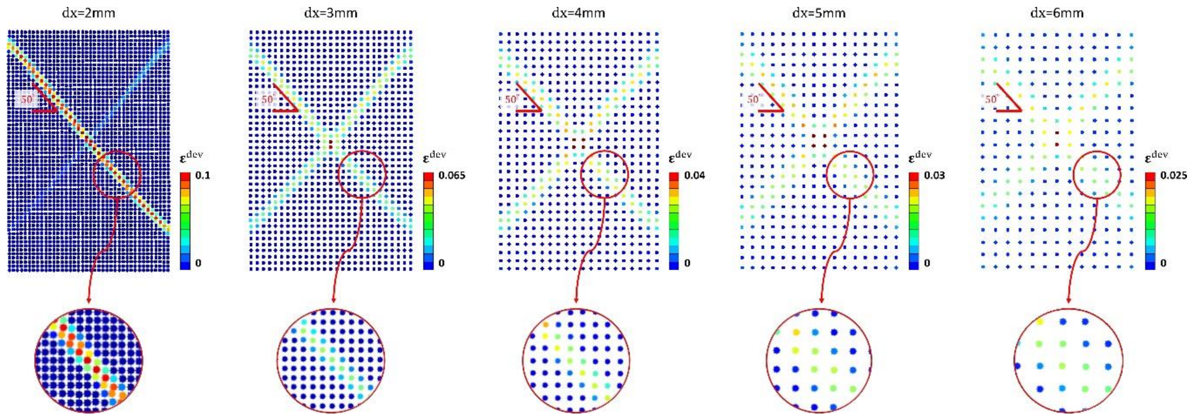

Figure 5.5: The contour of the deviatoric strain field from traditional SPH prediction of biaxial tests under various discretised resolutions.

Figure 5.5 shows the contour of the deviatoric (shear) strain field in the SPH domains when the materials just pass their peak strength. The plot clearly shows a dependency of the thickness of the area with intensive development of the shear strain (shear band) on the domain resolution. The finer resolution shows thinner shear bands while the coarser resolution shows thicker shear bands. As the resolution refines, the symmetry of the shear bands alters, showing more concentration in one shear band than the other (Figure 5.5). All shear bands in different samples feature a similar number of particles along their width, or specifically around three particles. This is closely related to the size of the kernel supporting domain with an effective radius of $2 \times \text{hsml}$, which governs the number of particles that are directly interacting in each kernel interpolation. The effective horizontal crossectional area in the sample also differs as the margin along sample edges becomes larger as the resolution increases. On the other hand, the inclination angle of the shear bands does not seem to be significantly influenced, with all results demonstrating an angle around 47 degrees.

<u>SPH with fixed kernel domain</u>

As the nonlocal feature in SPH is governed by the kernel function, its influence radius controls the energy evolution in the sample. Therefore, the above resolution-dependent pathology can be straightforwardly addressed through decoupling the relation between kernel influence radius and numerical discretisation size. A fixed kernel influence radius can be applied for all tests with various numerical resolutions, where the energy dissipation rates are consistent. In this section, a kernel influence radius of 5 mm is considered. Three resolutions are selected namely: $\text{dx} = 2\text{mm}$, $\text{dx} = 3\text{mm}$ and $\text{dx} = 4\text{mm}$. Accordingly, the coefficient in Equation (5.26) is calculated for each case and the corresponding smoothing length can be written as: $\text{hsml} =$

$2.5\mathrm{dx}$, $\mathrm{hsml} = 1.667\mathrm{dx}$ and $\mathrm{hsml} = 1.25\mathrm{dx}$. The obtained deviatoric stress and axial strain relationships and the contour plot for the deviatoric strain field are shown in Figure 5.6 and 5.7.

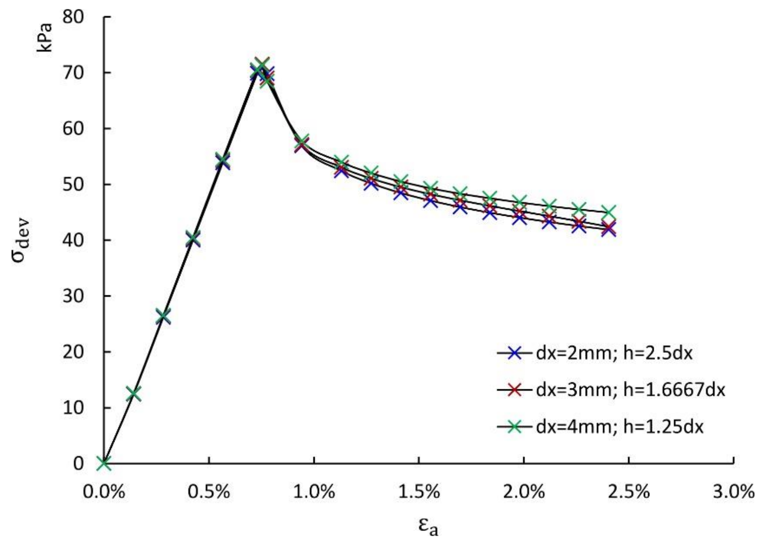

Figure 5.6: The deviatoric stress versus axial strain plot from biaxial tests under various discretised resolutions predicted by SPH with a fixed kernel domain.

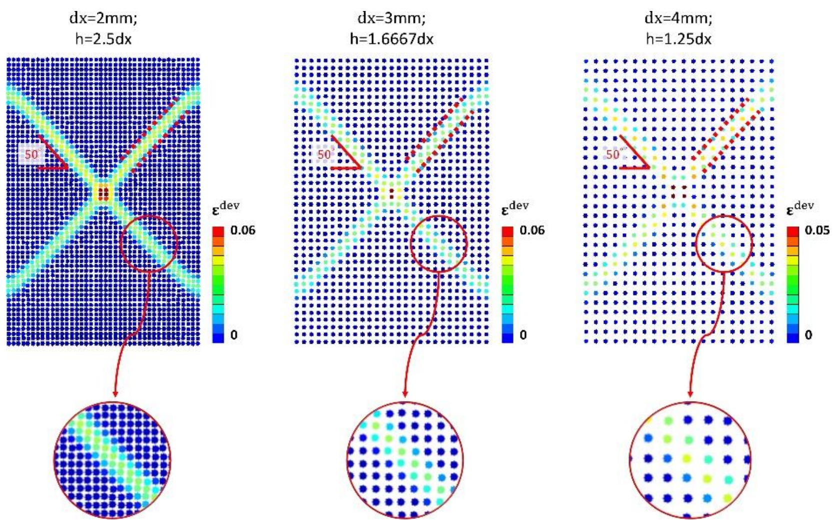

Figure 5.7: The contour of the deviatoric strain field from biaxial tests under various discretised resolutions predicted by SPH with a fixed kernel domain.

In Figure 5.6, the material responses to boundary conditions demonstrated by the deviatoric stress and axial strain relationship are nearly identical during the elastic range among tests with various resolutions. As to the post-peak behaviour, the samples demonstrate a very close plastic energy dissipation rate within 0.1% axial strain after the peak stress point. Then the stress path starts to deviate among different resolutions. Figure 5.7 shows a near-identical width and inclination angle of the shear bands in various samples. The shear bands in fine resolution samples include more particles in their cross-sectional area, and coarse resolutions samples show fewer particles in the shear bands crossectional area. The above results demonstrate that a fixed kernel influence domain in SPH is able to totally regularise the energy dissipation before a certain deformation is reached. Therefore, the smoothing length (hsml) can potentially perform as a characteristic length for the numerical domain. However, as the deformation continues during the tests, numerical instability and particle pairing issue start to develop in the SPH domain, and the curves in Figure 5.6 deviate from each other from 0.9% axial strain. The mechanism of this phenomenon has been explained in preceding sections, which is rooted in SPH kernels with second-order continuity. Apart from this, the attempt to apply either a finer resolution such as $\mathrm{dx} = 1\mathrm{mm}$ or a coarser resolution $\mathrm{dx} = 5\mathrm{mm}$ in this work would lead to a significant compromisation of the numerical stability, compromising the validity of the captured strain localisation. This is due to the fact that the SPH kernel is only able to maintain reasonable computational stability for including a certain number of particles in its interpolation process. Including either more or fewer particles that are outside of this stable range in the SPH kernel would lead to unsatisfactory numerical performance. Therefore, as a conclusion, the inherent kernel function in SPH can be decoupled with the numerical discretisation to facilitate regularising energy dissipation during plastic deformation. However, this approach is only applicable for a limited range of particles that the SPH kernel is able to contain and under small deformation condition for achieving an acceptable level of numerical stability. Therefore, it cannot be applied as a generic approach to regularise the plastic energy dissipation in traditional SPH domain for a wide range of geomechanical problems. In the next section, the application of a nonlocal operating function in SPH is introduced to further address this issue.

SPH with a nonlocal operator

As demonstrated above, a fixed kernel influence radius is able to regularise the energy dissipation in SPH domain as the peak stress is reached and maintain an objective prediction of the stress path for a short period (0.1% after peak stress). When the material softening continues, the energy dissipation diverges and the domain fails to maintain an objective energy dissipation path. To overcome this, in the current section, a nonlocal operator is incorporated into the strain-softening constitutive model in SPH to regulate the evolution of the equivalent plastic strain as described in Equation (5.12) and (5.28). This operator is calculated based on the bilinear function in Equation (5.27) featured with a distinct supporting domain as compared to the SPH kernel. Therefore, a separate searching and pairing process is conducted to identify particle relations for the nonlocal operator function. The biaxial tests conducted in this section have the same setup as in preceding sections. Two different characteristic lengths in the bilinear function namely $l_c = 3\text{mm}$ and $l_c = 5\text{mm}$ are first applied in the biaxial tests. The corresponding relations between deviatoric stress and axial strain are illustrated in Figure 5.8 and 5.9 below.

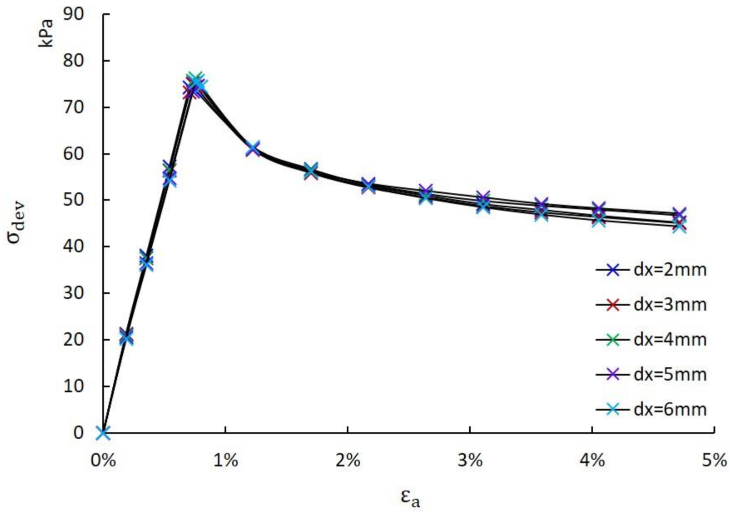

Figure 5.8: The deviatoric stress versus axial strain plot from biaxial tests under various discretised resolutions predicted by SPH with a nonlocal operator and $l_c = 3\text{mm}$.

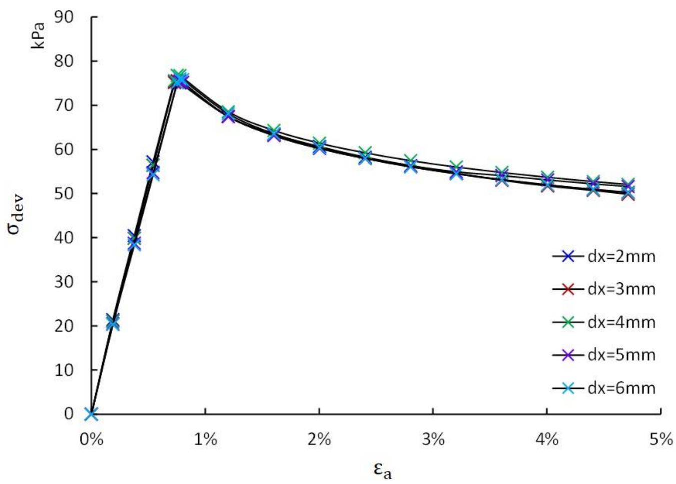

Figure 5.9: The deviatoric stress versus axial strain plot from biaxial tests under various discretised resolutions predicted by SPH with a nonlocal operator and $l_c = 5\text{mm}$.

In both Figure 5.8 and 5.9, the samples start from an equivalent state under 50 kPa confining stress. As the deviatoric load is applied, the samples respond with elastic behaviour until the peak shear stress of 78 kPa is reached at 0.8 axial strain. The peak stress is then followed by a reduction in material strength shown as the softening of the deviatoric stress. In these tests, SPH samples with various resolutions demonstrate very good agreement in predicting the plastic energy dissipation rate until the residual material strength is reached. The deviatoric stress versus axial strain curve among different numerical resolutions follow a very similar path for $l_c = 3\text{mm}$ and $l_c = 5\text{mm}$ respectively. For tests with $l_c = 3\text{mm}$, the plastic energy dissipation rate is faster, shown as a more rapid softening process and reduction of the material strength. On the other hand, tests with $l_c = 5\text{mm}$ feature a slower energy dissipation rate with a more ductile material response. During the material softening process, the SPH domains maintain very good stability shown as smooth softening curves (Figure 5.8 and 5.9) as the traditional hsml=1.25dx relation is applied for the kernel interpolation. Therefore, the nonlocal operator function demonstrates its advantage in both regularising the energy dissipation rate and facilitate maintaining very good computational stability. Apart from the stress path presented above, the shear strain contour is also illustrated in Figure 5.10 and 5.11 below.

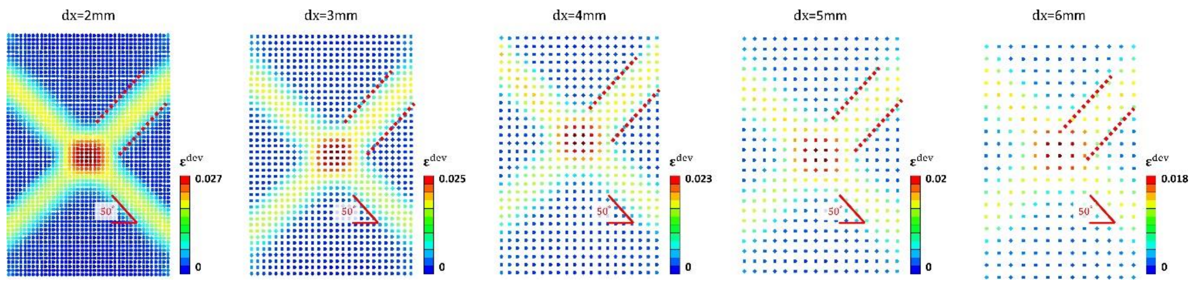

Figure 5.10: The contour of the deviatoric strain field from biaxial tests under various discretised resolutions predicted by SPH with a nonlocal operator and $l_c = 3\text{mm}$.

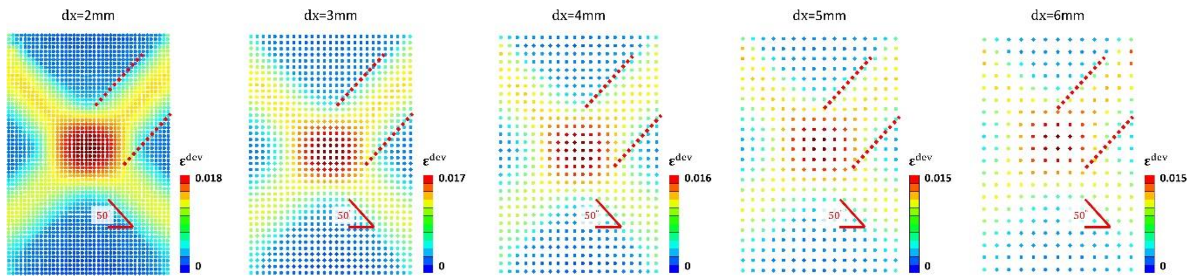

Figure 5.11: The contour of the deviatoric strain field from biaxial tests under various discretised resolutions predicted by SPH with a nonlocal operator and $l_c = 5\text{mm}$.

The deviatoric strain field in Figure 5.10 and 5.11 shows a concentration pattern with the X-shaped bands, which demonstrates very similar thickness among the various resolutions applied. The results indicate a well-regularised plastic strain evolution, showing the good capability of the applied nonlocal operator. The predicted shear bands above have larger width compared with those obtained from SPH with a fixed kernel domain, which is due to the distinct supporting domain between the bilinear function and SPH kernels. The width of the shear bands is closely related to R_c in Equation (5.27) as it defines an effective interaction between particles for the nonlocal operator. The biaxial tests with $l_c = 5\text{mm}$ predict thicker shear bands compared to those in test with $l_c = 3\text{mm}$, which is understandable as l_c controls the size of the supporting domain of the nonlocal function. The effect of the characteristic length parameter l_c and its influence on the prediction of the shear bands are discussed in the next section. Apart from this, the inclination angles of the shear bands maintain a consistent value of 47° for each test group with different resolutions, as well as among tests with different l_c values.

The influence of the selection of l_c on the predicted shear band configuration and shear stress versus axial strain relationships are examined in this section. The same biaxial setup has been applied considering a numerical discretisation size of $dx = 2\text{mm}$, which corresponds to 2800 SPH particles. Five different l_c values are selected including: $l_c = 0.5\text{mm}$, $l_c = 1\text{mm}$, $l_c = 2\text{mm}$, $l_c = 3\text{mm}$ and $l_c = 5\text{mm}$. The deviatoric stress versus axial strain curves are first illustrated in Figure 5.12.

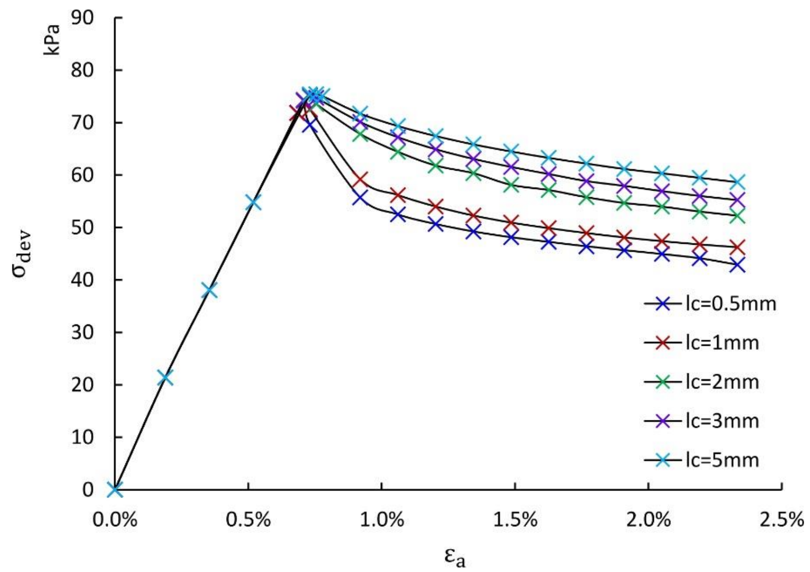

Figure 5.12: The deviatoric stress versus axial strain plot from biaxial tests under various length scale parameter l_c.

All tests initially yield the same elastic stiffness as the same numerical resolution is applied here. As the loading continues, the test samples reach their peak strength of 75 kPa at 0.75%

axial strain and enter the softening stage thereafter. The length parameter l_c demonstrates a significant influence on predicting the plastic energy dissipation rate. Small l_c shows fast dissipation and strength softening which corresponds to a brittle material behaviour, while larger l_c values show a slow energy dissipation and ductile material behaviour. This indicates that the length parameter l_c can be regarded in the numerical simulations as a characteristic length scale which could represent a certain range of material properties under specified boundary conditions. The l_c parameter can be calibrated to represent a particular material that is featured with a certain plastic energy dissipation rate. Therefore, this proposed SPH framework provides a basis for potentially linking the material characteristic scale to the numerical length parameter and allowing a physically meaningful numerical result to be predicted. Apart from this, the contour plot for the deviatoric strain is illustrated in Figure 5.13 for demonstrating the effect of various l_c values applied.

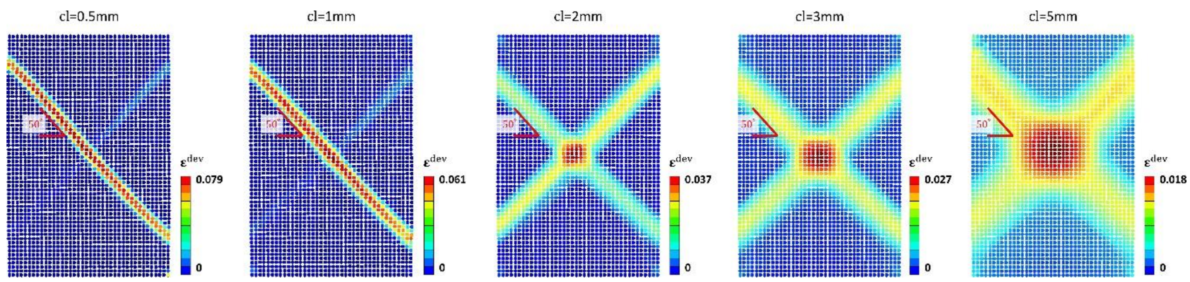

Figure 5.13: The contour of the deviatoric strain field from biaxial tests under various length scale parameter l_c.

Figure 5.13 illustrates the contour of the shear strain field in the SPH samples with various l_c values. It is clear that the l_c value dominates the width of the predicted shear bands. A smaller value of l_c corresponds to a thinner shear band width which leads to a more brittle material response. When increasing the l_c value, the numerical results of deviatoric strain field show a wider shear band thickness with a more ductile material response. This is consistent with the obtained relation between the deviatoric stress and the axial strain as demonstrated in Figure 5.12. Apart from this, it has been reported in the literature that the selection of l_c should not be smaller than the minimum size of the discretisation mesh when a FEM simulation is conducted, which will not be able to capture the shear band formation and development (Mánica et al., 2018). Nevertheless, is has been demonstrated in Figure 5.13 that with a SPH discretisation of $dx = 2mm$, the nonlocal operator can still capture the entire localisation of the deviatoric strain field even with a l_c value as small as 0.5mm. This can be attributed to the inherent nonlocal feature of SPH as it facilitates a natural prediction of the bifurcation and localisation phenomenon in the numerical domain. The above results demonstrate the advantage of applying SPH method to predict the localisation and large deformation plasticity problem in soils, which is advanced by applying a nonlocal operator showing very well-regularised plastic energy dissipation path. In the next section, the strain localisation condition and the evolution of shear bands are analysed using the above proposed SPH computational framework.

5.5.2 SPH modelling of the localised deformation in soil

In order to further investigate the evolution of the strain field in SPH domain under the plastic deformation and capture the localised shear bands, the proposed SPH framework is applied to simulate a group of biaxial tests in this section. The biaxial test setup is similar to the one applied in section 5.5.1. A loose sandy material is considered for the tests which are subjected to a confining pressure of 50 kPa. To account for the heterogeneity nature of sand, a randomly distributed porosity (through applying randomness to Young's modulus) and strength parameters are considered. The random parameter is generated using a bell-shaped Weibull distribution function. The key parameters that describe the mean value and skewness of the Weibull function are c_1 and c_2 as shown in Equation (5.31). The corresponding random state variable is calculated in Equation (5.32):

$$\zeta = \frac{c_1}{c_2}\left(\frac{r_d}{c_2}\right)^{c_1-1} \exp\left[-\left(\frac{r_d}{c_2}\right)^{c_1}\right] \tag{5.31}$$

$$\mathrm{Var} = \mathrm{Var}(1 - c_3\zeta) \tag{5.32}$$

where ζ is the Weibull parameter, $0 < r_d < 1$ is a pseudorandom number generated by Fortran built-in function "random_number", Var is any state variable that features heterogeneity and c_3 controls the degree of randomness. In this work, Var consists of both Young's modulus E and the effective friction angle ϕ. An illustration is shown in Figure 5.14 to show the plot of the random field in a biaxial test sample.

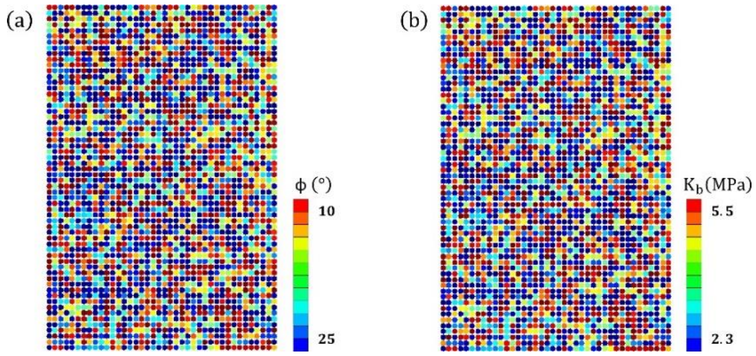

Figure 5.14: The heterogeneity in the (a) material bulk modulus and friction (b) angle generated by applying a Weibull distributive function.

In parallel with this, the incipient point of the bifurcation, and therefore the localisation of the deviatoric strain has been captured as well as interpreted based on two theories namely the strain localisation tensor (acoustic tensor) and the second-order work. Both of these approaches have been theoretically proposed for indicating a necessary condition for strain localisation to occur (Nicot et al., 2007; Nguyen et al., 2016). The acoustic tensor defines the incipient point of a bifurcation as the determinant of the tensor becomes zero or negative (in elastoplasticity theory) (Nguyen et al., 2016). The second-order work signals the bifurcation as a process of the vanishing of the total second-order work both globally in the sample and locally where the localisation occurs. In order to implement these two conditions in the SPH method, the acoustic tensor can be written similar to that in Equation (5.3) as in Equation (5.33) and the condition for the onset of the bifurcation point is expressed for an elastoplastic material as in Equation (5.34):

$$\mathbf{Q} = \mathbf{n}\mathbf{D}^{\mathrm{ep}}\mathbf{n} \tag{5.33}$$

$$\det(\mathbf{Q}) \leq 0 \tag{5.34}$$

In Equation (5.33), $\mathbf{n}$ is the normal vector along the discontinuous strain surface. $\mathbf{D}^{\mathrm{ep}}$ is the elastoplastic tangent stiffness matrix that coincides with the elastic stiffness matrix for elastic material behaviours. The normal vector $\mathbf{n}$ can be written for three-dimensional space as:

$$\mathbf{n} = \begin{bmatrix} n_x & 0 & 0 \\ 0 & n_y & 0 \\ 0 & 0 & n_z \\ n_y & n_x & 0 \\ 0 & n_z & n_y \\ n_z & 0 & n_x \end{bmatrix} \tag{5.35}$$

In this application, the **n** vector is calculated in the plane strain condition. Therefore, its expression for the plane is simplified from Equation (5.35) as follows:

$$\mathbf{n} = \begin{bmatrix} n_x & 0 \\ 0 & n_y \\ 0 & 0 \\ n_y & n_x \end{bmatrix} \tag{5.36}$$

The components n_x, n_y and n_z can be explicitly expressed following the work of Nguyen et al (2016) as:

$$\begin{bmatrix} n_x \\ n_y \\ n_z \end{bmatrix} = \begin{bmatrix} \sin\phi \cdot \cos\theta \\ \sin\phi \cdot \sin\theta \\ \cos\phi \end{bmatrix} \tag{5.37}$$

where the angles are defined in the spherical coordinate system. ϕ is the zenith angle that extends from z-axis and has the range $0 \leq \phi \leq \pi$. θ is the azimuthal angle from x-axis in the xy-plane with the range $0 \leq \theta \leq 2\pi$. In a plane strain condition, the angle $\phi = 90^{\circ}$. Therefore, to identify the potential plane of the weak discontinuity (shear band), the angle θ is searched over its range of 2π in the computational process to check if the elastoplastic tangent stiffness matrix satisfies Equation (5.33).

To close the formulation of the acoustic tensor, the elastoplastic tangent stiffness matrix $\mathbf{D}^{ep}$ can be explicitly defined as:

$$\mathbf{D}^{ep} = \mathbf{D}^{e} - \frac{\mathbf{D}^{e} \frac{\partial f}{\partial \sigma} \otimes \frac{\partial g}{\partial \sigma} \mathbf{D}^{e}}{\frac{\partial f}{\partial \sigma} \mathbf{D}^{e} \frac{\partial g}{\partial \sigma} - H} \tag{5.38}$$

where $\mathbf{D}^{e}$ is the elastic tangent stiffness matrix, and Equation (5.38) becomes $\mathbf{D}^{ep} = \mathbf{D}^{e}$ when the computational domain demonstrates elastic behaviour. H above corresponds to the hardening/softening derivatives which can be explicitly expressed in this work as:

$$H = \frac{\partial f}{\partial \phi} \frac{\partial \phi}{\partial \varepsilon_p^{eq}} \mathrm{val} + \frac{\partial f}{\partial c} \frac{\partial c}{\partial \varepsilon_p^{eq}} \mathrm{val} \tag{5.39}$$

This equation is, in fact, similar to the second half of the denominator of the plastic multiplier of the general elastoplastic softening model as described in Equation (3.89).

Now the parameters applied for each test sample in the groups of the parametric study are listed in Table 5.2. The evolutions of the deviatoric strain in the sample are first illustrated for random parameter $c_3 = 0.1$ and $c_3 = 0.3$ in Figure 5.15 and 5.16 respectively. The corresponding evolution of the acoustic tensor for each test is plotted in Figure 5.17 and 5.18.

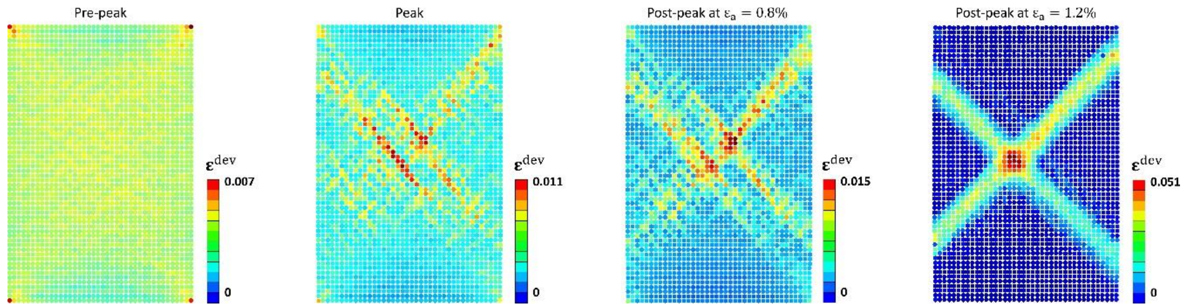

Figure 5.15: The contour plot for the deviatoric strain in SPH predicted biaxial test on sandy material with $c_3 = 0.1$ randomness.

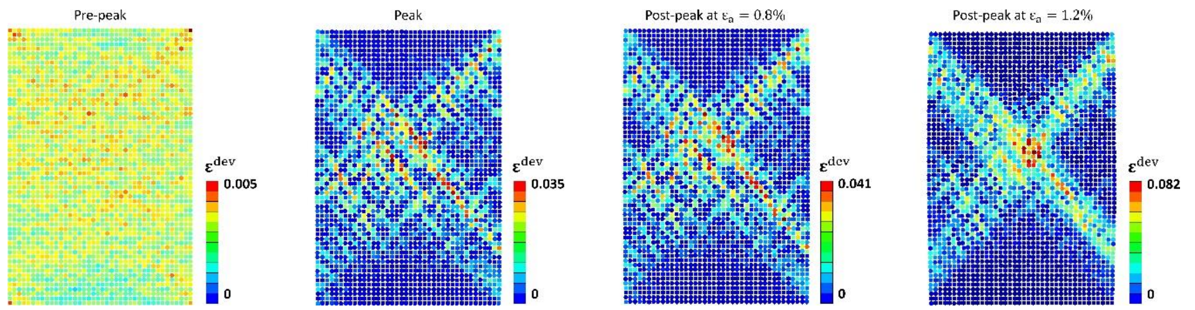

Figure 5.16: The contour plot for the deviatoric strain in SPH predicted biaxial test on sandy material with $c_3 = 0.3$ randomness.

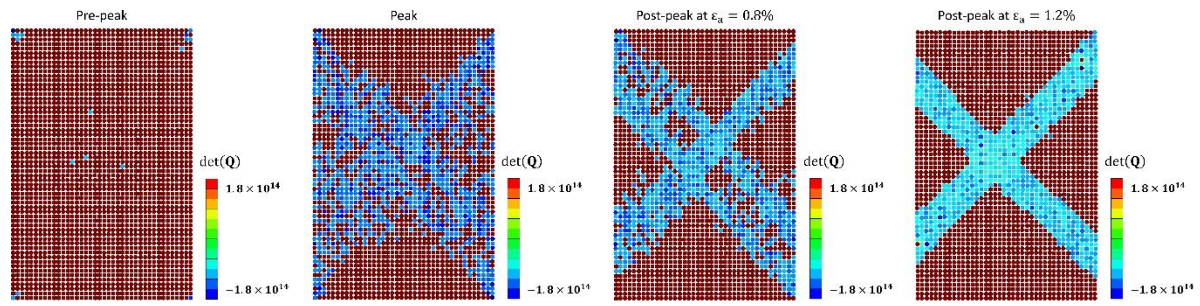

Figure 5.17: The plot for the evolution of the acoustic tensor in SPH predicted biaxial test on sandy material with $c_3 = 0.1$ randomness.

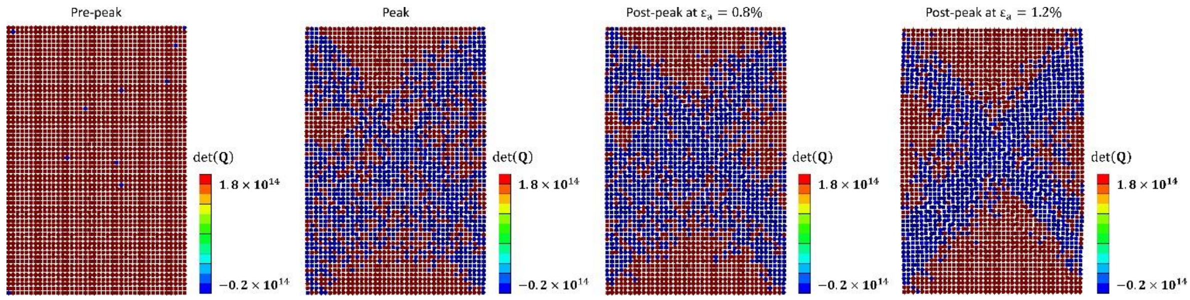

Figure 5.18: The plot for the evolution of the acoustic tensor in SPH predicted biaxial test on sandy material with $c_3 = 0.3$ randomness.

As shown in Figure 5.15 and 5.16, the deviatoric strain starts to show a localised pattern over the sample at the pre-peak point, which corresponds to the deviatoric stress state before its peak value. Depending on the degree of the randomness, the deviatoric strain localisation is less spread in the sample with $c_3 = 0.1$, while showing a more smeared distribution when $c_3 = 0.3$ is applied. As the axial load continues, the distributive pattern of the deviatoric strain localisation starts to converge, with some area demonstrating unloading and vanishing of the localised strain and other areas with a X-shaped configuration for the continuously localising shear bands. Once the post-peak state for the deviatoric stress state is reached, a clear localisation of the deviatoric strain field is observed for both results in Figure 5.15 and 5.16. It shows a non-symmetric configuration compared to the ones demonstrated for a homogenous material in Figure 5.10, which is due to the inclusion of the material heterogeneity. In parallel with this, the evolution of the acoustic tensor which indicates the incipient point of the localisation is also tracked for both tests with $c_3 = 0.1$ and $c_3 = 0.3$. The illustrations are presented in Figure 5.17 and 5.18. The determinant of the acoustic tensor $\det(\mathbf{Q})$ initially shows a positive value across the sample. As the pre-peak point is approached as the axial load continues, the $\det(\mathbf{Q})$become negative for particles that are corresponding to the localised deviatoric strain as shown in Figure 5.15 and 5.16. This agrees well with the theoretical interpretation of the onset of the bifurcation in Equation (5.34). At the peak deviatoric stress state, the negative value of the $\det(\mathbf{Q})$ becomes smeared in the sample indicating a potential development of the shear band, which is similar to the localised deviatoric strain field. When the stress state in the samples enter the post-peak range, the negative values of $\det(\mathbf{Q})$ coincides with the observed shear bands as shown in Figure 5.15 and 5.16, which demonstrates a localised pattern. The above process is also captured by the second-order work evolution in the sample, shown in Figure 5.19 and 5.20 below.

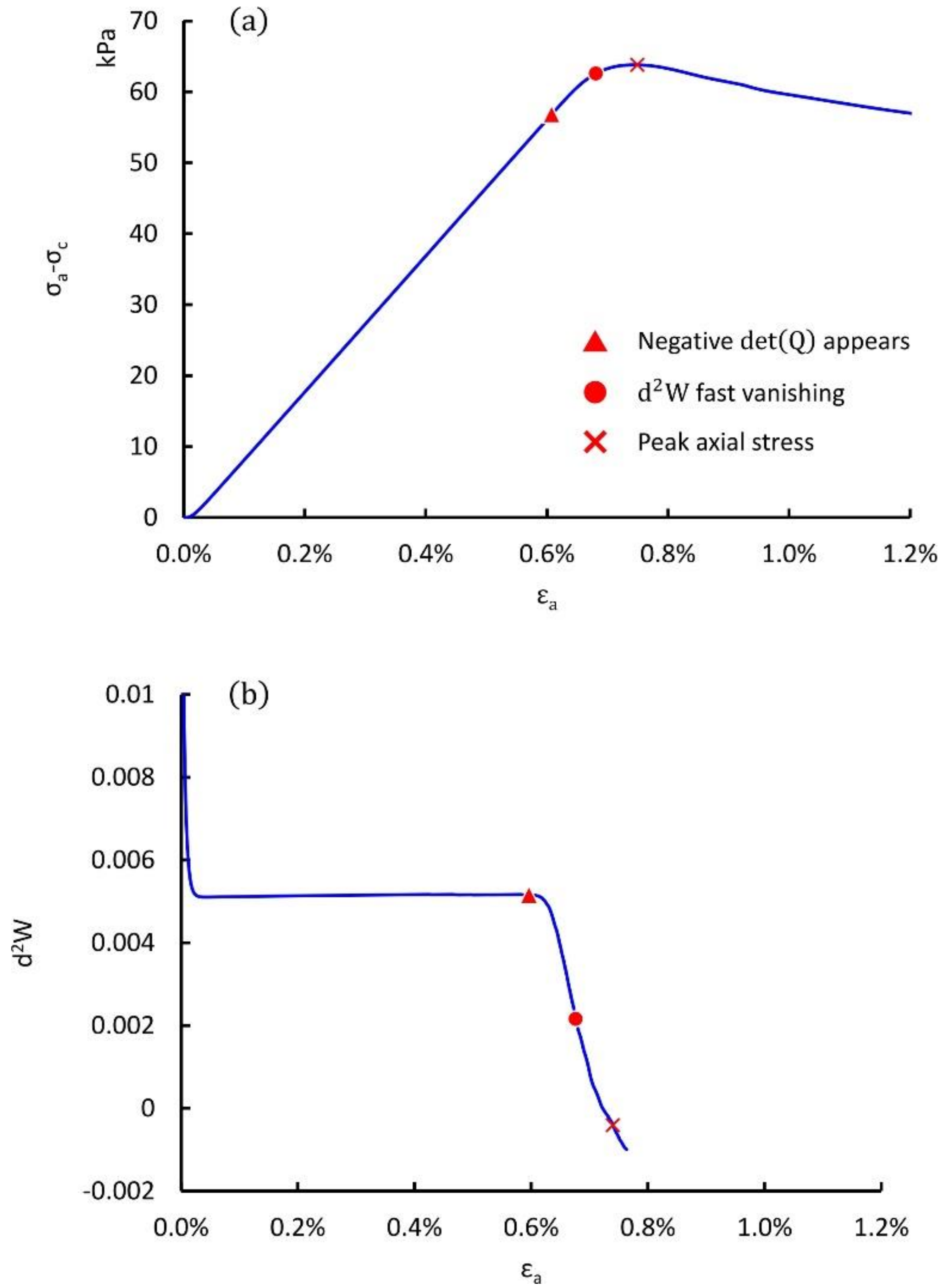

Figure 5.19: The SPH predicted biaxial test on sandy material with $c_3 = 0.1$ randomness: (a) the deviatoric stress versus axial strain plot; (b) the evolution of the second-order work with axial strain.

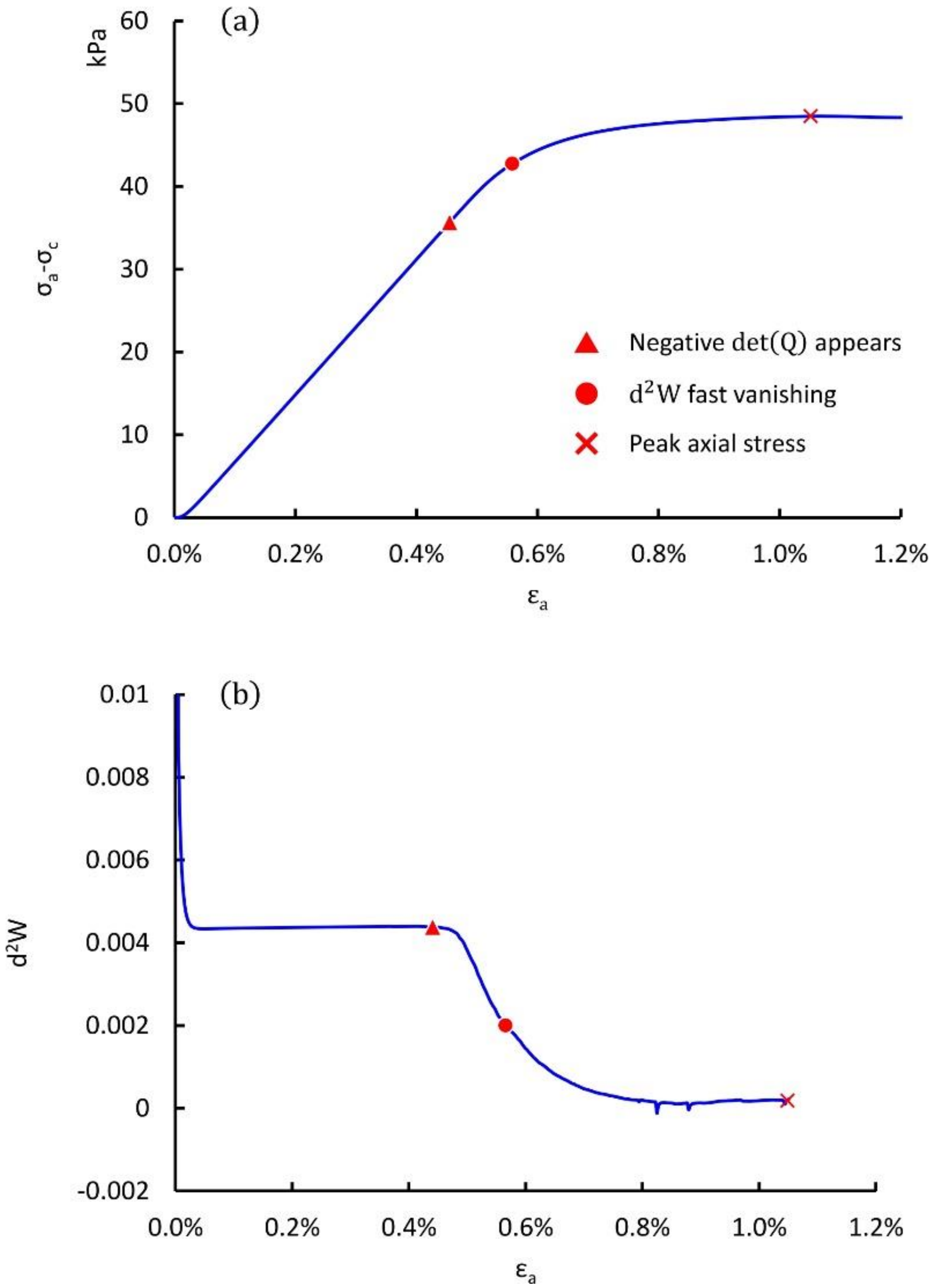

Figure 5.20: The SPH predicted biaxial test on sandy material with $c_3 = 0.3$ randomness: (a) the deviatoric stress versus axial strain plot; (b) the evolution of the second-order work with axial strain.

In Figure 5.19a and 5.20a, the peak shear stress is significantly influenced by the degree of randomness with much lower peak stress when larger randomness ($c_3 = 0.3$) is applied. Apart from this, the sample with $c_3 = 0.3$ enters the global plastic stage earlier than its counterpart with $c_3 = 0.1$, which agrees with the more smeared shear strain localisation pattern in Figure

5.16. As the material passes its peak stress, the test with $c_3 = 0.1$ demonstrates a faster softening process due to a more localised strain pattern, while test with $c_3 = 0.3$ has not entered its softening stage in the same range of axial strain. In order to further show the evolution of the stress state and its correspondence with the second-order work, three points have been selected and marked both on the stress path and the evolution of the second-order work plots as illustrated. The first point marks the first appearance of the negative determinant of the acoustic tensor, which is at the end of the elastic part of the stress paths in Figure 5.19a and 5.20a. It also signals the change of the second-order work from maintaining a stable state to a fast-vanishing stage. The second point corresponds to a fast-vanishing of the second-order work as shown in Figure 5.19b and 5.20b. In the stress path, this point marks the transition from elastic material behaviour to the material peak stress. Then, the material peak stress is achieved at the third point which corresponds to a negative value on the second-order work path as it just passes the zero point. The above results demonstrate the same process as what the second-order theory predicts during a bifurcation process, which also agrees well with the results of other tests that capture the bifurcation process as reported in the literature (Darve et al., 2007; Nicot et al., 2007).

5.6 Conclusion

In this chapter, a comprehensive study of the local and nonlocal features of the SPH method is conducted in the classical continuum mechanics background to analyse bifurcation and strain localisation problems. The generalised form of the nonlocality that has been incorporated into the classical continuum framework is first presented, which is then compared with the traditional SPH approximation of the soil governing equations. The comparison shows similarities between SPH and the nonlocal functions that demonstrates an inherent nonlocal character of SPH method. This feature is then further explored regarding the kernel interpolation function that governs the energy dissipation rate in the computational domain. The nonlocal kernel function demonstrates its capability to fully regularise the energy dissipation and correct the resolution dependency issue in the traditional SPH method when the kernel supporting domain is fixed. However, this approach features potential numerical instability and computational overburden as SPH kernel is closely related to the numerical stability during the interpolation. Therefore, a nonlocal operator is further incorporated into the SPH method. The proposed framework shows its capability to well regularise the energy dissipation and avoid any resolution dependency issue in a series of biaxial parametric studies.

In parallel with this, a Mohr-Coulomb elastoplastic strain-softening model is applied in this study to capture the strain localisation process. Two criteria, namely the acoustic tensor and second-order work, are used to check the incipient point of the bifurcation and subsequently the localisation in strain field. The obtained results in section 5.5.2 show a good agreement with the localisation theory. This demonstrates the capability of the proposed SPH framework to capture the bifurcation point and post-localisation process, indicating its potential to be applied to solve engineering problems with large plastic deformation such as the slope failure. This particular work will be demonstrated in the next chapter.

Chapter 6

A fully coupled multiphase framework in SPH for modelling the large deformation failure of the unsaturated soil

6.1 Introduction

In the previous chapters, it has been demonstrated that the proposed SPH computational framework is a powerful tool for capturing localised failure with large deformation under a range of mechanical boundary conditions. To further facilitate solving problems involving unsaturated soils, a fully coupled three-phase numerical framework is incorporated into the SPH method and the details are presented in this chapter. The kinematics of solid, liquid and air phases are taken into consideration with the corresponding conservation of the linear momentum and mass balance conditions in the governing equations. The effect of the change of the suction force on the mechanical behaviours of the soil domain is also taken into account through evolving state parameters in the Mohr-Coulomb model. Therefore, the reduction of the soil strength that has been observed during the rainfall-induced soils failures can be captured by the proposed numerical framework. To validate the multiphase SPH method, an infiltration test in soil column is first carried out with its result compared to the Terzaghi's theoretical solution. Then the water infiltration process in an embankment is modelled and compared to the experimental data. Lastly, two fullscale rainfall-induced failure tests are conducted on slopes containing sandy clay and Masa sand. For the Masa sand slope, the obtained results are further validated against the experiment, which demonstrates a very good agreement in predicting the slope run-off distance.

6.2 Problem background

The unsaturated soil condition refers to the coexistence of multiphase in the soil bulk, which mainly includes solid, liquid and air. It is the most commonly existed soil form in the natural geology (Fredlund & Rahardjo, 1993). Due to the existence of air component, soil properties including the shear strength, ductility and expansivity are significantly altered compared to the fully saturated and the dry soil conditions. Despite much work for understanding this particular soil condition, it was only until Fredlund and Rahardjo's systematic summary that a theoretical framework for unsaturated soil mechanics was established (Fredlund & Rahardjo, 1993). In parallel, numerous computational analysis has been conducted to facilitate understanding the unsaturated soil behaviours. The classical meshed based method is the most prevailing approach, represented by FEM. The work regarding FEM prediction of unsaturated soil behaviour mainly focuses on the development of the hydraulic constitutive models (Narasimhan & Witherspoon, 1978; Khalili et al., 2008; Sheng et al., 2008; Sheng 2011; Zhang & Ikariya, 2011; Sun & Sun, 2012). The coupling of the hydro-mechanical effect is described through elastoplasticity, elasto-viscoplasticity and critical state plasticity (Russell & Khalili, 2006; Sun et al., 2007; Oka et al., 2019). Attempts are also made in capturing the deformation of the soil bulk for biaxial test and rainfall-induced slope failures (Oka et al., 1995; 2002; 2011; 2019; Zhang & Ikariya, 2011; Cascini et al., 2013; Song & Borja, 2014). However, due to the limitations of the mesh discretisation, the prediction of any large deformation process can not be achieved by FEM. Another popular approach for modelling the unsaturated soil is the discrete element method, which has been applied for calibrating the hydraulic constitutive model during the soil collapse process (Liu & Sun, 2002; Liu et al., 2003; Jiang et al., 2004; Chalak et al., 2017). The DEM describes the capillary force at the micromechanical level by introducing an inter-particle force that mimics the suction effect among unsaturated soil particles. Therefore, it yields very good agreement with the experimental predicted stress path during the soil plastic behaviours as well as the hysteresis effect (Liu & Sun, 2002). The shear strength of the soil and the influence of the water content on altering soil strength is also captured by a capillary water contact model in DEM (Jiang et al., 2004). However, due to the computational-expensive nature of DEM, the current investigations of the unsaturated soil behaviour focus at microscale level and in a qualitative manner. A full-scale prediction of the soil large deformation process is not yet available for DEM applications. In parallel with the above two methods, the generalised interpolation material point method (GIMP) has gained much attention recently for capturing large plastic deformation in unsaturated soils (Yerro et al., 2015; 2016; Bandara & Soga, 2015; Bandara et al., 2016). In the GIMP, three phases of the unsaturated soil including solid, liquid and air are carried by Lagrangian particles following the continuum mechanics assumption of the numerical domain. Therefore, a large deformation process is achievable. It has been demonstrated that the rainfall-induced slope failure problems in unsaturated soil with a full run-off process can be well-captured (Yerro et al., 2016; Bandara et al., 2016). Despite the above progress, it has been summarised in Chapter 2 that the GIMP approach still faces difficulties in problems involving confining boundary conditions and irregular-shape numerical domains.

Therefore in this research work, to facilitate numerical modelling of unsaturated soils with large deformation predictions, a fully coupled multiphase framework is implemented into the Lagrangian meshfree SPH method. In the proposed method, the three phases including solid, liquid and air of the unsaturated soil are carried by each SPH particle. The generalised mass conservation condition is applied for all phases. The conservation of the linear momentum is also considered, which is combined with the mass conservation to govern the kinematics of SPH particles to describe unsaturated soil behaviour. The soil-water characteristic relationship is governed by the classic van Genuchten model, which may vary under different problem conditions. The proposed numerical approach is first validated in an infiltration test against Terzaghi's theoretical solution. It is then applied to simulate a water infiltration test in a soil embankment and the obtained results are compared to the experimental data. Lastly, the rainfall-induced slope failure process is simulated and compared to the experimental results, which demonstrate the capability of the proposed numerical framework in capturing the large deformation process in unsaturated soils.

6.3 The coupled multiphase framework for unsaturated soils in SPH

6.3.1 The basic concept in an unsaturated soil

The mixture of unsaturated soil can be idealised to contain three components: the solid skeleton of the soil, the liquid and air, where the liquid and air components fill the voids in the soil domain. The liquid component can contain both the fluid and dissolved air, while the air component can be a mixture of dry air and evaporated liquid (Figure 6.1). However, for the sake of simplicity, the mass exchange between liquid and air components is neglected in this study. In accordance with this concept, the total volume of an unsaturated soil domain can be expressed as:

$$\mathrm{V_{total}} = \mathrm{V_s} + \mathrm{V_l} + \mathrm{V_a} \tag{6.1}$$

The volume of each component can be related to the total volume by considering their volume fraction as:

$$\mathrm{V_c} = \mathrm{n_c V_{total}} \tag{6.2}$$

where $\mathrm{V_c}$ is the volume for each component and $\mathrm{n_c}$ is the volume fractions for each component. Now consider the definition of porosity n and degree of saturation $\mathrm{S_r}$, the volume fraction for each component can be explicitly written as:

$$\mathrm{n_s} = 1 - \mathrm{n} \tag{6.3}$$

$$\mathrm{n_l} = \mathrm{nS_r} \tag{6.4}$$

$$\mathrm{n_a} = \mathrm{n}(1 - \mathrm{S_r}) \tag{6.5}$$

The density (or mass) of the unsaturated soil mixture can be written in a similar manner by considering the above equations as:

$$\rho_{\mathrm{total}} = (1 - \mathrm{n})\rho_{\mathrm{s}} + \mathrm{nS_r}\rho_{\mathrm{l}} + \mathrm{n}(1 - \mathrm{S_r})\rho_{\mathrm{a}} \tag{6.6}$$

where ρ_{s}, ρ_{l} and ρ_{a} are the density for solid, liquid and air components.

In order to further describe the kinematics of the soil domain, the total stress tensor should be defined, which is a sum of solid, liquid and air stress as follows:

$$\boldsymbol{\sigma} = \boldsymbol{\sigma}^{\mathrm{s}} + \boldsymbol{\sigma}^{\mathrm{l}} + \boldsymbol{\sigma}^{\mathrm{a}} \tag{6.7}$$

By considering the volume fraction for each component, the partial stress tensor can be expressed as:

$$\boldsymbol{\sigma}^{\mathrm{s}} = \boldsymbol{\sigma}' - (1 - \mathrm{n})\mathbf{p}^{\mathrm{F}}\boldsymbol{\delta} \tag{6.8}$$

$$\boldsymbol{\sigma}^{\mathrm{l}} = -\mathrm{nS_r p^l}\boldsymbol{\delta} \tag{6.9}$$

$$\boldsymbol{\sigma}^{\mathrm{a}} = -\mathrm{n}(1-\mathrm{S_r})\mathrm{p^a}\boldsymbol{\delta} \tag{6.10}$$

where $\mathrm{p^l}$ and $\mathrm{p^a}$ are pressures of liquid and air, which will be used to derive the governing equations in later sections. $\boldsymbol{\delta}$ is the Kronecker's delta and $\mathbf{p}^{\mathrm{F}}$ accounts for the stress from liquid and air which can be written as:

$$\mathbf{p}^{\mathrm{F}} = \mathrm{S_r p^l} + (1-\mathrm{S_r})\mathrm{p^a} \tag{6.11}$$

The total stress tensor can be further written in a combination of $\mathbf{p}^{\mathrm{F}}$ and the Bishop's effective stress (skeleton stress) tensor as:

$$\boldsymbol{\sigma}' = \boldsymbol{\sigma} + \mathbf{p}^{\mathrm{F}}\boldsymbol{\delta} \tag{6.12}$$

where $\boldsymbol{\sigma}'$ is the effective stress tensor.

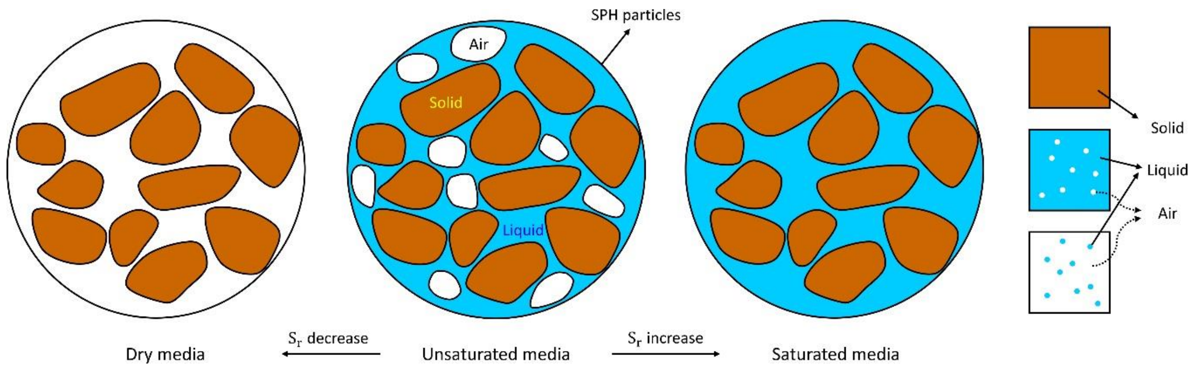

Figure 6.1: The framework for the unsaturated soil components.

6.3.2 Basic assumptions for the SPH unsaturated soil framework

Due to the complex nature of the unsaturated soil, it is necessary to impose certain simplifications and assumptions before a numerical analysis can be performed. In the proposed SPH unsaturated soil framework, the following assumptions are considered:

1. No mass exchange between solid and air components
2. The solid grains are incompressible
3. The soil is isothermal
4. Diffusive terms in liquid and air are neglected

With the above assumptions, the general mass and momentum balance for the soil domain can be now derived.

6.3.3 The general mass balance

The mass balance for a three-three phase (air, liquid, solid) porous media can be expressed in the following general form:

$$\sum_{\mathrm{c}}\left[\frac{\partial}{\partial \mathrm{t}}\left(\frac{\mathrm{m_c}}{\mathrm{V}}\right)+\nabla \mathbf{j}_{\mathrm{c}}\right]=0 \tag{6.13}$$

In above, $\mathrm{m_c}$ is the mass for each component. The fraction between the mass of each component and the corresponding volume is the density for each component. $\mathrm{j_c}$ is the sum of a diffusive and advective flux written as:

$$\mathbf{j}_{\mathrm{c}}=\mathbf{i}_c+\left(\frac{\mathrm{m_c}}{\mathrm{V}}\right)\mathbf{v}_c \tag{6.14}$$

In above, the diffusive flux represents the diffusion of liquid in air and air in liquid, which can be depicted through the Fick's law (Fick, 1855) as follows:

$$\mathbf{i}_{\mathrm{c}}=-\rho_{\mathrm{c}}\mathbf{D}_{\mathrm{c}}\mathbf{I}\nabla\omega_{\mathrm{c}} \tag{6.15}$$

where $\mathbf{D}_{\mathrm{c}}$ is a dispersion tensor. In Equation (6.14), if we consider no mass exchange between air and liquid phase for simplification, the diffusive term $\mathbf{i}_c$ is ignored, and the general mass balance for the three components can be simplified to:

$$\frac{\mathrm{d}\bar{\rho}_{\mathrm{c}}}{\mathrm{dt}}+\nabla(\bar{\rho}_{\mathrm{c}}\dot{\mathbf{u}}^{\mathrm{c}})=0 \tag{6.16}$$

where $\bar{\rho}_{\mathrm{c}}$ is the density for solid, liquid and air phases. $\dot{\mathbf{u}}^{\mathrm{c}}$ is the velocity tensor for each component. Now consider the definition of porosity and degree of saturation, the density for all three phases can be explicitly expressed as:

$$\bar{\rho}_{\mathrm{s}}=(1-\mathrm{n})\rho_{\mathrm{s}} \tag{6.17}$$

$$\bar{\rho}_{\mathrm{l}}=\mathrm{nS_r}\rho_{\mathrm{l}} \tag{6.18}$$

$$\bar{\rho}_{\mathrm{a}}=\mathrm{n}(1-\mathrm{S_r})\rho_{\mathrm{a}} \tag{6.19}$$

Substitute Equation (6.17) to (6.19) into the mass balance equation (6.16) we can obtain the general form of mass balance for an unsaturated soil as:

$$(1-\mathrm{n})\frac{\partial\rho_s}{\partial t}+\rho_s\frac{\partial(1-\mathrm{n})}{\partial t}+\rho_s\nabla[(1-\mathrm{n})\dot{\mathbf{u}}_s]+(1-\mathrm{n})\dot{\mathbf{u}}_s\nabla\rho_s=0 \tag{6.20}$$

$$\mathrm{nS_r}\frac{\partial\rho_l}{\partial t}+\rho_l\frac{\partial(\mathrm{nS_r})}{\partial t}+\rho_l\nabla[(\mathrm{nS_r})\dot{\mathbf{u}}_l]+\mathrm{nS_r}\dot{\mathbf{u}}_l\nabla\rho_l=0 \tag{6.21}$$

then multiply Equation (6.20) with $S_r\,\rho_l/\rho_s$ we can obtain:

$$S_r(1-\mathrm{n})\frac{\rho_l}{\rho_s}\frac{\partial\rho_s}{\partial t}+S_r\rho_l\frac{\partial(1-\mathrm{n})}{\partial t}+S_r\rho_l(1-\mathrm{n})\nabla\dot{\mathbf{u}}_s+S_r\frac{\rho_l}{\rho_s}(1-\mathrm{n})\dot{\mathbf{u}}_s\nabla\rho_s=0 \tag{6.22}$$

Adding the above Equation (6.21) and (6.22), considering that the spatial gradients of porosity and saturation are sufficiently small, we can obtain:

$$S_r\rho_l\left[\frac{\partial(1-\mathrm{n})}{\partial t}+\frac{\partial \mathrm{n}}{\partial t}\right]+\rho_l\nabla[\mathrm{nS_r}(\dot{\mathbf{u}}_l-\dot{\mathbf{u}}_s)]+S_r\rho_l\nabla\dot{\mathbf{u}}_s+\mathrm{nS_r}\left(\frac{\partial\rho_l}{\partial t}+\dot{\mathbf{u}}_l\nabla\rho_l\right)+\mathrm{n}\rho_l\frac{\partial S_r}{\partial t}$$

$$+S_r(1-\mathrm{n})\frac{\rho_l}{\rho_s}\left(\frac{\partial\rho_s}{\partial t}+\dot{\mathbf{u}}_s\nabla\rho_s\right)=0 \tag{6.23}$$

Further considering the material derivative as:

$$\frac{\partial\rho_l}{\partial t}+\dot{\mathbf{u}}_l\nabla\rho_l=\dot{\rho}_l \tag{6.24}$$

and recalling the assumption that the soil particles are incompressible, the last term in Equation (6.23) vanishes. Divide the Equation (6.23) by ρ_l, we can have:

$$\nabla[\mathrm{nS_r}(\dot{\mathbf{u}}_l-\dot{\mathbf{u}}_s)]+S_r\nabla\dot{\mathbf{u}}_s+\mathrm{nS_r}\frac{\dot{\rho}_l}{\rho_l}+\mathrm{n}\dot{S}_r=0 \tag{6.25}$$

The liquid density rate over liquid density in the above equation can be transformed according to the elastic relation between the volumetric strain and pressure as follow (Higo et al., 2010):

$$\frac{\dot{\rho}_l}{\rho_l}=-\frac{\dot{V}_l}{V_l}=-\mathrm{tr}\dot{\boldsymbol{\varepsilon}}_l=\frac{\dot{p}_l}{K_l} \tag{6.26}$$

where $\rho_l = -K_l \mathrm{tr}\boldsymbol{\varepsilon}_l$, and K_l is the volumetric elastic coefficient for water, which is a constant under isothermal condition. Incorporate Equation (6.26) into (6.25), the mass balance equation for the liquid component can be expressed as:

$$\nabla[nS_r(\dot{\mathbf{u}}_l - \dot{\mathbf{u}}_s)] + S_r\nabla\dot{\mathbf{u}}_s + nS_r\frac{\dot{\rho}_l}{K_l} + n\dot{S}_r = 0 \tag{6.27}$$

Similarly, the mass balance equation for air component can be derived following the process from Equation (6.16) to (6.25), which gives the final form as:

$$\nabla[n(1 - S_r)(\dot{\mathbf{u}}_a - \dot{\mathbf{u}}_s)] + (1 - S_r)\nabla\dot{\mathbf{u}}_s + n(1 - S_r)\frac{\dot{\rho}_a}{\rho_a} - n\dot{S}_r = 0 \tag{6.28}$$

Lastly, by incorporating Equation (6.17) into (6.16), the mass balance for solid phase is expressed as:

$$\dot{n} = (1 - n)\nabla\dot{\mathbf{u}}_s \tag{6.29}$$

6.3.4 The linear momentum balance

The general form of the linear momentum conservation law can be expressed for the solid, liquid and air phases respectively as follows (Oka et al., 2011):

$$\bar{\rho}_s\ddot{\mathbf{u}}_s - n(1 - S_r)\frac{\rho_a g}{\kappa_a}\dot{\mathbf{w}}_a - nS_r\frac{\gamma_w}{\kappa_l}\dot{\mathbf{w}}_l = \nabla\boldsymbol{\sigma}_s + \bar{\rho}_s\mathbf{b} \tag{6.30}$$

$$\bar{\rho}_l\ddot{\mathbf{u}}_l + nS_r\frac{\gamma_w}{\kappa_l}\dot{\mathbf{w}}_l = \nabla\boldsymbol{\sigma}_l + \bar{\rho}_l\mathbf{b} \tag{6.31}$$

$$\bar{\rho}_a\ddot{\mathbf{u}}_a + n(1 - S_r)\frac{\rho_a g}{\kappa_a}\dot{\mathbf{w}}_a = \nabla\boldsymbol{\sigma}_a + \bar{\rho}_a\mathbf{b} \tag{6.32}$$

where the relative velocity vectors for liquid and air are defined as:

$$\dot{\mathbf{w}}_l = nS_r(\dot{\mathbf{u}}_l - \dot{\mathbf{u}}_s) \tag{6.33}$$

$$\dot{\mathbf{w}}_a = n(1 - S_r)(\dot{\mathbf{u}}_a - \dot{\mathbf{u}}_s) \tag{6.34}$$

Incorporate Equation (6.33) into (6.31) and Equation (6.34) into (6.32), and neglect the acceleration difference $\ddot{\mathbf{w}}_l \cong 0$ and $\ddot{\mathbf{w}}_a \cong 0$ as well as the spatial gradient of saturation and porosity. The average relative velocity tensors can be derived and shown as follows:

$$\dot{\mathbf{w}}_l = -\frac{\kappa_l}{\gamma_w}(\nabla p_l + \rho_l \ddot{\mathbf{u}}_s - \rho_l \mathbf{b}) \tag{6.35}$$

$$\dot{\mathbf{w}}_a = -\frac{\kappa_a}{\rho_a g}(\nabla p_a + \rho_a \ddot{\mathbf{u}}_s - \rho_a \mathbf{b}) \tag{6.36}$$

Now the motion equation for the unsaturated soil domain can be expressed by adding Equation (6.30), (6.31) and (6.32) as:

$$\rho_{total}\ddot{\mathbf{u}}_s + nS_r\rho_l(\ddot{\mathbf{u}}_l - \ddot{\mathbf{u}}_s) + n(1 - S_r)\rho_a(\ddot{\mathbf{u}}_a - \ddot{\mathbf{u}}_s) = \nabla\boldsymbol{\sigma} + \rho_{total}\mathbf{b} \tag{6.37}$$

As the acceleration differences $\ddot{\mathbf{u}}_l - \ddot{\mathbf{u}}_s$ and $\ddot{\mathbf{u}}_a - \ddot{\mathbf{u}}_s$ are negligible compared to the solid acceleration tensor $\ddot{\mathbf{u}}_s$, therefore the above equation can be simplified to:

$$\rho_{total}\ddot{\mathbf{u}}_s = \nabla\boldsymbol{\sigma} + \rho_{total}\mathbf{b} \tag{6.38}$$

Equation (6.38) is the general form of the momentum conservation for the unsaturated soil mixture.

6.3.5 Continuity conditions for liquid and air

Recall the mass conservation for liquid and air in Equation (6.27) and (6.28), and relate them with the relative velocity tensors in Equation (6.35) and (6.36), the continuity equations for liquid and air are expressed as follows:

$$\nabla\left[-\frac{\kappa_l}{\gamma_w}(\nabla p_l + \rho_l \ddot{\mathbf{u}}_s - \rho_l \mathbf{b})\right] + S_r\nabla\dot{\mathbf{u}}_s + nS_r\frac{\dot{p}_l}{K_l} + n\dot{S}_r = 0 \tag{6.39}$$

$$\nabla\left[-\frac{\kappa_a}{\rho_a g}(\nabla p_a + \rho_a \ddot{\mathbf{u}}_s - \rho_a \mathbf{b})\right] + (1 - S_r)\nabla\dot{\mathbf{u}}_s + n(1 - S_r)\frac{\dot{\rho}_a}{\rho_a} - n\dot{S}_r = 0 \tag{6.40}$$

With an assumption of an ideal gas in the isothermal condition in Equation (6.41) (Oka et al., 2019), the continuity equation for the gas phase can be further expressed as:

$$\frac{\dot{\rho}_a}{\rho_a} = \frac{\dot{p}_a}{p_a} \tag{6.41}$$

$$\nabla\left[-\frac{\kappa_a}{\rho_a g}(\nabla p_a + \rho_a \ddot{\mathbf{u}}_s - \rho_a \mathbf{b})\right] + (1 - S_r)\nabla\dot{\mathbf{u}}_s + n(1 - S_r)\frac{\dot{p}_a}{p_a} - n\dot{S}_r = 0 \tag{6.42}$$

Equation (6.39) and (6.42) are the continuity condition for liquid and air components, which are applied to calculate the time rate for liquid and air pressures.

6.3.6 Transformation of the continuity conditions for liquid and air

In order to solve the above continuity Equation (6.39) and (6.42) in an explicit way, the kinematic variables: $\ddot{\mathbf{u}}_s$, $\dot{p}_l$ and $\dot{p}_a$ should be solved independently. Therefore, the continuity of liquid and air should be transformed in order to relate each unknown variable with known values. First, the gradient operator in Equation (6.39) and (6.42) should be expanded as follows:

$$\nabla\left[-\frac{\kappa_l}{\gamma_w}(\nabla p_l + \rho_l\ddot{\mathbf{u}}_s - \rho_l\mathbf{b})\right] = -\frac{1}{\gamma_w}[\rho_l\ddot{\mathbf{u}}_s\nabla\kappa_l + \rho_l\kappa_l\nabla\ddot{\mathbf{u}}_s + \nabla\kappa_l\nabla p_l + \kappa_l\nabla^2 p_l - \rho_l\mathbf{b}\nabla\kappa_l] \tag{6.43}$$

$$\nabla\left[-\frac{\kappa_a}{\rho_a g}(\nabla p_a + \rho_a\ddot{\mathbf{u}}_s - \rho_a\mathbf{b})\right] = -\frac{1}{\rho_a g}[\rho_a\ddot{\mathbf{u}}_s\nabla\kappa_a + \rho_a\kappa_a\nabla\ddot{\mathbf{u}}_s + \nabla\kappa_a\nabla p_a + \kappa_a\nabla^2 p_a - \rho_a\mathbf{b}\nabla\kappa_a] \tag{6.44}$$

The rate of saturation can be derived from the hydraulic constitutive model which will be elaborated in the next section, and $\dot{S}_r$ has the form:

$$\dot{S}_r = \frac{\partial S_r}{\partial p_s}\dot{p}_a - \frac{\partial S_r}{\partial p_s}\dot{p}_l \tag{6.45}$$

where $p_s = p_a - p_l$ is the suction due to capillary force.

To make further mathematical transformations of the above equations, the following notations are made for the sake of maintaining simplicity:

$$A = \nabla\left[-\frac{\kappa_l}{\gamma_w}(\nabla p_l + \rho_l\ddot{\mathbf{u}}_s - \rho_l\mathbf{b})\right] + S_r\nabla\dot{\mathbf{u}}_s \tag{6.46}$$

$$B = \nabla\left[-\frac{\kappa_a}{\rho_a g}(\nabla p_a + \rho_a\ddot{\mathbf{u}}_s - \rho_a\mathbf{b})\right] + (1 - S_r)\nabla\dot{\mathbf{u}}_s \tag{6.47}$$

$$C = \frac{\partial S_r}{\partial p_s} = -m(S_{rmax} - S_{rmin})\left[1 + (\alpha p_s)^{n'}\right]^{-(m+1)} n'(\alpha p_s)^{(n'-1)}\alpha \tag{6.48}$$

where C is derived based on the van Genuchten soil water characteristic model which will be presented in section 6.3.7.

From the above notation, the continuity equations for liquid and air in Equation (6.39) and (6.42) can be simplified to:

$$\mathrm{A} + \mathrm{Cn}\dot{\mathrm{p}}_\mathrm{a} - \mathrm{Cn}\dot{\mathrm{p}}_\mathrm{l} + \frac{\mathrm{nS_r}}{\mathrm{K_l}}\dot{\mathrm{p}}_\mathrm{l} = 0 \tag{6.49}$$

$$\mathrm{B} - \mathrm{Cn}\dot{\mathrm{p}}_\mathrm{a} + \mathrm{Cn}\dot{\mathrm{p}}_\mathrm{l} + \frac{\mathrm{n}(1-\mathrm{S_r})}{\mathrm{p_a}}\dot{\mathrm{p}}_\mathrm{a} = 0 \tag{6.50}$$

Now the liquid pressure rate can be expressed from above two equations as:

$$\dot{\mathrm{p}}_\mathrm{l} = \frac{\mathrm{A} + \mathrm{Cn}\dot{\mathrm{p}}_\mathrm{a}}{\mathrm{Cn} - \frac{\mathrm{nS_r}}{\mathrm{K_l}}} \tag{6.51}$$

Substitute Equation (6.51) into (6.50), we can obtain:

$$\mathrm{B} - \mathrm{Cn}\dot{\mathrm{p}}_\mathrm{a} + \frac{\mathrm{CnA}}{\mathrm{Cn} - \frac{\mathrm{nS_r}}{\mathrm{K_l}}} + \frac{\mathrm{CCnn}}{\mathrm{Cn} - \frac{\mathrm{nS_r}}{\mathrm{K_l}}}\dot{\mathrm{p}}_\mathrm{a} + \frac{\mathrm{n}(1-\mathrm{S_r})}{\mathrm{p_a}}\dot{\mathrm{p}}_\mathrm{a} = 0 \tag{6.52}$$

Rearrange the above equation and now the rate of air pressure can be expressed as:

$$\dot{\mathrm{p}}_\mathrm{a} = \frac{\mathrm{B} + \frac{\mathrm{CA}}{\mathrm{C} - \frac{\mathrm{S_r}}{\mathrm{K_l}}}}{\left[\mathrm{Cn} - \frac{\mathrm{CCn}}{\mathrm{C} - \frac{\mathrm{S_r}}{\mathrm{K_l}}} - \frac{\mathrm{n}(1-\mathrm{S_r})}{\mathrm{p_a}}\right]} \tag{6.53}$$

Now, substituting the above formulation into Equation (6.51), the rate for the liquid pressure can be expressed as:

$$\dot{p}_l = \frac{A + Cn\dfrac{B + \dfrac{CA}{C - \dfrac{S_r}{K_l}}}{\left[Cn - \dfrac{CCn}{C - \dfrac{S_r}{K_l}} - \dfrac{n(1 - S_r)}{p_a}\right]}}{Cn - \dfrac{nS_r}{K_l}} \tag{6.54}$$

The above Equation (6.53) and (6.54) can now be applied together with the motion equation for the porous mixture in Equation (6.38) to solve the field kinematic variables for unsaturated soil.

6.3.7 The hydraulic constitutive relations

Due to the existence of air and liquid pressures, the suction force is created due to the capillary effect. Generally, an unsaturated soil with lower saturation corresponds to a higher suction force due to the increase of the water surface tension that bonds soil particles. The relationship between the degree of saturation (water content) and the suction force can be mathematically described by a soil-water characteristic curve. In the current study, the classical van Genuchten model is adopted to describe this relationship as:

$$\frac{S_r - S_{rmin}}{S_{rmax} - S_{rmin}} = \left[1 + (\alpha p_s)^{n'}\right]^{-m} \tag{6.55}$$

where S_{rmin} and S_{rmax} are minimum and maximum saturation parameters which are selected based on certain problem context. α, m and n' are state variables, where $m = 1 - \frac{1}{n'}$. The above relationship, when directly applied for low permeability clays, may lead to numerical instability due to large inverse values of the permeability. Therefore, an updated permeability for both liquid and air components can be expressed as follows to minimise potential numerical instabilities (Oka et al., 2019):

$$\kappa_l = \kappa_l^s (S_{re})^a \left[1 - \left(1 - S_{re}^{1/m}\right)^{n'}\right] \tag{6.56}$$

$$\kappa_a = \kappa_a^s (1 - S_{re})^b \left[1 - \left(1 - S_{re}^{1/m}\right)^{n'}\right] \tag{6.57}$$

where a and b are material parameters, S_{re} is the effective saturation which can be expressed based on Equation (6.55) as:

$$S_{re} = \frac{S_r - S_{rmin}}{S_{rmax} - S_{rmin}} \tag{6.58}$$

κ_l^s and κ_a^s represent the saturated permeability of liquid and dry permeability of air, expressed in terms of void ratio as:

$$\kappa_l^s = \kappa_l^{s0} \exp[(e - e_0)/C_k] \tag{6.59}$$

$$\kappa_a^s = \kappa_a^{s0} \exp[(e - e_0)/C_k] \tag{6.60}$$

where κ_l^{s0} and κ_a^{s0} are initial values of permeabilities at the initial void ratio e_0, while C_k is a material parameter.

In order for the above framework to be implemented in the SPH method, the particle approximation form of the key components in the above mass and momentum conservation laws are presented in the next section.

6.3.8 SPH approximation of the governing equations

In order for Equation (6.38), (6.39) and (6.42) to be solved in the SPH environment, the constituents of these equations are written in SPH discretisation in this section. Starting from Equation (6.39), the gradient components are written particle approximation form as:

$$\nabla \kappa_l^i = \sum_{j=1}^{N} \frac{m_j}{\rho_j} \left(\kappa_l^j - \kappa_l^i\right) \nabla W_{ij} \tag{6.61}$$

$$\nabla p_l^i = \sum_{j=1}^{N} \frac{m_j}{\rho_j} \left(p_l^j - p_l^i\right) \nabla W_{ij} \tag{6.62}$$

$$\nabla \ddot{\mathbf{u}}_s^i = \sum_{j=1}^{N} \frac{m_j}{\rho_j} \left(\ddot{\mathbf{u}}_s^j - \ddot{\mathbf{u}}_s^i\right) \nabla W_{ij} \tag{6.63}$$

$$\nabla \dot{\mathbf{u}}_s^i = \sum_{j=1}^{N} \frac{m_j}{\rho_j} \left(\dot{\mathbf{u}}_s^j - \dot{\mathbf{u}}_s^i\right) \nabla W_{ij} \tag{6.64}$$

For approximating the second-order gradient in Equation (6.39) and (6.42), the Taylor expansion is applied during the derivation by ignoring higher-order terms, which yields the following form (Morris et al., 1997; Chen et al., 1999; Cleary & Monaghan, 1999):

$$\mathrm{\kappa_l^i \nabla^2 p_l^i = \sum_{j=1}^{N} 4 \frac{m_j}{\rho_j} \frac{\kappa_l^i \kappa_l^j}{\kappa_l^i + \kappa_l^j} \left(p_l^i - p_l^j\right) \frac{x_{ij}}{\left|x_{ij}\right|^2} \nabla W_{ij}} \tag{6.65}$$

The air counterparts of the above approximations for the liquid component in Equation (6.61) to (6.65) are expressed just by replacing l with a, therefore it is not necessary to repeat the formulations here. Considering the above SPH formulations, the liquid and air continuity equations can be explicitly written in their SPH particle approximation form as:

$$\begin{aligned} &-\frac{1}{\gamma_w}\left[\rho_l^i \ddot{\mathbf{u}}_s^i \sum_{j=1}^{N} \frac{m_j}{\rho_j}\left(\kappa_l^j - \kappa_l^i\right)\nabla W_{ij} + \rho_l^i \kappa_l^i \sum_{j=1}^{N} \frac{m_j}{\rho_j}\left(\ddot{\mathbf{u}}_s^j - \ddot{\mathbf{u}}_s^i\right)\nabla W_{ij}\right. \\ &\qquad + \sum_{j=1}^{N} \frac{m_j}{\rho_j}\left(\kappa_l^j - \kappa_l^i\right)\nabla W_{ij} \sum_{j=1}^{N} \frac{m_j}{\rho_j}\left(p_l^j - p_l^i\right)\nabla W_{ij} \\ &\qquad \left. + \sum_{j=1}^{N} 4 \frac{m_j}{\rho_j} \frac{\kappa_l^i \kappa_l^j}{\kappa_l^i + \kappa_l^j}\left(p_l^i - p_l^j\right) \frac{x_{ij}}{\left|x_{ij}\right|^2} \nabla W_{ij} - \rho_l^i \mathbf{b} \sum_{j=1}^{N} \frac{m_j}{\rho_j}\left(\kappa_l^j - \kappa_l^i\right)\nabla W_{ij}\right] \\ &\qquad + S_r^i \sum_{j=1}^{N} \frac{m_j}{\rho_j}\left(\dot{\mathbf{u}}_s^j - \dot{\mathbf{u}}_s^i\right)\nabla W_{ij} + n^i S_r^i \frac{\dot{p}_l^i}{K_l} + n^i \dot{S}_r^i = 0 \end{aligned} \tag{6.66}$$

$$\begin{aligned} &-\frac{1}{\rho_a^i g}\left[\rho_a^i \ddot{\mathbf{u}}_s^i \sum_{j=1}^{N} \frac{m_j}{\rho_j}\left(\kappa_a^j - \kappa_a^i\right)\nabla W_{ij} + \rho_a^i \kappa_a^i \sum_{j=1}^{N} \frac{m_j}{\rho_j}\left(\ddot{\mathbf{u}}_s^j - \ddot{\mathbf{u}}_s^i\right)\nabla W_{ij}\right. \\ &\qquad + \sum_{j=1}^{N} \frac{m_j}{\rho_j}\left(\kappa_a^j - \kappa_a^i\right)\nabla W_{ij} \sum_{j=1}^{N} \frac{m_j}{\rho_j}\left(p_a^j - p_a^i\right)\nabla W_{ij} \\ &\qquad \left. + \sum_{j=1}^{N} 4 \frac{m_j}{\rho_j} \frac{\kappa_a^i \kappa_a^j}{\kappa_a^i + \kappa_a^j}\left(p_a^i - p_a^j\right) \frac{x_{ij}}{\left|x_{ij}\right|^2} \nabla W_{ij} - \rho_a^i \mathbf{b} \sum_{j=1}^{N} \frac{m_j}{\rho_j}\left(\kappa_a^j - \kappa_a^i\right)\nabla W_{ij}\right] \\ &\qquad + \left(1 - S_r^i\right) \sum_{j=1}^{N} \frac{m_j}{\rho_j}\left(\dot{\mathbf{u}}_s^j - \dot{\mathbf{u}}_s^i\right)\nabla W_{ij} + n\left(1 - S_r^i\right) \frac{\dot{p}_a^i}{p_a^i} - n^i \dot{S}_r^i \end{aligned} \tag{6.67}$$

The momentum balance of the soil mixture in Equation (6.38) can be now expressed as:

$$\ddot{\mathbf{u}}_s^i = \sum_{j=1}^{N} m_j \left(\frac{\sigma_i'}{\rho_i^2} + \frac{\sigma_j'}{\rho_j^2} + C_{ij} \right) \nabla W_{ij} - \sum_{j=1}^{N} S_r^i m_j \left(\frac{p_l^j - p_l^i}{\rho_i \rho_j} \right) \nabla W_{ij}$$
$$- \sum_{j=1}^{N} (1 - S_r^i) m_j \left(\frac{p_a^j - p_a^i}{\rho_i \rho_j} \right) \nabla W_{ij} + \mathbf{b} \tag{6.68}$$

6.3.9 A suction dependent soil constitutive relation

In order to capture the effect of the change of saturation on the soil mechanical behaviour, which is widely observed in unsaturated soils involving problems such as rainfall-induced slope failures, a suction dependent Mohr-Coulomb softening model is highlighted in this section. In the elastoplastic Mohr-Coulomb strain-softening model introduced in Chapter 3, the state parameters ϕ' and c' are defined based on effective stress in the dry soil. However, to consider the effect of suction in unsaturated soil condition, another set of state parameters that evolve depending on the saturation state of the soil are introduced. We start by defining the friction angle and cohesion as a combination of an effective part and suction dependent part as follows:

$$\phi = \phi' + \phi_s \tag{6.69}$$

$$c = c' + c_s \tag{6.70}$$

where ϕ' and c' are the effective friction angle and cohesion that are evolving according to the total deviatoric plastic strain. ϕ_s and c_s are the friction angle and cohesion that are evolving with the state of saturation, or equivalently the suction p_s. ϕ_s and c_s can be defined as follows (Yerro et al., 2016):

$$\phi_s = A' \left(\frac{p_s}{p_{atm}} \right) \tag{6.71}$$

$$c_s = c_{max} \left[1 - e^{-B' \left(\frac{p_s}{p_{atm}} \right)} \right] \tag{6.72}$$

in above, the p_{atm} is the atmospheric pressure. A' and B' are coefficients controlling the rate of the variation of the friction angle and cohesion. c_{max} is a maximum cohesion value that suction force can bring up.

Since the total friction angle and cohesion are applied in the Mohr-Coulomb model, the consistency condition should be derived for both the effective and suction dependent parts of the state parameters. Therefore, the consistency condition is expressed as:

$$\begin{aligned}\dot{f} = \frac{\partial f}{\partial \sigma'^{,\alpha\beta}}\dot{\sigma}'^{,\alpha\beta} + \frac{\partial f}{\partial \phi}\frac{\partial \phi}{\partial \phi'}\frac{\partial \phi'}{\partial \varepsilon_p^{eq}}\dot{\varepsilon}_p^{eq} + \frac{\partial f}{\partial c}\frac{\partial c}{\partial c'}\frac{\partial c'}{\partial \varepsilon_p^{eq}}\dot{\varepsilon}_p^{eq} + \frac{\partial f}{\partial \phi}\frac{\partial \phi}{\partial \phi_s}\frac{\partial \phi_s}{\partial p_s}\dot{p}_s + \frac{\partial f}{\partial c}\frac{\partial c}{\partial c_s}\frac{\partial c_s}{\partial p_s}\dot{p}_s \\ = 0\end{aligned} \tag{6.73}$$

Recall the general stress-strain relationship for an elastoplastic material presented in Equation (3.46) as:

$$\dot{\sigma}'^{,\alpha\beta} = 2G\dot{e}^{\alpha\beta} + K\dot{\varepsilon}^{\gamma\gamma}\delta^{\alpha\beta} - \dot{\lambda}\left[\left(K - \frac{2G}{3}\right)\frac{\partial g}{\partial \sigma'^{,mn}}\delta^{mn}\delta^{\alpha\beta} + 2G\frac{\partial g}{\partial \sigma'^{,\alpha\beta}}\right] \tag{6.74}$$

Incorporate Equation (6.74) into the consistency condition in Equation (6.73), and apply $\dot{e}^{\alpha\beta} = \dot{\varepsilon}^{\alpha\beta} - (1/3)\dot{\varepsilon}^{\gamma\gamma}\delta^{\alpha\beta}$ we can obtain the plastic multiplier for an unsaturated Mohr-Coulomb soil with suction dependent state variables as:

$$\dot{\lambda} = \frac{2G\dot{\varepsilon}^{\alpha\beta}\frac{\partial f}{\partial \sigma'^{,\alpha\beta}} + \left(K - \frac{2G}{3}\right)\dot{\varepsilon}^{\gamma\gamma}\frac{\partial f}{\partial \sigma'^{,\alpha\beta}}\delta^{\alpha\beta} + \frac{\partial f}{\partial \phi}\frac{\partial \phi}{\partial \phi_s}\frac{\partial \phi_s}{\partial p_s}\dot{p}_s + \frac{\partial f}{\partial c}\frac{\partial c}{\partial c_s}\frac{\partial c_s}{\partial p_s}\dot{p}_s}{\left[2G\frac{\partial f}{\partial \sigma'^{,mn}}\frac{\partial g}{\partial \sigma'^{,mn}} + \left(K - \frac{2G}{3}\right)\frac{\partial f}{\partial \sigma'^{,mn}}\delta^{mn}\frac{\partial g}{\partial \sigma'^{,mn}}\delta^{mn}\right] - \left(\frac{\partial f}{\partial \phi}\frac{\partial \phi}{\partial \phi'}\frac{\partial \phi'}{\partial \varepsilon_p^{eq}}\mathrm{val} + \frac{\partial f}{\partial c}\frac{\partial c}{\partial c'}\frac{\partial c'}{\partial \varepsilon_p^{eq}}\mathrm{val}\right)} \tag{6.75}$$

Where val can be defined in terms of effective stress in a similar form as Equation (3.90) as:

$$\mathrm{val} = \sqrt{\frac{2}{3}\left(\frac{\partial g}{\partial \sigma'^{,\alpha\beta}}\frac{\partial g}{\partial \sigma'^{,\alpha\beta}} - \frac{1}{3}\frac{\partial g}{\partial \sigma'^{,mn}}\frac{\partial g}{\partial \sigma'^{,mn}}\right)} \tag{6.76}$$

6.4 Numerical validations

The proposed SPH framework for modelling unsaturated soil behaviours is validated in this section. The proposed approach is first applied for a water infiltration test in a soil column. The obtained results are compared to Terzaghi's theoretical solutions. A water infiltration test is then conducted on an embankment. The numerical simulations are compared with the results obtained in the experiment. To further capture plastic deformations in unsaturated soils with large deformation, a rainfall-induced slope failure on a sandy clay embankment is performed with the proposed method. Lastly, a full-scale slope failure experiment on Masa sand is reproduced with SPH, and the obtained results are compared to the experimental data.

6.4.1 Water infiltration test in a soil column

The behaviour for a two-phase saturated soil can be validated against the Terzaghi's consolidation theory. However, for a three-phase system, the hydraulic conductivity and soil saturation are nonlinear depending on specific liquid pressure states, therefore analytical solutions are not straightforwardly available as indicated in the literature (Yerro, 2015). To overcome this issue and recover the description of water flow in unsaturated media with the Richards equation, assumptions including vertical liquid flow, non-compressible soil grain, constant permeability, constant total stress state etc. are necessary (Yerro, 2015). The soil-water characteristic curve is further simplified with the following linear relation:

$$S_r = 1 - a_s(p_a - p_l) \tag{6.77}$$

where a_s is a constant. With the above conditions, the analytical expression for vertical water flow in 1D space can be expressed as:

$$\frac{\partial p_l}{\partial t} = c_i \frac{\partial^2 p_l}{\partial z^2} \tag{6.78}$$

Where z is the distance along the infiltration direction, and the coefficient c_i can be related to soil hydraulic properties as:

$$c_i = \frac{\kappa_l}{n\gamma_w a_s} \tag{6.79}$$

Equation (6.78) above has a similar form as the Terzaghi's theoretical solution for the dissipation of excess pore water pressure in 1D space, which is written as:

$$\frac{\partial p_l}{\partial t} = c_v \frac{\partial^2 p_l}{\partial z^2} \tag{6.80}$$

where c_v is the consolidation coefficient. Therefore, the theoretical solution for Equation (6.78) bears the same form as that for (6.80) which can be written as (Terzaghi et al., 1996) (Figure 6.3):

$$p_l = \sum_{m=0}^{m=\infty} \frac{2p_l}{M}\left(\sin\frac{Mz}{d}\right)\exp(-M^2T_v) \tag{6.81}$$

To conduct the test, a 1m long soil column is created in the SPH domain. An initial negative pore water pressure of 0.5 MPa is assigned to the sample to represent an unsaturated condition. The bottom and side boundaries of the column are assumed impermeable, while the top boundary is permeable. At the beginning of the test, a zero negative pore pressure is assigned to the top boundary to enforce a 100% saturated condition. The full saturation is then propagated along the column until reaching the bottom boundary. The suction is measured at different locations along the soil column and the obtained values are compared to the Terzaghi's solution. The simulation set up is illustrated in Figure 6.2, and the parameters are summarized in Table 6.1.

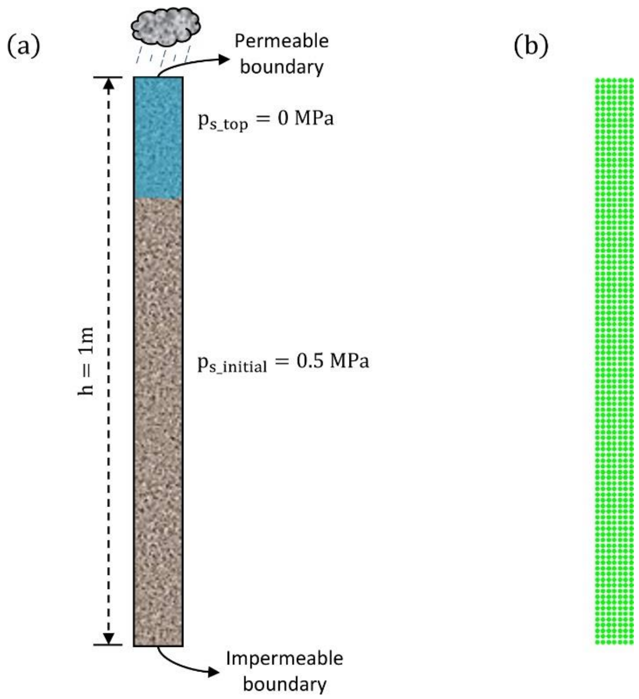

Figure 6.2: The simulation setup for the water infiltration into an unsaturated soil column: (a) the boundary conditions; (b) SPH sample.

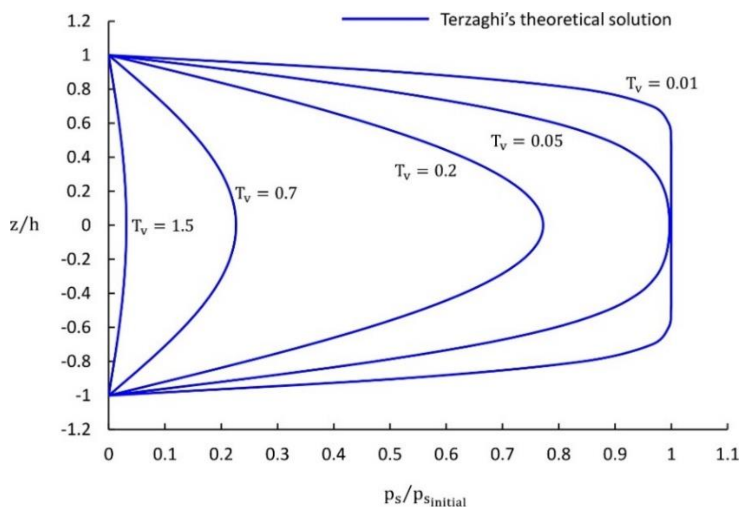

Figure 6.3: Terzaghi's theoretical solution for a 1D water infiltration process in a vertical soil column.

Table 6.1: The numerical parameters for the water infiltration to a soil column.

Young's modulus	E	1 MPa
Poisson's ratio	ν	0.3
Initial porosity	n	0.3
Soil density	ρ	$2000\,\mathrm{kg/m^3}$
Liquid permeability	κ_l	5×10^{-7}
Liquid bulk modulus	K_l	80 MPa
SWCC parameter	a_s	$10^{-3}\ \mathrm{kPa^{-1}}$

The water infiltration process predicted by the proposed SPH approach is illustrated in Figure 6.4 and the comparison between the measured suction and Terzaghi's solution is presented in Figure 6.5. During the infiltration process, the water travels vertically in the soil column with a smooth and parallel wetting front as shown in Figure 6.4. The SPH approximation of the pore pressure automatically satisfies the uniform pressure gradient without showing boundary deficiency effect, which could be attributed to the kernel gradient correction applied in the proposed method. The wetting front is advanced until the bottom boundary when the entire sample is submerged. For the measured suction in Figure 6.5, a very good agreement between the SPH results and the theoretical solution has been achieved for a range of time factors from

$T_v = 0.01$ to $T_v = 1.5$. This covers the entire infiltration process, showing a good prediction capability of the proposed approach. However, a minor disagreement has been observed for $T_v = 0.2$ and $T_v = 0.7$, with SPH results slightly lagging behind the theoretical suction. This could be attributed to the artificial viscosity term that applied to stabilise the computational domain, which creates additional viscosity to the fluid phase.

The above results have demonstrated a good capability for the proposed SPH approach to capture the seepage flow in the unsaturated soil domain. In order to further validate the method, a two-dimensional water infiltration process is simulated in a soil embankment. The obtained results and its comparison with the experimental data are presented in the next section.

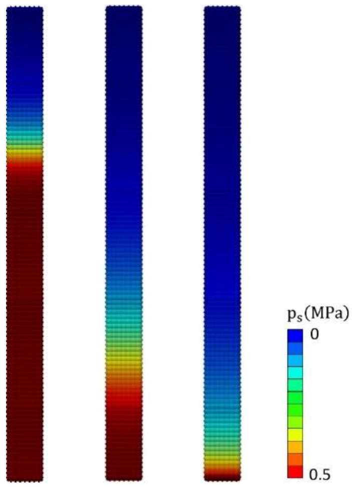

Figure 6.4: SPH predicted evolution of the suction in the soil column.

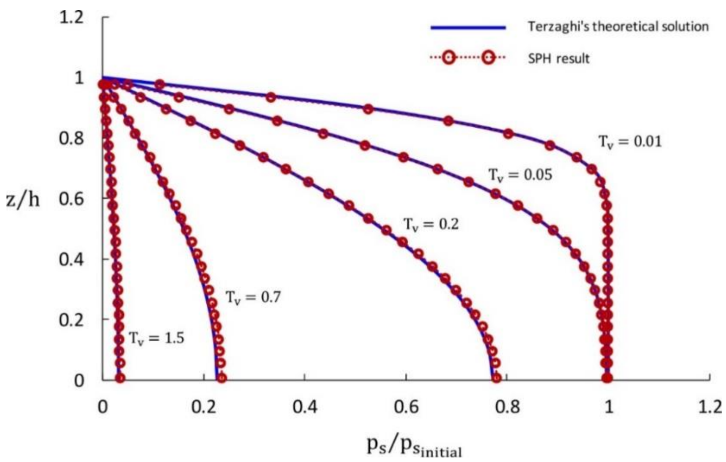

Figure 6.5: Comparison between SPH predicted and Terzaghi's theoretical solution for the suction evolution during the infiltration.

6.4.2 Water infiltration in a soil embankment

In this section, SPH simulations of a water infiltration experiment in Shirasu sand has been conducted. The test is performed on a sample with 1.8m length, 1.4m width and 0.8m depth and 45° side slope (Figure 6.6a). The sample has an initial water content of 38% with affusion applied on top of the embankment. The embankment surface is assumed permeable, while the bottom and side of the sample are impermeable (Figure 6.6b). The pore water pressure is measured at 15 different locations in the sample during the test, with the sensors shown in Figure 6.6c. The soil domina is considered to have elastic deformation only during the infiltration process. The initial inter-particle distance in the SPH domain is 2cm, which gives a total of 1980 particles representing the embankment. As the simulation starts, the affusion is applied to the top layer of SPH particles on the horizontal upper surface of the embankment body to initiate the infiltration process.

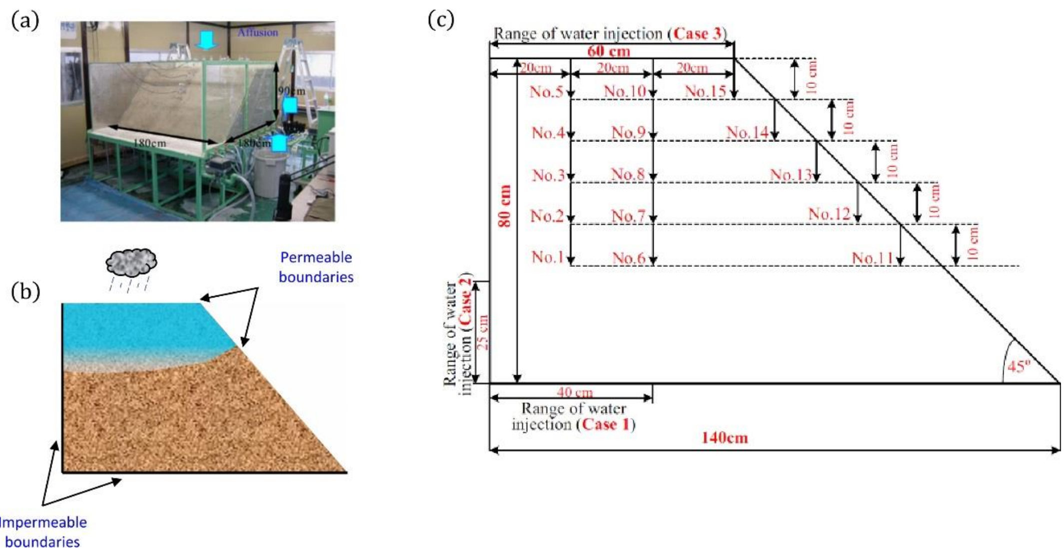

Figure 6.6: The experimental and numerical setup for the water infiltration test: (a) the experimental configuration (Kitamura et al., 2007); (b) the numerical test setup; (c) the location of pore water measure devices (Kitamura et al., 2007).

In order to capture the soil-water characteristic relation in this experiment, instead of the van Genuchten model, a simple model proposed by Zhang and Ikariya that captures the hydraulic hysteresis effect is applied here (2011). In this model, only the wetting process is considered in this study, with the following relationship describes the SWCC:

$$S_r = S_{rmax} - \frac{2}{\pi}(S_{rmax} - S_{rmin})\tan^{-1}[(e^{c_2 p_s} - 1)/e^{c_2 s_w}] \tag{6.82}$$

or equivalently:

$$p_s = \frac{1}{c_2} \ln\left[1 + e^{c_2 s_w} \tan\left(\frac{\pi}{2} \frac{S_{rmax} - S_r}{S_{rmax} - S_{rmin}}\right)\right] \tag{6.83}$$

where c_2, s_w are parameters corresponding to the wetting process, which are selected according to the specific problem context. In the suction p_s, the pore air pressure is assumed as zero for simplicity in this test. The soil properties, SWCC parameters are summarised in Table 6.2. The liquid and air permeabilities are calibrated for this experiment (Xiong et al., 2014) shown in Figure 6.7, which can be expressed in the following relationships:

$$\kappa_l = 3 \times 10^{-8}(e^{10.038 S_r}) \tag{6.84}$$

$$\kappa_a = 0.1226(e^{-9.814 S_r}) \tag{6.85}$$

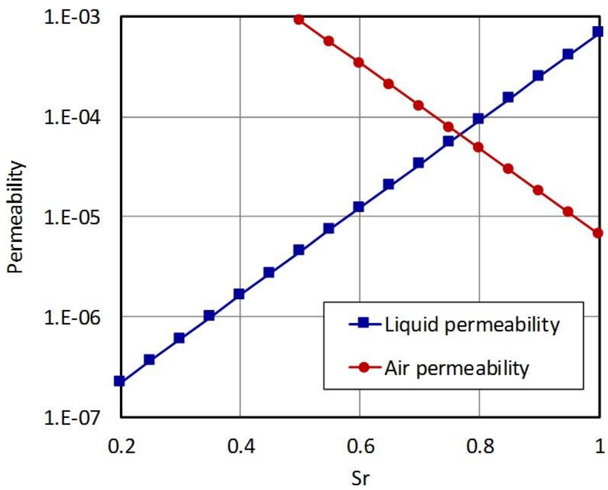

Figure 6.7: Relationship between liquid and air permeability with the degree of saturation.

Table 6.2: The soil properties and model parameters for the infiltration test on soil embankment.

Young's modulus	E	2 MPa
Poisson's ratio	ν	0.2
Initial porosity	n	0.61

Soil density	ρ	$2450\,\mathrm{kg/m^3}$
SWCC parameter	c_2	0.2
SWCC parameter	s_w	0.15
Maximum saturation	S_{rmax}	0.9
Minimum saturation	S_{rmin}	0.28
Liquid bulk modulus	K_l	2.15 GPa

The contour plots for the SPH predicted evolution of the degree of saturation and suction in the soil embankment are illustrated in Figure 6.8 and 6.9. The migration of the water is represented by the higher degree of saturation (70%) initiated on the top of the embankment. This corresponds to a small suction force of 2 kPa compared to the original 8 kPa in the domain. As a high-pressure potential difference is created by the hydraulic boundary, the saturated travels from top to the bottom of the sample, showing a wetting front that changes the S_r gradually from 38% to 70%. The reduce in suction has a similar propagation front with the wetting front. During the infiltration process, the thickness of the wetting from increases, which leads to a slower change of the suction from 8 kPa to 2kPa. This is different from the experimental results, which could be attributed to the SWCC model parameters.

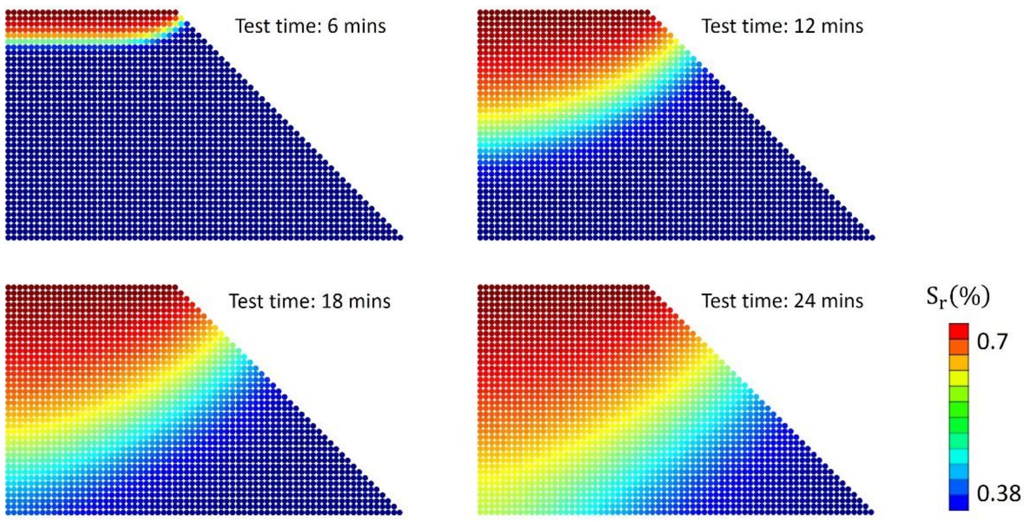

Figure 6.8: The contour plot for the SPH predicted evolution of the degree of saturation in the soil embankment.

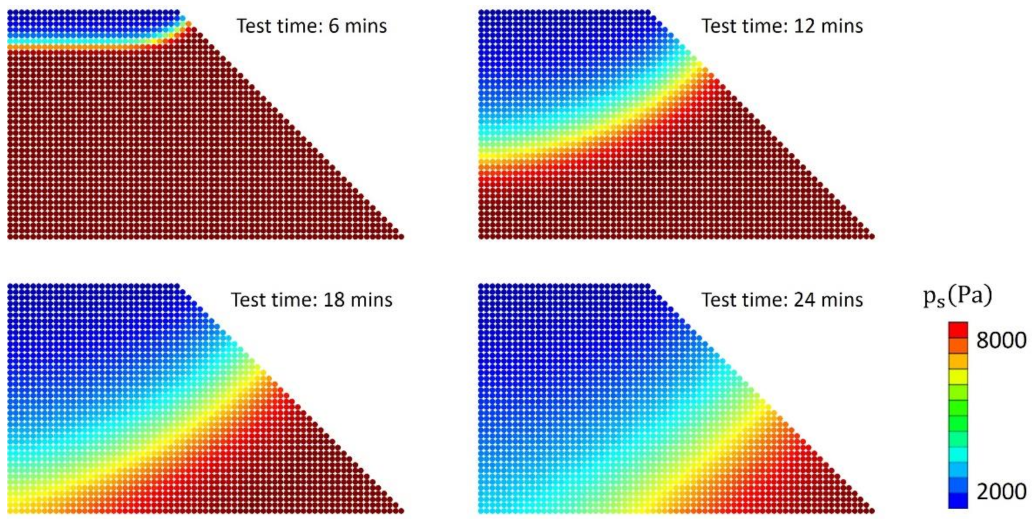

Figure 6.9: The contour plot for the SPH predicted evolution of the suction in the soil embankment.

To further quantitatively validate the SPH predicted infiltration process, the predicted negative pore water pressure (PWP) is compared with the experimentally measured ones for all 15 locations in the soil domain. The results are presented in Figure 6.10. For measuring point 1 to 5, the SPH method captures very well the initial and residual negative PWP compared to the experiment. The wetting process is also well captured showing a similar range for the negative PWP to change from -8 kPa to -2 kPa. The SPH results demonstrate a decrease in the rate for the wetting to propagate as the water travels into the soil bulk, shown as an increased thickness of the wetting front in Figure 6.8. For measuring point 6 to 10, the initial and residual negative PWP is well-captured by SPH results. The wetting process is slower compared to those in point 1 to 5 due to the fact that when water travels to the current locations, the increment in the wetting front thickness starts to show a more significant impact on the wetting rate as shown in Figure 6.10b. As to the measuring point 11 to 15, SPH captures both the initial and residual negative PWP in point 13, 14 and 15. However, due to the significant widening of the wetting front at point 11 and 12, the predicted negative PWP curves are not reaching the residual state during the test time. It is noted that the dramatic decrease in the experimentally measured negative PWP is due to the water infilling the opening voids during collapse of the embankment, which is not considered during the SPH simulation. Apart from this, the difference between the SPH predicted wetting rate and the experiment can be attributed to the fast infiltration in sandy materials in the experiment. For a better numerical prediction of this process, a more advanced hydraulic constitutive model may be required.

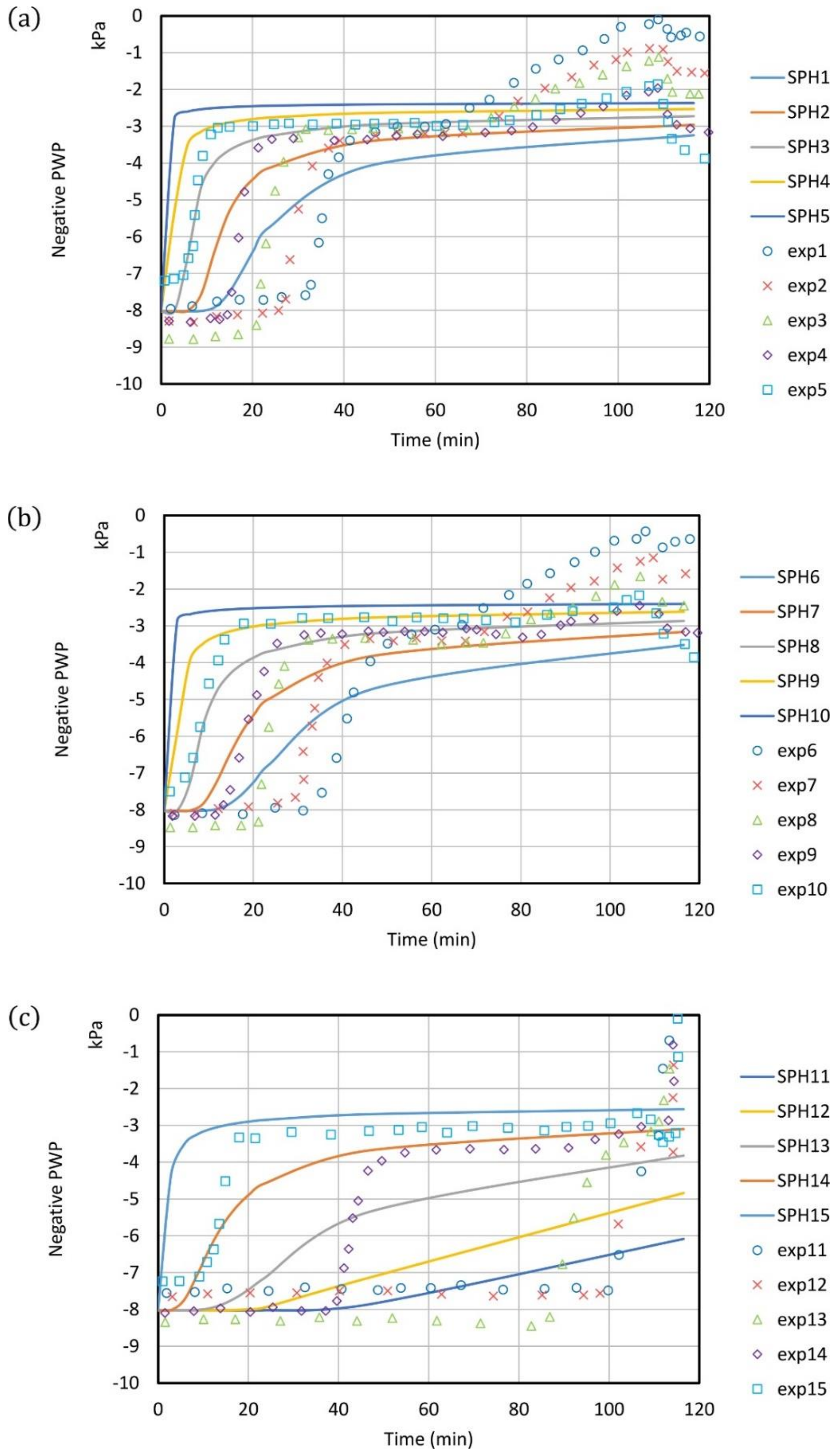

Figure 6.10: The comparison between the SPH predicted and experimental measured negative PWP evolution: (a) measuring point 1 to 5; (b) measuring point 6 to 10; (c) measuring point 11 to 15.

The proposed SPH approach shows its capability to well capture the water infiltration in a soil embankment, which yields comparable results with the experimental data. To further describe the large deformation process for unsaturated soil, the rainfall-induced slope failure cases are tests in the following sections.

6.4.3 The rainfall-induced slope failure on a soil embankment

In order to show the capability for the proposed SPH approach in capturing large deformation process in unsaturated soils, a simple rainfall-induced slope failure test is conducted in this section. The test is conducted on a full-scale slope with 32m length, 12m height at the slope top and 5m height at the slope toe (Figure 6.11). The slope is made of sandy clay with an initial negative PWP of -800 kPa which corresponds to a degree of saturation of 76%. A rainfall effect is continuously applied imposed on the open surface of the slope to trigger the failure process as shown in Figure 6.11, which increases the saturation to 99% with negative PWP of -1 kPa. The water retention curve that relates the suction and the degree of saturation is described by the van Genuchten model. When the problem domain is discretised by the SPH particles, the rainfall boundary condition is reproduced by assigning a lower negative PWP of -1 kPa to the particles that are the nearest to the open surface of the slope. To further account for the localised failure in the embankment, the soil strength parameters are defined as suction-dependent, which features the relation as described in Equation (6.71) and (6.72). According to these relations, the increasing saturation (decreasing of suction) would incur a reduction in the suction dependent soil strength parameters (ϕ_s and c_s), which leads to slope failure. In the meantime, the effective friction angle and cohesion (ϕ' and c') are kept constant. A schematic illustration for the evolution of the Mohr-Coulomb yield surface and the suction dependent soil strength parameters are illustrated in Figure 6.12. It shows that at the same deviatoric plane, the size of the Mohr-Coulomb hexagon shrinks with a decrease in the suction. When the yield surface becomes small enough, the current stress state in the soil embankment would demonstrate plastic deformation and therefore the collapse of the slope. All soil properties and numerical parameters have been summarised in Table 6.3.

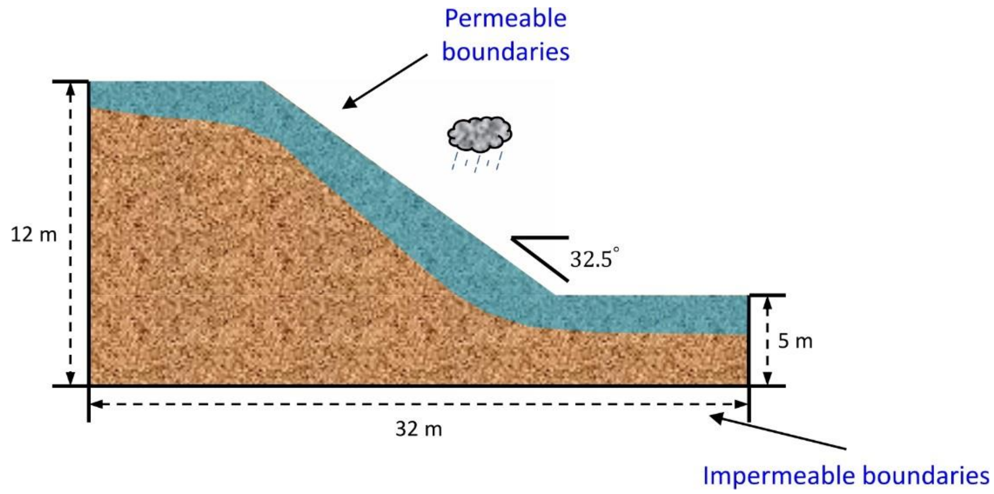

Figure 6.11: The simulation setup for the rainfall-induced slope failure in a soil embankment.

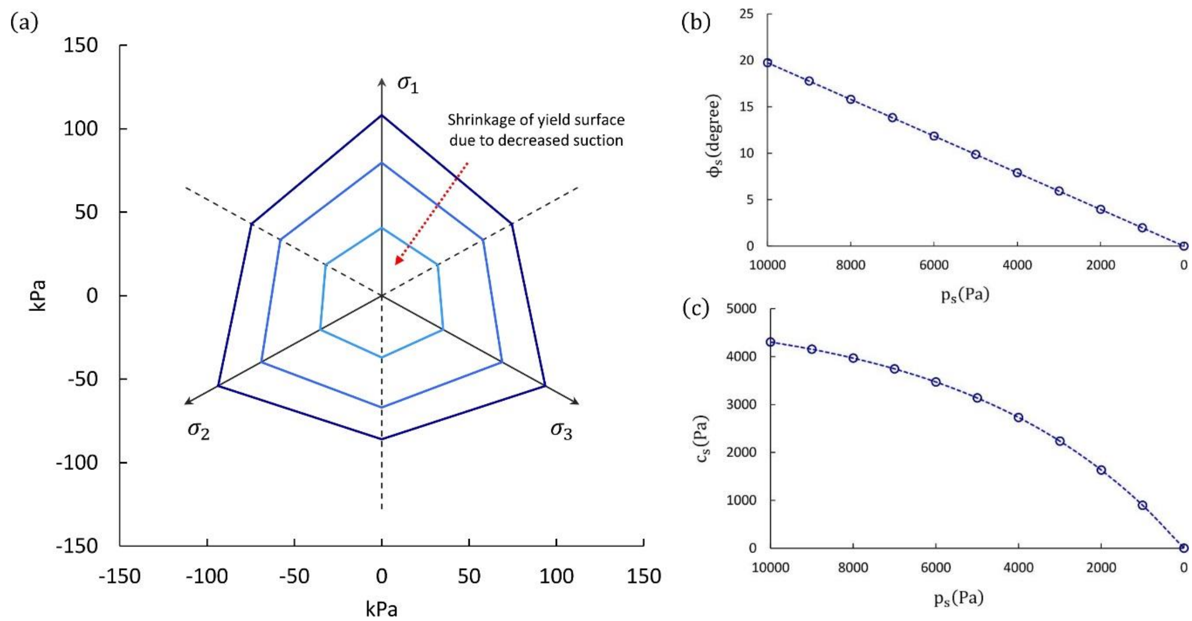

Figure 6.12: (a) The evolution of the Mohr-Coulomb yield surface in a deviatoric plane with the suction dependent soil strength parameters ϕ_s and c_s; (b) evolution of the ϕ_s with suction; (c) evolution of the c_s with suction.

Table 6.3: The soil properties and model parameters for the rainfall-induced slope failure in a sandy clay embankment.

Young's modulus	E	200 MPa

Poisson's ratio	ν	0.33
Intial porosity	n	0.35
Soil density	ρ	$2700\,\mathrm{kg/m^3}$
Effective friction angle	ϕ'	20°
Suction dependent parameters	A'	1×10^{-4}
Suction dependent parameters	B'	7×10^{-4}
Maximum suction cohesion	c_{max}	15 kPa
Effective cohesion	c'	10 Pa
SWCC parameter	α	0.01496
SWCC parameter	n	1.2
Maximum saturation	S_{rmax}	1
Minimum saturation	S_{rmin}	0
Liquid bulk modulus	K_l	2.15 GPa
Atmospheric pressure	p_{atm}	101 kPa
Liquid permeability	κ_l	$5 \times 10^{-6}\,\mathrm{m/s}$
Air permeability	κ_a	$1 \times 10^{-3}\,\mathrm{m/s}$

The obtained contour plot for the evolution of the suction in the soil domain is first plotted in Figure 6.13. The infiltration starts from the surface of the embankment, and the high degree of saturation quickly propagates through the zone for the potential slipe line of the slope (about 1.2 hours). This would start to destabilise the slope. The water infiltration continues to travel, which first saturates the toe of the embankment (about 2.5 hours). The water then flows both from top-to-bottom and right-to-left towards the bottom left corner due to a longer seepage distance in this region. This process brings a full saturation of the rainfall into the embankment (about 24.5 hours). As the plastic strain starts to develop along the slip surface in the slope, the suction shows a slightly higher value inside of the strain localisation zone. This indicates a slight decrease of water content in the shear band under extensive shearing deformations. As the failure finishes and the slope deformation approaches its maximum runoff distance, the suction in the shear band tends to reduce and become similar to the rest part of the embankment.

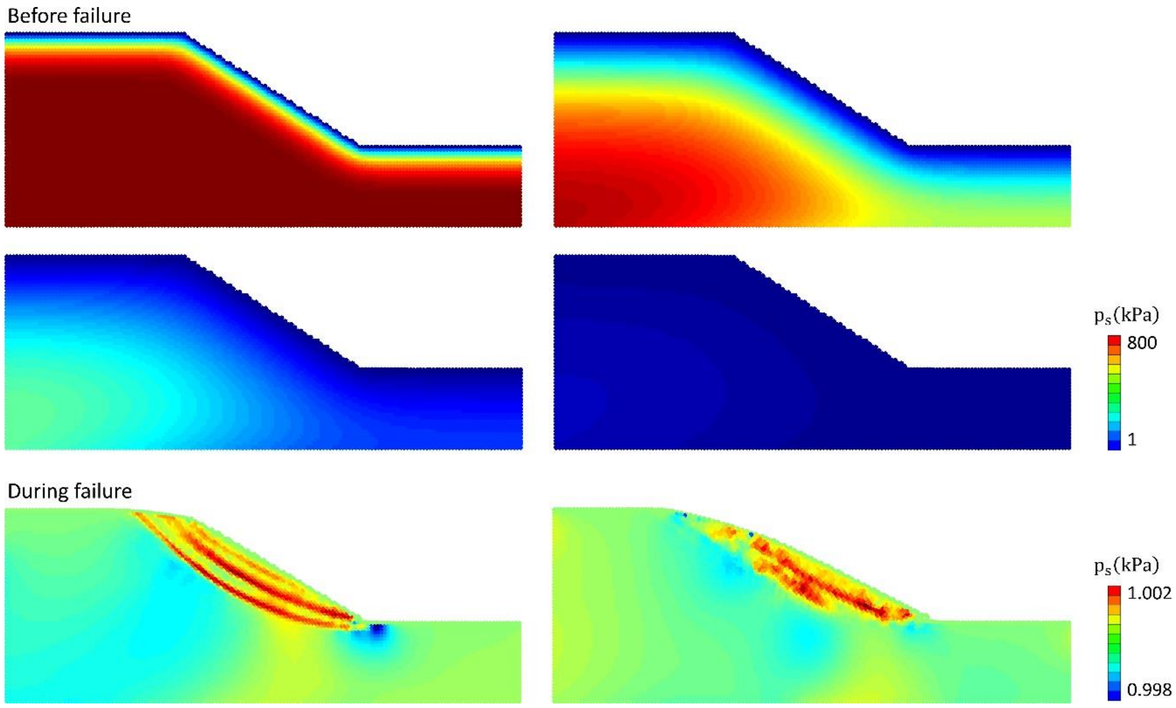

Figure 6.13: the evolution of the suction in the sandy clay embankment in the SPH test.

The evolutions of the shear strain and the total displacement during the embankment failure are further investigated with their contour plots in Figure 6.14 and 6.15. The slope is initially in equilibrium and stable condition as the pre-existed suction in the embankment provides enough strength for the soil. As the rainfall infiltration proceeds, the reduction in suction renders a reduction in total friction angle and cohesion. Therefore the balance between the soil strength and the gravitational force is no longer maintained. A localised pattern for the shear strain along a circular-shaped slipe surface becomes visible soon as the water travels through the soil slope (Figure 6.14). Since the failure condition has been triggered, the embankment demonstrates a continuous development in the localisation of the shear strain along the slip surface. The soil particles that are located above this slip surface maintain their relative location and slide towards the slope toe (Figure 6.15). The maximum total displacement of 2.5 meters has been predicted in the slope when the failure process is nearly finished, which corresponds to a maximum deviatoric strain of 1.2 in the shear band. This result has demonstrated that the proposed SPH approach is able to well-capture the failure problems in unsaturated soils involving large plastic deformations. However, quantitative calibrations are not considered in this test, therefore, to further validate the accuracy of the proposed method, a full-scale rainfall-induced slope failure test is conducted in the next section and compared with experimental results.

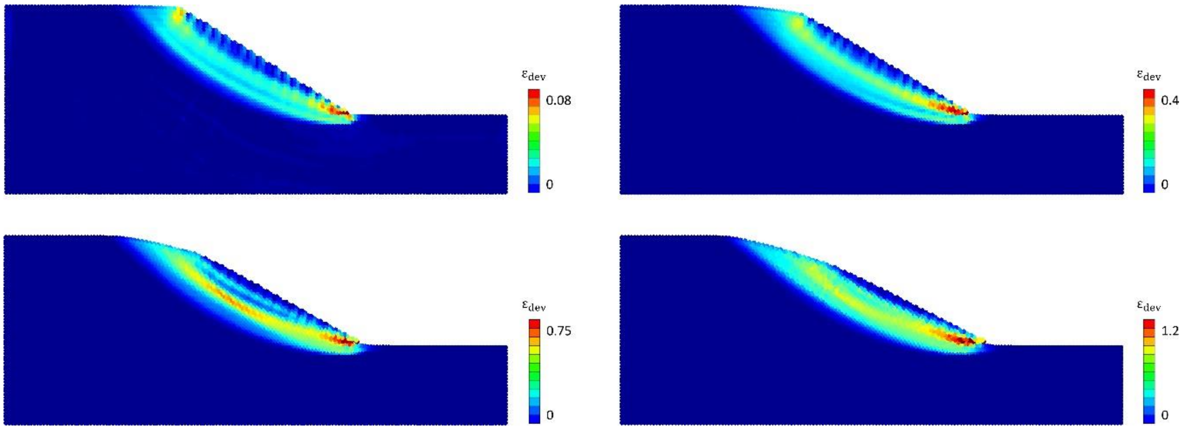

Figure 6.14: The evolution of the deviatoric strain in the embankment during the rainfall-induced failure.

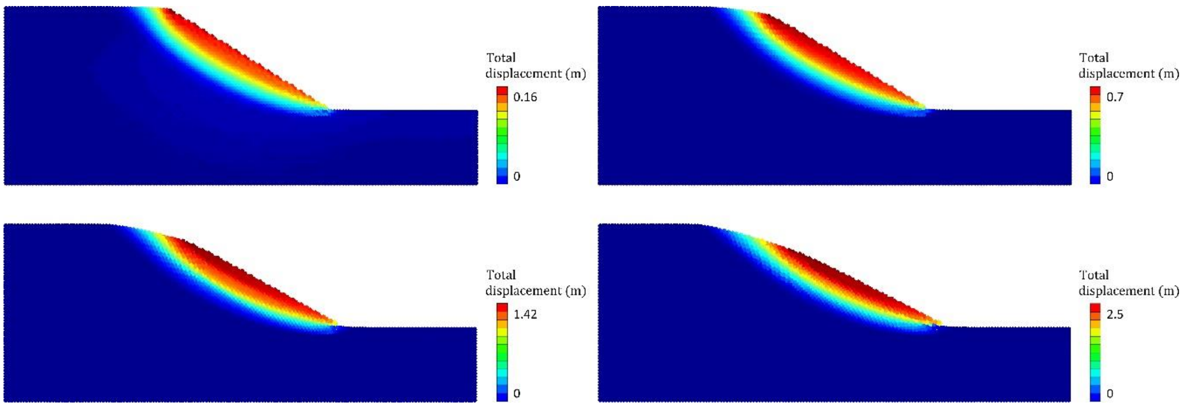

Figure 6.15: The evolution of the total displacement field in the embankment during the rainfall-induced failure.

6.4.4 The rainfall-induced failure in a full-scale slope experiment

A full-scale rainfall-induced slope failure experiment is conducted for the unsaturated Masa sand and the obtained results have been reported in the work of Danjo et al. (2012). In this section, the proposed SPH approach has been applied for simulating this experiment and the numerically predicted final slope configuration after failure as well as the negative PWP evolutions are compared to the experimental results. The soil slope is in 5 meters height and 7.87 meters long, which has a non-regular shape analogous to the infinite slope as shown in Figure 6.16a. The slope is supported by a non-deformable frame at the bottom with an inclination angle of 40°. Therefore, only the deformation for the 1-meter thick soil on top of this frame is considered in this experiment. The green line located under the slope is impermeable, while the red line at the toe of the slope is drainage layer with full permeability.

An artificial rainfall is produced inside the experiment site with an intensity of $15\sim200\ \mathrm{mm/hour}$. The rainfall effect is uniformly applied through a water-saturated membrane which covers the open surface of the slope. The characteristic relationship between the suction and the degree of saturation is described by the van Genuchten model. Before applying the rainfall, the slope soil is subjected to a moderate water content of 9.5% which corresponds to roughly a negative PWP of -2.5 kPa. As the water travels through the slope, a residual negative PWP of -0.75 kPa is achieved through a soil bulk. In the experiment, the negative PWP is measured at six locations along the middle and bottom sections in the slope as shown in Figure 6.16b. Apart from this, the experiment measured slope configuration before and after the failure process is illustrated in Figure 6.17, which is compared with the numerically obtained results in this section. To account for the loss of the material strength during rainfall, the elastoplastic Mohr-Coulomb model with suction dependent state parameters similar to the one in section 6.4.3 is applied. The evolution of the friction angle and cohesion are described by Equation (6.71) and (6.72). The parameters applied for the soil and the hydraulic constitutive model are summarised in Table 6.4.

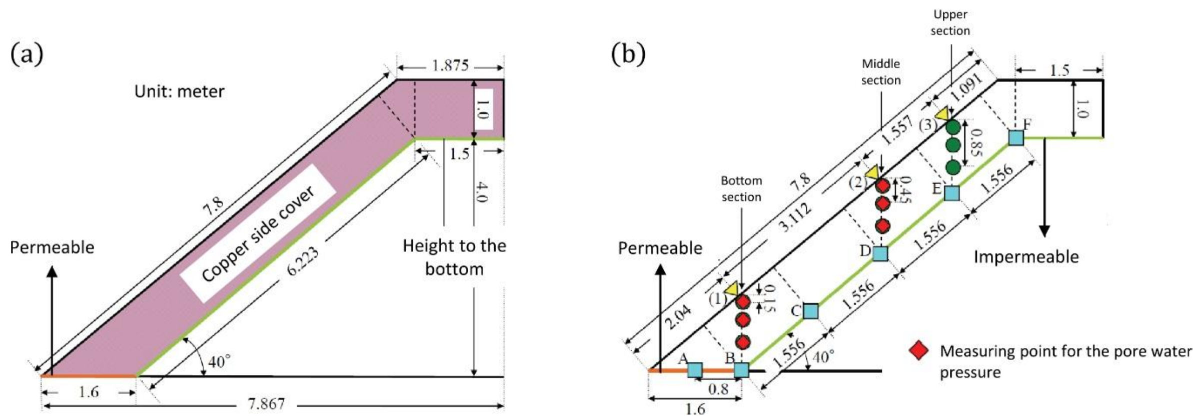

Figure 6.16: the rainfall-induced slope failure test on Masa sand: (a) the experimental configuration (Danjo et al., 2012); (b) locations of the measuring points for the negative PWP(Danjo et al., 2012).

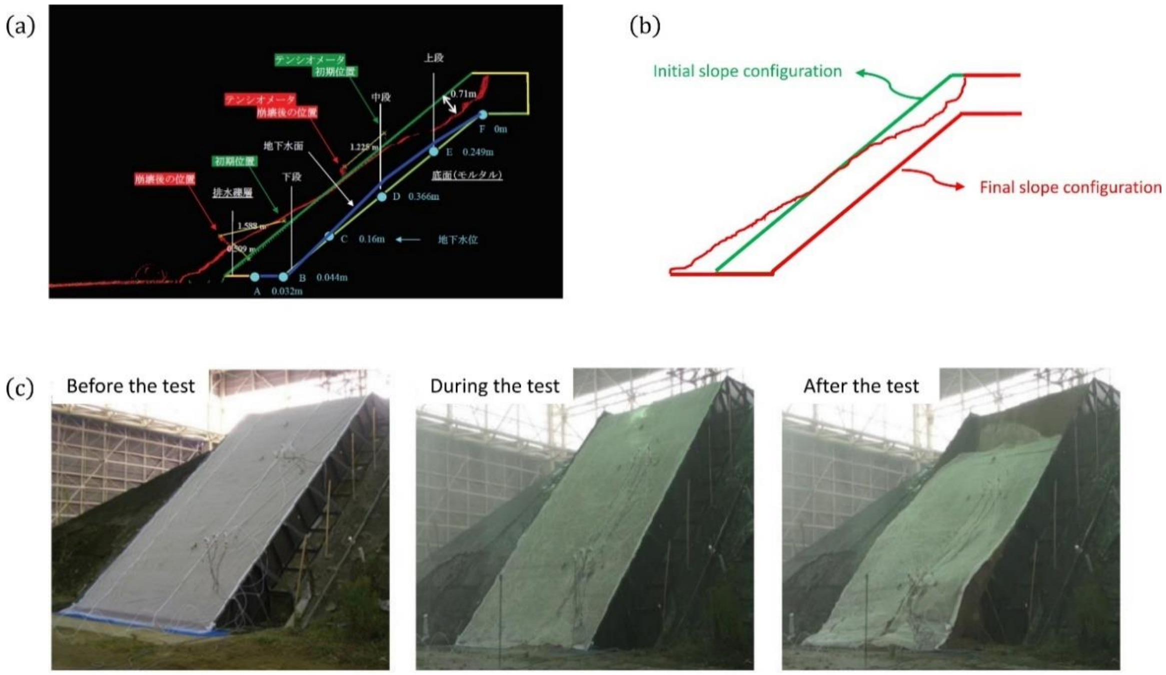

Figure 6.17: the slope configuration before and after the failure process: (a) the experiment measured configuration (Danjo et al., 2012); (b) the calibrated configuration; (c) the site photo for the slope during the failure process (Danjo et al., 2012).

Table 6.4: The soil properties and model parameters for the rainfall-induced failure in a full-scale slope experiment in Masa sand.

Young's modulus	E	5 MPa
Poisson's ratio	ν	0.2
Initial porosity	n	0.382
Soil density	ρ	$1773\,\mathrm{kg/m^3}$
Effective friction angle	ϕ'	30°
Suction dependent parameters	A'	2×10^2
Suction dependent parameters	B'	2×10^1
Maximum suction cohesion	c_{max}	5 kPa
Effective cohesion	c'	10 Pa
SWCC parameter	α	0.0015
SWCC parameter	n	1.6
Maximum saturation	S_{rmax}	0.9
Minimum saturation	S_{rmin}	0

Liquid bulk modulus	K_l	$2.15\ \mathrm{GPa}$
Atmospheric pressure	p_{atm}	$101\ \mathrm{kPa}$
Liquid permeability	κ_l	$3 \times 10^{-4}\ \mathrm{m/s}$
Air permeability	κ_a	$1 \times 10^{-4}\ \mathrm{m/s}$

The evolution of the negative PWP contour is first plotted in Figure 6.18 and the comparison between SPH predicted results with the experiment measured ones in Figure 6.19. The SPH soil domain for measuring the propagation of the negative PWP is considered elastic only as this process is relatively fast compared to the initiation of the slope failure. The grey part of the SPH domain represents the non-deformable supporting frame, which calculates the state variables using the interpolation technique presented in Chapter 3.3.3. At the beginning of the test, a uniform negative PWP of -2.5 kPa exists in the slope with the infiltration boundary condition applied to the slope surface. The horizontal top section of the slope is covered with an impermeable membrane, therefore not infiltrated by the rainfall (Figure 6.18). As the rainfall is applied to the boundary, the negative PWP is decreased at the measuring points and reaches the residual value of -0.75 kPa in about 3 hours time. The wetting rate in the SPH results is slower compared to the experiment, which is shown as the thicker wetting front in Figure 6.18 and the smaller increasing rate for the negative PWP in Figure 6.19. This phenomenon has been discussed in section 6.4.1, which is potentially due to the hydraulic constitutive model used in this study. As the water travel through the slope body, the decrease in suction reduces the soil strength and mobilises the slope. This initiates the slope failure process with significant development of the deviatoric strain in a failure circle and continuous translation of the soil on the slope surface, which is demonstrated as follows.

To further investigate the slope failure process, the evolution of the shear strain and total displacement contours are plotted in Figure 6.20 and 6.21 below. Since the water starts infiltrating from the slope surface, the soil near the open surface is first mobilised. The failure circle is developed in a relatively shallow depth in the slope. The shear strain is fast accumulating within this area and the localisation band forms (Figure 6.20). This an important characteristic to capture in the test. Since the problem domain is analogous to an infinite slope which generally has a slip circle that is adjacent to the bottom of the slope, a failure without water infiltration process would manifest shear band development near the bottom boundary. However, due to the rainfall effect which infiltrates the slope from its open surface and mobilises the unsaturated soil, the slip circle is developed similar to a normal slope with a relatively shallow depth in this test.

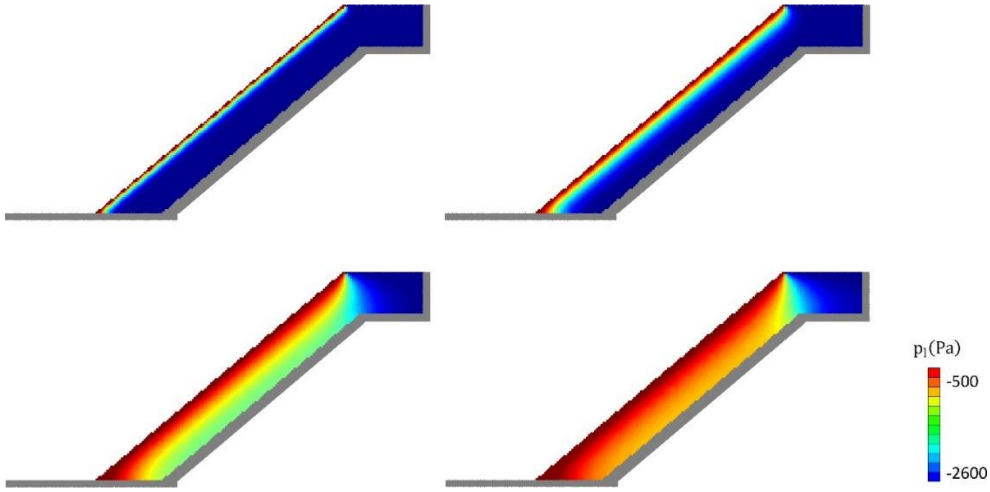

Figure 6.18: the contour of the evolution of the negative PWP in the infinite slope.

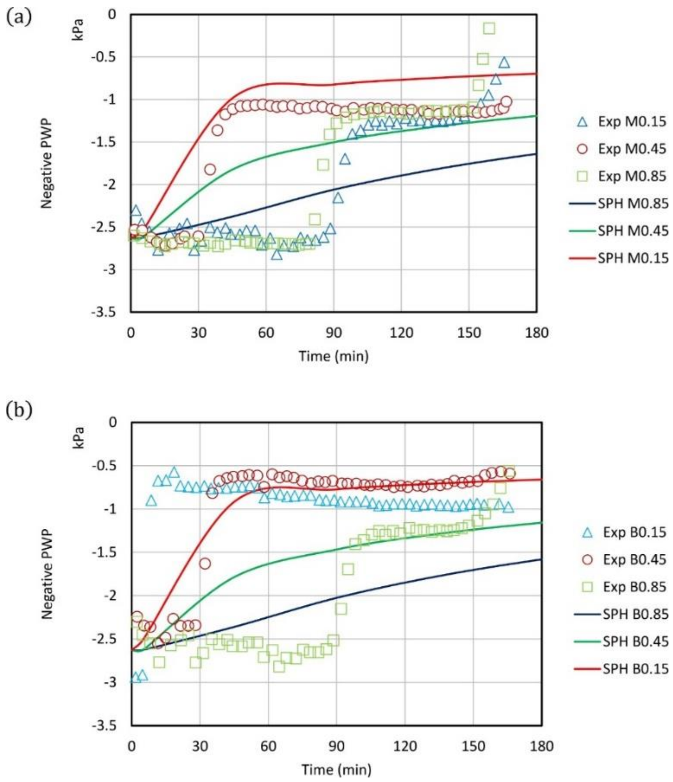

Figure 6.19: the comparison between the SPH predicted result and the experimental data for the evolution of the negative PWP in (a) middle section; (b) bottom section.

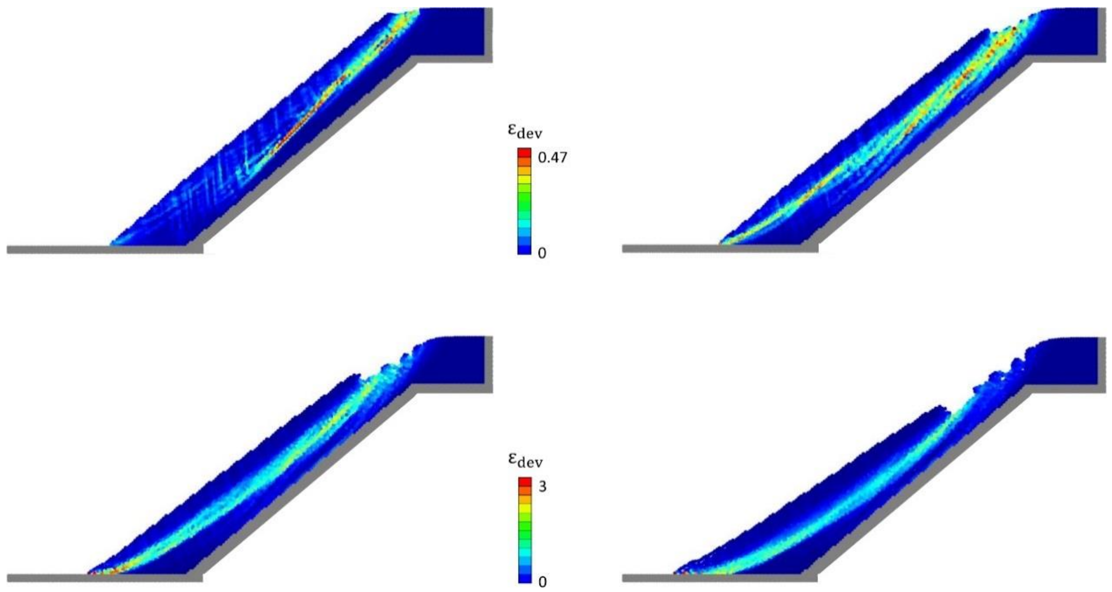

Figure 6.20: The evolution of the deviatoric strain contour in the slope.

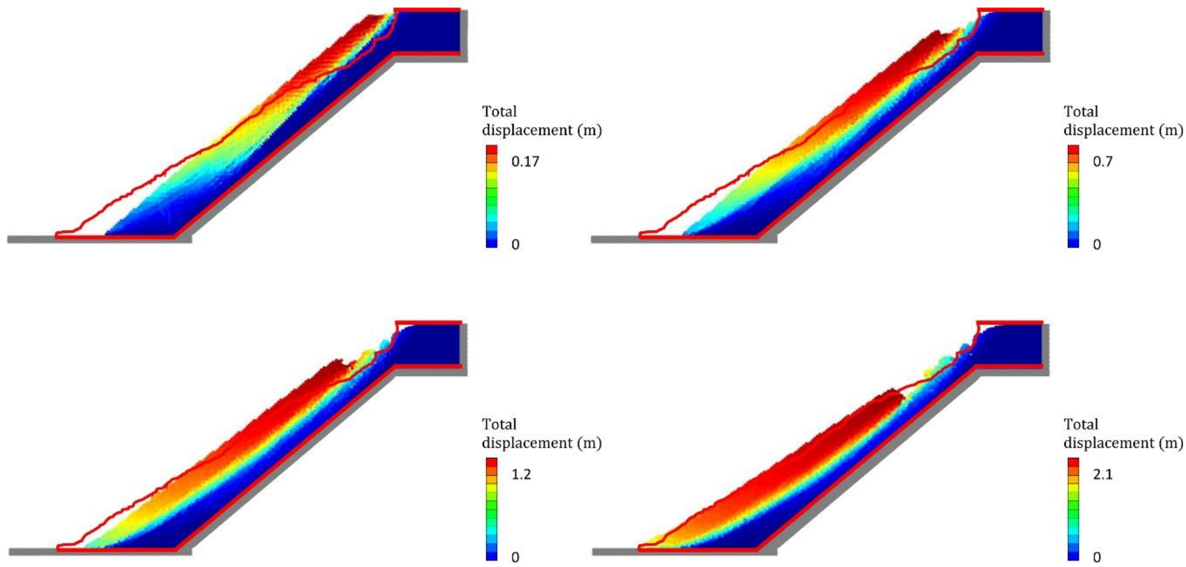

Figure 6.21: The evolution of the total displacement contour in the slope and the comparison between the SPH and experiment results for both initial and final slope configurations.

As the failure continues, the soil bulk above the slip surface slides towards the slope toe and detaches from the undeformed part at the top of the slope. The soil below the slip surface also slides to the bottom of the slope at a much slower rate as the infiltration has significantly reduced its strength. At the slope toe, a total runoff distance of roughly 1.2 meters is captured, which matches the experimental result very well. The final slope configuration of the SPH prediction is compared to the experiment measured one in Figure 6.21, showing nearly exact match of the slope surface after the failure. Both the circular slip surface at the top of the slope initiated at the beginning of the test and the total runoff of soil at the bottom of the slope are very well predicted. The above results have demonstrated the capability of the proposed numerical framework to capture very large deformation problems in unsaturated soils under relatively complex boundary conditions with a stable, accurate and time-efficient performance.

6.5 conclusion

In this chapter, a fully coupled multiphase (solid, liquid and air) framework has been implemented in the SPH method for modelling the behaviour of the unsaturated soil. The detailed formulations in this framework and their SPH approximation forms are presented. The mathematical description of the multiphase soil kinematics is derived based on the general mass and linear momentum conservation laws. A few key assumptions are made to simplify this framework, which includes the incompressible soil grain, the non-exchange mass between all phases and the isothermal condition in the unsaturated soil. To account for the relationship between the hydraulic state variables such as the suction and degree of saturation, the van Genuchten SWCC is considered. The proposed method is first validated with an infiltration test in a 1m long soil column. The measured evolution of the suction is compared to Terzaghi's theoretical solution at different locations in the sample, which shows very good agreement. Then a seepage flow test is conducted on an elastic slope structure. In this test, a simple SWCC is applied instead of the van Genuchten model, which has been calibrated to better match the soil-water characteristic relationship. The evolution of the negative PWP against time is output and compared to the experiment measured results, which shows well-agreed results. To further examine the performance of the method in large deformation problems, two slope failure tests are conducted. The first test is for a normal slope with sandy clay soil and the second test is for an infinite slope with Masa sand. The slope failure process in both tests is triggered by rainfall effect applied on the open surface of the slope. In both tests, the SPH captures the initiation and development of the shear strain localisation along the slip surface, which achieves large deformation at the end of the failure. In the second test, the numerical prediction of the negative PWP evolution and the final configuration of the slope are compared to the experimental measurement. Very good agreement has been observed for both results, which further validates the accuracy of this method. Therefore, it can be concluded that the proposed multiphase SPH framework performs very well in capturing the unsaturated soil behaviours. It is able to model practical geomechanical problems that involve very large plastic deformation and relatively complex hydraulic boundary conditions in an accurate and stable manner.

Chapter 7

Conclusion and future work

7.1 Conclusion

In this research, the existing SPH method applied in the computational geomechanics has been much advanced to facilitate its modelling of the localised failure in dry and unsaturated soils with large plastic deformations. The proposed numerical framework extends the SPH application to a wide range of soil mechanics problems that could involve confining flexible boundaries such as biaxial and triaxial tests showing a localised failure mode with both dry and unsaturated soils. Apart from this, the plastic behaviours of large scale soil structures, for instance, the rainfall-induced slope failures can also be well-captured. During the development, some fundamental characteristics of the SPH method are also investigated in detail, which facilitates the improvement on treating existing numerical pathologies such as the resolution bias which is observed in almost all types of numerical methods. The main conclusions regarding this research work can be drawn from three aspects in the following sections.

7.1.1 A generic approach to applying confining boundary condition in SPH

A new approach to applying confining stress to flexible boundaries in the SPH method is first proposed. Unlike the conventional SPH methods that impose confining boundary conditions by creating extra boundary particles, the proposed approach takes advantage of the SPH kernel truncation that occurs naturally at free-surface boundaries. This allows this approach to automatically enforce the confining condition on arbitrary-shaped free-surface boundaries and tacking the curvature change during the computation. Therefore, complicated geomechanics problems that involve moving confining boundaries such as confining triaxial tests with large plastic deformations can be simulated without difficulties. In parallel with this, an elastoplastic constitutive model with Mohr-Coulomb yield criterion is implemented to the numerical framework for allowing the accurate description for the fundamental soil mechanics. Both 2D and 3D validations including plane strain biaxial and axisymmetric tests are conducted using this approach, which shows very good agreements with both the analytical solutions and the experimental data. To further highlight the significance of this method, the key contributions are listed as follows:

- The proposed method is not an upgraded version of any existing methods to enforce confining boundary conditions in SPH. Instead, it is a novel approach to solve the difficulties in SPH applications of confining boundaries showing very high accuracy, stability and efficiency.

  The proposed computational method incorporates a generic framework of the classical Mohr-Coulomb elastoplastic model into SPH for the first time, which is able to capture a wide range of geomechanics phenomena.

- SPH validations on plane strain biaxial and axisymmetric triaxial tests have produced stable and accurate numerical results that are comparable with the classical mesh-based method FEM before excessive mesh distortion is observed in FEM domain. The numerical predictions also match well with the experimental results.

7.1.2 A study for the local and nonlocal characteristic for SPH

In this part, the characteristic of the SPH nonlocal interpolation process has been investigated in detail. The importance of this characteristic is emphasized as for allowing SPH to naturally capture the bifurcation and localisation process in the classical continuum domain, which is not achievable for FEM without regularisation techniques. Accordingly, the effect for the nonlocal interpolation to control the energy dissipation during the localisation process is studied through three comparison biaxial tests. This includes using the traditional SPH method; SPH with fixed-radius kernel function and SPH method with a nonlocal operating function. In parallel with this, a generic elastoplastic constitutive model with Mohr-Coulomb strain-softening yield surface is implemented in SPH to account for the post-localisation behaviour of the soil.

In the biaxial tests, the variation of the energy dissipation rate during the post localisation process is accounted for through applying different numerical resolutions (different particle numbers). When using the traditional SPH, the initiation and evolution of the localisation process are well captured, however, showing distinct predictions for the shear band thickness and plastic energy dissipation path (through the deviatoric stress versus axial strain plot). This result indicates that although SPH naturally possesses a nonlocal length parameter (the kernel smoothing length), the resolution bias pathology is still observed in the traditional SPH domain. The reason behind the above issue has been demonstrated due to the coupling between the kernel smoothing length and the numerical resolution, which means different SPH resolutions feature different kernel smoothing length.

To overcome this issue, the kernel smoothing length is decoupled with the numerical resolution in the second group of biaxial tests and assigned a fixed value. The obtained results show very good control over the plastic energy dissipation rate with the same shear band thickness and converged post-localisation stress path predicted for samples with different numerical resolutions. However, the above decoupling would lead to significant numerical instability and inaccuracy in problems with large deformation and high stress levels due to the second-order continuity of the SPH kernel.

Therefore, to solve this problem, an additional nonlocal operating function with bilinear shape is further implemented into SPH without the above decoupling process. The obtained biaxial test results show very good regularisation of the plastic energy dissipation rate, as well as preserving very good stability and accuracy in the computational domain. Applying this SPH framework with the nonlocal operating function and elastoplastic Mohr-Coulomb softening model, the strain localisation in biaxial tests is investigated for soils with heterogeneous properties. The initiation of the strain localisation is determined by the acoustic tensor and second-order work conditions, which show exact agreement between the SPH results with the theoretical interpretation.

7.1.3 A fully coupled multiphase framework in SPH for modelling unsaturated soil behaviour

The current SPH applications in the computational geomechanics are available for dry and saturated soils only. To allow characterising the unsaturated soil behaviours, a fully coupled multiphase framework has been proposed and implemented in the above SPH approach. The kinematics of the solid, liquid and air phases are derived based on the general mass and linear momentum balance laws. The state variables that are solved to describe the kinematics for the unsaturated soil mixture are liquid pressure, air pressure and velocity of soil grains. In parallel with this, an elastoplastic Mohr-Coulomb model with both effective and suction-dependent state parameters (friction angle and cohesion) is implemented in SPH. This allows accounting for the change of soil strength due to the variation of the soil water content, which is observed during events such as the rainfall-induced slope failures.

The above SPH framework is first validated with an infiltration test in a soil column. The dispersion of the water can be described by Terzaghi's consolidation theory. Therefore, the SPH measured evolution of the suction at different locations in the soil column is compared to the analytical solution. The numerical predictions agree quite well with the theory, which suggests that the proposed multiphase framework is able to correctly and accurately capture the diverging of the liquid in a porous media. The travelling of the liquid in a Shirasu sand embankment is then modelled to compare with the experimental results. The soil-water characteristic curve is described by a simple hydraulic model with hysteresis effect. The change of the negative pore-water pressure at fifteen locations are output and compared to the measured data. SPH predicts comparable evolution curves of the pore pressure during the 2-hour test as compared to the experiment. The above results demonstrate the capability of the proposed multiphase framework to capture the liquid diffusion process accurately with different hydraulic models.

The effect of the change of water content on the soil strength is then considered with the proposed elastoplastic model to capture the full-scale rainfall-induced slope failure problems. The increase in water content renders a reduction in suction-dependent friction angle and cohesion, while the effective strength parameters are considered constant. As the water flux travels through the slopes, soil strength reduction triggers the failure process and the intensive shear strain is well captured in the slipe circle. Comparable result for negative pore water pressure evolution in a Masa sand slope is obtained between the numerical prediction and the experiment data. The final configuration and runoff distance at the end of the failure are very well predicted by the multiphase SPH approach when compared to the experimental measurements. This indicates that the proposed method is able to not only well capture the liquid travelling process in unsaturated soils, but also accurately reproduce the process of full-scale rainfall-induced slope failure events. This has established a solid basis for this numerical framework to be applied for a wide range of geomechanical problems and engineering projects.

7.2 Future work

An advanced computation approach has been established based on the Lagrangian meshfree SPH method in this research to capture the localisation failure process in both dry and unsaturated soils. The proposed approach has been proofed with very good stability and high accuracy in solving geomechanical problems involving large deformation fields. Applying this approach, a wide range of soil boundary value problems can now be solved by SPH. However, to acquire a better understanding of the microscale mechanics of the soil as well as account for a wider spectrum of material characteristic behaviours, the following work is recommended for future research:

7.2.1 A micromechanics-based soil constitutive model

The elastoplastic Mohr-Coulomb model applied in this research captures well some general soil behaviours. However, its fundamental theory is based on phenomenological calibration with experiments at the macroscale. The micromechanics characteristic that governs basic soil kinematics such as the critical state behaviour is not considered. Therefore, a more advanced constitutive model that is based on the micromechanics theory of soil is preferred. Apart from this, to predict the strain localization in a more physically meaningful manner, a rigorous definition for the thickness and orientation of the shear band that is linked with the material characteristic scale parameters should be further incorporated.

7.2.2 An advanced hydraulic constitutive model for the unsaturated soil

In this research, the proposed multiphase SPH framework uses simplified classical models (van Genuchten) to account for the soil-water characteristic curves. Some of the more complicated, however, fundamental unsaturated soil behaviours such as the hysteresis during drying and wetting process are not considered. To address this issue, more advanced hydraulic constitutive models are preferred. The drying, wetting and scanning curves should be specifically defined for modelling a particular type of unsaturated soil. Apart from this, the transition between fully saturated and unsaturated soil conditions should be further improved to allow a natural capture this process. Therefore, both unsaturated liquid transition and saturated seepage flows can be modelled using the same numerical framework.

7.2.3 A high-performance computing framework

The current computational process of the SPH program applied in this research resort to a single CPU during each calculation. With problem domains that consist of hundreds of thousands or even millions of particles, the corresponding computational time would be prohibitively high. Therefore, a parallel computing framework which accesses multiple computer processors at the same time would greatly increase the current computational efficiency. It is acknowledged that such framework has been already incorporated in the SPH method with other research applications, which is currently under tests. Therefore, it will be readily available in the short future.

Reference

Abbo, A. J., Lyamin, A. V., Sloan, S. W., & Hambleton, J. P. (2011). A C2 continuous approximation to the Mohr-Coulomb yield surface. International Journal of Solids and Structures, 48(21), 3001-3010.

Abbo, A. J., & Sloan, S. W. (1995). A smooth hyperbolic approximation to the Mohr-Coulomb yield criterion. Computers & structures, 54(3), 427-441.

Amann, F., Button, E. A., Evans, K. F., Gischig, V. S., & Blümel, M. (2011). Experimental study of the brittle behavior of clay shale in rapid unconfined compression. Rock Mechanics and Rock Engineering, 44(4), 415-430.

Anderson, J. D., & Wendt, J. (1995). Computational fluid dynamics (Vol. 206). New York: McGraw-Hill.

Andò, E., Hall, S., Viggiani, G., Desrues, J., & Bésuelle, P. (2012). Experimental micromechanics: grain-scale observation of sand deformation.

Argilaga, A., Desrues, J., Dal Pont, S., Combe, G., & Caillerie, D. (2018). FEM× DEM multiscale modeling: Model performance enhancement from Newton strategy to element loop parallelization. International Journal for Numerical Methods in Engineering, 114(1), 47-65.

Arthur, J. R. F., Dunstan, T., Al-ani, Q. A. J. L., & Assadi, A. (1977). Plastic deformation and failure in granular media, Geothechnique, 27, No 1, 53-74

Babuvška, I., & Rheinboldt, W. C. (1978). Error estimates for adaptive finite element computations. SIAM Journal on Numerical Analysis, 15(4), 736-754.

Badel, P., Vidal-Sallé, E., & Boisse, P. (2008). Large deformation analysis of fibrous materials using rate constitutive equations. Computers & Structures, 86(11-12), 1164-1175.

Bandara, S., Ferrari, A., & Laloui, L. (2016). Modelling landslides in unsaturated slopes subjected to rainfall infiltration using material point method. International Journal for Numerical and Analytical Methods in Geomechanics, 40(9), 1358-1380.

Bandara, S., & Soga, K. (2015). Coupling of soil deformation and pore fluid flow using material point method. Computers and geotechnics, 63, 199-214.

Bardenhagen, S. G., Brackbill, J. U., & Sulsky, D. (2000). The material-point method for granular materials. Computer methods in applied mechanics and engineering, 187(3-4), 529-541.

Bardenhagen, S. G., & Kober, E. M. (2004). The generalized interpolation material point method. Computer Modeling in Engineering and Sciences, 5(6), 477-496.

Bažant, Z. P., & Jirásek, M. (2002). Nonlocal integral formulations of plasticity and damage: survey of progress. Journal of Engineering Mechanics, 128(11), 1119-1149.

Bažant, Z. P., & Lin, F. B. (1988). Nonlocal smeared cracking model for concrete fracture. Journal of Structural Engineering, 114(11), 2493-2510.

Belheine, N., Plassiard, J. P., Donzé, F. V., Darve, F., & Seridi, A. (2009). Numerical simulation of drained triaxial test using 3D discrete element modeling. Computers and Geotechnics, 36(1-2), 320-331.

Benz, W. (1990). Smooth particle hydrodynamics: a review. The Numerical Modelling of Nonlinear Stellar Pulsations, Problems and Prospects, 302, 269-293.

Bésuelle, P., Desrues, J., & Raynaud, S. (2000). Experimental characterisation of the localisation phenomenon inside a Vosges sandstone in a triaxial cell. International Journal of Rock Mechanics and Mining Sciences, 37(8), 1223-1237.

Bonet, J., & Lok, T. S. (1999). Variational and momentum preservation aspects of smooth particle hydrodynamic formulations. Computer Methods in applied mechanics and engineering, 180(1), 97-115.

Borja, R. I. (2008). Assumed enhanced strain and the extended finite element methods: A unification of concepts. Computer Methods in Applied Mechanics and Engineering, 197(33-40), 2789-2803.

Borja, R. I., Sama, K. M., & Sanz, P. F. (2003). On the numerical integration of three-invariant elastoplastic constitutive models. Computer methods in applied mechanics and engineering, 192(9-10), 1227-1258.

Brace, W. F. (1972). Laboratory studies of stick-slip and their application to earthquakes. Tectonophysics, 14(3-4), 189-200.

Bruhns, O. T., Xiao, H., & Meyers, A. (2005). A weakened form of Ilyushin's postulate and the structure of self-consistent Eulerian finite elastoplasticity. International journal of plasticity, 21(2), 199-219.

Bui. H. H. (2007). Lagrangian mesh-free particle method (SPH) for large deformation and post-failure of geomaterial using elasto-plastic constitutive models (Doctoral dissertation, 立命館大学).

Bui, H. H., Fukagawa, R. (2009). A first attempt to solve soil-water coupled problem by SPH. Japanese Terramechanics, vol 29, 33-38.

Bui, H. H., & Fukagawa, R. (2013). An improved SPH method for saturated soils and its application to investigate the mechanisms of embankment failure: Case of hydrostatic pore‐water pressure. International Journal for numerical and analytical methods in geomechanics, 37(1), 31-50.

Bui, H. H., Fukagawa, R., & Sato, K. (2006). Smoothed particle hydrodynamics for soil mechanics. proceedings of Numerical Methods in Geotechnical Engineering, Graz, 275-281.

Bui, H. H., Fukagawa, R., Sako, K., & Ohno, S. (2008a). Lagrangian meshfree particles method (SPH) for large deformation and failure flows of geomaterial using elastic–plastic soil constitutive model. International Journal for Numerical and Analytical Methods in Geomechanics, 32(12), 1537-1570.

Bui, H. H., Fukagawa, R., Sako, K., & Wells, J. (2011). Slope stability analysis and discontinuous slope failure simulation by elasto-plastic smoothed particle hydrodynamics (SPH). Geotechnique, 61(7), 565-574.

Bui, H. H., Kodikara, J. A., Pathegama, R., Bouazza, A., & Haque, A. (2015). Large deformation and post-failure simulations of segmental retaining walls using mesh-free method (SPH). arXiv preprint arXiv:1501.04000.

Bui, H. H., & Nguyen, G. D. (2017). A coupled fluid-solid SPH approach to modelling flow through deformable porous media. International Journal of Solids and Structures, 125, 244-264.

Bui, H. H., Sako, K., & Fukagawa, R. (2007). Numerical simulation of soil–water interaction using smoothed particle hydrodynamics (SPH) method. Journal of Terramechanics, 44(5), 339-346.

Bui, H. H., Sako, K., Fukagawa, R., & Wells, J. C. (2008b, October). SPH-based numerical simulations for large deformation of geomaterial considering soil-structure interaction. In The 12th International Conference of International Association for Computer Methods and Advances in Geomechanics (IACMAG) (Vol. 1, pp. 570-578).

Bui, H. H., Sako, K., Satomi, T., & Fukagawa, R. (2008c). Numerical simulation of slope failure for mitigation of rainfall induced slope disaster of an important cultural heritage. Proc. of Urban Cultural Heritage Disaster Mitigation, 2.

Cascini, L., Cuomo, S., Pastor, M., & Sacco, C. (2013). Modelling the post-failure stage of rainfall-induced landslides of the flow type. Canadian Geotechnical Journal, 50(9), 924-934.

Chalak, C., Chareyre, B., Nikooee, E., & Darve, F. (2017). Partially saturated media: from DEM simulation to thermodynamic interpretation. European Journal of Environmental and Civil Engineering, 21(7-8), 798-820.

Chang, J., Chu, X., & Xu, Y. (2014). Finite-element analysis of failure in transversely isotropic geomaterials. International Journal of Geomechanics, 15(6), 04014096.

Chang, C. S., & Hicher, P. Y. (2005). An elasto-plastic model for granular materials with microstructural consideration. International journal of solids and structures, 42(14), 4258-4277.

Chen, J. K., Beraun, J. E., & Carney, T. C. (1999). A corrective smoothed particle method for boundary value problems in heat conduction. International Journal for Numerical Methods in Engineering, 46(2), 231-252.

Chen, W. F., & Mizuno, E. (1990). Nonlinear analysis in soil mechanics (No. BOOK). Amsterdam: Elsevier.

Chessa, J., Wang, H., & Belytschko, T. (2003). On the construction of blending elements for local partition of unity enriched finite elements. International Journal for Numerical Methods in Engineering, 57(7), 1015-1038.

Cil, M. B., & Alshibli, K. A. (2014). 3D analysis of kinematic behavior of granular materials in triaxial testing using DEM with flexible membrane boundary. Acta Geotechnica, 9(2), 287-298.

Cleary, P. W., & Monaghan, J. J. (1999). Conduction modelling using smoothed particle hydrodynamics. Journal of Computational Physics, 148(1), 227-264.

Cnudde, V., & Boone, M. N. (2013). High-resolution X-ray computed tomography in geosciences: A review of the current technology and applications. Earth-Science Reviews, 123, 1-17.

Cosserat, E., & Cosserat, F. (1909). Deformable Bodies. Scientific Library A. Hermann and Sons.

Coulomb, C. A., 1773. Sur une application des regles de maximis et minimis a quelques problemes de statique, relatifs a l'architecture. Academie Royale des Sciences, 1-40.

Cundall, P. A., & Strack, O. D. (1979). A discrete numerical model for granular assemblies. geotechnique, 29(1), 47-65.

Danjo, T., Sako, K., Fukagawa, R., Sakai, N., Iwasa, N., & Quang, N. M. (2012). Verification on the Process of Rainfall-Induced Surface Failure from Rainfall Intensity, Unsaturated Seepage and Deformation Results (Japanese Title: 降雨量， 不飽和浸透挙動， 変位量の観

測結果に基づく降雨時表層すべり型崩壊過程の検証). Journal of Japan Society of Civil Engineers, Ser. C (Geosphere Engineering), 68, 508-525.

Darve, F., Sibille, L., Daouadji, A., & Nicot, F. (2007). Bifurcations in granular media: macro- and micro-mechanics approaches. Comptes Rendus Mécanique, 335(9-10), 496-515.

Das, A., Nguyen, G. D., & Einav, I. (2013). The propagation of compaction bands in porous rocks based on breakage mechanics. Journal of Geophysical Research: Solid Earth, 118(5), 2049-2066.

De Borst, R. (1991). Simulation of strain localization: a reappraisal of the Cosserat continuum. Engineering computations, 8(4), 317-332.

De Borst, R., Sluys, L. J., Muhlhaus, H. B., & Pamin, J. (1993). Fundamental issues in finite element analyses of localization of deformation. Engineering computations, 10(2), 99-121.

Dehnen, W., & Aly, H. (2012). Improving convergence in smoothed particle hydrodynamics simulations without pairing instability. Monthly Notices of the Royal Astronomical Society, 425(2), 1068-1082.

Desrues, J., & Andò, E. (2015). Strain localisation in granular media. Comptes Rendus Physique, 16(1), 26-36.

Desrues, J., Lanier, J., & Stutz, P. (1985). Localization of the deformation in tests on sand sample. Engineering fracture mechanics, 21(4), 909-921.

Desrues, J., & Viggiani, G. (2004). Strain localization in sand: an overview of the experimental results obtained in Grenoble using stereophotogrammetry. International Journal for Numerical and Analytical Methods in Geomechanics, 28(4), 279-321.

Desrues, J., Bésuelle, P., & Lewis, H. (2007). Strain localization in geomaterials. Geological Society, London, Special Publications, 289(1), 47-73.

Di Luzio, G., & Bažant, Z. P. (2005). Spectral analysis of localization in nonlocal and over-nonlocal materials with softening plasticity or damage. International Journal of Solids and Structures, 42(23), 6071-6100.

Donzé, F. V., Richefeu, V., & Magnier, S. A. (2009). Advances in discrete element method applied to soil, rock and concrete mechanics. Electronic Journal of Geotechnical Engineering, 8(1), 44.

Druckrey, A. M., Alshibli, K. A., & Al-Raoush, R. I. (2017). Discrete particle translation gradient concept to expose strain localisation in sheared granular materials using 3D experimental kinematic measurements. Géotechnique, 68(2), 162-170.

Evans, B., Fredrich, J. T., & Wong, T. F. (1990). The brittle-ductile transition in rocks: Recent experimental and theoretical progress. The Brittle-Ductile Transition in Rocks, Geophys. Monogr. Ser, 56, 1-20.

Fick, A. (1855). V. On liquid diffusion. The London, Edinburgh, and Dublin Philosophical Magazine and Journal of Science, 10(63), 30-39.

Fredlund, D. G., & Rahardjo, H. (1993). Soil mechanics for unsaturated soils. John Wiley & Sons.

Froude, M. J., & Petley, D. (2018). Global fatal landslide occurrence from 2004 to 2016. Natural Hazards and Earth System Sciences, 18, 2161-2181.

Fu, P., & Dafalias, Y. F. (2011). Study of anisotropic shear strength of granular materials using DEM simulation. International Journal for Numerical and Analytical Methods in Geomechanics, 35(10), 1098-1126.

Galavi, V., & Schweiger, H. F. (2010). Nonlocal multilaminate model for strain softening analysis. International Journal of Geomechanics, 10(1), 30-44.

Gao, Z., & Zhao, J. (2013). Strain localization and fabric evolution in sand. International Journal of Solids and Structures, 50(22-23), 3634-3648.

Gao, M., Tampubolon, A. P., Jiang, C., & Sifakis, E. (2017). An adaptive generalized interpolation material point method for simulating elastoplastic materials. ACM Transactions on Graphics (TOG), 36(6), 223.

Gingold, R. A., & Monaghan, J. J. (1977). Smoothed particle hydrodynamics: theory and application to non-spherical stars. Monthly notices of the royal astronomical society, 181(3), 375-389.

Gingold, R. A., & Monaghan, J. J. (1982). Kernel estimates as a basis for general particle methods in hydrodynamics. Journal of Computational Physics, 46(3), 429-453.

Gotoh, M. (1986). An inquiry into the spin of a deforming body. Bulletin of the JSME-Japan Society of mechanical engineers, Vol. 29, No. 258, pp. 4459-4459.

Grassl, P., & Jirásek, M. (2006). Plastic model with non - local damage applied to concrete. International Journal for Numerical and Analytical Methods in Geomechanics, 30(1), 71-90.

Gray, J. P., Monaghan, J. J., & Swift, R. P. (2001). SPH elastic dynamics. Computer methods in applied mechanics and engineering, 190(49-50), 6641-6662.

Guo, Y., & Curtis, J. S. (2015). Discrete element method simulations for complex granular flows. Annual Review of Fluid Mechanics, 47, 21-46.

Guo, N., & Zhao, J. (2014). A coupled FEM/DEM approach for hierarchical multiscale modelling of granular media. International Journal for Numerical Methods in Engineering, 99(11), 789-818.

Guo, N., & Zhao, J. (2016a). Multiscale insights into classical geomechanics problems. International Journal for Numerical and Analytical Methods in Geomechanics, 40(3), 367-390.

Guo, N., & Zhao, J. (2016b). 3D multiscale modeling of strain localization in granular media. Computers and Geotechnics, 80, 360-372.

Guo, N., & Zhao, J. (2016c). Parallel hierarchical multiscale modelling of hydro-mechanical problems for saturated granular soils. Computer Methods in Applied Mechanics and Engineering, 305, 37-61.

Hadamard, J. (1903): Lecons sur la Propagation des Ondes et les Equations de l'Hydrodynamique, Chap. VI. Paros: Hermann

Handin, J., & Hager Jr, R. V. (1957). Experimental deformation of sedimentary rocks under confining pressure: Tests at room temperature on dry samples. AAPG Bulletin, 41(1), 1-50.

Handin, J., & Hager Jr, R. V. (1958). Experimental deformation of sedimentary rocks under confining pressure: Tests at high temperature. AAPG Bulletin, 42(12), 2892-2934.

Handin, J., Hager Jr, R. V., Friedman, M., & Feather, J. N. (1963). Experimental deformation of sedimentary rocks under confining pressure: pore pressure tests. Aapg Bulletin, 47(5), 717-755.

Hernquist, L., & Katz, N. (1989). TREESPH-A unification of SPH with the hierarchical tree method. The Astrophysical Journal Supplement Series, 70, 419-446.

Higo, Y., Oka, F., Kimoto, S., Morinaka, Y., Goto, Y., & Chen, Z. (2010). A coupled MPM-FDM analysis method for multi-phase elasto-plastic soils. Soils and foundations, 50(4), 515-532.

Higo, Y., Oka, F., Sato, T., Matsushima, Y., & Kimoto, S. (2013). Investigation of localized deformation in partially saturated sand under triaxial compression using microfocus X-ray CT with digital image correlation. Soils and Foundations, 53(2), 181-198.

Hill, R. (1962). Acceleration waves in solids. Journal of the Mechanics and Physics of Solids, 10(1), 1-16.

Huang, M., Qu, X., & Lü, X. (2018). Regularized finite element modeling of progressive failure in soils within nonlocal softening plasticity. Computational Mechanics, 62(3), 347-358.

Iwashita, K., & Oda, M. (1998). Rolling resistance at contacts in simulation of shear band development by DEM. Journal of engineering mechanics, 124(3), 285-292.

Jiang, M. J., Leroueil, S., & Konrad, J. M. (2004). Insight into shear strength functions of unsaturated granulates by DEM analyses. Computers and Geotechnics, 31(6), 473-489.

Jiang, M. J., Yan, H. B., Zhu, H. H., & Utili, S. (2011). Modeling shear behavior and strain localization in cemented sands by two-dimensional distinct element method analyses. Computers and Geotechnics, 38(1), 14-29.

Jirásek, M. (2007). Mathematical analysis of strain localization. Revue européenne de génie civil, 11(7-8), 977-991.

Kelly, D. W., De SR Gago, J. P., Zienkiewicz, O. C., & Babuska, I. (1983). A posteriori error analysis and adaptive processes in the finite element method: Part I—Error analysis. International journal for numerical methods in engineering, 19(11), 1593-1619.

Khalili, N., Habte, M. A., & Zargarbashi, S. (2008). A fully coupled flow deformation model for cyclic analysis of unsaturated soils including hydraulic and mechanical hystereses. Computers and Geotechnics, 35(6), 872-889.

Khoei, A. R., & Karimi, K. (2008). An enriched-FEM model for simulation of localization phenomenon in Cosserat continuum theory. Computational Materials Science, 44(2), 733-749.

Kiriyama T. Numerical simulations of progressive failure of triaxial compression tests using generalized interpolation material point method (Japanese Title: GIMPM を用いた三軸圧縮試験の破壊シミュレーション). J Jpn Soc Civ Eng Ser A2 (Appl Mech (AM)). 2013;69(2):I_321-I_332.

Kiriyama, T. (2016). Numerical study of shear band formation in triaxial compression tests. Japanese Geotechnical Society Special Publication, 2(18), 697-702.

Kitamura, R. (2007). Soil tank test on seepage and failure behaviors of Shirasu slope during rainfall. Japanese Geotechnical Journal, 2(3), 149-168.

Kozicki, J., & Tejchman, J. (2009). Numerical simulations of triaxial test with sand using DEM. Archives of Hydro-Engineering and Environmental Mechanics, 56(3-4), 149-172.

Kulasingam, R., Malvick, E. J., Boulanger, R. W., & Kutter, B. L. (2004). Strength loss and localization at silt interlayers in slopes of liquefied sand. Journal of Geotechnical and Geoenvironmental Engineering, 130(11), 1192-1202.

Laniel, R., Alart, P., & Pagano, S. (2008). Discrete element investigations of wire-reinforced geomaterial in a three-dimensional modeling. Computational Mechanics, 42(1), 67-76.

Larsson, R., & Runesson, K. (1996). Implicit integration and consistent linearization for yield criteria of the Mohr‐Coulomb type. Mechanics of Cohesive‐frictional Materials: An International Journal on Experiments, Modelling and Computation of Materials and Structures, 1(4), 367-383.

Le, L. A., Nguyen, G. D., Bui, H. H., Sheikh, A. H., & Kotousov, A. (2018). Localised failure mechanism as the basis for constitutive modelling of geomaterials. International Journal of Engineering Science, 133, 284-310.

Leiba, M. (2013). Impact of landslides in Australia to December 2011. Australian Journal of Emergency Management, 28(1), 28.

Lenoir, N., Bornert, M., Desrues, J., Bésuelle, P., & Viggiani, G. (2007). Volumetric digital image correlation applied to X‐ray microtomography images from triaxial compression tests on argillaceous rock. Strain, 43(3), 193-205.

Liang, W., & Zhao, J. (2019). Multiscale modeling of large deformation in geomechanics. International Journal for Numerical and Analytical Methods in Geomechanics, 43(5), 1080-1114.

Libersky, L. D., & Petschek, A. G. (1991). Smooth particle hydrodynamics with strength of materials. In Advances in the free-Lagrange method including contributions on adaptive gridding and the smooth particle hydrodynamics method (pp. 248-257). Springer, Berlin, Heidelberg.

Liu, P. (2015). Extended finite element method for strong discontinuity analysis of strain localization of non-associative plasticity materials. International Journal of Solids and Structures, 72, 174-189.

Liu, W. K., Jun, S., & Zhang, Y. F. (1995). Reproducing kernel particle methods. International journal for numerical methods in fluids, 20(8‐9), 1081-1106.

Liu, G. R., & Liu, M. B. (2003). Smoothed particle hydrodynamics: a meshfree particle method. World scientific.

Liu, G. R., Liu, M. B., & Li, S. (2004). Smoothed particle hydrodynamics—a meshfree method. Computational Mechanics, 33(6), 491-491.

Liu, M. B., & Liu, G. R. (2006). Restoring particle consistency in smoothed particle hydrodynamics. Applied numerical mathematics, 56(1), 19-36.

Liu, S. H., & Sun, D. A. (2002). Simulating the collapse of unsaturated soil by DEM. International Journal for Numerical and Analytical Methods in Geomechanics, 26(6), 633-646.

Liu, S. H., Sun, D. A., & Wang, Y. (2003). Numerical study of soil collapse behavior by discrete element modelling. Computers and Geotechnics, 30(5), 399-408.

Luding, S. (2004). Micro–macro transition for anisotropic, frictional granular packings. International Journal of Solids and Structures, 41(21), 5821-5836.

Lucy, L. B. (1977). A numerical approach to the testing of the fission hypothesis. The astronomical journal, 82, 1013-1024.

Mahabadi, O. K., Randall, N. X., Zong, Z., & Grasselli, G. (2012). A novel approach for micro‐scale characterization and modeling of geomaterials incorporating actual material heterogeneity. Geophysical Research Letters, 39(1).

Mandel, J. (1966). Conditions de stabilité et postulat de Drucker. In Rheology and Soil Mechanics/Rhéologie et Mécanique des Sols (pp. 58-68). Springer, Berlin, Heidelberg.

Mánica, M. A., Gens, A., Vaunat, J., & Ruiz, D. F. (2018). Nonlocal plasticity modelling of strain localisation in stiff clays. Computers and Geotechnics, 103, 138-150.

Marketos, G., & Bolton, M. D. (2009). Compaction bands simulated in discrete element models. Journal of structural Geology, 31(5), 479-490.

Masad, E., Somadevan, N., Bahia, H. U., & Kose, S. (2001). Modeling and experimental measurements of strain distribution in asphalt mixes. Journal of Transportation Engineering, 127(6), 477-485.

Monaghan, J. J. (1992). Smoothed particle hydrodynamics. Annual review of astronomy and astrophysics, 30(1), 543-574.

Monaghan, J. J. (1994). Simulating free surface flows with SPH. Journal of computational physics, 110(2), 399-406.

Monaghan, J. J. (1996). Gravity currents and solitary waves. Physica D: Nonlinear Phenomena, 98(2-4), 523-533.

Monaghan, J. J. (2000). SPH without a tensile instability. Journal of Computational Physics, 159(2), 290-311.

Monaghan JJ, Lattanzio JC. (1985). A refined particle method for astrophysical problems. Astronomic and Astrophysics, 149, 135-143.

Morris, J. P. (1996). Analysis of smoothed particle hydrodynamics with applications. Australia: Monash University.

Morris, J. P., Fox, P. J., & Zhu, Y. (1997). Modelling low Reynolds number incompressible flows using SPH. Journal of computational physics, 136(1), 214-226.

Müller, A., & Vargas, E. A. (2019). Stability analysis of a slope under impact of a rock block using the generalized interpolation material point method (GIMP). Landslides, 16(4), 751-764.

Narasimhan, T. N., & Witherspoon, P. A. (1978). Numerical model for saturated‐unsaturated flow in deformable porous media: 3. Applications. Water Resources Research, 14(6), 1017-1034.

Needleman, A. (1988). Material rate dependence and mesh sensitivity in localization problems, Comput. Methods. Appl. Mech. Eng., 67, 69-86.

Nemat-Nasser, S. (2000). A micromechanically-based constitutive model for frictional deformation of granular materials. Journal of the Mechanics and Physics of Solids, 48(6-7), 1541-1563.

Nguyen, G. D. (2011). A damage model with evolving nonlocal interactions. International Journal of Solids and Structures, 48(10), 1544-1559.

Nguyen, G. D. (2014). An enriched constitutive model for fracture propagation analysis using the material point method. In Applied Mechanics and Materials (Vol. 553, pp. 731-736). Trans Tech Publications.

Nguyen, C. T., Bui, H. H., & Fukagawa, R. (2013). Two-dimensional numerical modelling of modular-block soil retaining walls collapse using meshfree method. Int J Geomate, 5(1), 647-652.

Nguyen, N. H., Bui, H. H., Kodikara, J., Arooran, S., & Darve, F. (2019). A discrete element modelling approach for fatigue damage growth in cemented materials. International Journal of Plasticity, 112, 68-88.

Nguyen, T. T., Bui, H. H., Ngo, T. D., & Nguyen, G. D. (2017). Experimental and numerical investigation of influence of air-voids on the compressive behaviour of foamed concrete. Materials & Design, 130, 103-119.

Nguyen, T. T., Bui, H. H., Ngo, T. D., Nguyen, G. D., Kreher, M. U., & Darve, F. (2019). A micromechanical investigation for the effects of pore size and its distribution on geopolymer foam concrete under uniaxial compression. Engineering Fracture Mechanics, 209, 228-244.

Nguyen, N. H., Bui, H. H., Nguyen, G. D., Kodikara, J., Arooran, S., & Jitsangiam, P. (2017a). A thermodynamics-based cohesive model for discrete element modelling of fracture in cemented materials. International Journal of Solids and Structures, 117, 159-176.

Nguyen, N. H., Bui, H. H., Nguyen, G. D., & Kodikara, J. (2017b). A cohesive damage-plasticity model for DEM and its application for numerical investigation of soft rock fracture properties. International Journal of Plasticity, 98, 175-196.

Nguyen, N. H., Bui, H. H., Kodikara, J., Arooran, S., & Darve, F. (2019a). A discrete element modelling approach for fatigue damage growth in cemented materials. International Journal of Plasticity, 112, 68-88.

Nguyen, N. H., Bui, H. H., Arooran, S., Nguyen, G. D., & Kodikara, J. (2019b). Discrete element method investigation of particle size distribution effects on the flexural properties of cement-treated base. Computers and Geotechnics, 113, 103096.

Nguyen, T. K., Combe, G., Caillerie, D., & Desrues, J. (2014). FEM× DEM modelling of cohesive granular materials: numerical homogenisation and multi-scale simulations. Acta Geophysica, 62(5), 1109-1126.

Nguyen, G. D., Einav, I., & Korsunsky, A. M. (2012). How to connect two scales of behaviour in constitutive modelling of geomaterials. Géotechnique Letters, 2(3), 129-134.

Nguyen, G. D., Korsunsky, A. M., & Belnoue, J. P. H. (2015). A nonlocal coupled damage-plasticity model for the analysis of ductile failure. International Journal of Plasticity, 64, 56-75.

Nguyen, G. D., Korsunsky, A. M., & Einav, I. (2014). A constitutive modelling framework featuring two scales of behaviour: fundamentals and applications to quasi-brittle failure. Engineering Fracture Mechanics, 115, 221-240.

Nguyen, G. D., Nguyen, C. T., Bui, H. H., & Nguyen, V. P. (2016). Constitutive modelling of compaction localisation in porous sandstones. International Journal of Rock Mechanics and Mining Sciences, 83, 57-72.

Nguyen, C. T., Nguyen, C. T., Bui, H. H., Nguyen, G. D., & Fukagawa, R. (2017). A new SPH-based approach to simulation of granular flows using viscous damping and stress regularisation. Landslides, 14(1), 69-81.

Nguyen, G. D., Nguyen, C. T., Nguyen, V. P., Bui, H. H., & Shen, L. (2016). A size-dependent constitutive modelling framework for localised failure analysis. Computational Mechanics, 58(2), 257-280.

Niandou, H., Shao, J. F., Henry, J. P., & Fourmaintraux, D. (1997). Laboratory investigation of the mechanical behaviour of Tournemire shale. International Journal of Rock Mechanics and Mining Sciences, 34(1), 3-16.

Nicot, F., Darve, F., & Dat Vu Khoa, H. (2007). Bifurcation and second‐order work in geomaterials. International journal for numerical and analytical methods in geomechanics, 31(8), 1007-1032.

Nonoyama, H., Moriguchi, S., Sawada, K., & Yashima, A. (2015). Slope stability analysis using smoothed particle hydrodynamics (SPH) method. Soils and foundations, 55(2), 458-470.

Oger, G., Doring, M., Alessandrini, B., & Ferrant, P. (2007). An improved SPH method: Towards higher order convergence. Journal of Computational Physics, 225(2), 1472-1492.

Oka, F., Adachi, T., & Yashima, A. (1995). A strain localization analysis using a viscoplastic softening model for clay. International journal of plasticity, 11(5), 523-545.

Oka, F., Higo, Y., & Kimoto, S. (2002). Effect of dilatancy on the strain localization of water-saturated elasto-viscoplastic soil. International Journal of Solids and Structures, 39(13-14), 3625-3647.

Oka, F., Kimoto, S., Higo, Y., Ohta, H., Sanagawa, T., & Kodaka, T. (2011). An elasto‐viscoplastic model for diatomaceous mudstone and numerical simulation of compaction bands. International Journal for Numerical and Analytical Methods in Geomechanics, 35(2), 244-263.

Oka, F., Shahbodagh, B., & Kimoto, S. (2019). A computational model for dynamic strain localization in unsaturated elasto-viscoplastic soils. International Journal for Numerical and Analytical Methods in Geomechanics, 43(1), 138-165.

Oliver, J. (1989). A consistent characteristic length for smeared cracking models. International Journal for Numerical Methods in Engineering, 28(2), 461-474.

Oliver, J. (1996). Modelling strong discontinuities in solid mechanics via strain softening constitutive equations. Part 1: Fundamentals. International journal for numerical methods in engineering, 39(21), 3575-3600.

Oliver, J., Cervera, M., Oller, S. and Lubliner, J., Isotropic damage models and smeared crack analysis of concrete, in: N. Bicanic et. al. (eds.), Proc. SCI-C Computer Aided Analysis and Design of Concrete Structures, Pineridge Press, Swansea, 1990, pp. 945-951.

Oliver, J., Huespe, A. E., Pulido, M. D. G., & Chaves, E. (2002). From continuum mechanics to fracture mechanics: the strong discontinuity approach. Engineering fracture mechanics, 69(2), 113-136.

Oliver, J., Huespe, A. E., & Sánchez, P. J. (2006). A comparative study on finite elements for capturing strong discontinuities: E-FEM vs X-FEM. Computer methods in applied mechanics and engineering, 195(37-40), 4732-4752.

Oliver, J., Linero, D. L., Huespe, A. E., & Manzoli, O. L. (2008). Two-dimensional modeling of material failure in reinforced concrete by means of a continuum strong discontinuity approach. Computer Methods in Applied Mechanics and Engineering, 197(5), 332-348.

Olsson, W. A. (1999). Theoretical and experimental investigation of compaction bands in porous rock. Journal of Geophysical Research: Solid Earth, 104(B4), 7219-7228.

Oñate, E., Zárate, F., Miquel, J., Santasusana, M., Celigueta, M. A., Arrufat, F., ... & Ring, L. (2015). A local constitutive model for the discrete element method. Application to geomaterials and concrete. Computational particle mechanics, 2(2), 139-160.

O'Sullivan, C. (2011). Particle-based discrete element modeling: geomechanics perspective. International Journal of Geomechanics, 11(6), 449-464.

Pardoen, B., Levasseur, S., & Collin, F. (2015). Using local second gradient model and shear strain localisation to model the excavation damaged zone in unsaturated claystone. Rock Mechanics and Rock Engineering, 48(2), 691-714.

Pastor, M., Peraire, J., & Zienkiewicz, O. C. (1991). Adaptive remeshing for shear band localization problems. Archive of applied mechanics, 61(1), 30-39.

Paterson, M. S. (1958). Experimental deformation and faulting in Wombeyan marble. Geological Society of America Bulletin, 69(4), 465-476.

Perzyna, P. (1966). Fundamental problems in viscoplasticity. In Advances in applied mechanics (Vol. 9, pp. 243-377). Elsevier.

Pijaudier-Cabot, G., & Bažant, Z. P. (1987). Nonlocal damage theory. Journal of engineering mechanics, 113(10), 1512-1533.

Pinyol, N. M., Alonso, E. E., Corominas, J., & Moya, J. (2012). Canelles landslide: modelling rapid drawdown and fast potential sliding. Landslides, 9(1), 33-51.

Qian, J., You, Z., Huang, M., & Gu, X. (2013). A micromechanics-based model for estimating localized failure with effects of fabric anisotropy. Computers and Geotechnics, 50, 90-100.

Randles, P. W., & Libersky, L. D. (1996). Smoothed particle hydrodynamics: some recent improvements and applications. Computer methods in applied mechanics and engineering, 139(1-4), 375-408.

Rattez, H., Stefanou, I., Sulem, J., Veveakis, M., & Poulet, T. (2018). The importance of Thermo-Hydro-Mechanical couplings and microstructure to strain localization in 3D continua with application to seismic faults. Part II: Numerical implementation and post-bifurcation analysis. Journal of the Mechanics and Physics of Solids, 115, 1-29.

Read, J. I., Hayfield, T., & Agertz, O. (2010). Resolving mixing in smoothed particle hydrodynamics. Monthly Notices of the Royal Astronomical Society, 405(3), 1513-1530.

Rice, J. R. (1976). Localization of plastic deformation (No. COO-3084/43; CONF-760835-1). Brown Univ., Providence, RI (USA). Div. of Engineering.

Rudnicki, J. W., & Rice, J. R. (1975). Conditions for the localization of deformation in pressure-sensitive dilatant materials. Journal of the Mechanics and Physics of Solids, 23(6), 371-394.

Russell, A. R., & Khalili, N. (2006). A unified bounding surface plasticity model for unsaturated soils. International Journal for Numerical and Analytical Methods in Geomechanics, 30(3), 181-212.

Sadeghirad, A., Brannon, R. M., & Burghardt, J. (2011). A convected particle domain interpolation technique to extend applicability of the material point method for problems involving massive deformations. International Journal for numerical methods in Engineering, 86(12), 1435-1456.

Sanborn, S. E., & Prévost, J. H. (2011). Frictional slip plane growth by localization detection and the extended finite element method (XFEM). International Journal for Numerical and Analytical Methods in Geomechanics, 35(11), 1278-1298.

Scholtès, L., Donzé, F. V., & Khanal, M. (2011). Scale effects on strength of geomaterials, case study: coal. Journal of the Mechanics and Physics of Solids, 59(5), 1131-1146.

Sheng, D. (2011). Review of fundamental principles in modelling unsaturated soil behaviour. Computers and Geotechnics, 38(6), 757-776.

Sheng, D., Gens, A., Fredlund, D. G., & Sloan, S. W. (2008). Unsaturated soils: from constitutive modelling to numerical algorithms. Computers and Geotechnics, 35(6), 810-824.

Simo, J. C. (1989). Strain softening and dissipation: a unification of approaches. Cracking and damage: strain localization and size effect, 440-461.

Simo, J. C., Oliver, J. A. V. I. E. R., & Armero, F. (1993). An analysis of strong discontinuities induced by strain-softening in rate-independent inelastic solids. Computational mechanics, 12(5), 277-296.

Simo, J., & Oliver, J. (1994). A new approach to the analysis and simulation of strong discontinuities. Fracture and damage in quasi-brittle structures, 25-39.

Soga, K., Alonso, E., Yerro, A., Kumar, K., & Bandara, S. (2015). Trends in large-deformation analysis of landslide mass movements with particular emphasis on the material point method. Géotechnique, 66(3), 248-273.

Song, X., & Borja, R. I. (2014). Mathematical framework for unsaturated flow in the finite deformation range. International Journal for Numerical Methods in Engineering, 97(9), 658-682.

Steffen M, Wallstedt P, Guilkey J, Kirby R, Berzins M. Examination and analysis of implementation choices within the material point method (MPM). Comput Model Eng Sci. 2008;31(2):107 - 127.

Stránský, J., & Jirásek, M. (2012). Open source FEM-DEM coupling. Engineering Mechanics, 18. Sulem, J., & Vardoulakis, I. G. (2014). Bifurcation analysis in geomechanics. CRC Press.

Sukumaran, B., McCarron, W. O., Jeanjean, P., & Abouseeda, H. (1999). Efficient finite element techniques for limit analysis of suction caissons under lateral loads. Computers and Geotechnics, 24(2), 89-107.

Sulsky, D., & Schreyer, L. (2004). MPM simulation of dynamic material failure with a decohesion constitutive model. European Journal of Mechanics-A/Solids, 23(3), 423-445.

Sultanov, L. U., & Davydov, R. L. (2014). Mathematical modeling of large elastic-plastic deformations. Applied Mathematical Sciences, 8(57-60), 2991-2996.

Summersgill, F. C., Kontoe, S., & Potts, D. M. (2017). Critical assessment of nonlocal strain-softening methods in biaxial compression. International Journal of Geomechanics, 17(7), 04017006.

Sun, D. A., Sheng, D. C., Cui, H. B., & Sloan, S. W. (2007). A density - dependent elastoplastic hydro - mechanical model for unsaturated compacted soils. International journal for numerical and analytical methods in geomechanics, 31(11), 1257-1279.

Sun, W., & Sun, D. A. (2012). Coupled modelling of hydro - mechanical behaviour of unsaturated compacted expansive soils. International Journal for Numerical and Analytical Methods in Geomechanics, 36(8), 1002-1022.

Swegle, J. W., Hicks, D. L., & Attaway, S. W. (1995). Smoothed particle hydrodynamics stability analysis. Journal of computational physics, 116(1), 123-134.

Takeda, H., Miyama, S. M., & Sekiya, M. (1994). Numerical simulation of viscous flow by smoothed particle hydrodynamics. Progress of theoretical physics, 92(5), 939-960.

Tang, H., Guan, Y., Zhang, X., & Zou, D. (2017). Low-order mixed finite element analysis of progressive failure in pressure-dependent materials within the framework of the Cosserat continuum. Engineering Computations, 34(2), 251-271.

Tang, C. S., Shi, B., Cui, Y. J., Liu, C., & Gu, K. (2012). Desiccation cracking behaviour of polypropylene fibre–reinforced clayey soil. Canadian Geotechnical Journal, 49(9), 1088-1101.

Tejchman, J. (2003). A non-local hypoplastic constitutive law to describe shear localisation in granular bodies. Archives of Hydro-Engineering and Environmental Mechanics, 50(4), 359-379.

Tejchman, J., & Bobiński, J. (2012). Continuous and discontinuous modelling of fracture in concrete using FEM. Springer Science & Business Media.

Terzaghi, K., Peck, R. B., & Mesri, G. (1996). Soil mechanics. New York: John Wiley & Sons.

Thomas, T. Y. (1961). Plastic Flow and Fracture in Solids by Tracy Y Thomas (Vol. 2). Elsevier.

Ti, K. S., Huat, B. B., Noorzaei, J., Jaafar, M. S., & Sew, G. S. (2009). A review of basic soil constitutive models for geotechnical application. Electronic Journal of Geotechnical Engineering, 14, 1-18.

Tran, K. M., Bui, H. H., Kodikara, J., & Sanchez, M. (2019). Soil curling process and its influencing factors. Canadian Geotechnical Journal, (ja).

Tran, H. T., Bui, H. H., Nguyen, G. D., Kodikara, J., & Sanchez, M. (2017). A continuum based approach to modelling tensile cracks in soils. In Poromechanics VI (pp. 337-344).

Tran, V. T., Donzé, F. V., & Marin, P. (2011). A discrete element model of concrete under high triaxial loading. Cement and Concrete Composites, 33(9), 936-948.

Tran, H. T., Wang, Y., Nguyen, G. D., Kodikara, J., Sanchez, M., & Bui, H. H. (2019). Modelling 3D desiccation cracking in clayey soils using a size-dependent SPH computational approach. Computers and Geotechnics, 116, 103209.

Utili, S., & Nova, R. (2008). DEM analysis of bonded granular geomaterials. International Journal for Numerical and Analytical Methods in Geomechanics, 32(17), 1997-2031.

Vardoulakis, I. (1980). Shear band inclination and shear modulus of sand in biaxial tests. International Journal for Numerical and Analytical Methods in Geomechanics, 4(2), 103-119.

Verghese, S. J., Nguyen, C. T., & Bui, H. H. (2013). Evaluation of plasticity-based soil constitutive models in simulation of braced excavation. Int J Geomate, 5(2), 672-677.

Vermeer, P.A., Brinkgreve, R.B.J., 1994. A new effective non-local strain measure for softening plasticity. In: Chambon, R., Desrues, J., Vardoulakis, I. (Eds.), Localization and Bifurcation Theory for Soil and Rocks. Balkema, Rotterdam, pp. 89–100.

Wang, Y., Bui, H. H., Nguyen, G. D., & Ranjith, P. G. (2017a). A mesh-free continuum based computational approach to modelling rock fracture. In Poromechanics VI (pp. 2041-2048).

Wang, Y., Bui, H. H., Nguyen, G. D., & Gamage, R. P. (2017b). Numerical simulation of size effect on rock fracture using SPH and a size-dependent constitutive model. In 9th Australasian Congress on Applied Mechanics (ACAM9) (p. 741). Engineers Australia.

Wang, Y., Bui, H. H., Nguyen, G. D., & Ranjith, P. G. (2019). A new SPH-based continuum framework with an embedded fracture process zone for modelling rock fracture. International Journal of Solids and Structures, 159, 40-57.

Wang, J., & Gutierrez, M. (2010). Discrete element simulations of direct shear specimen scale effects. Géotechnique, 60(5), 395.

Wang, Y., & Tonon, F. (2009). Modeling Lac du Bonnet granite using a discrete element model. International Journal of Rock Mechanics and Mining Sciences, 46(7), 1124-1135.

Wang, J., & Yan, H. (2013). On the role of particle breakage in the shear failure behavior of granular soils by DEM. International Journal for Numerical and Analytical Methods in Geomechanics, 37(8), 832-854.

Wawersik, W. R., & Fairhurst, C. H. (1970, September). A study of brittle rock fracture in laboratory compression experiments. In International Journal of Rock Mechanics and Mining Sciences & Geomechanics Abstracts (Vol. 7, No. 5, pp. 561-575). Pergamon.

Xiao, H., Bruhns, O. T., & Meyers, A. (2006). Elastoplasticity beyond small deformations. Acta Mechanica, 182(1-2), 31-111.

Xiong, Y., Bao, X., Ye, B., & Zhang, F. (2014). Soil–water–air fully coupling finite element analysis of slope failure in unsaturated ground. Soils and Foundations, 54(3), 377-395.

Yang, Y., & Misra, A. (2012). Micromechanics based second gradient continuum theory for shear band modeling in cohesive granular materials following damage elasticity. International Journal of Solids and Structures, 49(18), 2500-2514.

Yerro Colom, A. (2015). MPM modelling of landslides in brittle and unsaturated soils (Doctoral dissertation, Universitat Politècnica de Catalunya (UPC)).

Yerro Colom, A., Alonso Pérez de Agreda, E., & Pinyol Puigmartí, N. M. (2015). The material point method for unsaturated soils. Géotechnique, 65(3), 201-217.

Yerro, A., Alonso, E. E., & Pinyol, N. M. (2016). Run-out of landslides in brittle soils. Computers and Geotechnics, 80, 427-439.

Yin, Z. Y., Chang, C. S., Hicher, P. Y., & Karstunen, M. (2009). Micromechanical analysis of kinematic hardening in natural clay. International Journal of Plasticity, 25(8), 1413-1435.

Zárate, F., Cornejo, A., & Oñate, E. (2018). A three-dimensional FEM–DEM technique for predicting the evolution of fracture in geomaterials and concrete. Computational particle mechanics, 5(3), 411-420.

Zárate, F., & Oñate, E. (2015). A simple FEM–DEM technique for fracture prediction in materials and structures. Computational particle mechanics, 2(3), 301-314.

Zhang, F., & Ikariya, T. (2011). A new model for unsaturated soil using skeleton stress and degree of saturation as state variables. Soils and Foundations, 51(1), 67-81.

Zhao, J. (2017). Hierarchical multiscale modeling of strain localization in granular materials: A condensed overview and perspectives. In International Workshop on Bifurcation and Degradation in Geomaterials (pp. 349-359). Springer, Cham.

Zhao, S., Bui, H. H., Lemiale, V., & Nguyen, G. D. (2017a). SPH Simulation of Strain Localisation in Geomaterials Using a Visco-Plastic Constitutive Model. In Poromechanics VI (pp. 1876-1883).

Zhao, S., Bui, H. H., Lemiale, V., & Nguyen, G. D. (2017b). Numerical modelling of shear band localisation in biaxial test with Smoothed Particle Hydrodynamics method. In 9th Australasian Congress on Applied Mechanics (ACAM9) (p. 842). Engineers Australia.

Zhao, S., Bui, H. H., Lemiale, V., Nguyen, G. D., & Darve, F. (2019). A generic approach to modelling flexible confined boundary conditions in SPH and its application. International Journal for Numerical and Analytical Methods in Geomechanics, 43(5), 1005-1031.

Zhao, J., & Guo, N. (2015). The interplay between anisotropy and strain localisation in granular soils: a multiscale insight. Géotechnique, 65(8), 642-656.

Zi, G., & Belytschko, T. (2003). New crack - tip elements for XFEM and applications to cohesive cracks. International Journal for Numerical Methods in Engineering, 57(15), 2221-2240.